HRC Ground Calibration
Revision A

Smithsonian Astrophysical Observatory
60 Garden St.
Cambridge, MA 02138

September 16, 1998
SAO-HRC-CR-98-345

S.M. Murray, Principal Investigator

M.V. Zombeck, Report Editor

HRC Science Team

J.H. Chappell
A.T. Kenter
K. Kobayashi
R.P. Kraft
G.R. Meehan
M.V. Zombeck

AXAF Science Center

H. Donnelly
M. Juda
D. Patnaude
D. Pease

University of Leicester

A. N. Brunton
G.W. Fraser
J.E. Lees
S.E. Pearce
J.F. Pearson
R.M. Rideout

Osservatorio Astronomico di Palermo G.S. Vaiana

M. Barbera
A. Collura
A. Dara
S. Serio

`hrccalib/hrccalib.tex`

LIMITED WARRANTY

The HRC team warrants that:

the material presented is not defective

the data products have been properly recorded

The HRC team makes no warranties, express or implied, that the data products are free of error or that they will meet your requirements for any particular application. The HRC team disclaims all responsibility for direct, incidental, or consequential damages resulting from your use of the data products or any subsequent updates.

Contents

List of Figures

List of Tables

Preface

This report presents the results of the ground calibration of the High Resolution Camera (HRC) on AXAF. From time-to-time it will be revised to take into account new or amended results. The web site located at

`http://hea-www.harvard.edu/HRC/calib/calib.html`

should always be consulted to obtain the latest data products. In the event of a conflict between what is contained in this document and what is posted at the web site, you should consider the latter to be correct.

Please consult the CMDB Summarizer at

`http://asc.harvard.edu/cal/expander/viewer/pick_var.cgi`

in order to obtain a description of all XRCF measurements.

A list of the HRC Calibration Interface Products can be found at

`http://asc.harvard.edu/cal/hrc_cip/hrc_cip.html`

Contact Hank Donnelly (rdonnelly@cfa.harvard.edu) for information about raw data from the ground calibration.

1 INTRODUCTION

This document is a report on the ground calibration of the High Resolution Camera (HRC) on the Advanced X-ray Astrophysics Facility (AXAF). It includes subassembly calibration, X-ray Calibration Facility (XRCF) calibration, and post XRCF calibration at the Smithsonian Astrophysical Observatory (SAO) and at the Thermal-Vacuum test at the Marshall Space Flight Center (MSFC).

AXAF is a major space observatory designed to perform high resolution imaging and spectral observations in the 0.1 to 10 keV x-ray energy band. This NASA observatory is scheduled for launch in early 1999. The major observatory components are the High Resolution Mirror Assembly (HRMA), two sets of objective transmission gratings (OTG) and two focal plane instruments. The HRMA consists of four pairs of nested iridium coated Wolter type I optics. The objective transmission gratings consist of the Low Energy Transmission Gratings (LETG) and the High Energy Transmission Gratings (HETG). The two focal plane instruments are the AXAF CCD Imaging Spectrometer (ACIS) and the HRC.

The HRMA has a 10 meter focal length and a plate scale of 50μm per arc-sec. The largest paraboloid-hyperboloid pair of optics, P1H1, has a 1.2 meter diameter. The LETGs in conjunction with the HRMA and the HRC detector will perform high resolution dispersive spectroscopy with $\frac{E}{\Delta E} > 1000$ in the 0.1 to 2.0 keV x-ray band. The HETG, in conjunction with the HRMA and the ACIS, will operate in the 0.4 to 10 keV range with $\frac{E}{\Delta E} > 1000$. The ACIS consists of two detectors; one for simultaneous spatial and spectral imaging, and the other primarily for reading out the HETGs. The ACIS spatial and non-dispersive spectral resolutions are 0.6 arc-sec and $\frac{E}{\Delta E} \approx 50$ @6keV, respectively.

The HRC also consists of two distinct detector units packaged in a common housing and sharing event processing electronics. A photograph of the detector units is shown in Figure 1. A schematic diagram of the focal plane layout is shown in Figure 2.

The square MCP detector (HRC-I) has been optimized for direct x-ray imaging. Its large field of view (1/2° on a side) and extremely low background will permit high sensitivity deep exposures to be taken. The internal HRC background measured during the XRCF tests was well below 0.1 $ct\ cm^{-2} sec^{-1}$, a result of the use of low background MCP's manufactured using radioactive isotope free glass. The combination of the AXAF plate scale of 50$\mu m\ arcsecond^{-1}$ (10m focal length) and the high quality of the telescope (about 1 arc-second HEW) allow source detection to be carried out using arc-second cell sizes. The non-x-ray background in a 1 arc-second image element is of the order 1 count per fortnight (i.e., about 1 $ct\ arcsecond^{-2}$ per $10^6 seconds$).

The HRC-I can also be used as a readout device for the High Energy Transmission Grating Spectrometer (HETGS) that disperses X-rays along the diagonal of the detector. This mode of operation serves as a backup to the primary HETGS readout, the spectroscopy array of CCD's that are part of the AXAF Imaging CCD Spectrometer (ACIS).

The long segmented MCP detector (HRC-S) has been optimized for reading out the Low Energy Transmission Grating Spectrometer (LETGS) that disperses X-rays according to their energy along the Y-axis of the spacecraft (which corresponds to the long axis of the HRC-S). The internal background of this detector is very low, comparable to the HRC-I, and long exposure times are possible without significant background contributions.

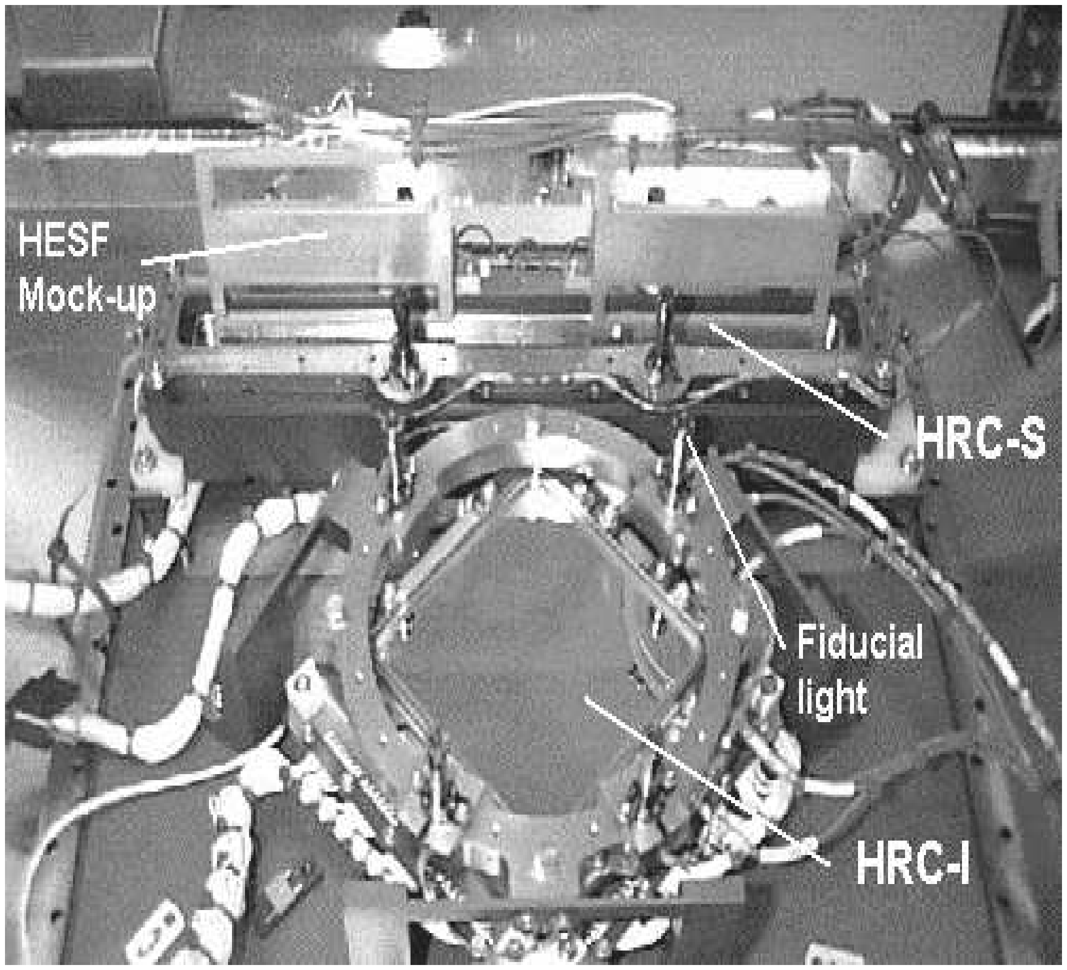

Figure 1: A photograph of the HRC detector assembly. A mock-up of the High Energy Suppression Filter (HESF) is shown.

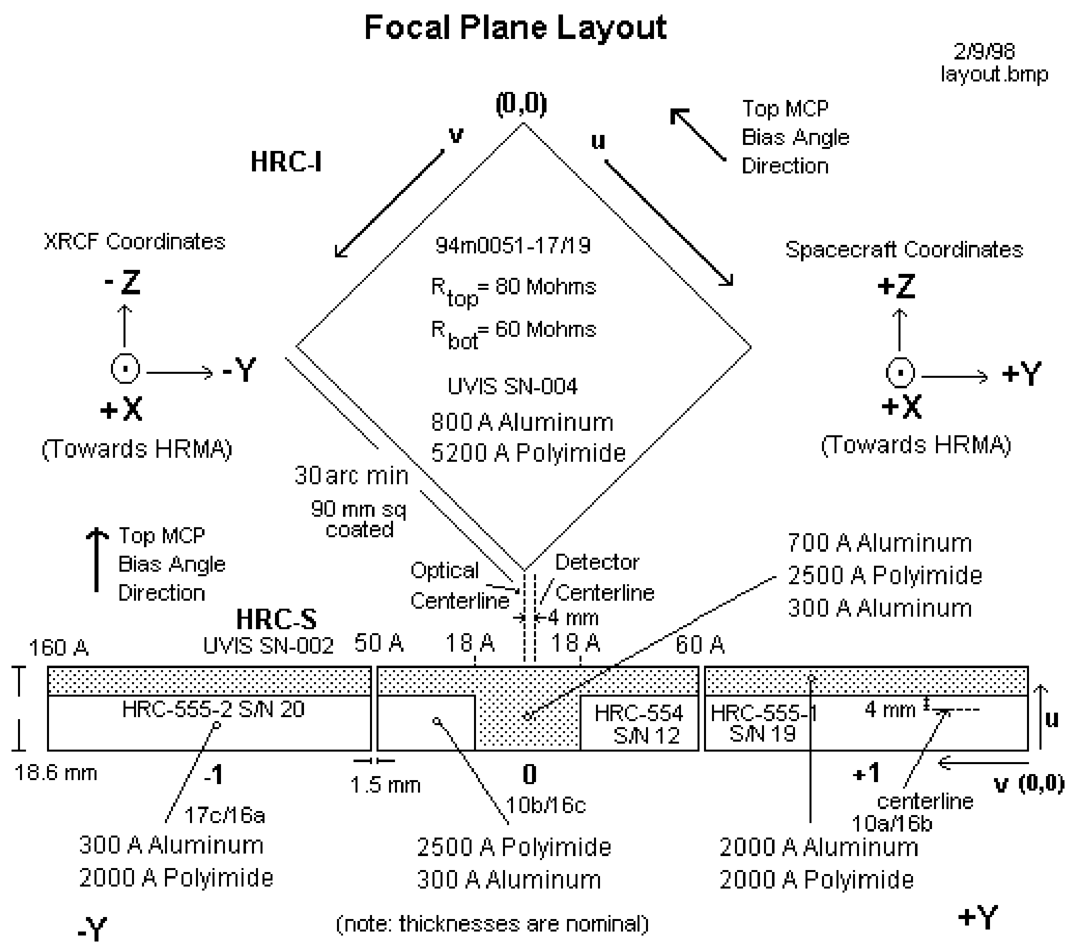

Figure 2: Layout of the HRC focal plane as viewed looking into the detector housing from the telescope. The serial numbers of the MCPs and UV/Ion shields are given. The UV/Ion shield thicknesses are nominal. Both the XRCF and Spacecraft coordinate systems are shown.

1.1 HRC-I

The HRC-I MCPs are 100mm × 100mm square plates with both input and output bias angles of 6°. Modeling of the detector quantum efficiency versus input MCP bias angle has shown that this arrangement has the highest QE when averaged over the AXAF mirror cone angles.

The HRC-I MCPs were manufactured by the Galileo Electro Optics Corporation (GEOC) of Sturbridge, MA (USA) using a special radioisotope free lead oxide glass. The GEOC MCPs have 10μm pore diameters on 12μm centers with an L/D ratio of 120:1; (i.e. they are 1.2mm thick). The serial numbers of the flight HRC-I MCPs are: **94m0051-17** (input) and **94m0051-19** (output).

The major source of background events in previous microchannel plate based detectors was internal radioactivity due to either ^{40} K or ^{87} Rb in the MCP glass. Elimination of these elements in the MCP glass formulations has resulted in a dramatic decrease in the background. Present laboratory measurements with lead shielding and HRC MCPs have achieved background counting rates of $\approx 0.04cm^{-2}sec^{-1}$. The high levels of PbO in the MCP glass and the large L/D ratios of the HRC MCPs makes the HRC susceptible to high energy X/γ-ray induced events. The high-energy out of band quantum efficiency of the HRC has been measured to be $\sim$ 18% at $\sim$ 20keV and 7% at just above the Pb K edge (88keV). For x-rays of $<$ 20keV it is practical to shield the detectors using a high Z metal. For this purpose, rigidized and non rigidized tantalum sheet metal of 0.010" thickness has been formed into a shield around the exterior of the HRC instrument.

To enhance the HRC-I quantum efficiency(QE) a $\sim 14000\AA$ CsI photocathode was vacuum evaporated on to the input face of the top MCP. The resulting photocathode enhances quantum efficiency; however, it is susceptible to damage from exposure to humid air. For this reason, the CsI coated HRC MCPs are continually either under vacuum or in a dry nitrogen atmosphere.

The HRC-I UV/Ion shield (UVIS) consists of $800\AA$ Aluminum on $5200\AA$ polyimide (nominal thicknesses). The UVIS was manufactured by the Luxel Corporation of Friday Harbor WA. UVIS filters are made by first spin casting polyimide on an 8" diameter wafer. The aluminum is then applied by a vacuum-thermal deposition process. A rotating planetary system is employed to assure uniform coating. Prior to any testing each UVIS underwent a rigorous visual inspection; shields were inspected for defects such as pinholes, inclusions or other damage.

The UV/Ion shields on the HRC detectors perform several functions. The primary UVIS function is to block ultraviolet radiation and ions; however, they also eliminate time varying structured background and act as electrodes to collect stray electrons emitted from the MCPs. Photoemission from the MCP inter-pore web has been observed to cause a faint halo about point images in ROSAT data; this halo was also observed during the development of the HRC. By applying a thin layer of conductive material to the UVIS and maintaining the UVIS at +100 Volts or greater with respect to the top MCP surface, the halo is eliminated. In the HRC detectors the UVIS are maintained at 0 Volts and are thus $\sim +3000V$ with respect to the input MCP.

The charge exiting the output MCP is collected by the Crossed Grid Charge Detector (CGCD). For the HRC-I, The CGCD consists of two planes of orthogonal Au alloy wires (Neyoro-G-SR). The Au wires are .00405" diameter and they are separated by 0.0081" giving an open area ratio for each grid of 50%. The center to center separation between the two orthogonal planes of wires is 0.008". The wires are wound on a alumina-ceramic block which has been laser ruled to ensure uniform and accurate wire location. The ceramic block material is 99.5% Alumina ceramic obtained from Coors Ceramics Co. of Golden CO. The base material is certified to be low in potassium content. Machining was performed by Insaco of Quakertown PA. The ruling was performed by Laser Services, Inc. of Westford MA. An Au plane is deposited on the ceramic block beneath the bottom grid. This Au plane is biased to act as a "reflector-plane" electrode to ensure $\approx$ 100% charge collection. The "reflector-plane" is 0.015" below the center line of the bottom grid of wires. Each wire of a CGCD axis is connected to each of its neighbors with a 10kΩ laser trimmed thin film resistor. Every eighth wire is "tapped" and connected to a charge sensitive preamplifier and postamplifier. For the HRC-I, there are 60 such taps per axis.

To eliminate the background component due to minimally ionizing cosmic rays the HRC instrument has a five-sided anti-coincidence shield. The anti-coincidence shield provides 4π Steradian coverage and rejects events which register in the HRC and the anti-co shield within a narrow coincidence time window ($\sim 500ns$). The anti-co shield is made from two types of Bicron plastic scintillator; BC 404 V and BC 428 V. The walls of the detector are BC 404 and the baseplate is BC 428V. The "V" formulation is a special minimally outgassing formulation. The detector makes use of a single fluorescence conversion across a small gap between the walls and the baseplate. The baseplate itself acts as a scintillator and a light pipe to two redundant EMR model $541E$ photomultiplier tubes. The light collection scheme was designed to minimize the number of PMTs required and associated electronics. The anti-co shield is placed outside the HRC enclosure to reduce the possibility of any volatilization of plastic and subsequent contamination of the HRC detectors. The shape of the anti-co shield was driven by the need for 4π coverage and the layout and service requirements of the HRC subassemblies.

Figure 3 is a schematic diagram illustrating the basic principles of the detector.

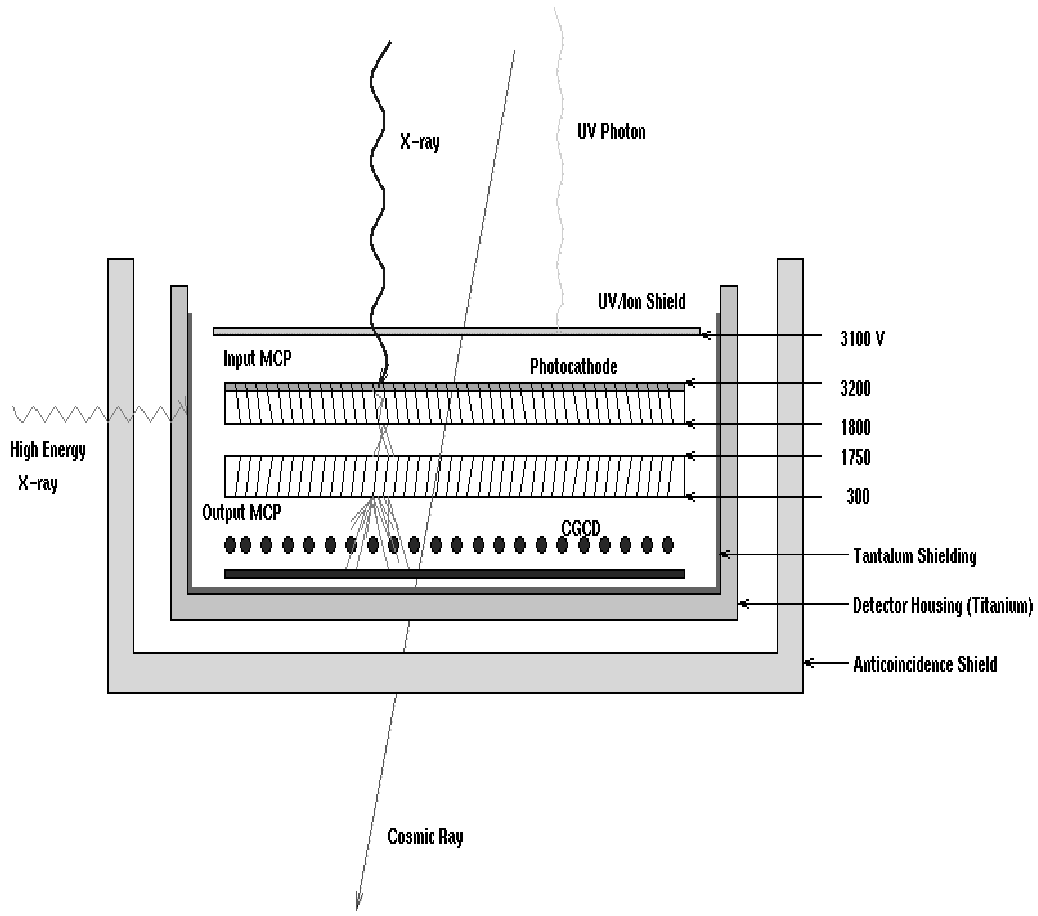

Figure 3: Schematic representation of HRC type detectors showing UV ion shield, photocathode, chevron pair of MCPs Crossed Grid Charge Detector (CGCD) readout and anti-coincidence shielding. The voltages shown are nominal. (Note: The UV/Ion shield voltage for the flight model is 0 Volts)

1.2 HRC-S

The HRC-S consists of three pairs, or segments, of microchannel plates (MCPs) in a chevron configuration with Al/polyimide UV/Ion shields (UVIS). All three segments share a single hybrid crossed grid charge detector (CGCD) readout. Each segment is 30mm×100mm (approx.), and the three segments are abutted such that the detector is ∼300mm in length in the LETG dispersion direction, with 1.5 mm (approx.) gaps between each segment. The spectral range of the LETG and HRC-S extends to 160Å, with a dispersion of 1.15Å/mm. The center segment is aligned perpendicular to the optical axis of the telescope, while the outer two segments are tilted to more closely match the Rowland circle of the LETG. The centerline of the detector is offset from the optical axis by 4 mm so that the gaps between the segments are not located at the same wavelength. A schematic diagram of the arrangement of the three segments is contained in Figure 4.

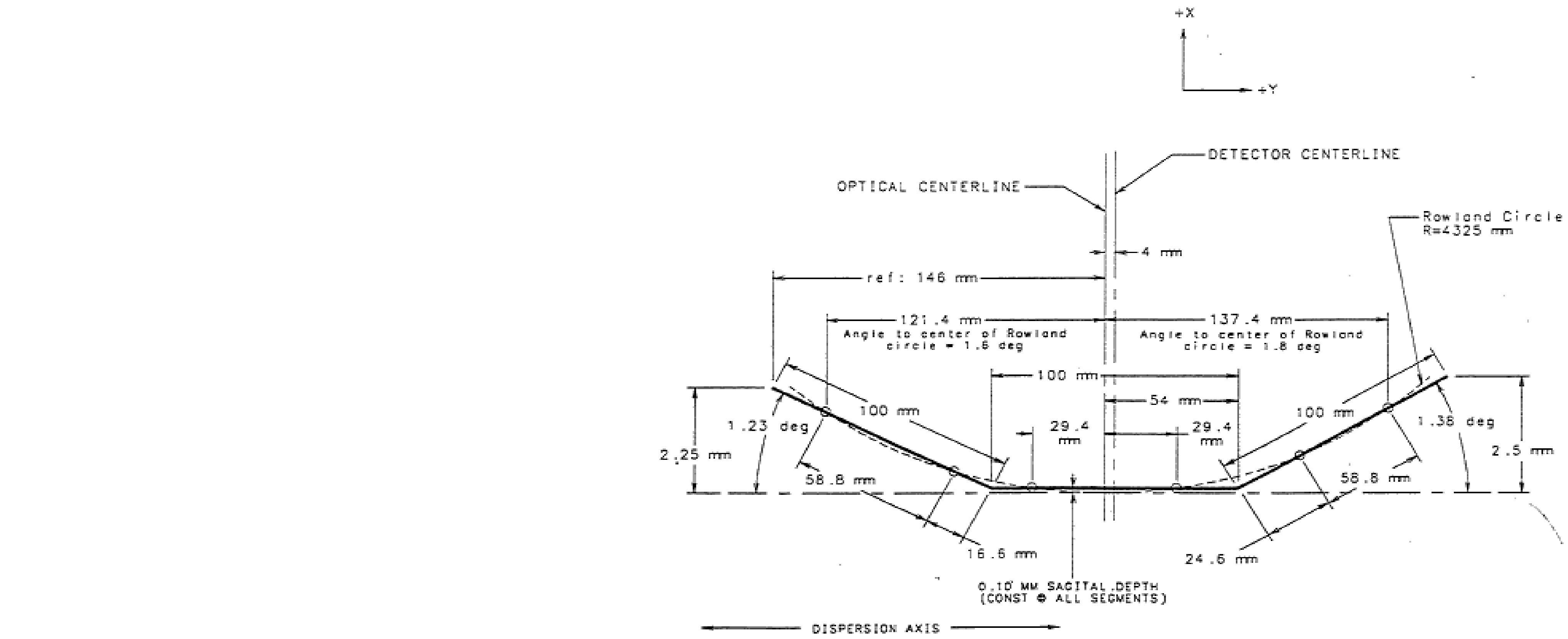

Figure 4: Schematic diagram of the layout of the three segments of the HRC-S. Note the tilt of the two wing segments relative to the center segment.

The MCPs in the HRC-S were manufactured by the Phillips Photonics Corporation (now Photonis) of Brieve, France. They have 12.5 μm diameter pores on 15 μm centers with an L/D ratio of 120:1. The pores are biased at 6 degrees in the cross-dispersion direction. The 6 degree bias maximizes the HRC QE with respect to the cone angles of the 4 shells of the HRMA. The tilt in the cross-dispersion direction minimizes QE variations in the dispersion direction due to the variation of the angle between the incident photon and the MCP wall.

β -rays from the decay of ^{40}K were found to be the largest source of internal background in MCPs manufactured by Phillips Photonics. The HRC-S MCPs have been manufactured from a glass virtually free of potassium. The internal background of the HRC-S is 0.04 cts/(cm^2 s), a factor of 10 reduction over conventional MCPs. The HRC is also provided with active and passive shielding to reduce background in the space environment. The HRC is surrounded by a tantalum shield to block hard X-rays and gamma-rays, A five-sided anti-coincidence shield consisting of a plastic scintillator and photomultiplier tubes vetos charged particle events. The background on orbit from all sources is expected to be $\sim 4\times10^{-7}$ cts/arcsec^2/s.

The UV/Ion shields of the HRC-S are composed of aluminum and polyimide, and have a complex structure to optimize the detector for use with the LETG. Their primary purpose is to block ultraviolet light, low energy electrons, and ions. The shield is also necessary to eliminate the time variable background seen on MCP detectors without a shield. It is grounded to prevent photoelectrons from the web between the pores creating a halo (as was seen on ROSAT). Schematic diagrams of the shields (which were manufactured by Luxel Corporation) are given in Figure 2 and Figure 5 . The central shield has 2500 Å of polyimide, the two wing segments 2000 Å. Each segment also has two regions with different Al thicknesses. The central segment has a central 'T' region with 1000 Å of Al, and 300 Å elsewhere. The two wing segments have 2000 Å of Al across a thin strip, and 300 Å elsewhere. The thicknesses given hereare nominal. The measured thicknesses are to be found in Tables ?? through 13. This design maximizes the soft X-ray QE at the longest wavelengths of the AXAF bandpass, but minimizes the UV flux in zero order. The thick region of Al on the wings can be used to estimate higher order spectral contamination.

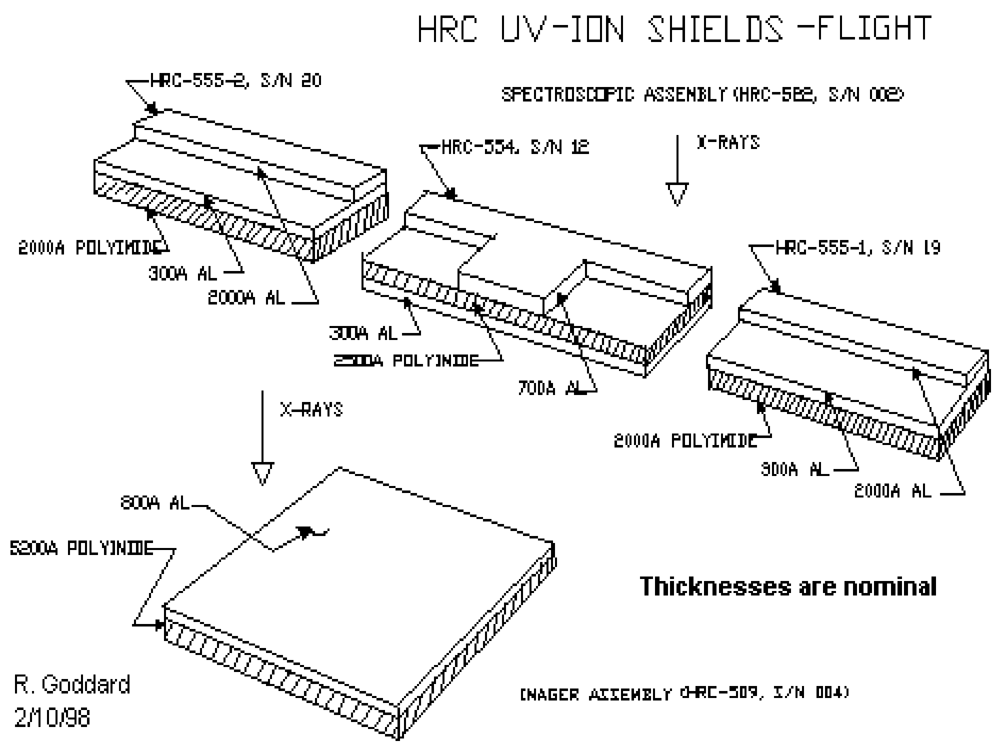

Figure 5: Schematic diagram of the HRC-I and HRC-S UVIS.

There is a single 300 mm × 20 mm Crossed Grid Charge Detector readout for all three segments of the HRC-S. A single readout is used to minimize the gaps between the segments, and the ends of the CGCD are tilted to match the orientation of the wing segments. The substrate of the grid was machined from a fine grained, isostatically pressed Al_2O_3 powder. Normally a CGCD is composed of two planes of discrete wires (as is the case for the HRC-I). This is not practical for the HRC-S. The HRC-S is composed of conventionally wound Au alloy wires for the plane in which the wires are perpendicular to the dispersion direction. For the other plane, electroplated Au strips (190 μm wide on 200 μm centers) were deposited along the dispersion direction. There is no measureable difference in grid performance between the HRC-S and HRC-I.

Every wire or Au strip is connected to its adjacent neighbor by a resistor (10 kΩ for the wires, 30 kΩ for the strips), and every eighth wire/strip (called a tap) is attached to a charge sensitive preamplifier for position determination. The CGCD contains 16×192 taps for the HRC-S. In order to make the HRC-S and HRC-I readouts redundant (the HRC-I has 64×64 taps) a multiplexing readout scheme is used, and every 64th tap along the dispersion axis is connected together. There is then a threefold degeneracy along the dispersion direction in the position of any event. This degeneracy is removed by determining which segment the event originated from by reading a signal from the bottom electrode of each of the three output MCPs. The centroid of each event is determined by using the three taps on each axis having the largest signals. The temporal resolution of the readout and associated electronics is 16 microseconds.

To enhance the HRC-S quantum efficiency(QE) a $\sim 14000\AA$ CsI photocathode was vacuum evaporated on to the input face of the top MCP. The resulting photocathode enhances quantum efficiency; however, it is susceptible to damage from exposure to humid air. For this reason, the CsI coated HRC MCPs are continually either under vacuum or in a dry nitrogen atmosphere.

The HRC-S has little intrinsic energy resolution, and order sorting in astrophysical spectra will therefore be a complex problem. In an effort to overcome this, a High Energy Suppression Filter (HESF) was added to the original HRC-S design. The HESF (shown schematically in Figure 6) is a Cr/C coated mirror mounted to the HRC-S. The detector can be moved to place the HESF in the field. Above the Cr L/C K edges, the reflectivity of the mirror is low, and it can be used to suppress the higher orders. The HESF will provide an order of magnitude or more suppression of higher orders. There is a gap in the HESF along the center of the center segment so that all high energy photons in zeroth or first order will not be reflected by the filter. The two facets are necessary to accommodate the spread of the HRMA cone angles.

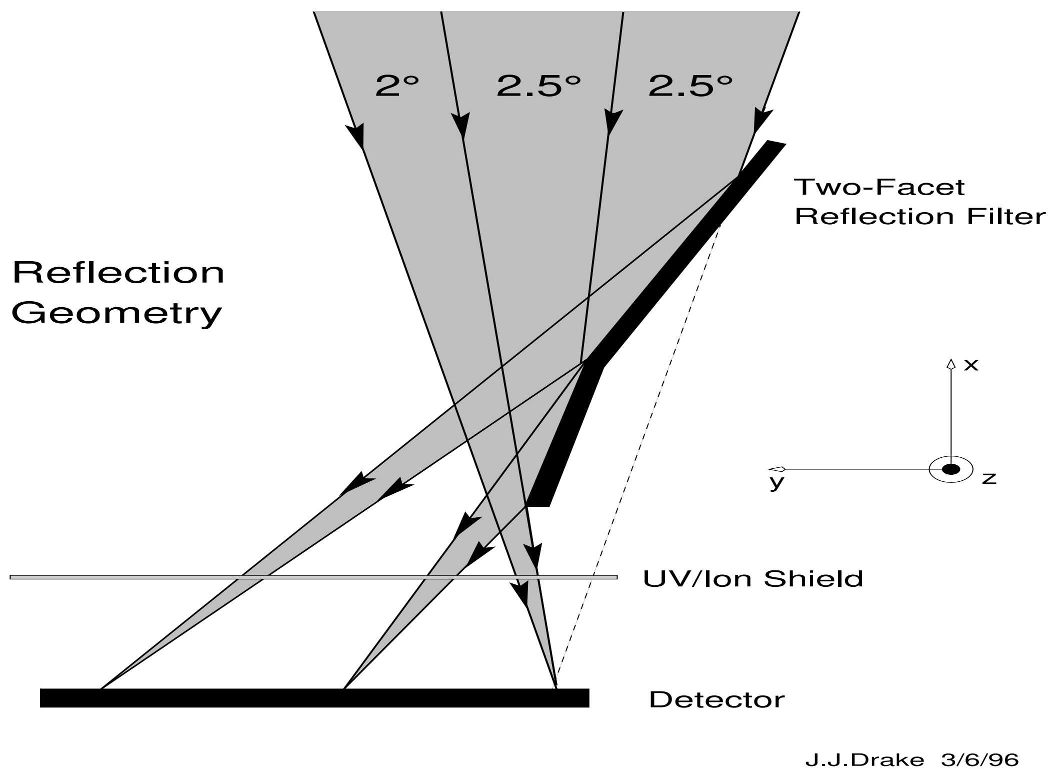

Figure 6: Schematic diagram of the layout of the three segments of the HRC-S. Note the tilt of the two wing segments relative to the center segment.

2 Calibration Definitions and Goals

For the purposes of using the HRC on AXAF for astronomical investigations, several quantities are of primary interest. These quantities are: the effective area of the HRC in conjunction with the HRMA (and the OTG's); the point spread function (PSF) of the HRC in conjunction with the HRMA (and the OTG's); count rate linearity; spatial variation of the response; geometrical non-linearity; background and background non-uniformity.

To fulfill the scientific goals of the HRC mission, a thorough calibration program was planned. This program was intended to calibrate the HRC/AXAF at various levels of integration from subassembly up through an end-to-end calibration encompassing the HRMA, the OTG's and the detectors. The subassembly testing was to be performed at the Smithsonian Astrophysical Observatory (SAO) in Cambridge MA, the Osservatorio Astronomico di Palermo G.S. Vaiana in Palermo, Italy, and the X-ray Astronomy Group of the University of Leicester in Leicester, England prior to shipping the completed instrument to the X-ray Calibration Facility (XRCF) at Marshall Space Flight Center (MSFC) in Huntsville AL. "End-to-end" testing at XRCF was to determine the Effective Area of the HRC instruments in conjunction with the HRMA and the OTG's for both on and off axis. The Point Spread Function (PSF) of the instrument/HRMA was to be determined as well as count rate linearity and geometrical linearity.

The original subassembly plan included detailed testing and calibration of the UVIS characteristics, including uniformity, X-ray and UV transmission. The QE of the HRC detectors was to be determined at 22 discrete energies and at various angles of incidence. These angles of incidence were to encompass the cone angles of the HRMA. The HRC resolution, spatial linearity, count rate linearity were also to be determined. These calibration data were then to be incorporated into empirical models of the HRC performance. Due to scheduling pressure to complete and deliver the final HRC, only a fraction of the original calibration was accomplished. During final assembly, some additional design modifications were also implemented to accommodate the incorporation of all the additional flight hardware; namely it was decided that it would be necessary to operate with the UVIS at ground potential as opposed to the original +100 volts with respect to the top MCP. Laboratory tests were performed with non-flight HRC detectors to examine the effects of this late design change and at that time none were observed.

Upon delivery of the flight HRC to XRCF for end-to-end testing, several problems were discovered. First, a very high amplitude 90kHz ripple was observed from the high voltage power supplies. This ripple was present on the trigger signal for the HRC and necessitated operating the HRC at a much higher trigger threshold. This higher trigger threshold resulted in much lower effective HRC QE values, especially for the HRC-S detector. Second, a low intensity secondary image in the PSF was observed in the HRC-I detector. Later it was determined that this secondary image was due to operating the UVIS at ground potential. Third, the MCPs showed a higher than expected gain causing some event pulses to be saturated.

Following the XRCF calibration, the gain saturation problem was fixed and the HRC was returned to the SAO laboratory in Cambridge, MA. At SAO, the HRC detectors were calibrated for absolute quantum efficiency and spatial uniformity. Furthermore, at this time the HVPS ripple was fixed by installing some filter networks into the high voltage power supplies.

After flat field testing of the HRC at SAO, the HRC was returned to XRCF for vibration and thermal-vacuum testing. During the last stages of thermal-vacuum testing, the HRC was tested for off band response to visible and UV light.

2.1 Quantum Efficiency and Effective Area

The quantum efficiency QE at a given energy E is a measure of the response of a detector to an incident monochromatic flux ψ, i.e. the detector count rate CR is given by

$$CR(E) = QE(E)\psi(E). \tag{1}$$

The effective area EA at a given energy of an optic and detector is the response of the combination to a uniform monochromatic incident flux density Ψ from a point source at infinity, i.e. the detector count rate is given by

$$CR(E) = EA(E)\Psi(E). \tag{2}$$

Knowing the incident flux density in photons $cm^{-2}\ s^{-1}$ and the count rate in counts s^{-1} immediately provides the effective area in cm^2.

The QE of an HRC detector varies not only with energy but with the azimuth ϕ and polar angle θ of the incident rays and their intersection u,v with the detector plane. Thus the effective area of the combined HRMA and HRC can be expressed as sum over the four mirror shells of the HRMA

$$EA(E, u, v) = \sum_{i=1,2,4,6} \frac{1}{2\pi} \int_0^{2\pi} d\phi A_i(E, \phi) QE(E, \phi, \theta_i, u, v), \tag{3}$$

where the sum is over the four mirror shells of the HRMA, $A_i(E, \phi)$ is the energy dependent and possibly azimuthally dependent area of the i'th mirror shell per unit azimuth angle, ϕ and θ_i are the azimuth of the incident rays and the average cone angle of the i'th mirror shell, respectively. This equation can be used to predict the effective area of the combined HRMA and HRC providing the areas of the four mirror shells and the quantum efficiency of the HRC are known from independent measurements. This prediction can then be compared to a direct measurement of the effective area of the combined HRMA and HRC at the same energy. By combining all the measurements of effective area, mirror shell area, and HRC quantum efficiencies, a consistent model of the effective area can be constructed over the operational energy range (0.1 - 10 keV) of the AXAF. The goal of the calibration is to accomplish this with a relative accuracy of $\pm 7\%$.

2.2 Spatial Uniformity

Spatial uniformity refers to the variation of the quantum efficiency of a two-dimensional detector with position and is expressed by a function of the form $QE(u, v, E)$, where u, v are the two spatial coordinates of the detector and E is the incident energy. It is usually determined by illuminating the detector with a spatially uniform beam. This is also referred to as flat-fielding.

2.3 On-axis Point Spread Function

The spatial distribution of the monochromatic image of a point source object, $h(u, v; \alpha, \beta)$, is called the point spread function (PSF) of the optical system. u and v are the coordinates of the image points and α and β are the coordinates of the ideal image of the object (a point). If $f(\alpha, \beta)$ is the ideal image of an extended monochromatic object, the image produced by the optical system is given by

$$g(u, v) = \int\int h(u, v; \alpha, \beta) f(\alpha, \beta) d\alpha d\beta. \tag{4}$$

In some cases, the optical system is shift-invariant (at least, over a restricted field)

$$h(u, v; \alpha, \beta) = K(u - \alpha, v - \beta), \tag{5}$$

and the integral above can be written as a convolution:

$$g = K \star f, \tag{6}$$

or

$$g(u,v) = \int\int K(u-\alpha, v-\beta) f(\alpha,\beta) d\alpha d\beta. \tag{7}$$

The HRMA PSF can be considered shift-invariant over the central few arc minutes of its field-of-view (FOV) and the HRC is shift-invariant over its entire FOV. The PSF of the combined HRMA and HRC is a convolution of the individual PSF's over the central FOV

$$h_{HRMA+HRC} = h_{HRMA} \star h_{HRC}. \tag{8}$$

If the combined PSF is radially symmetric, we can also calculate an encircled energy function $E(r)$, the fraction of the total imaged photons that are within a circle of radius r

$$E(r) = \frac{\int_0^r K(r) r dr}{\int_0^\infty K(r) r dr}, \tag{9}$$

where K(r) is the radially-symmetric PSF of the combined HRMA and HRC.

The radius of the circle which contains 50% of the imaged photons, the half-power radius $r_{\frac{1}{2}}$ is defined by

$$E(r_{\frac{1}{2}}) \equiv 0.50 = \frac{\int_0^{r_{\frac{1}{2}}} K(r) r dr}{\int_0^\infty K(r) r dr}. \tag{10}$$

2.4 Point Source Count Rate Linearity

A photon detector with a linear response is characterized by the following relationship between the incident flux ϕ and the detector count rate CR:

$$CR = k\phi + B \tag{11}$$

where k is a constant and B is a background term. From the discussion above we see that k is equivalent to the quantum efficiency of the detector.

For rates considerably below the AXAF telemetry limit (184 cts s^{-1}), the relationship between the count rate of the HRC and the incident flux of a point source is determined by the response of the detector microchannel plates (MCP's). When a photon is absorbed by a pore in an MCP, producing a cascade of electrons, the charge available for re-establishing the electric field in the pore is temporarily reduced. If the interval between photon absorption in a given pore is shorter than the charge replenishment time, the electric field will not be completely re-established leading to a temporary, localized reduction in the gain. This in turn may lead to a reduction in the quantum efficiency, if the amount of charge detected from an event falls below the Lower Level Discriminator (LLD) cut off.

For most normal operating conditions (flux $<$ 2 cts s^{-1} $pore^{-1}$, or 5 cts s^{-1} in the focused beam of AXAF), we expect the response of the detector to be linear requiring no correction. However, there remains the possibility via either serendipitous detections or transient phenomena that the normal operation limitation (5 cts s^{-1} may be violated and we can expect a non-linear relationship between the input flux and the detector count rate.

2.5 Diffuse Source Count Rate Linearity - Dead Time

The electronic processing time for determining the position of a detected events is 68.5 ms. If this were the only contribution to deadtime, for extended objects less than 1.5% of detectable events would be lost at rates up to 200 s^{-1}. However, the maximum telemetry rate is 184 cts s^{-1} and this leads to a rapid increase in deadtime when the the count rate exceeds the telemetry rate. The count rate can be corrected by using the secondary science rate (basically an event counter) which tracks the rate of detected, but not necessarily fully processed events, with very low deadtime.

2.6 Spatial Linearity - Geometric Distortion

An imaging detector produces geometric deviations from a perfect image of an object. Let (x, y) represent the coordinates of points in the geometrically correct image and (u, v) the points in the real image. The two coordinate systems can be related via a pair of mapping functions U and V such that

$$u = U(x, y), \tag{12}$$

$$v = V(x, y). \tag{13}$$

The mapping functions are usually chosen as simple polynomials of first, second, or third order. For example, a second order polynomial mapping is given by

$$u = a_0 + a_1 x + a_2 y + a_3 xy + a_4 x^2 + a_5 y^2, \tag{14}$$

$$v = b_0 + b_1 x + b_2 y + b_3 xy + b_4 x^2 + b_5 y^2. \tag{15}$$

If the coefficients a_i and b_i are known, the transformation can be applied in reverse to obtain the true image from the distorted one.

A linear mapping is represented by a first order polynomial

$$u = a_0 + a_1 x + a_2 y, \tag{16}$$

$$v = b_0 + b_1 x + b_2 y, \tag{17}$$

and represents a simple displacement, stretching, and rotation of the image. We expect deviations from linearity for the HRC of the order of two detector pixel (approx. $\frac{1}{4}$ arc second) over the entire FOV.

2.7 Background

The detector internal background $B(u, v)$ is given by a spatial map of event rate $cts^{-1} pixel^{-1}$ when there is no external source of stimulation (high energy particles, uv and visible light, X-rays, or gamma-rays).

2.8 Spectral Resolution

The HRC has very limited intrinsic spectral resolution. The resolving power $R(E)$ at energy E is defined by

$$R(E) = \frac{E}{\delta E}. \tag{18}$$

where δE is the full-width at half-maximum (FWHM) of the HRC pulse height distribution in energy units. Since the pulse amplitude of the HRC is non-linear with incident energy, the resolving power is not a sufficient measure of the HRC's ability to determine the energy of an incident photon; the non-symmetrical shape and non-linearity of the pulse height distribution must be taken into account. In fact, above 2 keV the pulse amplitude is independent of incident energy, thereby restricting the HRC's usefulness as a non-dispersive spectrometer to energies below 2 keV.

2.9 Detector Geometry

Relevant dimensions in both physical and detector electronic coordinate space (u,v) will be provided in this report. These include detector open areas (coated and uncoated), locations of fiducials ("splotchos"), HRC-S segment gaps and tilts, relative x, y, and z coordinates of HRC-I and HRC-S, UVIS structure dimensions, and wire spacings of the readouts.

2.10 Timing

The HRC time tags each detected photon to a precision of 16 cycles of the spacecraft's 1024 kHz clock, or

$$\delta t = 15.6 \mu s. \tag{19}$$

However, the absolute accuracy of the time tagging depends upon the accuracy of the spacecraft clock which is expected to be relatable to within 0.1 ms of UTC after routine ground processing.

2.11 UV/Ion Shield Transmission

The HRC UV/Ion Shield (UVIS) is a filter designed to block UV, visible light, and slow ions and electrons while still transmitting x-rays.

If we have a collimated beam of x-rays of intensity I_{in} and energy E normally incident on an absorber (filter), the residual intensity of unaffected primary photons I_{out} is given by

$$I_{out}(E) = T(E) I_{in}(E), \tag{20}$$

where T is defined as the transmission.

If the filter is made up of N layers each with transmission T_i, the transmission of the multilayered filter is

$$T(E) = \prod_{i=1}^{N} T_i(E). \tag{21}$$

The transmission T_i can be determined from the physical properties of the material of the layer

$$T_i(E) = e^{-(\frac{\mu(E)}{\rho})_i(\rho t)_i}, \tag{22}$$

where $(\frac{\mu}{\rho})_i$ is the mass attenuation coefficient of the material of the i th layer, and the product of the material density and thickness, ρ and t, respectively, is called the mass areal density.

If the i th layer is a chemical compound of M elements, $(\frac{\mu(E)}{\rho})_i$ is given by

$$(\frac{\mu(E)}{\rho})_i = \sum_{J=1}^{M} \omega_{i,j}(\frac{\mu(E)}{\rho})_J, \tag{23}$$

where $\omega_{i,J}$ is the fraction by weight of element J in compound i. The elemental mass attenuation coefficient $(\frac{\mu(E)}{\rho})_J$, for the AXAF x-ray range of interest (where only photabsorption is important), is given by

$$(\frac{\mu(E)}{\rho})_J = 2r_e hcN_o \frac{f_2}{(At.Wt.)_J E}, \tag{24}$$

where r_e is the classical electron radius, h is Plank's constant, c is the speed of light, N_o is Avogadro's number, and $(At.Wt.)_J$ is the atomic weight of element J.

By making measurements at discrete energies and using tables of f_2 it is possible to derive the material property ρt and then construct a model for the filter at every energy where f_2 is available.

On AXAF the UVIS is in a converging beam so that we must consider a possible correction for the increased path length. The transmission of the UVIS in the converging beam is given by

$$T(E) = \sum_{i=1,2,4,6} W_i(E) T_n(E)^{sec(\theta_i)}, \tag{25}$$

where

$$W_i(E) = \frac{A_i(E)}{\sum_{j=1,2,4,6} A_j(E)} \tag{26}$$

is the weighting function of the i th mirror pair.

$T_n(E)$ is the transmission of the UVIS for normal incidence, θ_i is the angle of incidence for the i th mirror pair, and $A_i(E)$ is the effective area for the i th mirror pair.

Using the nominal compositions of the HRC UVIS's, the maximum deviation of their transmissions from the case of normal incidence is less than 0.5% (relative) and we can set

$$T(E) = T_n(E). \tag{27}$$

The UVIS plays a significant role in determining the quantum efficiency of the HRC

$$QE(E, \phi, \theta_i, u, v) = T(E) QE_{mcp}(E, \phi, \theta_i, u, v), \tag{28}$$

where QE_{mcp} is the quantum efficiency of the microchannel plate alone. The UVIS transmission does not have any significant spatial variation so we have not shown any explicit spatial dependence of $T(E)$. We can use the equation above to model the HRC quantum efficiency over the AXAF energy range using separate models of the mcp quantum efficiency and UVIS transmission.

3 Ground Calibration Overview

3.1 Subsystem Calibration at SAO

Calibration of the HRC began with subsystem level measurements of the detector components. Uncoated MCP's were screened and flat fielded at Al-K (1.5keV) prior to selection for flight. After coating with CsI, the absolute efficiency was measured at 8 energies using a multi-anode Manson electron impact source to generate characteristic x-ray lines, and flow proportional counters as an absolute flux monitor. Flat fields were also obtained at these energies. Sufficient counts were collected to give at least 3% statistical precision on a 0.8x0.8 mm^2 scale. Figure 7 shows the quantum efficiency measurements for the HRC-I obtained in this calibration. It is remarkable that these efficiencies are virtually the same as those estimated in the original HRC proposal of 1984.

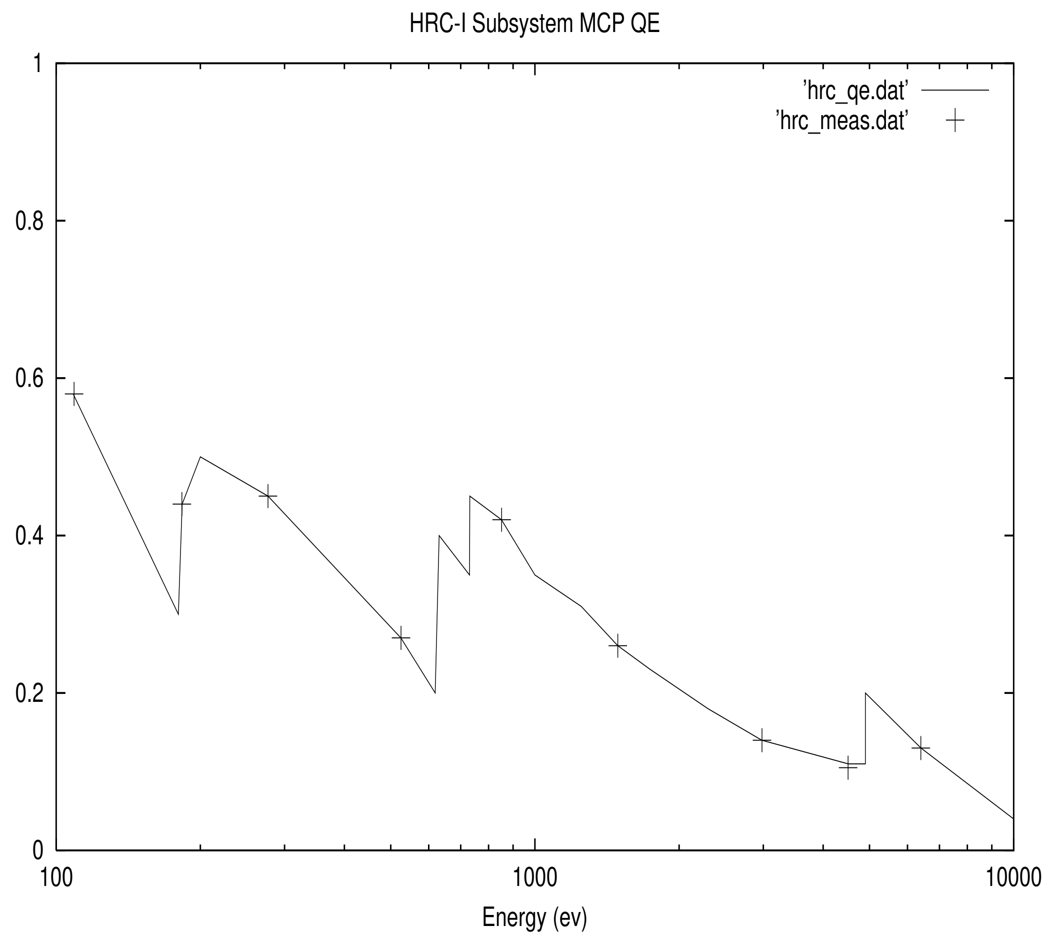

Figure 7: HRC-I quantum efficiency measured at subsystem level at SAO prior to detector housing assembly. The solid line is a coarse model of the efficiency versus energy taking into account only major absorption edges.

Uniformity and transmission of the UVIS's in X-rays were measured using a non-flight HRC and taking the difference between images with the filters in and out of the beam. We also measured the absolute transmission of witness samples of the shields using an X-ray fluorescence source (X-Kit) and a grazing incidence monochromator. EUV transmission measurements of witness samples were made using band-pass filters and gas discharge lamps. UV and visible light transmission measurements were made using a spectrophotometer.

3.2 Synchrotron Calibrations

In order to determine the fine structure response of the HRC, qe measurements were made on witness samples (36 mm diam MCPs coated with CsI) at the Daresbury (UK) Synchrotron Radiation Source. Using three beamlines the following energy regions were covered: $50 - 350$ eV, $250 - 1400$ eV, and $2000 - 6000$ eV.

Fine structure x-ray transmission measurements were also carried out on UVIS witness samples at the Physikalisch-Technische Bundesanstalt (PTB) radiometry laboratory at the BESSY I (Berlin) synchrotron.

3.3 Flight Calibration at XRCF

When the detector housing was fully assembled, verification measurements were made to confirm that the completed unit was working properly. Overall absolute efficiency for the HRC was measured at the same 8 energies used previously. During this time period, the flight UVIS's were damaged and replaced. Unfortunately, there was no time to completely calibrate the replacement filters to the same level as the original flight items. However, the comprehensive witness sample program has allowed us to confidently infer the replacement filter characteristics. We found no significant changes in the detector efficiency nor any significant spatial non-uniformities.

Following these subsystem calibrations and full assembly verification tests, the HRC was shipped to MSFC for further calibration with the AXAF X-ray telescope. The majority of the tests planned were measurements of the overall effective area (telescope plus detector) at numerous energies. One of the features of the XRCF is the X-ray Source System (XSS) which includes a Double Crystal Monochromator source (DCM) and a High Resolution Erect Field Spectrometer source (HIREF). These sources provided "dial-up" energy selection allowing us to examine the system performance near known features (e.g. absorption edges in the UVIS, MCP, and CsI coating) as well as in regions well away from such features. With the presence of the HRMA, it was also possible to measure the effects of a converging beam on to the MCP pores in the same geometry as for flight (to be compared with laboratory tests using collimated beams) and the the reflectivity of the HESF mirrors at the same angles as in flight. Other tests involved measuring the count rate linearity of the detectors, the spatial linearity over large and small scales, and verifying the point response function of the total system on and off axis.

The availability of the transmission grating spectrometers at the XRCF also provided an opportunity for calibrating the performance of the HRC-S/LETGS and HRC-I/HETGS. These tests were included in the overall calibration plan at XRCF. They were mainly measurements of total effective area for the combined instruments, and measurements of the point spread function convolved with the grating response to obtain the energy resolution of the spectrometers. The primary analysis of these data is being carried out by the Grating teams.

Since two detectors were being calibrated as well as two spectrometers, the number of individual tests quickly became large. Each test is characterized by many parameters - the source configuration, the geometry of the X-ray telescope and HRC, the grating status, and the configuration of the various beam monitors. To manage these tests and generate a test sequence, a Calibration Master Data Base (CMDB):

`(http://asc.harvard.edu/cal/cal.html)`

was created by the AXAF Science Center, and scheduling software was written to maximize the total throughput of the system. Sustained 24 hour a day, seven day a week operation was required to complete the calibration program within the allowed time, which for HRC plus LETGS was just 24 days of beam time. In that time we successfully completed the entire planned program as well as numerous added tests, for a total of 1111 measurements. The overall testing efficiency achieved in this phase of the XRCF very good. We were collecting data for about 70% of real time over the time period 19 March, 1997 to 12, April 1997.

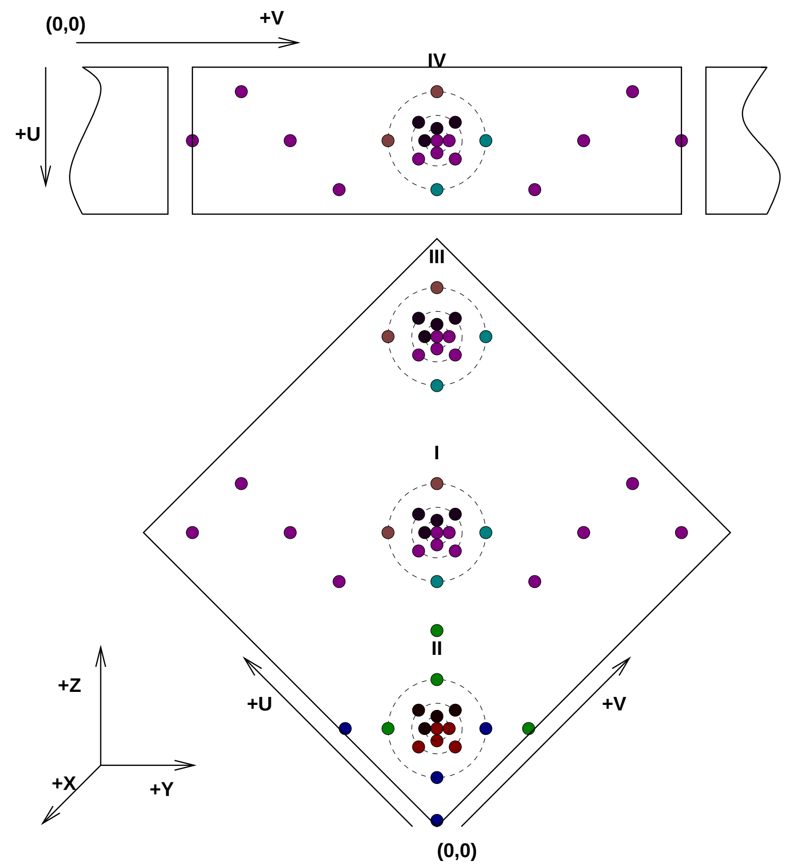

Figure 8: Aim points on the HRC as it appears at XRCF looking from the telescope towards the focal plane. The dots are locations where the image of the point source may be located during the calibration. Each detector has a local coordinate system corresponding to the EGSE display system - these are labeled U,V. The facility coordinate system is indicated as X,Y,Z (this is NOT the spacecraft system). The pattern of aim points allows on-axis and off-axis measurements sampling different regions of the the detector and different azimuths.

Figure 8 shows the locations of aim points on the HRC for the XRCF. Due to the count life restrictions of an MCP detector, we were very careful to avoid long X-ray exposure at any single location of the detector. In many cases this was achieved by deliberately positioning the HRC slightly out of focus and spreading out the incident flux. This strategy was well suited for effective area measurements since our flat field data showed that the detector does not have large variations in response on the scale of about a millimeter. In actual observations, the AXAF spacecraft will be slowly dithered in a 2-D pattern with about a 1 millimeter amplitude averaging out small scale variations, and avoiding high exposure to any single MCP pore.

The first light x-ray image for the HRC in the XRCF was obtained using the HRC-I and with the detector located about 25 mm in front of the focal plane. This image is shown in Figure 9. Two out of 16 mirror shutters were closed during this test, one each on HRMA shells 3 and 4 in order to verify the orientation of the HRC UV plane with respect to the calibration facility, and to confirm that the detector was properly located in the axial (X) direction.

For those cases where defocus was not an option (e.g. measurement of the point spread function or grating resolution), we used a simulated dither mode by moving the detector in the Y-Z plane in small steps for small time intervals. A typical "dither" consisted of a serpentine pattern of $40\mu m$ steps every 5 seconds, first in the Y-axis and then in the Z-axis (see Figure 10). In the data analysis, these motions can be "taken out" in the same manner as an aspect correction made to the detected coordinates of each photon.

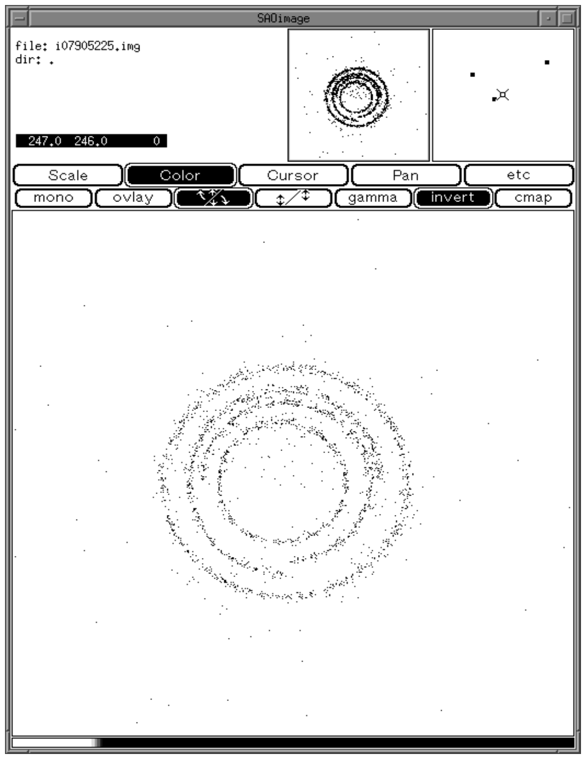

Figure 9: The first X-ray image at XRCF using the HRC-I. The detector is situated about 25 mm in front of the focal plane, with two quadrant shutters closed on shells 3 and 4 of the HRMA.

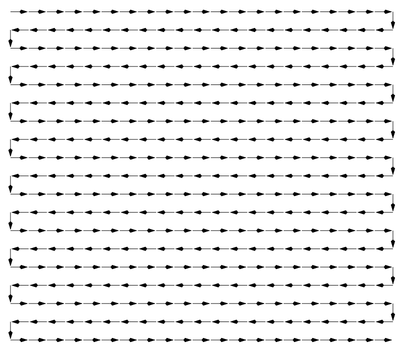

Figure 10: Typical serpentine "dither" pattern used at XRCF to simulate the spacecraft motion and to avoid over exposure on the HRC.

Figure 11a shows an uncorrected image taken while dithering in a 800μm box. The HRC-I detector is rotated approximately 45° relative to the facility. In Figure 11b, the corrected image is shown. The corrections were made by selecting out X-ray events that occurred only when the detector was not moving and re-mapping those photon positions by the offset of the detector from a nominal reference position. Time tagging for each detected event is a part of the HRC data structure. An independent time tag is provided for the focal plane mount that holds the HRC. This assembly, provided by Ball Aerospace, consists of a Simulated Science Instrument Module (LASSZ), and a movable table (the FAM) which can move in X,Y,Z in 10μm steps and also can rotate about each axis (θ_x, θ_y, θ_z). The HRC and FAM clocks are referenced to IRIG-B (Inter-Range Instrumentation Group) time generators for synchronization.

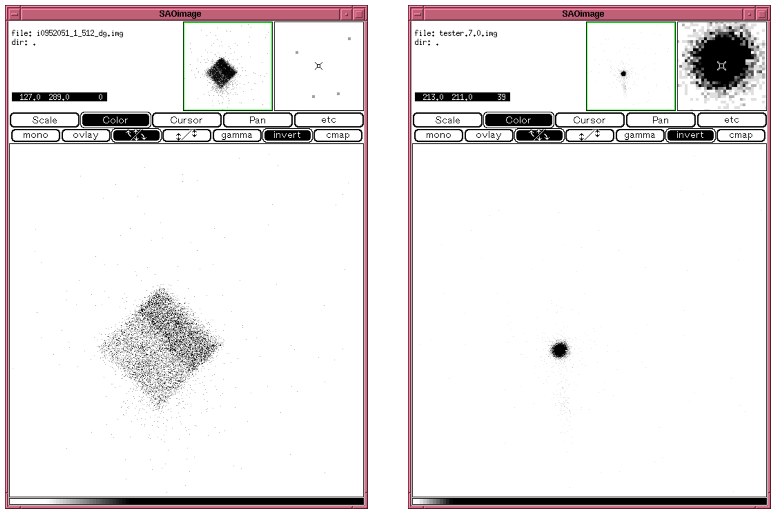

(a) Uncorrected "dithered" image (b) Corrected image

Figure 11: An HRC-I image taken at XRCF while dithering to avoid over exposure of the MCP. The test was made using the C-K EIPS source, and the HRC was place at the focus of the telescope. (a) is the uncorrected image,(b) is the image after correcting for the FAM motion.

In Figure 12 we show the energies at which effective area measurements were made for the HRC-I. For reference, the plot shows shows a smooth curve of QE versus energy with little or no detail at the locations of expected features due to absorption. The vertical lines show the energies at which we measured the effective area. These bracket expected features (shown as points) so that any jumps can be measured. We also included intermediate energies to constrain the curve in featureless regions. In all, approximately 50 energies were selected spanning the 0.1 to 10 keV region of the spectrum. With the exception of a few electron impact source lines (e.g. B-K, Be-K, C-K), these energies were achieved with the DCM and HIREFS sources.

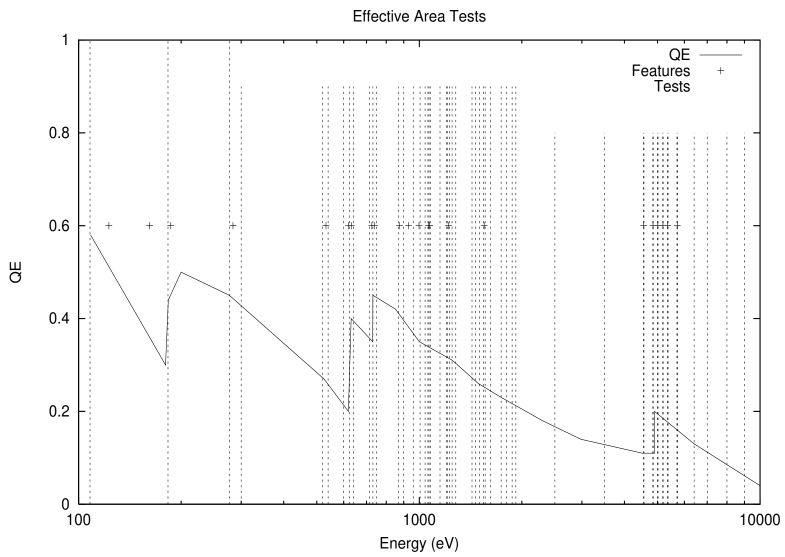

Figure 12: Plot of the approximate QE versus Energy for the HRC-I detector. The "pluses" indicate energies where a feature is expected in a detailed plot, usually due to some absorption edge in the materials of the UVIS, MCP, or coating. The lines show the energies that were planned for measurement at the XRCF.

3.3.1 Anomalous Behavior

Following the tests using the mirror and gratings, we had planned to conduct a series of flat field exposures at the XRCF taking advantage of the very uniform beam (due to the long distance from the source to the detector), and the excellent ancillary beam monitoring equipment. However, these tests were not carried out at the XRCF.

Prior to the start of the XRCF tests, the HRC was baked out in a special MSFC facility to make sure that the instrument would not contaminate the HRMA. During the bakeout test, we were able to operate the fully assembled system for the first time. In these tests we noted a large number of event trigger signals with no valid readout signal. We were we able to access only a few test points on the detector in the bakeout facility and examined some of the readout signals. We discovered a 91 KHz noise signal that was only present when MCP high voltage was turned on. The amplitude of the noise correlated with the high voltage value. Although we could not monitor the event trigger signal directly, we concluded that this 91 KHz noise was also present on the MCP trigger signal, resulting in the large number of false events.

A quick remedy was to change the threshold level for event triggers. This level is commandable and it was raised to eliminate the false triggers. Specifically, the HRC-I threshold was raised from about 10 DU to 32 DU (out of a maximum of 255), and the HRC-S threshold was increased from about 10 DU to 40 DU. Post XRCF tests showed that the HRC-I threshold setting could have been as low as about 20 DU while still eliminating most false triggers. At the time, this seemed to be a minor change in the operation of the HRC, as the threshold was only changed by the equivalent of a few percent of its adjustment range. In retrospect, this resulted in a significant change in performance (as discussed below).

When the HRC was finally installed in the XRCF and we began the the test sequence with X-rays through the telescope, we noted that a large fraction of detected events had total pulse heights at the saturation limit of the readout electronics. As many as 20–30% of HRC-I events were being incorrectly located due to electronic saturation in the readout amplifiers and/or A-to-D conversion. With the instrument already in the XRCF chamber, we made the decision to lower the MCP gain until the signals no longer saturated the electronics. For both HRC-I and HRC-S, we lowered the MCP voltages by about 40 volts/plate. This reduced the fraction of events with saturated pulse height to at most a few percent.

Despite the problems described above, the actual XRCF calibration for the HRMA plus HRC started on day 078 (19 March, 1997) and continued through day 102 (12 April, 1997). In that time there were 1111 individual HRC test sequences. The HRC was operated at reduced MCP high voltage and increased event trigger thresholds in order to maintain the very constrained XRCF schedule. Operations were through the same interfaces that will be in place during flight. The data and command formats were identical to flight, although non-flight hardware was used to emulate the configuration. The software systems used to control the instrument, receive and archive the data, and perform real-time display and analysis were the same as those planned for flight. This arrangement gave us a chance to develop and test these interfaces and software. One very positive result was the development of various command sequences for initializing the HRC, and valuable experience in the operational aspect of the detectors.

During the calibration, a huge number of data files are generated. There was a primary instrument data set generated by the HRC EGSE which contains the complete AXAF telemetry stream. From the XRCF X-ray source system there were files that monitor the source. From the SAO Mission Support Team there were files from the various beam monitors used for flux calculations, incident spectra, and spatial uniformity across the telescope aperture. From the Kodak HRMA EGSE there was data on the orientation of the X-ray telescope and the status of grating assemblies. From the Ball FAM EGSE there was data on the location of the instruments in the focal plane. And from the TRW Test Conductor's Log there was a time line of all activities and a listing of the desired parameters for that test. All of these data sources needed to be correlated so that the appropriate information for each test could be extracted. Each data source was time tagged using an IRIG-B time generator, so that this correlation can be made. Unfortunately, during the HRC calibration phase,there were problems with the IRIG system resulting in unreliable time stamps in the data streams. The process of sorting out these inconsistent times has made a complete analysis of the calibration more difficult then expected.

The overall effective areas for HRC-I and HRC-S are close to that expected values based on the subsystem calibration data and the HRMA model, and generally follow the predicted shapes. The HRC-S appears to have about 20% less efficiency than the HRC-I, which is attributed to the changes in MCP voltage and trigger threshold that were used at the XRCF.

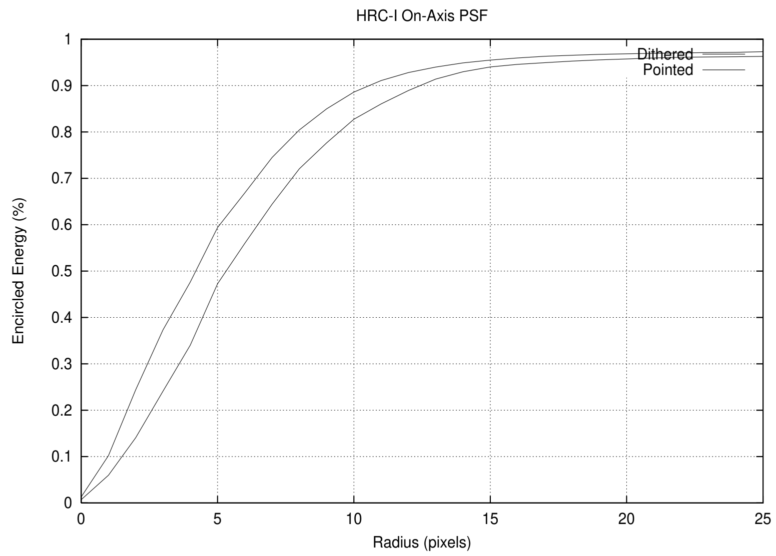

Figure 13: Encircled energy versus radius for dithered and pointed measurements with C-K X-rays

The measured HRMA plus HRC-I point spread function is shown in Figure 13. We find about 50% of the power within a 1 arc-second diameter. A similar measurement that was made without dithering (obtained during the count rate linearity tests) is also shown in Figure 13. This gives a somewhat better PSF indicating that the accuracy of the dither correction is not as good as we expected, or that there are uncorrected motions in the focal plane when dithering.

A long "ring focus" image was made with the HRC-I at 1.25 keV (Mg-K) from which the azimuthal dependence of the HRC quantum efficiency was measured. The AXAF optics generate a cone of X-rays with half angle ranging from about 1.5 to 3.5 degrees relative to the optical axis. The HRC MCPs have a bias angle of about 6 degrees so that some of the X-rays strike the detector at angles as small as 2.5 degrees relative to the MCP pores. Since the MCP quantum efficiency depends on the angle of incidence, there will be a variation of the counting rate around a ring image. Figure 14 shows the results from the ring focus test. The azimuthal variations are within ±10% for all four shells.

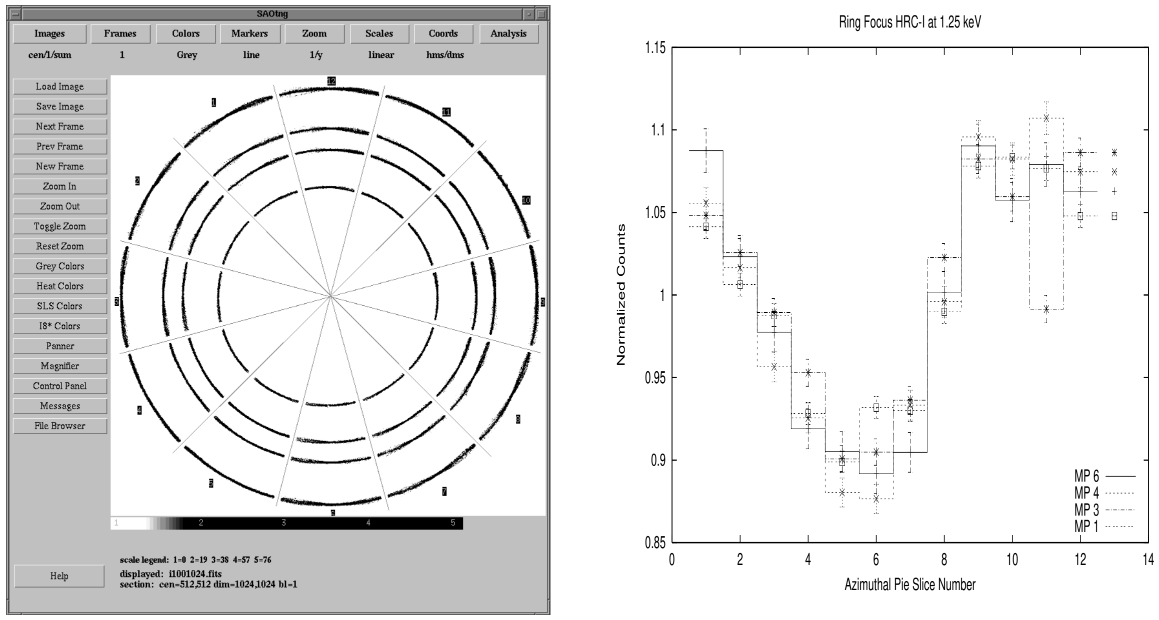

(A) **(B)**

Figure 14: Ring Focus image and the normalized rate versus azimuthal slice for Ring Focus. There is a small azimuthal count dependence of $\pm10\%$ from the mean. This variation is essentially the same for all four shells, and it is aligned (and consistent) with the direction of the MCP bias angle.

4 HRC Calibration

4.1 Hardware Modifications and Calibration Post-XRCF (Overview)

After the XRCF testing was completed the HRC was returned to SAO so that the 91 KHz and high gain problems could be addressed. It was also more convenient to make the flat field measurements at the SAO facilities where a high speed data tap could be used to permit data rates 10 times higher than available at the XRCF.

With the HRC at SAO it was possible to make better diagnostic measurements to help in understanding the root causes of both the 91 KHz ripple seen at MSFC, and also the unexpected higher gain of the analog electronics. The HRC was mounted in a test configuration where there was access to interior test points while the detector housing was held at vacuum allowing the MCPs to be illuminated with X-rays. While diagnosing the HRC problems in this configuration, we carried out a series of flat field measurements for both HRC-S and HRC-I to establish a baseline set of measurements corresponding to the XRCF state of the instrument. Measurements were made at the same 8 energies as the subassembly calibrations. These measurements (taken at the lower MCP high voltage settings, and increased trigger threshold levels) clearly showed significant energy dependent spatial variations in detection efficiency.

4.1.1 High Gain

The desired electronic gain was determined during the early phase of the instrument development cycle and this value was incorporated into the specifications for the hybrid preamplifier vendor. In retrospect, that gain requirement was probably derived from laboratory tests of MCPs that were either not coated with CsI, or were not of the same type (e.g. low noise) as the flight MCPs. However, this discrepancy was not noted prior to the XRCF tests. Due to the pressing AXAF schedule, the fully assembled HRC was not tested before being shipped to MSFC, so there was no data to suggest a problem.

The front end electronic gain of the HRC is controlled by settings on each of the 128 charge sensitive hybrid preamplifiers (64 per axis). There are two sets of these preamps for a grand total of 256 devices. The gain is controlled by a resistor in the operational amplifier feedback loop of each preamp. The hybrid units are individually trimmed, sealed in hermetic cans, and wave soldered to printed wire circuit boards. Each hybrid preamp PWC holds 8 units, for a total of 16 such boards.

The most direct solution was to modify all of the 256 hybrid preamplifiers; however, the risk would have been much too high. Fortunately an alternative solution was found. In Figure 15 we show a simplified block diagram of the HRC Front End Electronics (FEA). The linear range of the grid hybrid preamps is 50% greater than the linear range of the rest of the analog processing chain. By adding 3:2 resistive dividers at the inputs of the three fine position analog to digital converters (for each axis), the overall electronic gain was decreased by 50% allowing the MCPs to operated at their nominal high voltage (and gain) without producing electronic saturation. These changes were relatively easy to implement.

4.1.2 91 KHz Ripple

While still at the XRCF, this problem was traced to the R-C filter network between the HVPS and the detector. Due to schedule pressures, the fully assembled HRC instrument was never completely tested prior to shipment to the XRCF. The detector subsystem tests discussed above were all made with non-flight high voltage power supplies and filter networks. At the XRCF, repair or replacement of the filter network was considered and rejected since it involved a major disassembly of the certified clean instrument, and would have meant that the HRC and HRMA could not be calibrated together. (The overall AXAF schedule required the HRMA to be shipped to TRW to begin spacecraft integration by the end of April.)

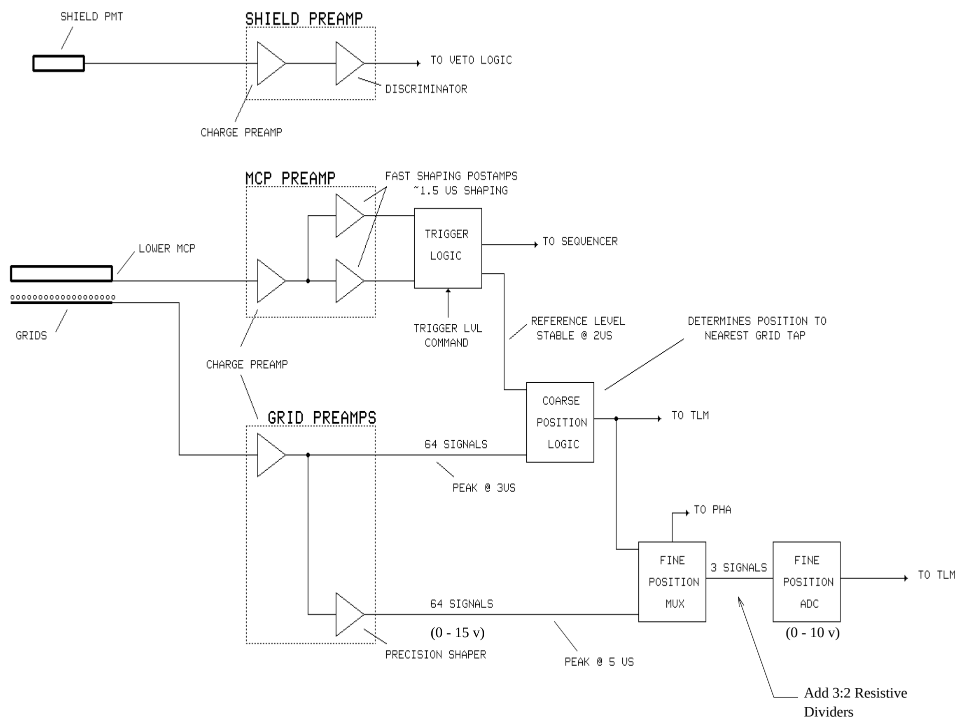

Figure 15: Block diagram of the front end electronics. The hybrid preamps have a linear range of 0 – 15 v, while the subsequent fine position ADC has a 0 – 10 v linear range. By inserting a 3:2 resistive divider at the inputs to the fine position ADC's the extended range of the preampliers will not result in saturation in the ADC.

However, we did begin the work of redesigning the filter network, adding an additional R-C stage to better isolate the DC-DC converter from the MCPs. By the time the HRC was returned to SAO, we had these new filters available for testing and replacement. When the initial flat field tests were completed, the HRC was taken from the X-ray calibration system and placed in a clean room so that the electronics box containing the high voltage power supplies and filter networks could be removed. The disassembly of the unit, was followed by the removal of the faulty filter networks and their replacement.

4.1.3 Recalibration

The re-assembled unit was then placed back in the SAO calibration facility for a additional flat field measurements. Both the high voltage and the trigger level were varied. The high voltage settings were close to the values used during the subsystem level tests, and the event trigger levels were set to 8 DU for both the HRC-I and HRC-S.

Figure 16 shows a flat field surface plot for the HRC-I taken at the three configurations used. The number of counts in a 0.8mm square pixel is plotted versus the U-V position of the pixel. The counts are plotted in arbitrary units where 100 is the the average for the field. Also plotted are contours of constant counts, The lower left panel is status during the XRCF calibration, showing the rapid fall off in detector response around the detector edges. This behavior present at all energies and explains the decrease in HRC-I off-axis efficiency. In the lower right panel the MCP high voltage was increased, and there is considerable reduction in the fall off of the detector response. In the upper left panel , the effect of also lowering the event trigger level is seen. The detector response is much more uniform (±5% over 95% of the active area). There is also a small increase in the peak absolute efficiency of the HRC-I in this final operating configuration.

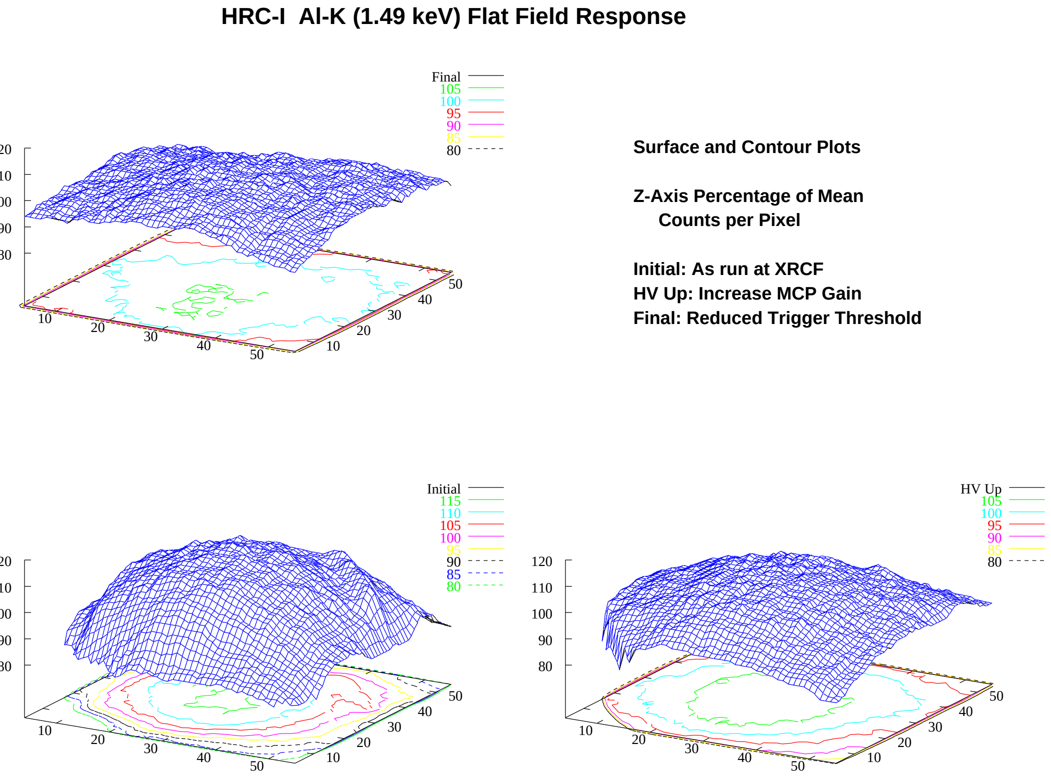

Figure 16: Surface plots of an HRC-I flat field measurement at Al-K (1.49 keV). Lower left: nitial, as run at XRCF; lower right: HV up to increase MCP gain; upper left: final, reduced trigger threshold.

Figure 17 is a surface plot for the +1 segment of the HRC-S. This is the segment along the +Y axis of AXAF and was the section of the HRC-S that showed greatest spatial non-uniformity during the XRCF. The number of counts in 0.8mm pixels (normalized to arbitrary units) is plotted versus the U-V pixel coordinates. The leftmost plot (A) is for the XRCF operating conditions. Variations in the detector efficiency are as large as 50% along the V (dispersion) direction. The center plot (B) shows the effects of increasing the MCP high voltage. The plot shows much less variation than for the XRCF configuration. At the same time, the absolute efficiency at this voltage is almost 40% higher than the previous configuration. This improvement results from driving more of the MCP area into saturation at the higher operating voltage. Finally the rightmost plot (C) shows the effect of also decreasing the trigger threshold level after removing the 91 KHz feedthrough. The response is much more uniform along the V-axis, variations are only about ±10%, and the U-axis variations have also decreased. With these modifications, all three HRC-S segments now show similar behavior. The left-right asymmetry seen during the XRCF has been greatly reduced, and the absolute detection efficiency is close to the subsystem values obtained prior to the XRCF tests.

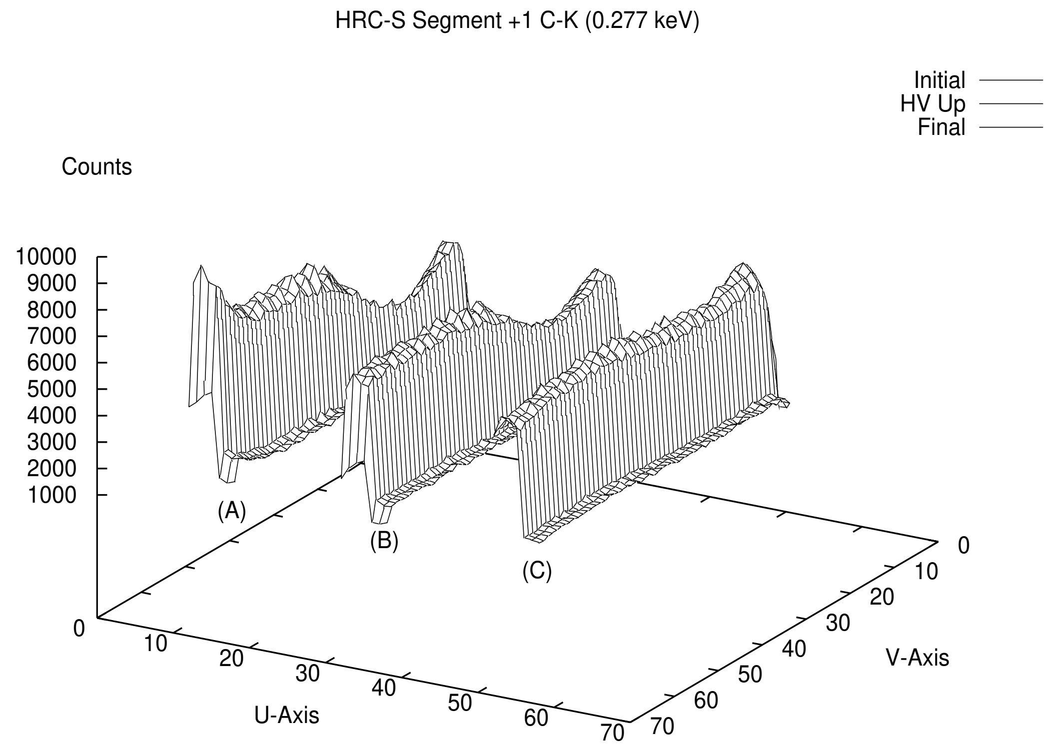

Figure 17: Surface plots of an HRC-S flat field measurement at C-K. The +1 segment of the spectroscopy detector is shown

4.2 HRC-I (QE, EA, PSF, Resolving Power)

4.2.1 XRCF Calibration

The Facility

The x-ray calibration Facility, depicted in Figure 18, consists of an X-ray Source System (XSS), a long $\sim$ 500m pipe and an $\sim$ 23m long $\times$ 7.3m diameter instrument chamber. In addition there is an X-ray beam monitoring station 38m from the XSS. The features of the XRCF were optimized for calibrating AXAF. The XSS consists

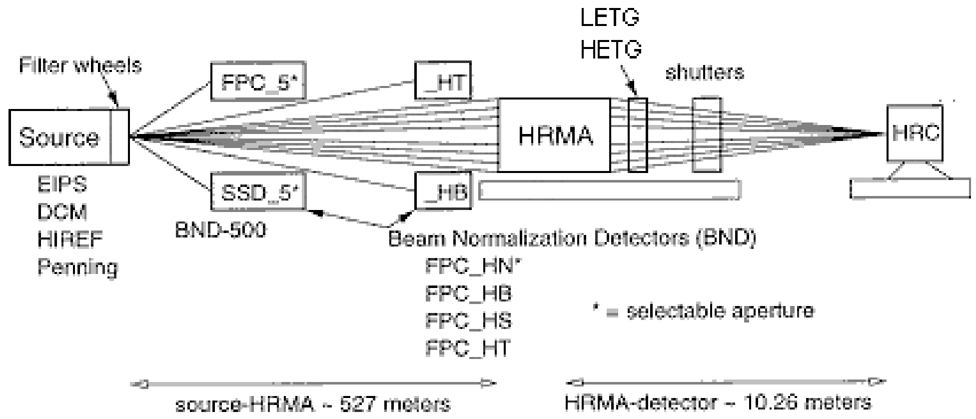

Figure 18: X-ray Calibration Facility showing the X-ray Source System, instrument chamber, HRMA and FAM.

of several X-ray sources, namely: an Electron Impact Source (EIPS); a tungsten Rotating Anode Source (RAS) with Double Crystal Monochromator (DCM); a Penning Source and a RAS with a High Resolution Erect Field Spectrometer (HIREFS). The EIPS was used with various anode-filter combinations to produce characteristic X-ray lines. The DCM provided X-rays from $\sim$ 1.5 to 10 keV. The HIREFS, a grating monochromator provided X-rays from $\sim$ 300eV to 2 keV. For the purpose of HRC-I testing only the DCM, the HIREFS, and the EIPS with Be, B and C anodes were used.

In addition to the sources, the XRCF employed six X-ray detectors for monitoring the beam during the calibration. Four of these detectors, Beam Normalization Detectors (BND's) were flow proportional counters (FPCs) located near the front of the HRMA. Two other detectors, a Solid State Detector (SSD) and another FPC were located $\sim$ 38m from the XSS. The SSD was used to monitor the beam flux and this FPC was used to monitor and spatially map the beam.

During calibration, the the orientation of the HRMA was changed in pitch and yaw to simulate the performance of the AXAF telescope to off axis illumination. In addition various quadrants of the HRMA could be occulted to determine the location of best focus.

The HRC was attached to a Five Axis Mount (FAM). This FAM provided instrument selection,instrument motion and focusing. During long in-focus measurements, the FAM executed a small scale serpentine motion to prevent damage to the detectors due to excessive localized charge extraction. The majority of the other calibration data were taken with the instruments slightly out of focus for the same reason. In flight, spacecraft "dither" will provide the same function.

Effective Area

The effective area EA at a given energy of the HRMA and HRC (including the UVIS) is the response of the combination to a uniform monochromatic incident flux density Ψ from a point source, i.e. the HRC count rate is given by

$$R = EA(E)\Psi(E) \tag{29}$$

Knowing the incident flux density in photons $cm^{-2}\ s^{-1}$ and the count rate in counts s^{-1} immediately provides the effective area in cm^2.

The calibration of the HRC-I effective area involved simultaneously exposing the HRC-I, in the focal plane of the HRMA, and a set of Beam Normalization Detectors (BND) to X-rays. The BNDs consisted of a set of four Flow Proportional Counters (FPC) positioned around the perimeter of the HRMA entrance aperture, denoted as BND-HN, BND-HS, BND-HT, and BND-HB for the north, south, top and bottom quadrants respectively. A fifth FPC (FPC–500), used for beam mapping, as well as a Solid State Detector (SSD–500), were positioned 38m from the source. The BND's are used to determine the incident flux density Ψ.

On-axis effective area measurements for HRC-I were performed at 63 energies ranging from $\sim$ 110 eV up to 9 keV. Not all energies could be used to derive effective areas because of incomplete data and archiving problems. In total 56 energies for the HRC-I were available for our analysis. All of these measurements were taken out of focus to protect the detector from permanent gain degradation. The focal plane rates were determined by placing a 750 pixel radius ($\sim$ 4.82 mm) aperture around the source. An annulus from 800 pixels ($\sim$ 5.14 mm) to 900 pixels ($\sim$ 5.78 mm) was used for background subtraction.

The HRC's intrinsic (non-dispersive) spectral resolution is limited ($E/\Delta E \sim 1$), which means that even two discrete spectral lines appear as a single broad feature in the output PHA. Unfortunately, while the monochromators were designed to generate a single spectral line, they often produced multiple orders, as well as contamination from the tungsten source anode. Since the majority of the effective area measurements were performed with the HIREFS or DCM, this required that the fluxes from "contaminating" lines first be measured in the BND spectra. Then their contribution to the HRC's output count rate must be modeled and removed before we could properly characterize the quantum efficiency at the energy of interest. Our procedure for handling this is discussed in detail below.

By comparing the X-ray flux density in front of the HRMA with the count rate detected in the focal plane, one should be able to determine the HRMA/HRC-I effective area. However, due to various problems such as low flux and beam non-uniformity, we were required to use a more complicated approach which involved applying beam uniformity corrections and weighting the flux based upon the mirror effective area.

Beam Normalization Detector Data Analysis

PHA Analysis

The ultimate goal behind the spectral fitting procedure was to model the incident source flux. In general, this consisted of the flux in a set of spectal lines, plus a set of parameters describing the flux per keV in the continuum. For the case of the HRC effective area measurements this problem is greatly simplified because the vast majority of the measurements were performed with the monochromators (which, by definition, have no continuum component). Those few measurements made with the EIPS contained a filter which was designed to block out the continuum. The problem then reduced to modelling the flux $F_k(E_i)$ in the i^{th} line observed by the k^{th} BND.

We have chosen to use the Jahoda-McCammon-Kramer model (JMKmod) adapted by the AXAF Mission Support Team (MST) for fitting within the XSPEC X-ray spectral fitting package. JMKmod convolves a model of an X-ray source spectrum with a model of the reponse of an FPC. The model contains a number of parameters which can be divided into three distinct groups: instrumental parameters which did not change from detector to detector, variable detector parameters (e.g. Fano factor and various model normalizations[1]), and variable source parameters (e.g. line energy, filters, and high voltage). The advantage of using JMKmod versus simpler functions (Gaussian, Prescott, etc.) is that JMKmod gives a physical representation of the source/detector system, which can be adjusted as more is learned about the FPC.

Several complications arose in the spectral fitting because the XSS was run in low-flux mode to avoid gain degredation in the HRC. In particular, the BND background made a non-negligible contribution to the count rate. To correct for this, we fit background measurements taken independently with a power-law – for a tail in the lower channels– combined with a broad Gaussian ($\sigma \approx 400$ channels) for the entire detector. This was then combined, as a constant component, with the rest of the JMKmod in XSPEC. This approach avoided the unphysical situation of channels with negative counts, which often resulted from a manual background subtraction. A typical BND spectrum is shown in Figure 19. In this figure, JMKmod fits the two spectral components, but above channel 360 the data is fit better by the background model. The low channel noise is not very evident in this example due to a shelf from channels 40–100. This type of shelf, which was common in the data, was caused by incomplete charge transfer in the FPC gas.

Another result of the intrinsically low signal-to-noise was the underestimation of model normalizations. Cash (1979) has shown that a standard χ^2 treatment of data with few counts per bin leads to an underestimation of the fit in the wings (Bevington 1992). A better method involves using a maximum likelihood estimator, also known as a C-statistic. A comparison of the results of fitting identical datasets with the two methods indicates that χ^2 minimization can underestimate our fit global and line normalizations by as much as $\sim 20\%$. As a result, we chose to use the C-statistic for our spectral fitting.

We begin the analysis of a BND PHA by determining the count rate in the i^{th} line, $R_k(E_i)$, in each BND. This is determined from the fits by the global normalization for the k^{th} BND (N_k^{global}), and the fractional normalization for the i^{th} line ($N_k(E_i)$):

$$R_k(E_i) = N_k^{global} \times N_k(E_i) \qquad cts\ s^{-1}. \tag{30}$$

This rate is then divided by the open area of the FPC, A_k, and the detector quantum efficiency $\eta_k^{BND}(E_i)$, to determine the modeled flux at the k^{th} BND ($F_k(E_i)$):

$$F_k(E_i) = \frac{R_k(E_i)}{A_k \times \eta_k^{BND}(E_i)} \qquad photons\ s^{-1}\ cm^{-2}. \tag{31}$$

The errors are statistical and are added in quadrature.

In principle we can then determine the telescope/detector effective area ($A'_{total}(E_i)$) given by:

$$A'_{total}(E_i) = \frac{R^{FP}(E_i)}{< F(E_i) >} \qquad cm^2, \tag{32}$$

where $R^{FP}(E_i)$ is the photon count rate in the focal plane detector, and we have assumed that $< F(E_i) >$ is the flux averaged over the four BNDs. Because there were large spatial variations in intensity across the front of the HRMA, this was not representative of the average flux. To correct for this effect we have used a beam uniformity analysis provided by the AXAF Project Science group to appropriately weight the fluxes measured by each BND.

Beam Uniformity Analysis

[1] The normalizations include the global normalization (N_{global}) and the line normalization ($N(E_i)$). These two normalizations are combined in the model such that the total count rate in the line is determined by the product of the two.

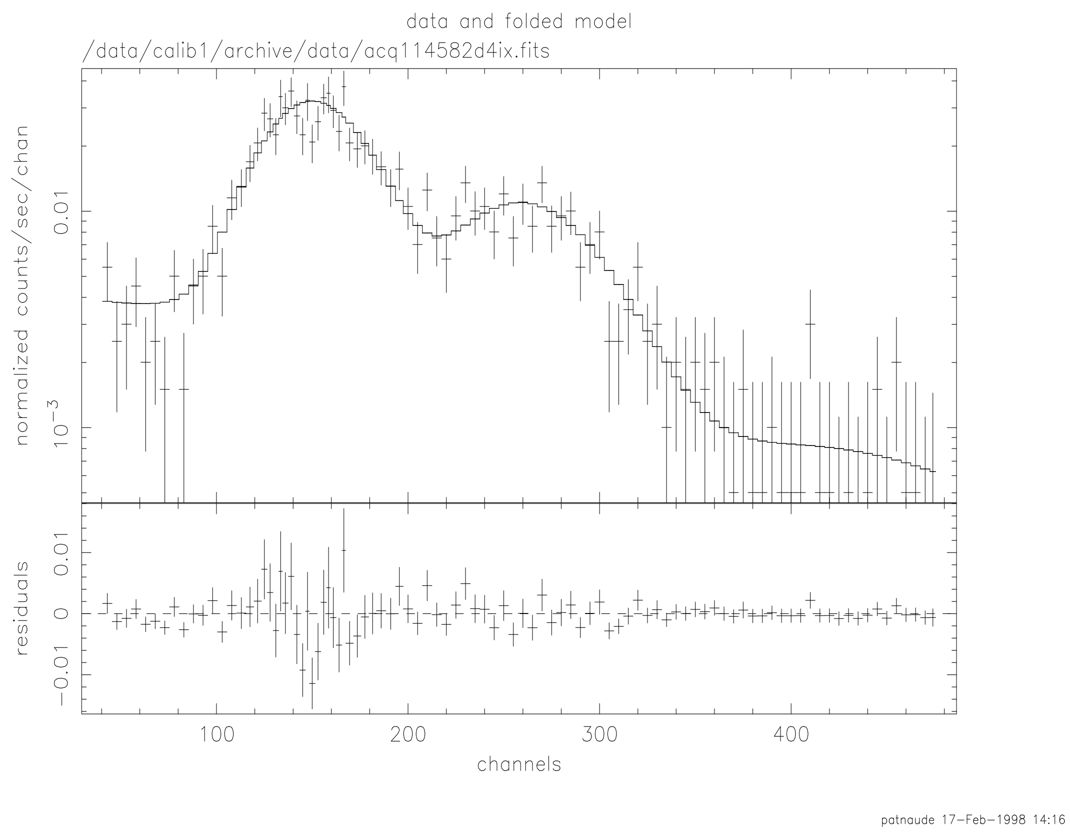

Figure 19: Example BND PHA from a HIREFS measurement showing a second order contribution. The primary energy is 900 eV, but there is a significant contribution from 1800 eV.

For some of the source settings, a map of the beam was generated to determine the spatial intensity of the source. For each map, the FPC–500 measured the average flux at each quadrant-shell position of the HRMA. This data was fit with a polynomial and Gaussian to produce a surface describing the beam

We first determined the modeled flux per unit source current incident on the focal plane. This is the product of the beam uniformity modeled average flux density ($F^{PS}_{q,s}(E_i)$) at each of the 16 quadrant–shell (q, s) positions and the appropriate mirror effective area ($A'_{q,s}(E_i)$):

$$\tilde{F}_{q,s}(E_i) = A'_{q,s}(E_i) \times F^{PS}_{q,s}(E_i) \qquad photons\ s^{-1}\ mA^{-1}. \tag{33}$$

This weighted the flux with the mirror effective area, allowing a direct sum over the quadrants and shells, giving a total photon rate per mA ($\mathcal{F}(\mathcal{E}_\rangle)$) at each energy incident upon the focal plane. The errors are independent, and were added in quadrature.

The ratio, $\lambda_q(E_i)$, of our modeled flux density in a BND ($F_k(E_i)$) from Equation 31 to the flux density per mA in the same BND modeled from the beam uniformity maps ($F^{PS}_k(E_i)$) gives the scale factor (i.e. current) required to get the photon rate incident on the focal plane detector:

$$\lambda_k(E_i) = \frac{F_k(E_i)}{F^{PS}_k(E_i)} \qquad mA. \tag{34}$$

Each scaling factor was applied to the modeled focal plane photon rate per milliamp, $\mathcal{F}(\mathcal{E}_\rangle)$, to generate a photon rate ($f_k(E_i)$) incident on the focal plane as projected by each BND:

$$f_k(E_i) = \mathcal{F}(\mathcal{E}_{)}) \times \lambda_{||}(\mathcal{E}_{)}) \ , \tag{35}$$

The four values ($f_k(E_i)$) were then averaged to determine the photon rate incident upon the focal plane for the i^{th} line ($\overline{\mathcal{F}}(E_i)$). The average was weighted with the errors $\sigma_{f_k(E_i)}$ in order to account for a systematic bias in the scaling factor in the north detector between 0.6 and 1.5 keV, which was purely an artifact of the polynomial fits (Swartz, 1998):

$$\overline{\mathcal{F}}(E_i) = \frac{\sum_k f_k(E_i)/\sigma^2_{f_k(E_i)}}{\sum_k (1/\sigma^2_{f_k(E_i)})} \qquad photons\ s^{-1}, \tag{36}$$

It is worth noting that if the beam were perfectly uniform, the scale factor, $\lambda_k(E_i)$, would be equal to the source current used for the beam uniformity map, and the projected rate would be equivalent to the average BND rate multiplied by the mirror effective area.

In the case where no beam uniformity data exists (as well as data taken with the EIPS), a less complex method was used which involved averaging the modeled flux ($F_k(E_i)$) in each BND and using the total HRMA effective area to get an incident photon rate.

Once the incident rate was determined at each energy, we determined the quantum efficiency of the HRC-I by comparing the incident rate to the detected count rate. We then generated a continuous curve for the quantum efficiency. This was then used in conjunction with the HRMA effective area to generate an ensemble effective area for the HRMA/HRC-I system.

Effective Area Analysis

As noted above, a lack of spectral resolution in both the HRC-I and HRC-S made it difficult to analyze the multi-component spectra sometimes produced by the monochromators. For instance, the HIREFS produces multiple orders up to the M edge of Gold at 2 keV (*i.e.* A HIREFS setting of 600 eV would generate lines at 600 eV, 1.2 keV, and 1.8 keV). There is also contamination from two groups of Tungsten M lines at $\sim$ 1.38 and $\sim$ 1.77 keV, which appear in all the spectra though with varying power. A further complication was that often the count rate in contamination lines was significantly higher than the rate from the line of interest. We have identified three distinct and progressively more complex spectra.

The first set consists of measurements taken right at the Tungsten contamination lines. At 1.38 keV, the flux is almost solely due to Tungsten line located there. The 1.77 keV line is present but extremely weak– $\sim$ 1%. At 1.77 keV the sense of the ratio is reversed, although the 1.38 is moderately strong, contributing $\sim$ 20% of the flux. Because these lines were present in all the other spectra, we began by first analyzing the data at 1.38 keV and then using this to bootstrap our analysis for the 1.77 keV line.

From here we proceeded to the second set of spectra which had energies above 1 keV. Because this energy range was not susceptible to higher order contamination the spectra consisted of the line of interest and the Tungsten contamination lines.

Finally, we were prepared to work on the data from energies below 1 keV, where we found the Tungsten contamination lines as well as higher order lines. This process obviously had the potential of propagating substantial errors, so it was important to determine the photon flux in each line as accurately as possible. Our final results indicate that we have had mixed success in determining the effective area below 1 keV, especially when third order lines– thus four contaminating lines– are present.

With multiple lines present in the source spectra, we first determined the HRC count rate ($R'(E_{i\neq 1})$) in each line other than the principle line ,E_1, at which the source was tuned. In general:

$$R'(E_{i\neq1}) = \overline{\mathcal{F}}(E_{i\neq1}) \times \eta'(E_{i\neq1}) \qquad counts\ s^{-1}, \tag{37}$$

where $\overline{\mathcal{F}}(E_{i\neq1})$ is the flux incident upon the detector (as calculated from Equation 36 or Equation 31) and the HRC quantum efficiencies $\eta'(E_{i\neq1})$, are previously determined via our bootstrapping process. Then,

$$R''(E_1) = R_{TOT} - \sum_{j\neq1} R'(E_j) \tag{38}$$

and,

$$\eta''(E_1) = \frac{R''(E_1)}{\overline{\mathcal{F}}(E_1)} \quad . \tag{39}$$

Once the quantum efficiency ($\eta''(E_1)$) of the detector (UVIS and MCP) was determined at each discrete energy, we divided out the transmission of the UVIS (η_{UVIS}) to arrive at the quantum efficiency of the MCP (η_{MCP}). This is a function of how easily the electrons generated by the absorption of an X-ray can escape the photocathode. The electrons fall into two categories: primary electrons, consisting of those ejected by the photoelectric effect or Auger transitions, and secondary electrons produced by the interaction of the primary electrons with the photocathode. The primary electrons have an energy proportional to the incident photon, while the energy of the secondary electron is very nearly 1 keV, independent of incident photon energy . Nominally, the combined yield of primary and secondary electrons should determine the quantum efficiency. Due to the complex physics of the photocathode deposited on the front of the MCP the data is unfortunately neither smooth nor easily described by a single function.

Instead we opted to fit the absorption range of the secondary electrons produced by each photon interaction . Nominally, this is a smooth and continuous function as all the edge structure has been removed. In practice however, although the smoothness and continuity of the data has improved significantly, it still requires several components.

We have defined the absorption range of the secondary electrons as:

$$L(E) = \frac{-\ln(1 - \frac{\eta_{MCP}(E)}{f_{pore}})}{\mu\rho_{CsI}(E) \cdot \rho_{CsI}}, \tag{40}$$

where $\eta_{MCP}(E)$ is the HRC quantum efficiency, f_{pore} is the packing fraction of the MCP, ρ_{CsI} is the bulk density of Cesium Iodide, and $\mu\rho_{CsI}(E)$ is the mass absorption cross section at E.

We found that there are several regimes requiring separate fits, possibly indicating edge structure for which we have not accounted or accounted for incompletely. We have empirically fit the range versus the energy on a log–log scale with quadratic functions ($\Lambda(E)$) for each region.

By inverting equation 40,

$$\eta_{model}(E) = (1 - \exp^{-y(E)}) \cdot f_{pore} \ , \tag{41}$$

where

$$y(E) = \Lambda(E) \cdot \rho_{CsI} \cdot \mu\rho_{CsI}(E) \ , \tag{42}$$

and using our newly generated range values ($\Lambda(E)$), we generated a curve modeling the MCP quantum efficiency. This was then recombined with the UVIS transmission and HRMA effective area to give us the full HRC/HRMA effective area.

Results

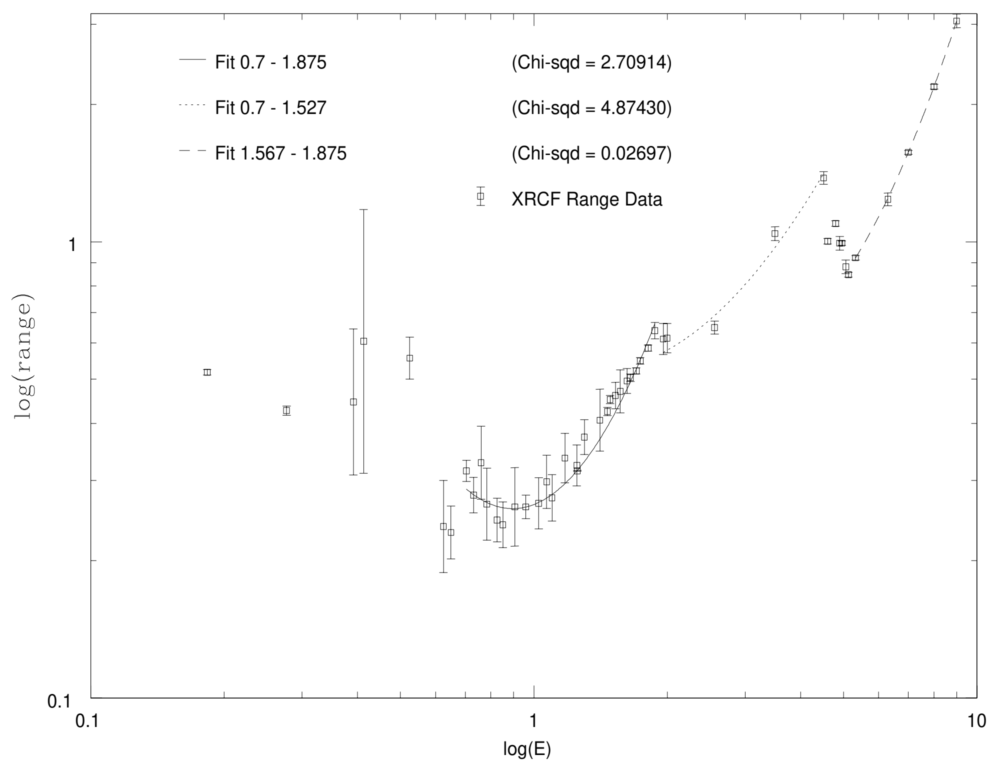

Figure 20: Effective range of secondary electrons in the HRC-I MCP

From Figure 20 we have identified three regions: from 5.32 keV to 9 keV, from 2 keV to 4.51 keV and below 1.875 keV. In all three regions a quadratic fit provided significantly better fit than a linear solution. Between 4.51 and 5.32 keV there is an obvious discontinuity in the range data due to a series of Cesium and Iodine absorption edges (Fraser *et al.*, 1995). We have used a simple linear interpolation between the data points in conjunction with synchrotron data – to locate the edges– to produce a fit in this region.

We are uncertain about the source of the discontinuity at 2 keV. It is possibly due to residual errors in the mirror effective area in that region, due to an edge at 2 keV. Small deviations in the mirror effective area would have a substantial impact on the calculated range of the detector. For the time being we have simply separated the data above and below this boundary into separate fits.

As we proceed to lower energies from 2 keV, we find that the quality of the results declines. This is most likely due to a progressive increase in the uncertainty due to the removal of multiple orders discussed above. This is further complicated by the sensitivity of the calculated quantum efficiency to small changes in incident flux and count rate. Between 700 eV and 1.82 keV the data appears reasonably well behaved and we have selected this region for our range fitting procedure. Furthermore, an extrapolation of this fit to lower energies produces unphysical results. We note that the cutoff point that we have selected based on the data quality coincides with the energies where contamination by third order lines becomes possible.

The curve in Figure 20 was then used with Equation 41 to generate the model for the MCP quantum

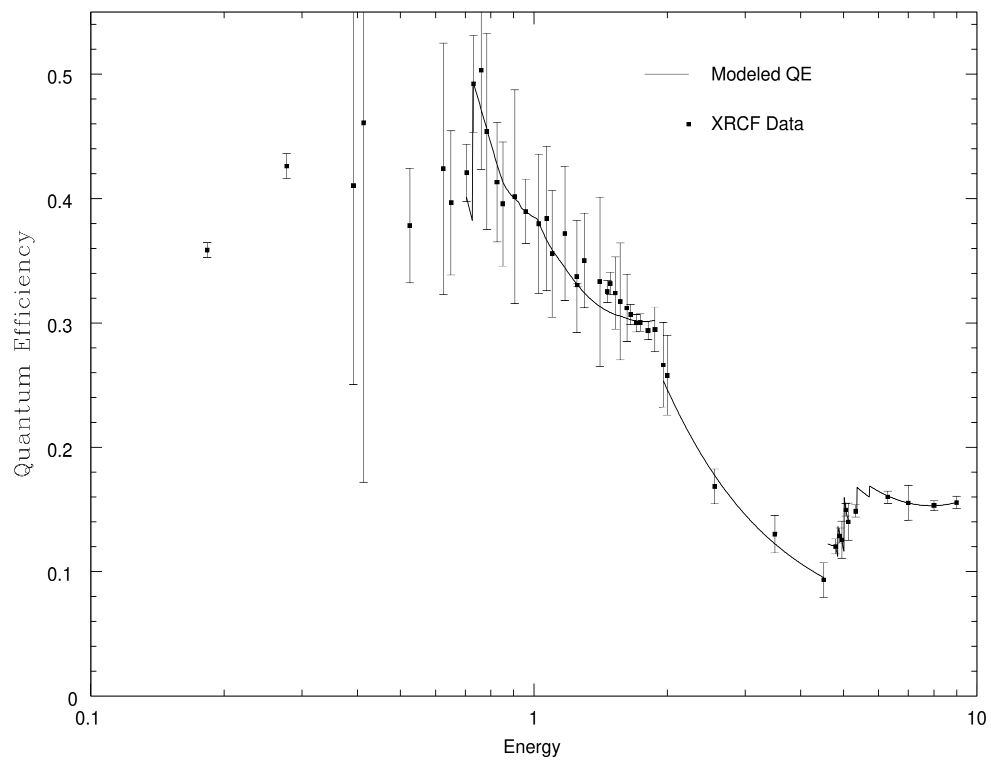

Figure 21: Modeled MCP quantum efficiency between 700 eV and 9 keV.

efficiency (Figure 21). Combining our results with the UVIS transmission , as well as the most recent HRMA effective area yielded our model for the HRC-I/HRMA effective area (Figure 22).

The original instrument team model between 0.7 and 2 keV was a conservative estimate lending confidence to our higher result. We have also included a Ring Focus measurement made with the EIPS Mg anode at 1.254 keV. The EIPS source spectrum did not have any order contamination and had a very weak continuum component, resulting in a very robust measurement of the efficiency at this energy. Happily the calculated efficiency is in good agreement with the HIREFS data taken at 1.25 keV. Above 2.0 keV, we find excellent agreement with subassembly calibration data. As noted above, below 700 eV our data is in poor agreement with all available models.

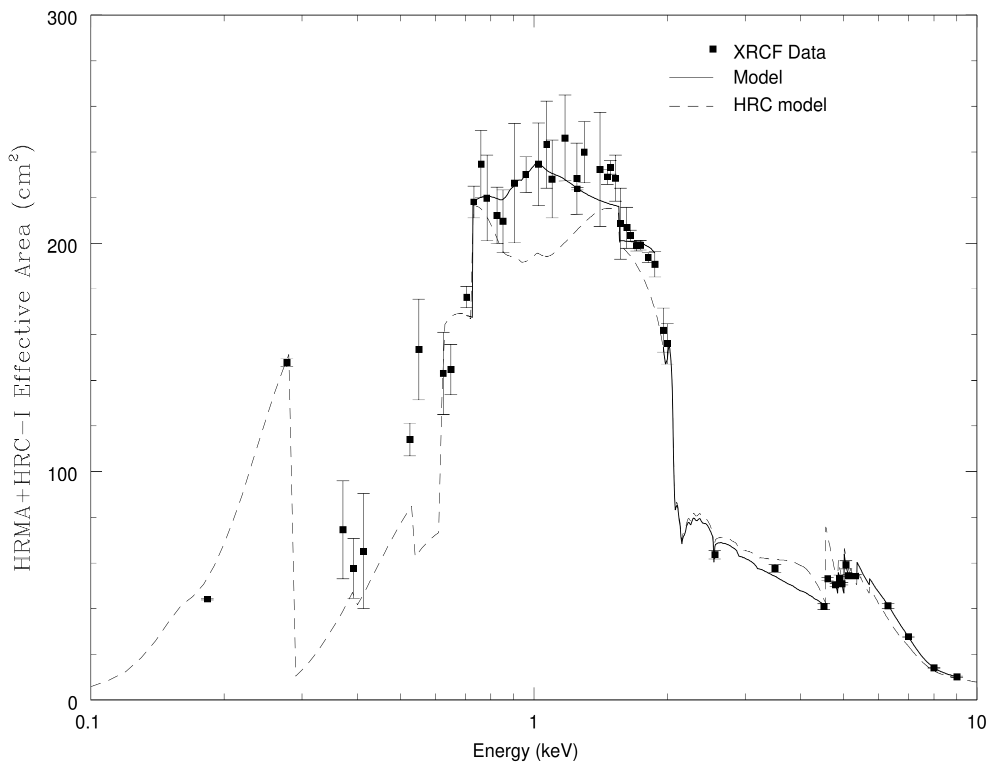

Figure 22: Modeled effective area (solid curve) for the HRC-I as compared to the HRC Instrument Team modeled effective area (dashed curve). We have adopted the instrument team model below 700 eV.

Effective area versus off axis angle for various energies is presented in Figure 23. The drop in EA with increasing off-axis angle is due primarily to the geometric vignetting of the telescope.

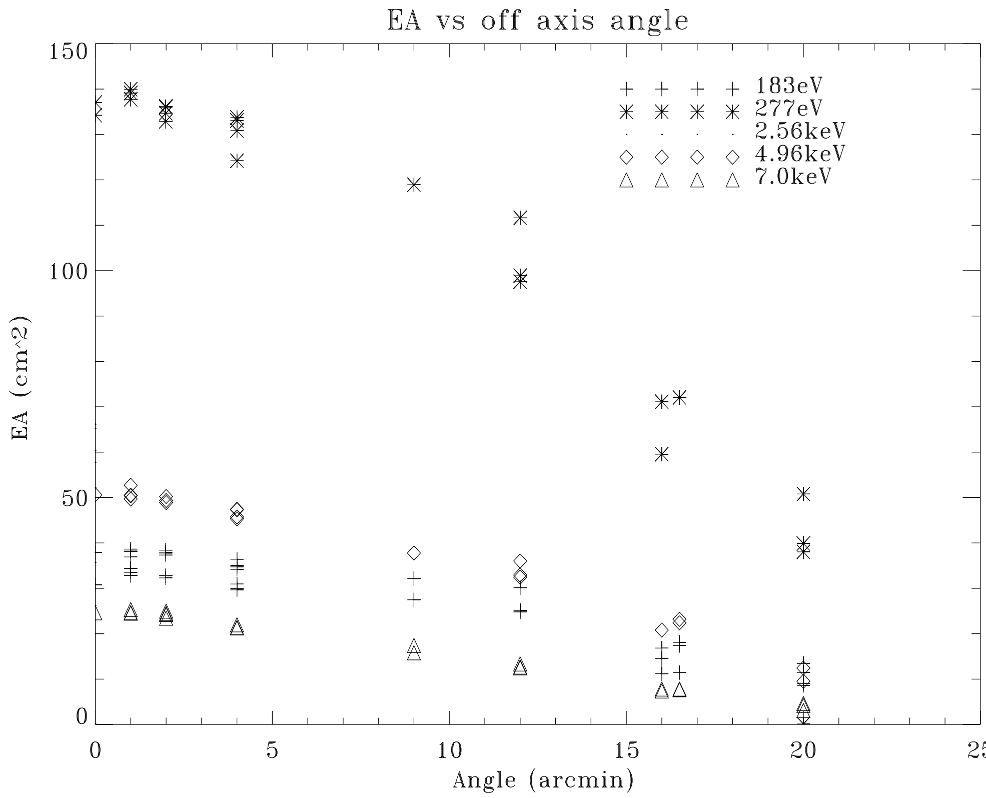

Figure 23: Effective Area of the HRC-I with the HRMA versus off-axis angle. Telescope vignetting is the primary cause of the drop off in EA. Each data point represents $\sim 10,000$ photons. Multiple points indicate identical HRMA pitch and yaw on different parts of the detector.

After completion of the testing at the XRCF, the HRC-I was modified to improve its performance. Following these modifications, a series of lab measurements were performed to provide data to bootstrap the XRCF results to the flight configuration.

Point Spread Function (PSF)

The PSF was determined from a second set of CRL data taken with a carbon anode in the EIPS source. Results for these PSF measurements are presented in Figures 24 through 26. Orthogonal slices through the center of the PSF were fit to a Gaussian and the Encircled Energy (EE) versus radius was determined. The FWHM of the PSF slices are 47.3μm and 43.9μm. The half power radius for the EE is 22.5μm.

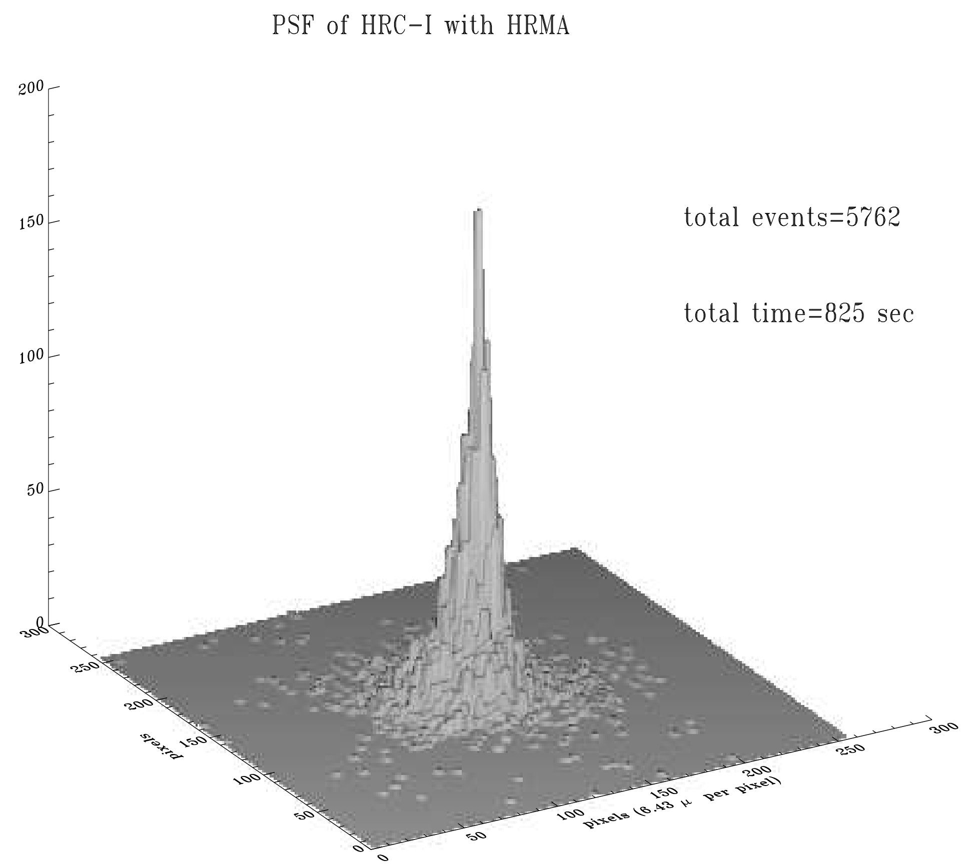

Figure 24: Surface plot of HRC-I/HRMA point spread function. Data taken with no FAM motion during count rate linearity test. C X-rays at 277eV from EIPS source were used.

This PSF analysis was performed with limited statistics and no effort was made to eliminate effects of gravity sag on the HRMA. Previous laboratory measurements of the PSF of flight-like MCPs combined with flight-like electronics yielded a σ of 10.0μm (FWHM of 23.5μm) for a Gaussian PSF.

As previously discussed, during flight assembly of the HRC instrument it was decided to operate the HRC detectors with the UVIS at ground potential. As a result, the UVIS to MCP potential changed from +100V to $\sim$ +3000V. Subsequent testing at SAO has shown that this change is responsible for producing a faint, $\approx 1\%$ secondary image displaced about 0.5 mm in one direction from the true PSF image.

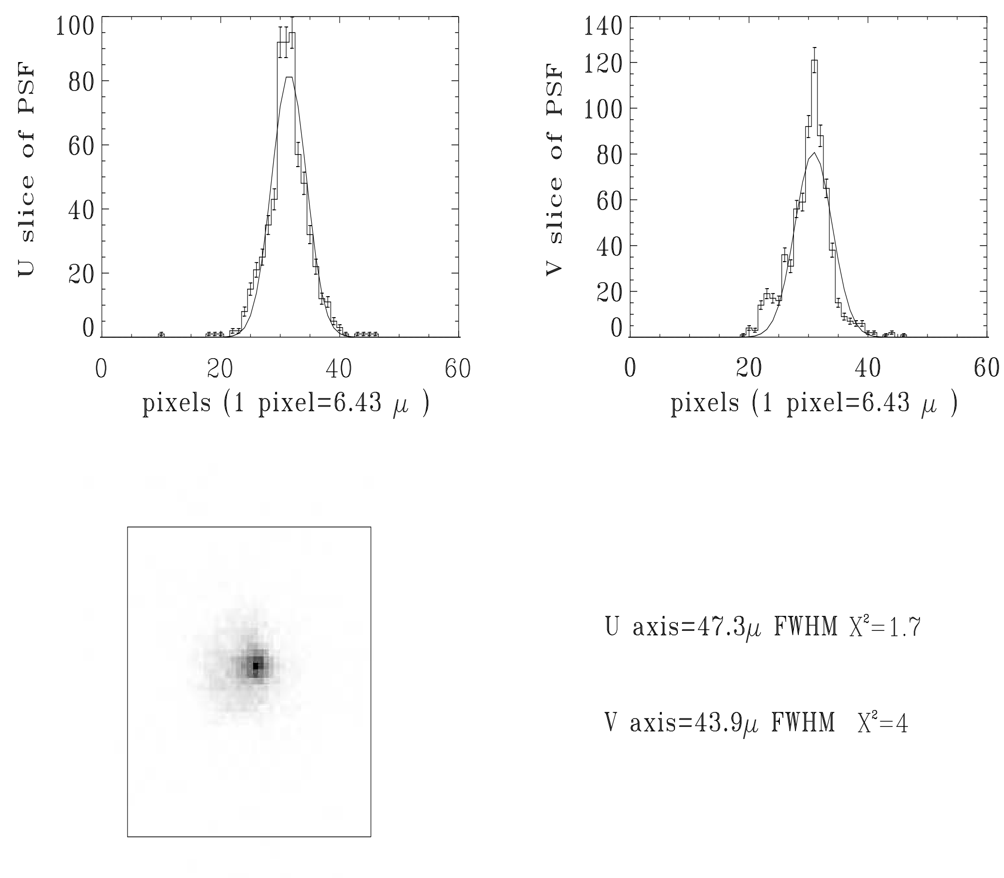

Figure 25: Point Spread Function (PSF) of HRC-I/HRMA. Data taken with no FAM motion during count rate linearity test. C X-rays at 277eV from EIPS source were used.

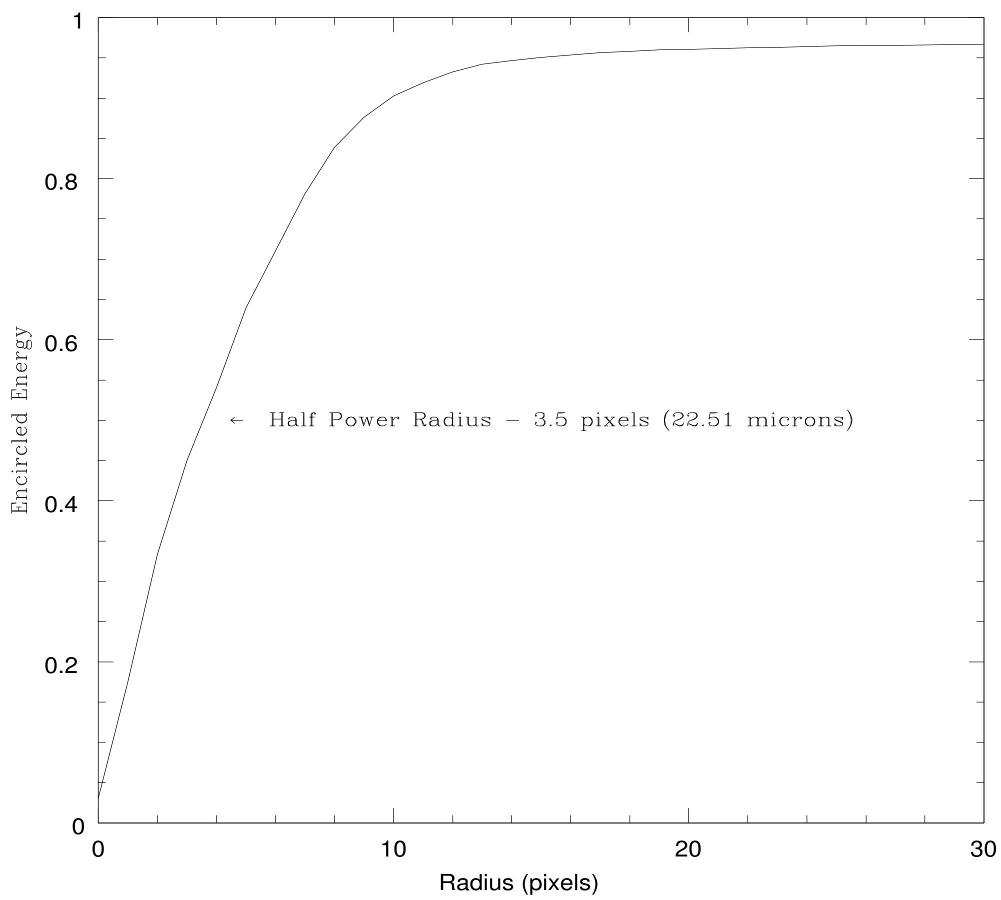

Figure 26: Encircled Energy for the HRC-I/HRMA point spread function.

4.2.2 Flat Field Testing

Following calibration at XRCF, the HRC instrument was returned to the SAO HRC laboratory in Cambridge, MA for hardware modification and uniform field X-ray illumination. The uniform field X-ray illumination was done to determine the absolute Quantum Efficiency of the HRC detectors as well as their spatial uniformity of response. The SAO facility was better suited than XRCF for such testing on account of the higher X-ray flux levels attainable.

The Facility

The SAO HRC laboratory is depicted in Figure 27. The facility consisted of a Manson model 5 multi-anode X-ray source, two Manson 04 flow proportional counters and a $\approx$ 7m long evacuated X-ay pipe. The HRC instrument was mounted to the end of the pipe with a series of different fittings. Each fitting was tailored so that the HRC-I detector and the HRC-S segments could each be uniformly illuminated. At the same time, this setup allowed full access to the HRC electronics for diagnostics and modification. During this testing a temporary modification to the HRC electronics was implemented that allowed data rates 10$\times$ greater than normal HRC event telemetry rate of $\approx 184 sec^{-1}$.

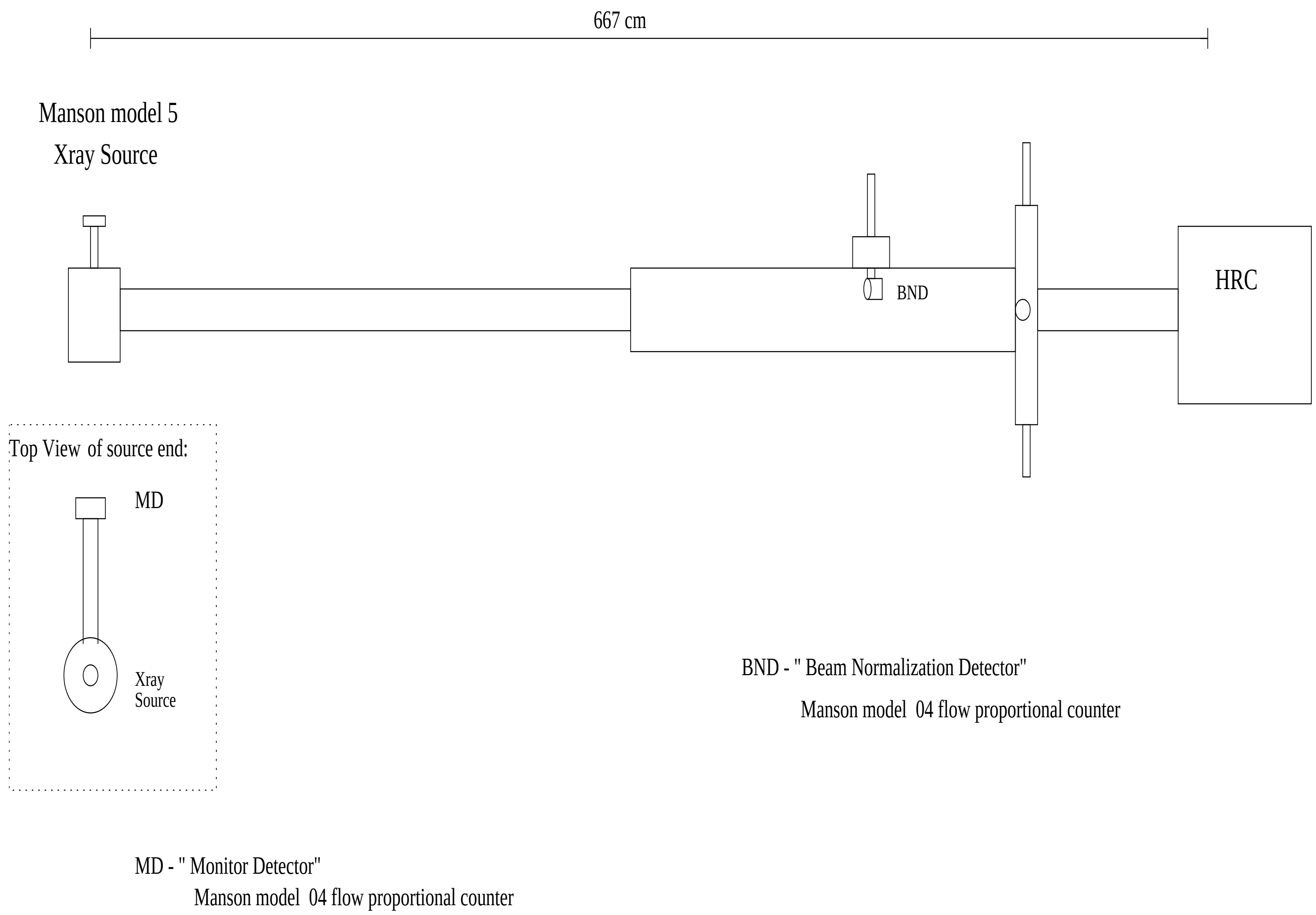

Figure 27: Facilities at the SAO HRC laboratory used for flat-field illumination of the HRC detectors.

Spatial Uniformity, QE, and Effective Area

X-ray illumination was provided with a Manson model 5 multi-anode electron impact source. The anodes and filter combinations listed in Table 1 were used for the HRC-I detector flat field illumination tests.

During the uniform field illumination tests, the HRC was exposed for a fixed period of time so that a minimum 10×10^6 photons were detected for all anodes excepting boron, for which 3×10^6 photons were detected; low flux levels from boron would have necessitated excessive integration times.

The beam flux close to the input of the HRC was measured using one of the Manson Model 04 flow proportional counters which was mounted on a retractable arm. This Beam Normalization Detector (BND) was not operated concurrently with the HRC on account of the slow gas leak through the thin flow counter window and the proximity of the detector to the HRC.

Absolute flux measurement and temporal monitoring were performed by first "cross-calibrating" the BND to a second Monitor Detector (MD) close to the X-ray source. With the HRC off, the BND was inserted into the center of the beam; the BND and the MD flow proportional counter were then operated concurrently and cross-calibrated.

During the flat field illuminations of the HRC, the BND was evacuated and retracted from the beam. The MD was operated to monitor the temporal stability of the beam and by using the BND to MD cross-calibration, the photon flux at the input of the HRC was determined.

In off-line analysis, the photon flux at the input of the HRC was used to determine the absolute Quantum Efficiency (QE) of the HRC-I detector. In addition the spatial uniformity of the HRC-I detector response was measured.

During these test, the electronics were modified so as to allow a data rate $\approx 10\times$ the telemetry limit of ≈ 184 sec^{-1}. In practice, data rates were intentionally limited to $1200 - 1400$ sec^{-1} for the HRC-I for all energies except for Boron. The Boron data were flux limited. The dead time per valid event for the HRC detectors has been measured to be $\tau = 68.5\mu$-seconds. The lion's share of this is due to the ADC conversion time.

Due to the nature of the dead time, dead time corrections can be applied to the Flat-Field HRC QE values by considering the instrument as a non-paralyzable (non-extendable dead time) detector with a characteristic dead time of $\tau = 68.5\mu$-seconds. At measured rates of ~ 1200 sec^{-1} this will cause an underestimate of the true rate of $\sim 9\%$. QE values as determined from these measurements will underestimate the QE values at low ("zero") count rates by the same factor.

It can be easily shown under the above assumptions that:

$$\frac{QE_{true}}{QE_{meas}} = \frac{R_{true}}{R_{meas}} = \frac{1}{1 - R_{meas}\tau} \tag{43}$$

Where the true values are the "zero-rate" limits. The values of these corrections are 1% at 0.183 KeV and 10% at all other energies.

Table 1: Summary of line energies, filters, thicknesses, anode voltages, and predicted line-to-continuum ratio of the X-ray source for HRC-I flat fields.

Line	Energy	Filter	MFPs	V_A	L/C
B Kα	183 eV	7 μ parylene-C	5.87	600 V	48.4
C Kα	277 eV	33 μ polypropylene	5.94	1000 V	171
O Kα	525 eV	2 μ Cr	4.67	1000 V	29.3
Ni Lα	851 eV	2 μ Cu	3.80	2500 V	2.55
Al Kα	1487 eV	50 μ Al	5.40	4000 V	38.9
Ag Kα	2984 eV	10 μ Ag	4.86	6000 V	0.60
Ti Kα	4511 eV	150 μ Ti	6.80	10000 V	6.73
Fe Kα	6404 eV	125 μ Fe	6.97	10000 V	1.78

Table 2: QE of HRC-I averaged over entire detector. $\sim 10^7$ photons collected for all energies except $\sim 3 \times 10^6$ for B (183)eV.

HRC-I QE		
Element	Energy (eV)	QE
B	183	0.063
C	277	0.203
O	525	0.119
Ni	851	0.280
Al	1487	0.309
Ti	4511	0.109
Fe	6404	0.148

The absolute QE at the eight energies are presented in Table 2. These values are averages over the entire CsI coated HRC-I active area and have been corrected for deadtime losses.

Surface plots of the detector flat field response, and of the average gain for the HRC-I detector at one of the energies (1.48keV), are presented in Figures 28 and 29. The detector efficiency is seen to be uniform at the $\sim 10\%$ level even though the detector gain shows considerable variation.

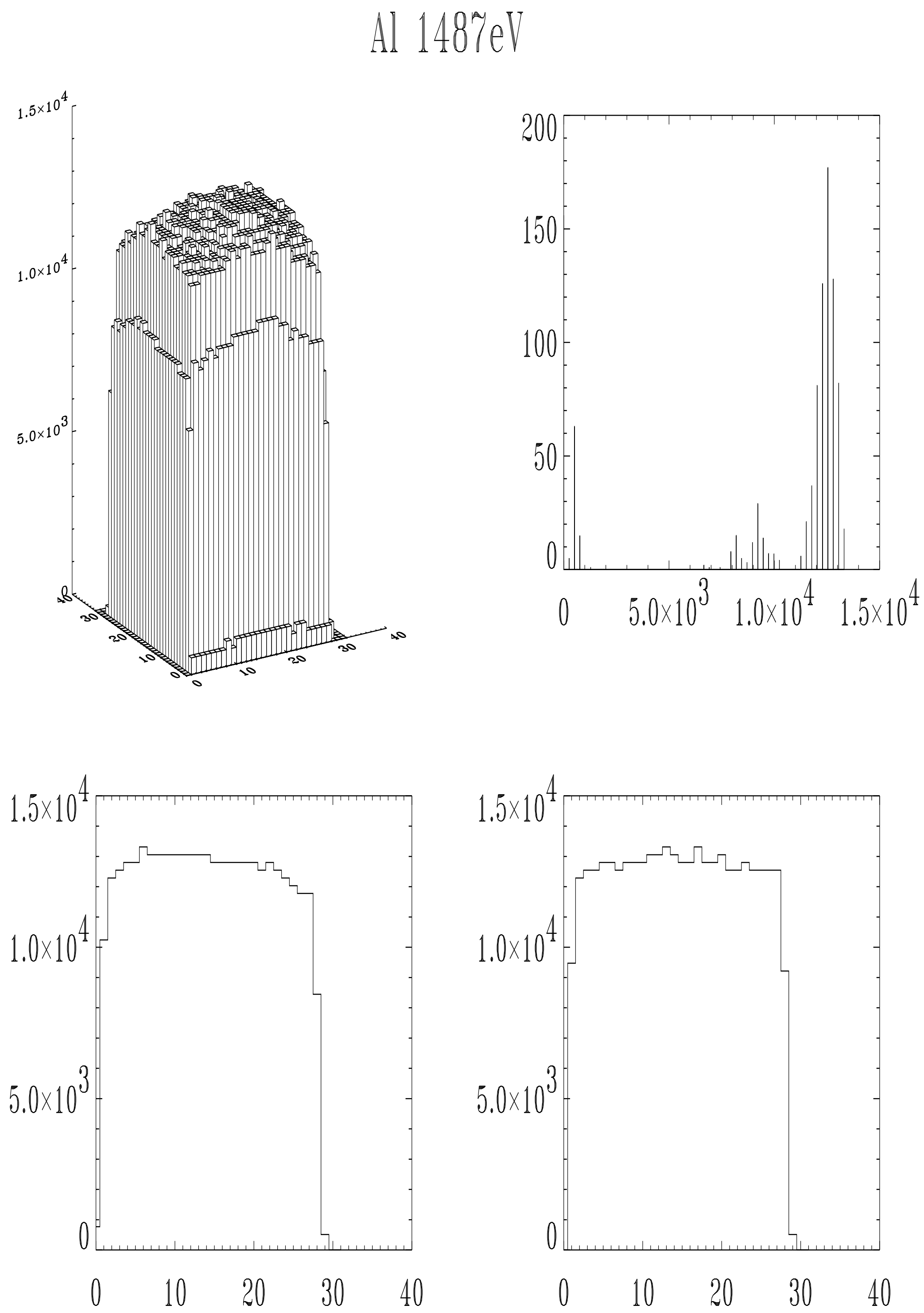

Figure 28: Surface plot of flat field response of HRC-I detector at 1.48keV. The efficiency is uniform at the $\sim 10\%$ level.

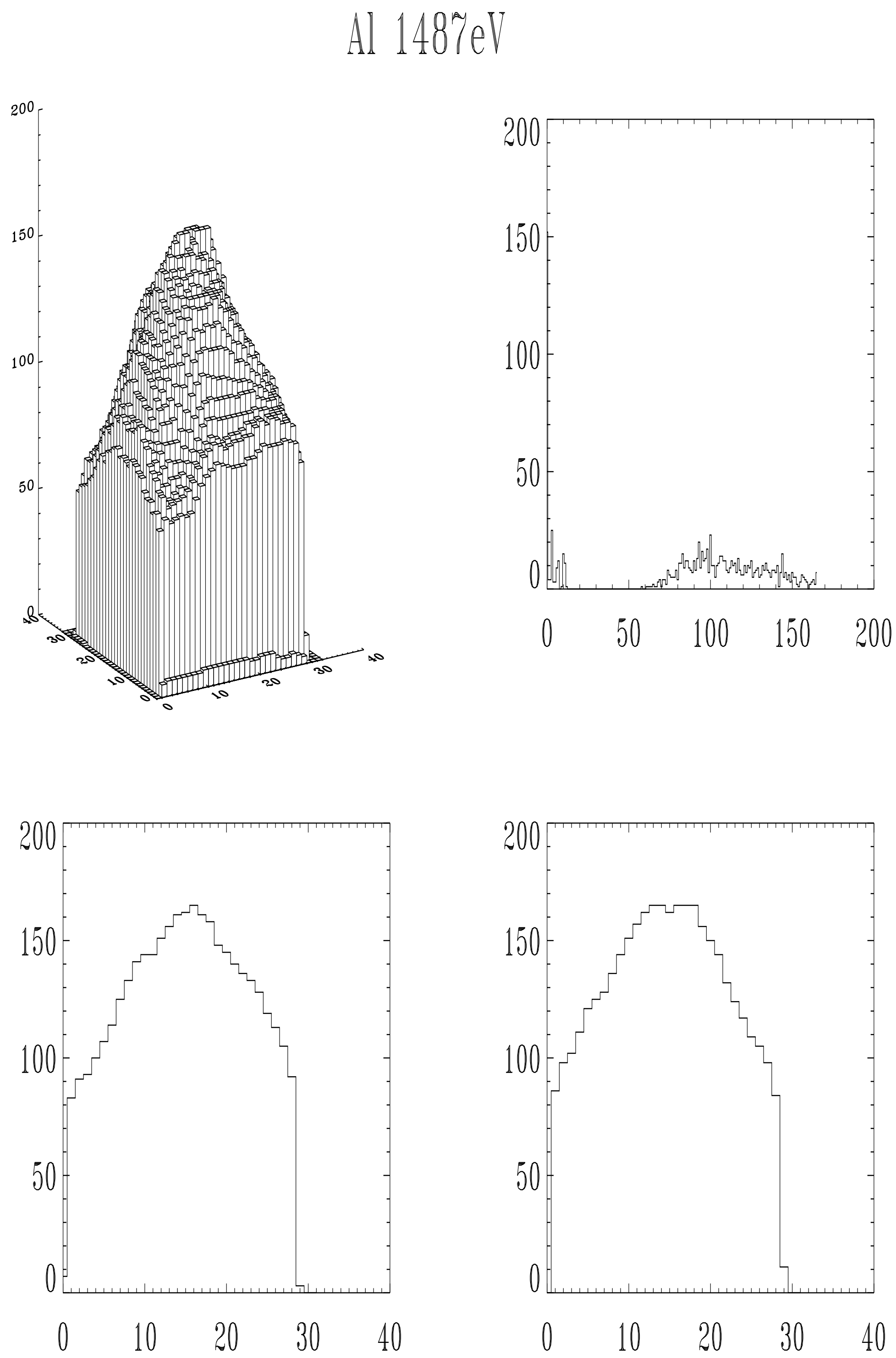

Figure 29: Surface plot of average gain of HRC-I detector at 1.48keV. Large variations in gain over the HRC-I are evident. These large gain variations do not affect the detector efficiency

An on-axis effective area model for the HRC-I detector was produced using: Flat Field and XRCF determined MCP quantum efficiencies; the UVIS transmission; and a HRMA effective area (Figure 30) model (flight: model du jour).

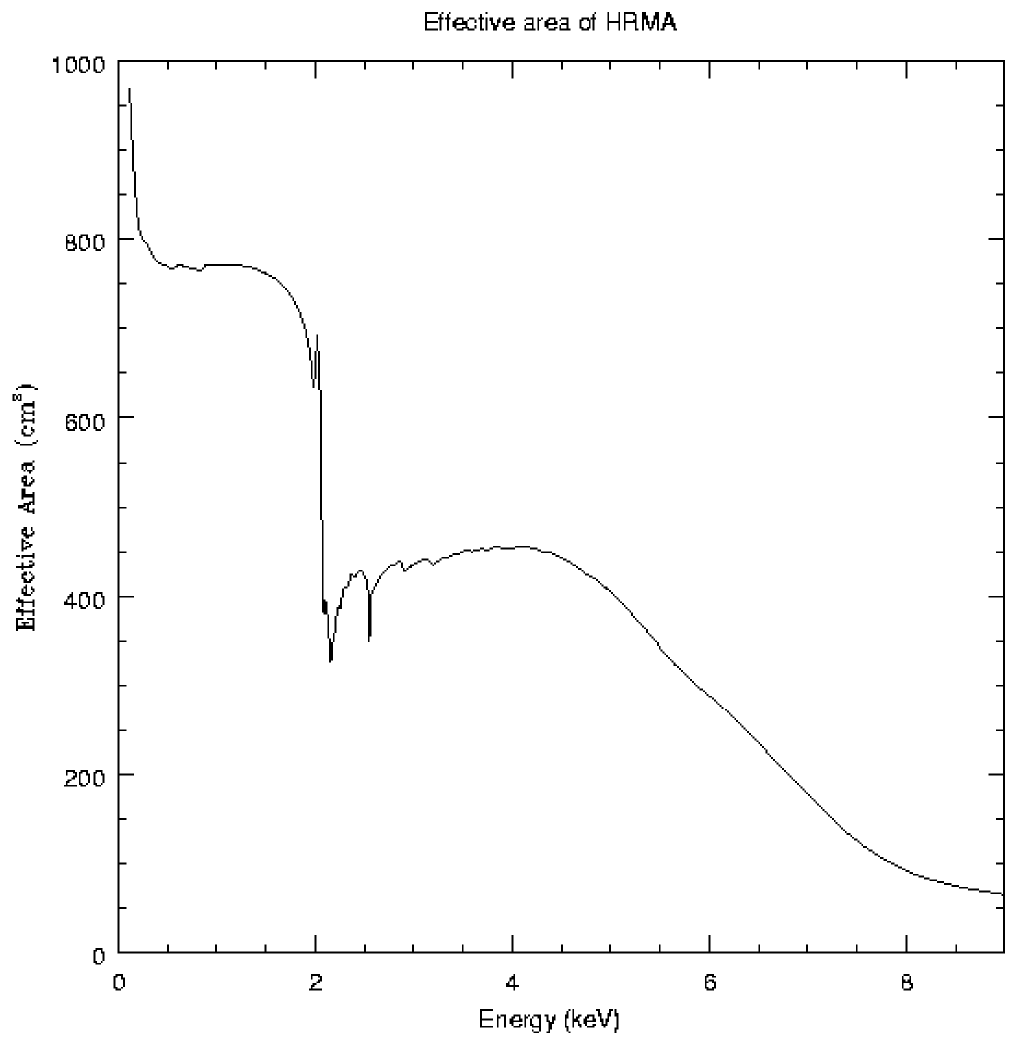

Figure 30: HRMA effective area (HRMA flight model du jour).

Of the three elements, QE,UVIS transmission and HRMA EA, the least well known is the detector QE. With only a few measured data points it is necessary to develop a model which can be used in interpolating between the discrete measured QE values.

The QE model, based on earlier work on photocathodes (Henke, Knauer, and Premaratne 1981), is as outlined in Mike Juda's memorandum. In short, the model uses primary and secondary electron yield to predict the QE of CsI coated MCPs. The primary and secondary yields depend on the mass absorption coefficients of CsI and the primary and secondary electron ranges. Given a fixed electron range, no linear combination of primary and secondary yields give an adequate fit to the measured HRC-I MCP QE values. A complete description of this model is given elsewhere:

(http://hea-www.harvard.edu/~juda/memos/mcad_QE_model.ps)

Turning the problem around, the measured QE values can be used to determine an empirical electron range versus energy curve. This electron range curve can then be used to predict electron yield and a therefore a continuous functional form for the HRC-I MCP QE (Figure 31).

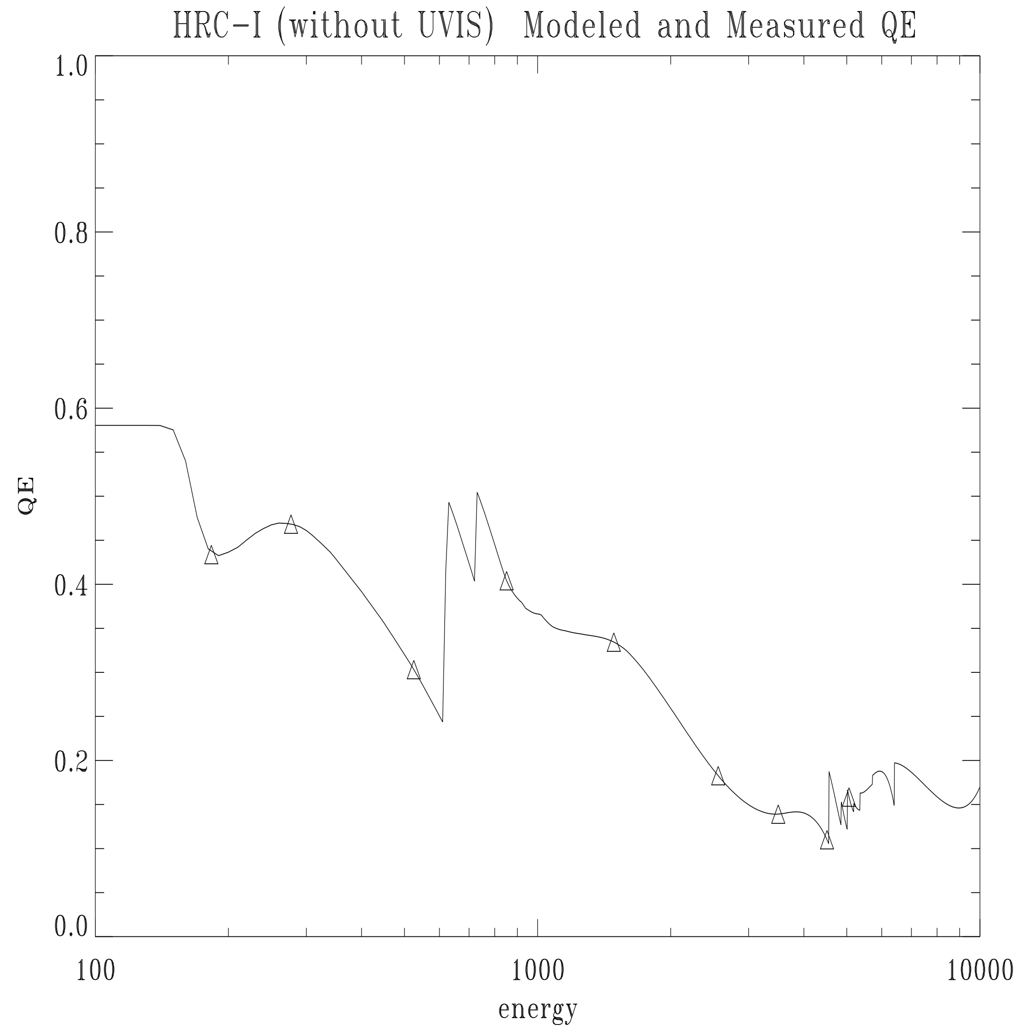

Figure 31: HRC-I MCP modeled quantum efficiency and data.

The above procedure was performed for the HRC-I detector using both flat field and XRCF determined QE values. This HRC-I MCP QE model was then combined with the transmission model for the UV Ion Shield and the HRMA effective area ray-trace model to produce a HRC-I/HRMA Effective Area (Figure 32).

Post-XRCF flat field quantum efficiencies were determined at only eight energies: 183,277,525,851,1487,2980, 4511 and 6404 eV. One of these flat field QE values (for Ag L) was discarded on account of large uncertainties. Initial attempts to model QE and EA with this minimal set of points produced large and unphysical results. In particular, the predicted QE and EA in the 2 to 4 keV and the 4.5 to 6 keV regions were too high.

Since post-XRCF detector modification raised only the low energy detector response, the QE at some higher energies determined from XRCF EA measurements was also used as input to the model. This inclusion of XRCF data was deemed appropriate as the effects of the detector modification were minimal for the HRC-I.

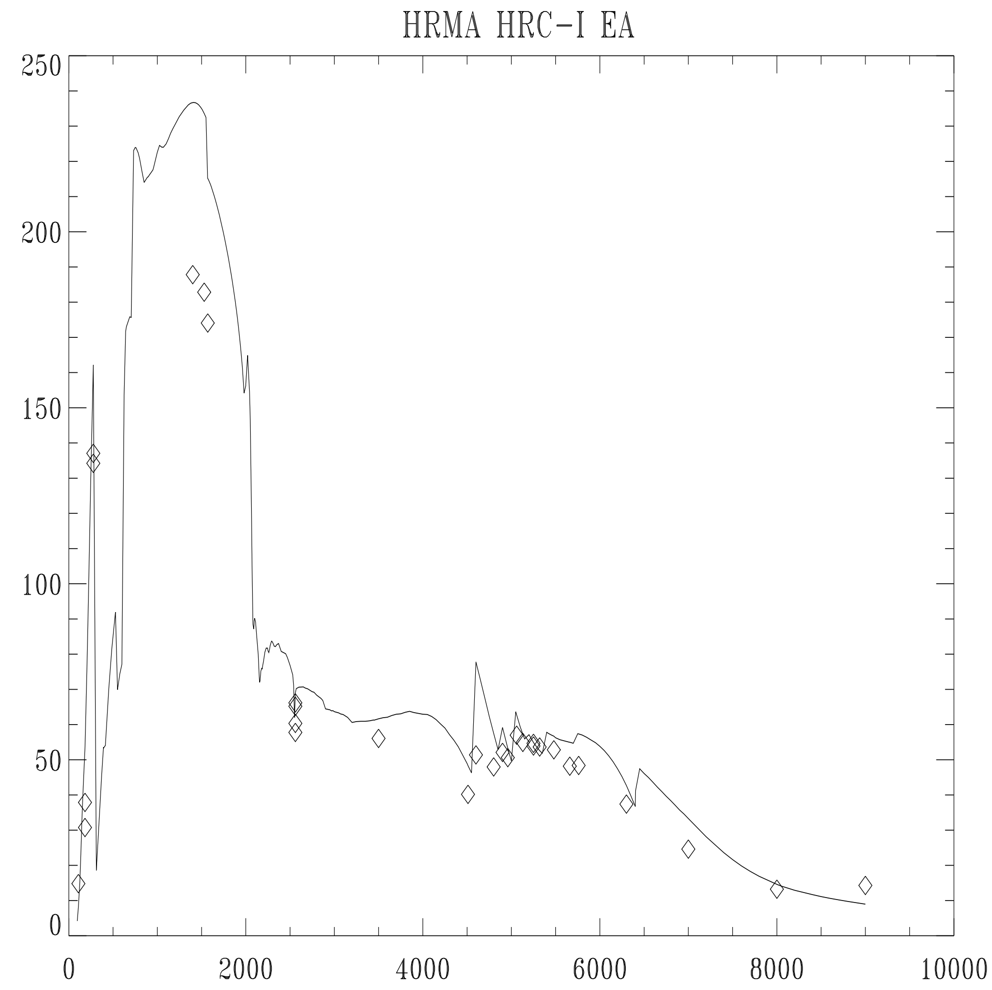

Figure 32: HRC-I modeled effective area and XRCF data (HRMA flight model du jour).

Table 3: Energies and quantum efficiency values used to construct the HRC-I MCP QE model.

HRC-I QE		
Element	Energy (eV)	QE
B	183	0.063
C	277	0.203
O	525	0.119
Ni	851	0.280
Al	1487	0.309
-	2560	0.176
-	3500	0.137
Ti	4511	0.109
-	5060	0.158
-	5660	0.149
Fe	6404	0.148
-	9000	0.146

The energies and QE values used as input to the model are given in Table 3:

Two XRCF determined QE values (at 5060 eV and 5660) near the Cs and I L edges were scaled by the ratio of flat-field QE to XRCF QE at 4510 eV. The scaling factor was 1.1. This inclusion served to better constrain the model near the Cs and I L edges. The XRCF QE values at 2.56 keV and 3.5 keV were similarly scaled and included.

This procedure has produced a "pleasing" model for the HRC-I/HRMA EA. The ratio of model/XRCF EA (Figure 33) reflects what was expected from the hardware changes; the EA at lower energies has been increased and at higher energies the EA is approximately the same. The ratio shows that there is still some discrepancy near the UVIS and the photocathode edges. In addition, the measured effective area at 9 keV appears too high.

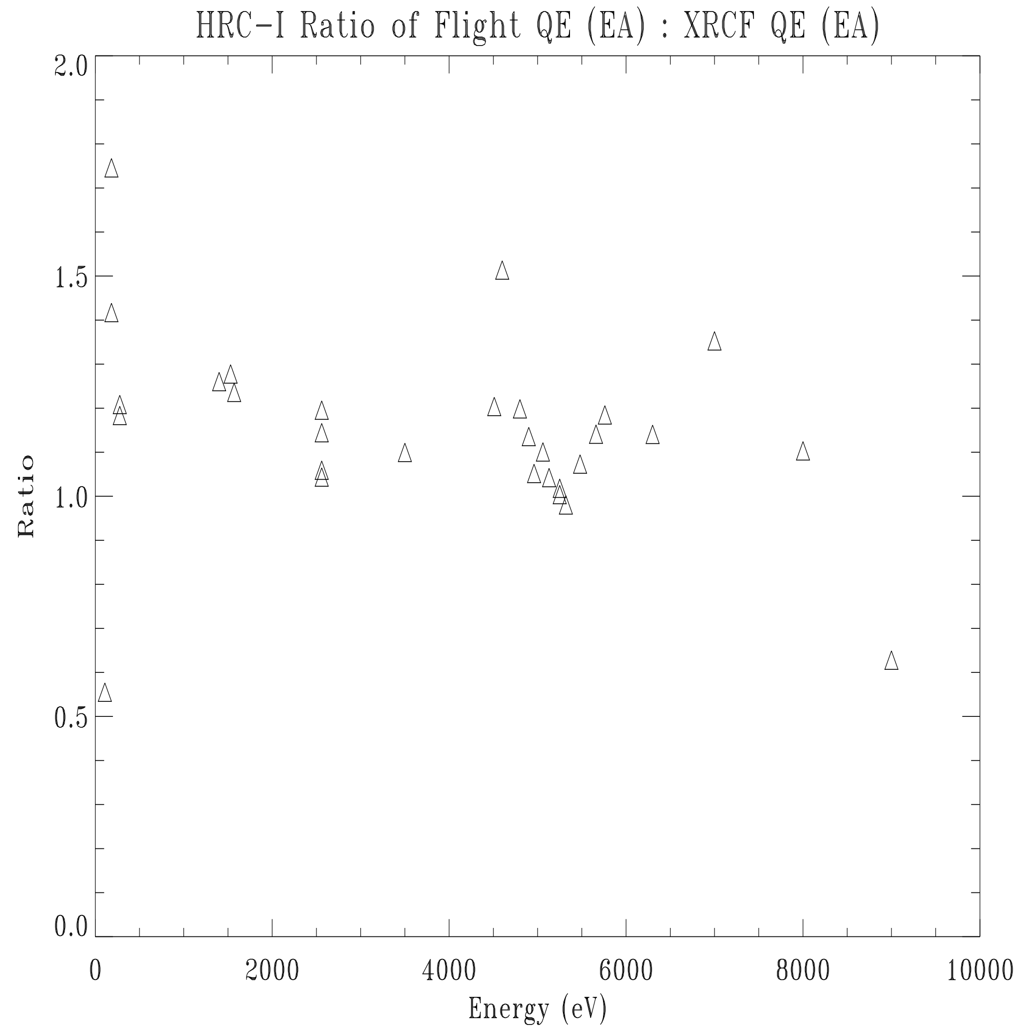

Figure 33: HRC-I modeled effective area and XRCF data (HRMA flight model du jour).

Spectral Resolution

The inherent energy resolution of the HRC-I detector was investigated by examining the effect of incident X-ray energy on detected pulse height. The detected pulse height of the HRC-I versus incident energy is presented in Figure 34. It is evident that the HRC-I has some limited energy resolution for an ensemble of photons, particularly at energies < 1keV.

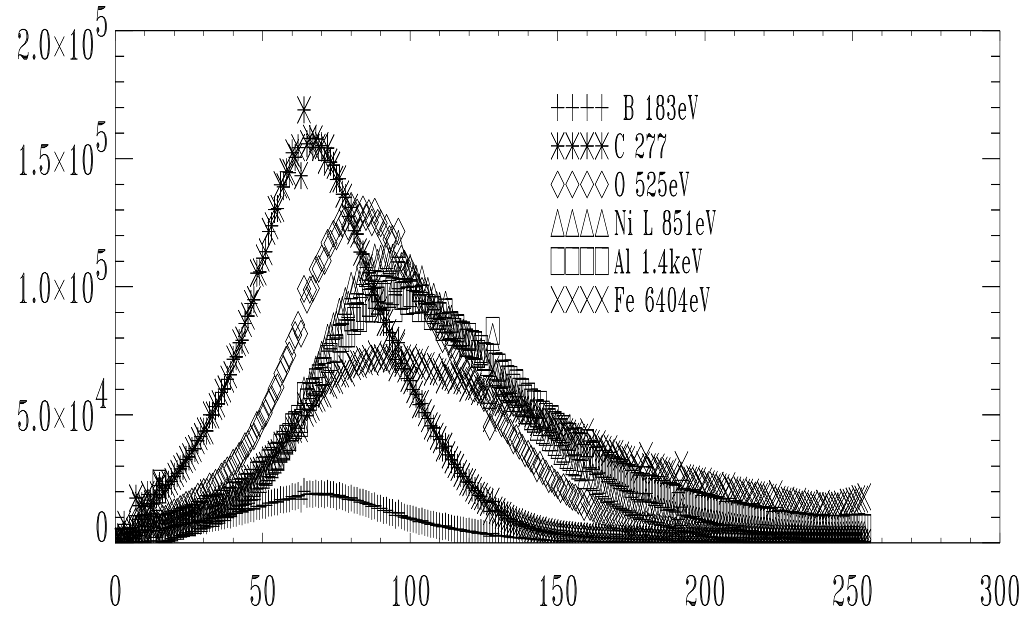

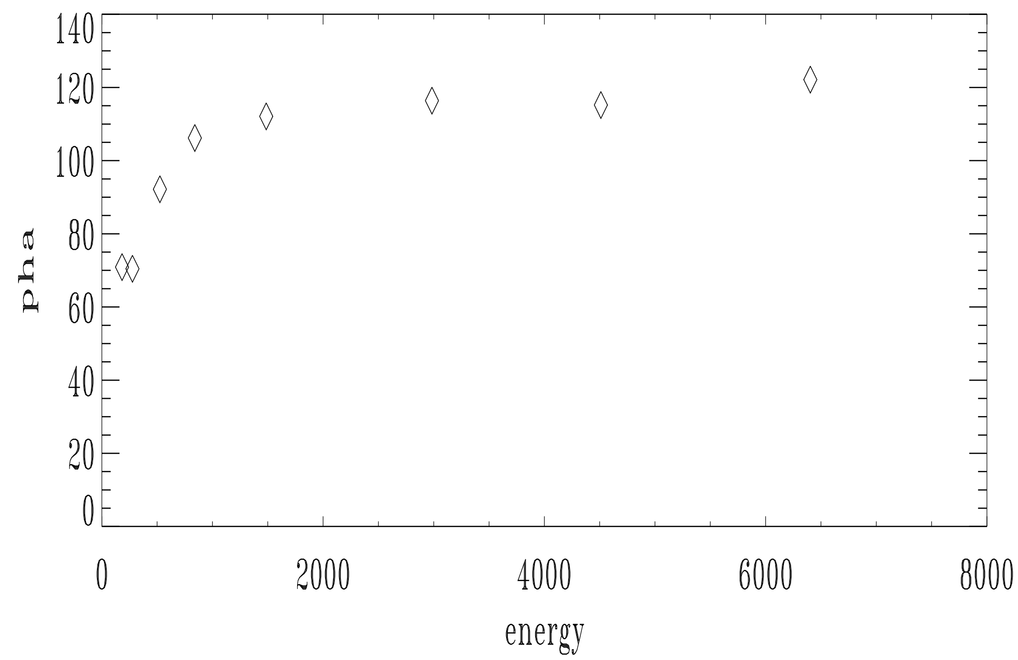

Figure 34: Pulse height distributions versus energy and centroids of pulse height versus energy for the HRC-I detector. It is evident that the HRC-I has some limited inherent energy resolution.

UV/Optical Sensitivity Measurements

During HRC thermal-vacuum tests, the HRC detectors were tested for sensitivity to off band UV and optical radiation. These tests consisted of illuminating the detectors to radiation from several calibrated light sources and measuring the response. The light sources were: a mercury lamp with 2537Å filter; a mercury lamp with a 1850Å filter; a xenon light/filter at 1470Å; and a tungsten-halogen light filtered at 4500Å. The sources were calibrated at SAO to $\sim 10\%$ using a NIST calibrated photodiode. The measured and predicted response is indicated in Figure 35. Also shown is the HRC-I specification for maximum sensitivity. The predicted response of the detector is a product of the transmission of the UVIS and the photocathode sensitivity. The UVIS transmission model was determined from laboratory measurements and from published optical constants. Photocathode response was estimated from previously reported measurements. The uncertainty in the resulting model of HRC-I response is large. No gross leaks through or around the UVIS were detected.

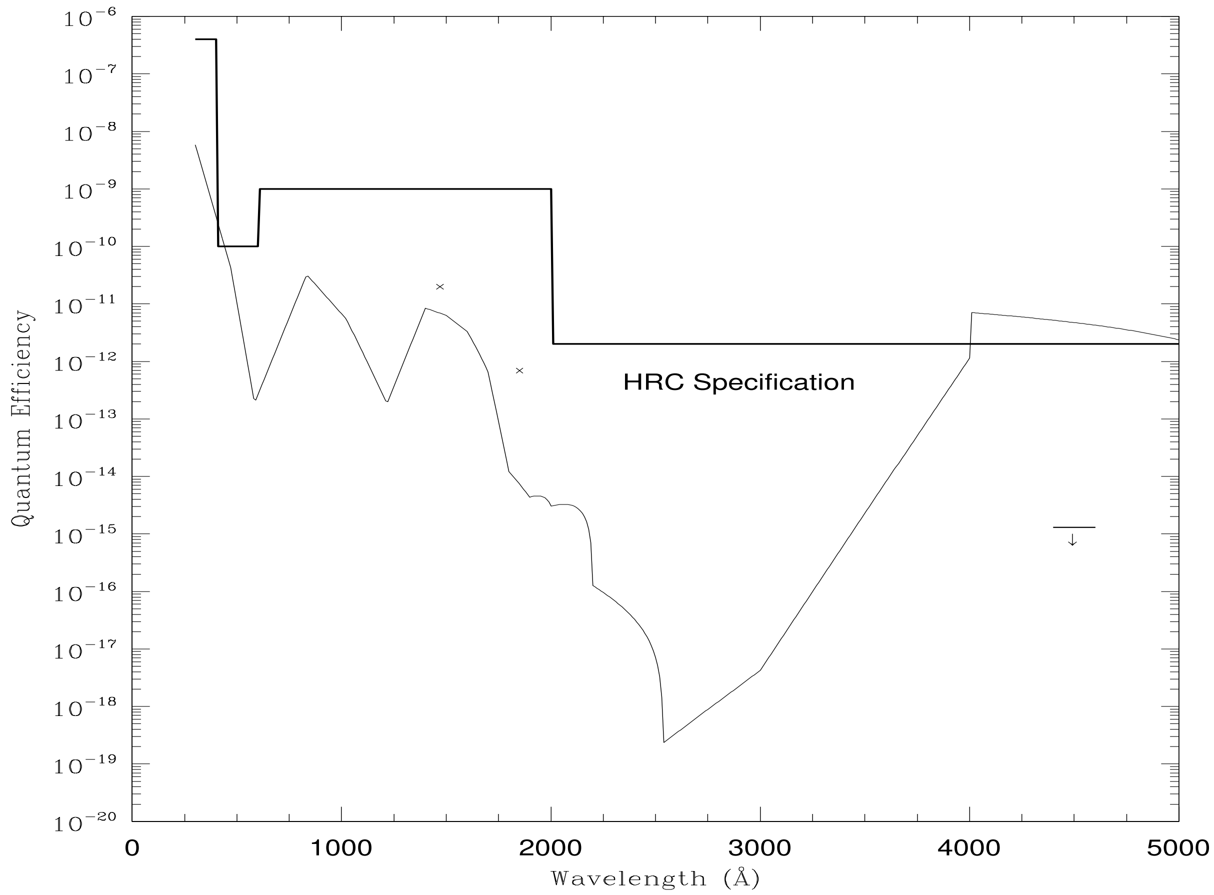

Figure 35: Measured, predicted and specification for UV and optical response of the HRC-I detector. The optical response (4500Å) is an upper limit. No measurement was made with the mercury lamp.

4.3 HRC-S (QE, EA, PSF, Resolving Power)

4.3.1 XRCF Calibration

The HRC-S was tested and calibrated in the spring of 1997 with the HRMA and gratings at the X-ray Calibration Facility (XRCF) at Marshall Space Flight Center. This facility was designed to meet the unprecedented level of calibration required for AXAF. A schematic diagram of the XRCF is contained in Figure 36. The XRCF consists of three buildings and a long (518 m) vacuum pipe. One building houses three X-ray sources. A second contains two beam monitor detectors (a gas flow proportional counter and a solid state detector). The proportional counter is mounted on a stage to map out the X-ray beam across the HRMA. The third building contains the instrument chamber and control rooms. The telescope, gratings, and detectors were mounted in the instrument chamber for testing. Four proportional counters (the BND-H counters) were placed symmetrically around the front of the HRMA to continuously monitor the X-ray flux and beam uniformity at the telescope.

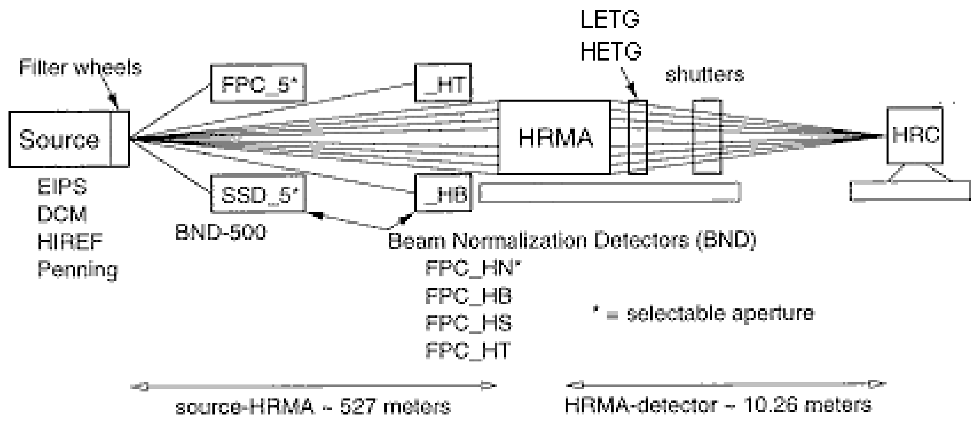

Figure 36: Schematic diagram of the X-ray Calibration Facility.

Four different X-ray sources/monochromators were used to generate X-rays over the AXAF bandpass. An electron impact source (EIPS) was used to generate characteristic lines from a variety of anodes (26 different anodes were available). Each anode also had filters that could be used to reduce the flux to acceptable levels and reduce continuum (bremsstrahlung) contamination. A gold coated reflection grating (HIREFS) and a W rotating anode source were used to generate monochromatic X-rays between 200 eV and 2000 eV. Higher order contamination and beam non-uniformity (up to a factor of 2 across the HRMA) make interpretation of this data difficult. Four different double crystal monochromators (DCM) were available to provide spectrally pure X-rays above 1.5 keV (in conjunction with the W rotating anode source). The beam uniformity of this source was good (about 10% across the HRMA), and higher orders contributed only a few percent of the flux. A gas discharge Penning source was used to generate soft X-ray and EUV lines from ionized Ar and Al.

XRCF measurements were made of the effective area (with and without the LETG), the count rate linearity, the point spread function, and the energy resolution of the HRC-S/HRMA and HRC-S/LETG/HRMA combinations. Over 1000 different measurements were made using the HRC-I or HRC-S. In this section, we present results from calibrations of the HRC-S/HRMA, and briefly discuss the HRC-S/LETG/HRMA calibrations. Measurements of the position (relative to the HRC-S and HRMA) and reflectivity of the TFRF were also made, but will not be discussed here

Effective Area

We have made effective area measurements with the LETG+HRC-S and with the HRC-S alone at various energies and angles of incidence. The effective area was measured by simultaneously illuminating the HRMA/HRC-S and the four BND-H proportional counters with X-rays from the EIPS, DCM, or HIREFS. The telescope was defocused for all effective area measurements to avoid extracting a large amount of charge from a small region. As above, the BNDs are used as absolute detectors. 60 energies were available for our analysis.

Our analysis of the HRC-S's quantum efficiency proceeded similarly to that described for the HRC-I. Producing a range plot with, as one would expect, extremely similar features. The data below 700 eV still appears to be unreliable and was again excluded from our fits. Furthermore, based on our experiences with the HRC-I and the expected similarity of the two detectors, we have divided the data into the same three energy regimes.

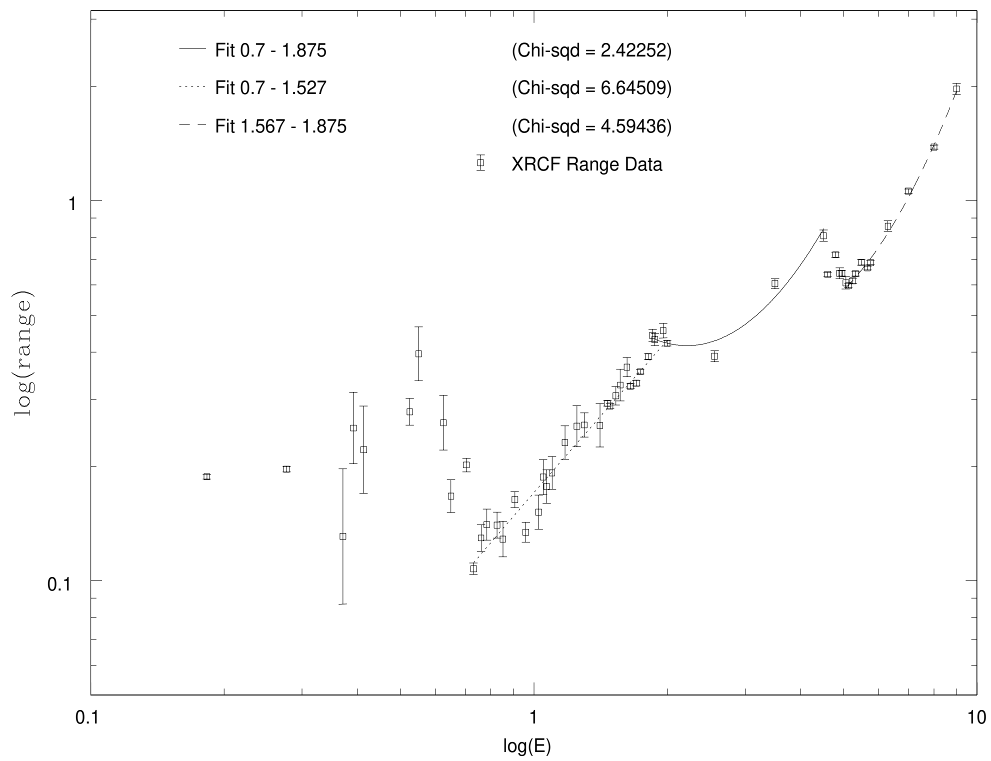

Figure 37: Range of secondary electrons in the HRC-S MCP.

Figure 37 shows the results of our quadratic fits to the three energy regimes in the data. Figure 38 gives the HRC-S quantum efficiency and Figure 39 the convolved HRMA/HRC-S effective area . As with the HRC-I, we have adopted the instrument team model below 700 eV.

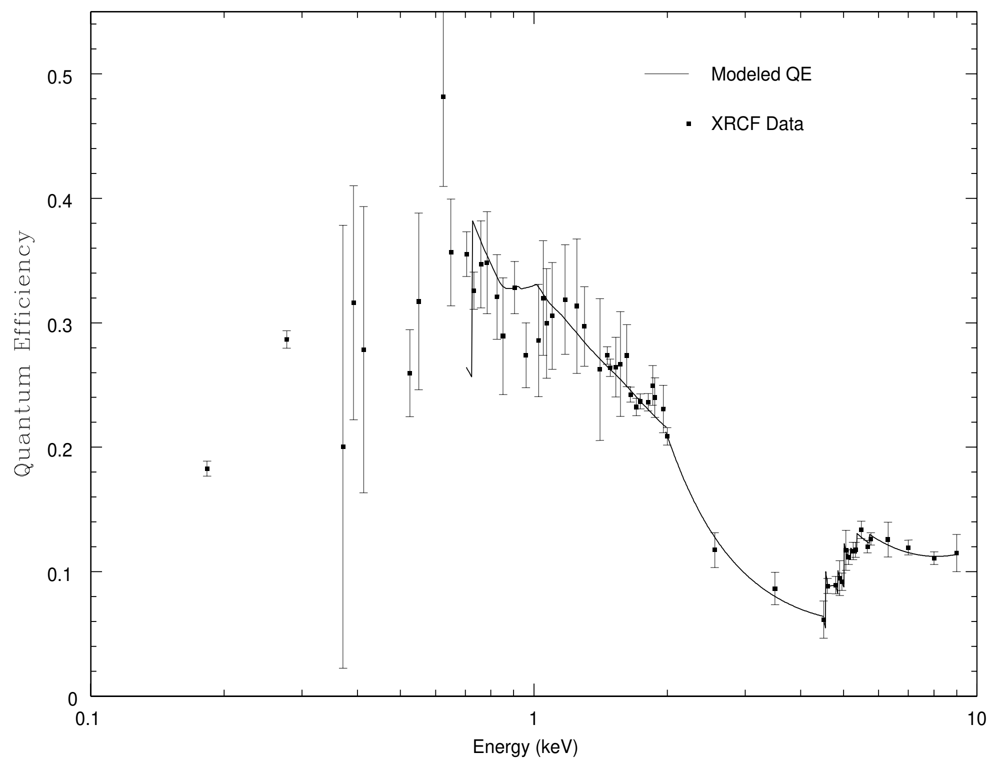

Figure 38: Modeled MCP quantum efficiency for the HRC-S central MCP.

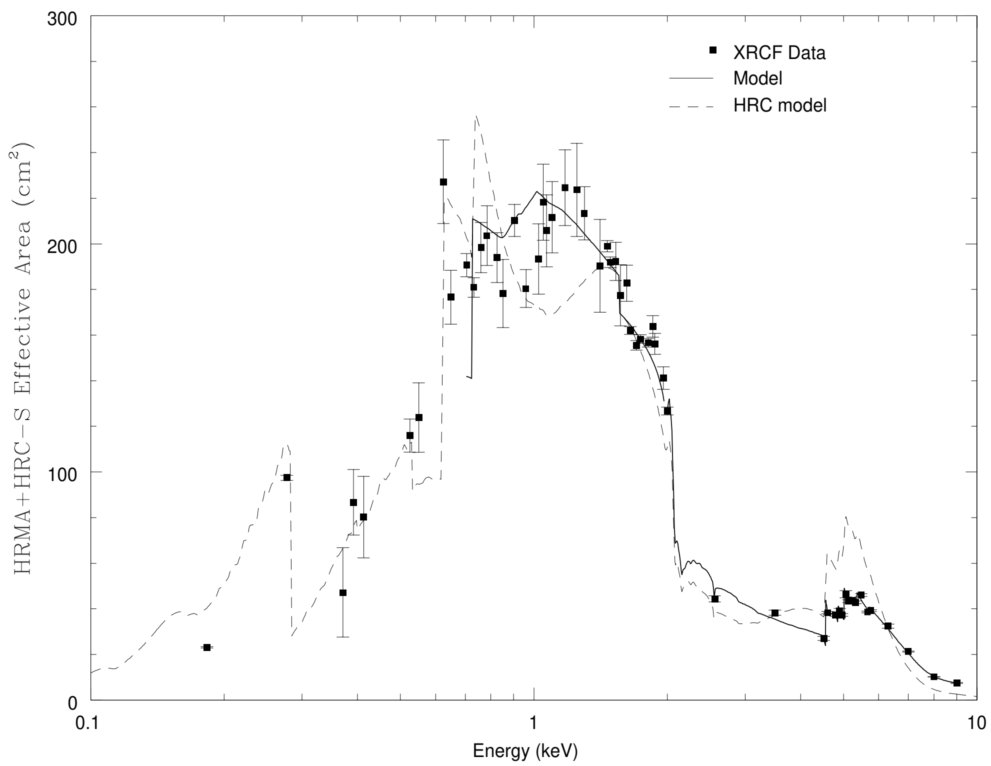

Figure 39: Modeled effective area (solid curve) compared to the HRC Instrument Team modeled effective area (dashed curve)for the HRC-S. As with the HRC-I, below 700 eV where our fitting is inadequate we have incorporated the model developed by the instrument team.

After completion of the testing at the XRCF, the HRC-S was modified to improve its performance. Following these modifications, a series of lab measurements were performed to provide data to bootstrap the XRCF results to the flight configuration.

HRC-S + LETG performance

A series of effective area measurements were also made with the HRC-S and LETG. As a typical example, the HRC-S + LETG spectrum of the EIPS with the Ti anode and Ti filter is shown in Figure 40. The Ti L_α and L_η lines can clearly be seen, as well as continuum and C K_α contamination. The width of the Ti L_α line (27.4 Å) is in this spectrum is $\sim$0.72 Å(11.9 eV), and is the intrinsic width of the line. The resolution of the grating is much higher (more than 1000 at the longest wavelengths). A more detailed discussion of the LETG effective area and energy resolution measurements is given elsewhere.

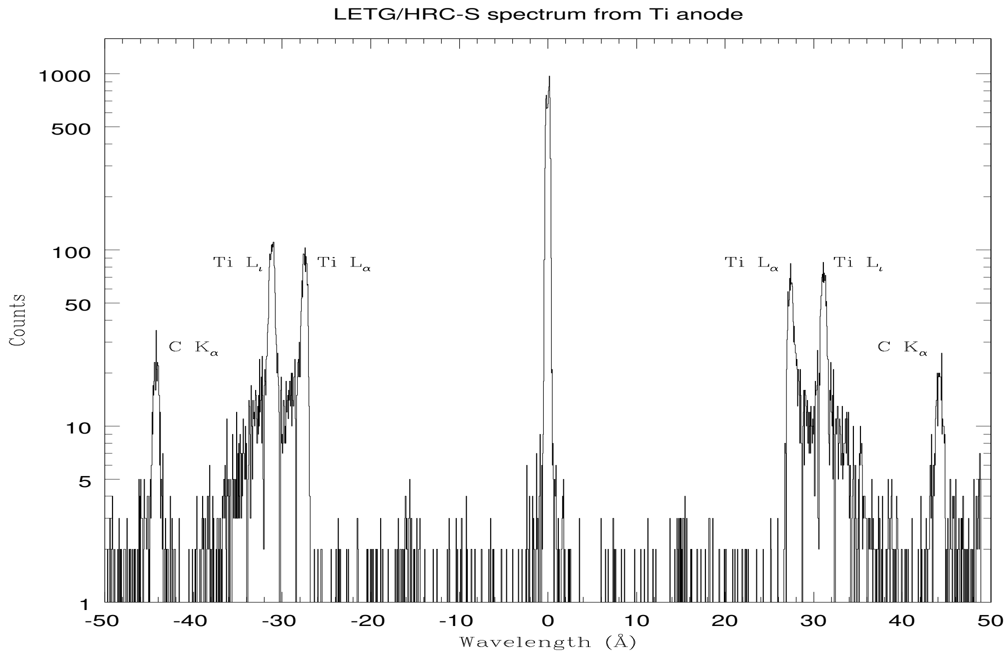

Figure 40: LETG/HRC-S spectrum of Ti anode with Ti filter. This plot is a projection of the HRC-S image along the dispersion direction.

Point Spread Function

The point spread function (PSF) of the HRMA+HRC-S was measured at several energies at the XRCF. The telescope was in focus, and the HRC-S was moved in a serpentine pattern to avoid a large amount of charge from being extracted from a small region. We are working to remove the effect of this serpentine motion on the images. As a preliminary analysis, we have used data from the count rate linearity measurements described above to estimate the PSF. These measurements were made with the telescope in focus and the detector undithered. A surface plot of the sum of the images taken for the CRL measurements described above (E=277 eV) is contained in Figure 41. Gaussians were fit to slices of the data along the U and V axes. The width (FWHM) of the PSF in the central 135 μm of the image is 42.95 μm in the U axis and 45.85 μm in the V axis (approximately 1 arcsec angular resolution). These data slices and best fit Gaussians for each axis are plotted in Figure 42. As an alternative, the encircled energy as a function of radius is plotted in Figure 43. The half power radius is 25.72 μm. Laboratory measurements of the PSF of flight-like MCPs and flight-like electronics yielded a σ of 9.4 μm(FWHM of 22.2 μm) for a Gaussian PSF.

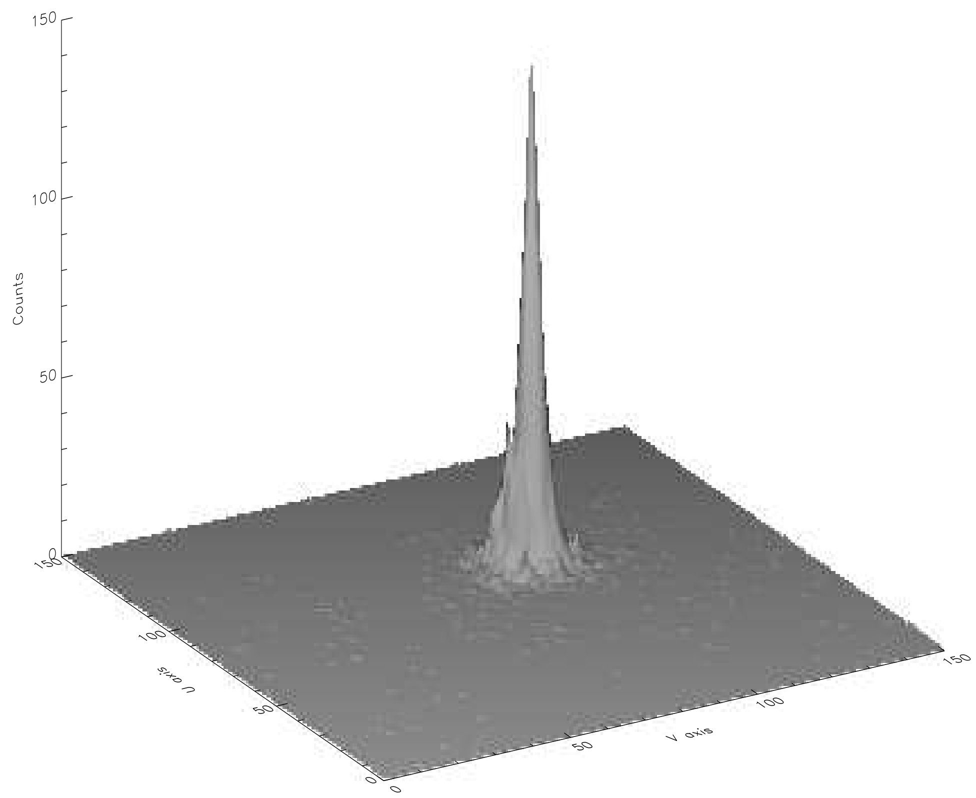

Figure 41: Point spread function of the HRC-S and HRMA

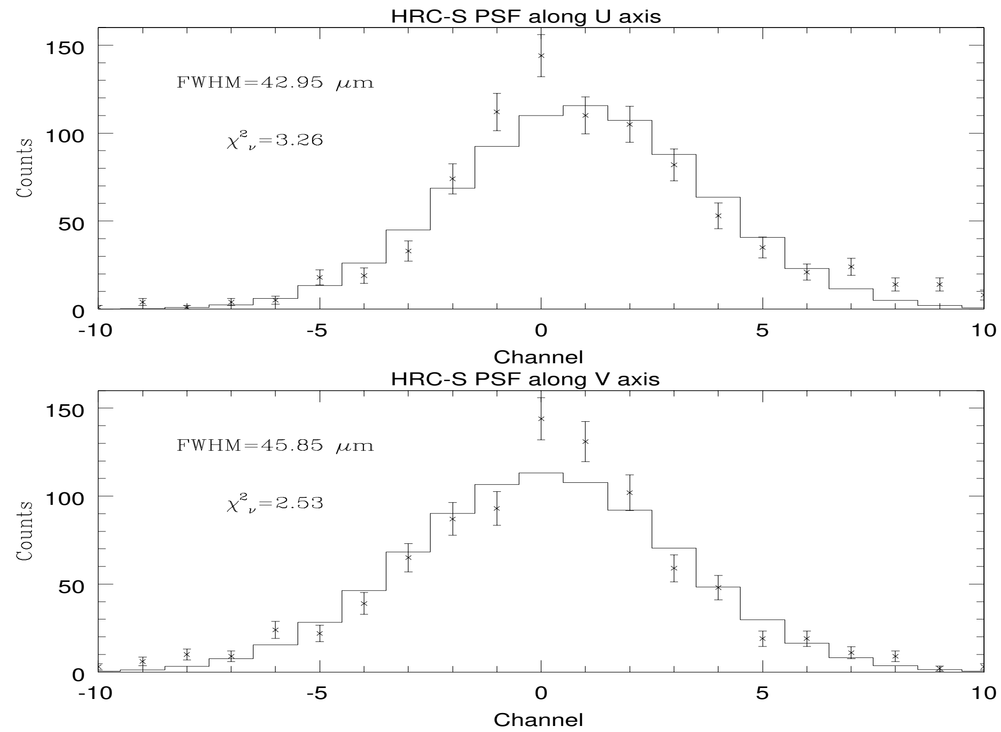

Figure 42: Best fit Gaussians to slices of the PSF along the U and V axes.

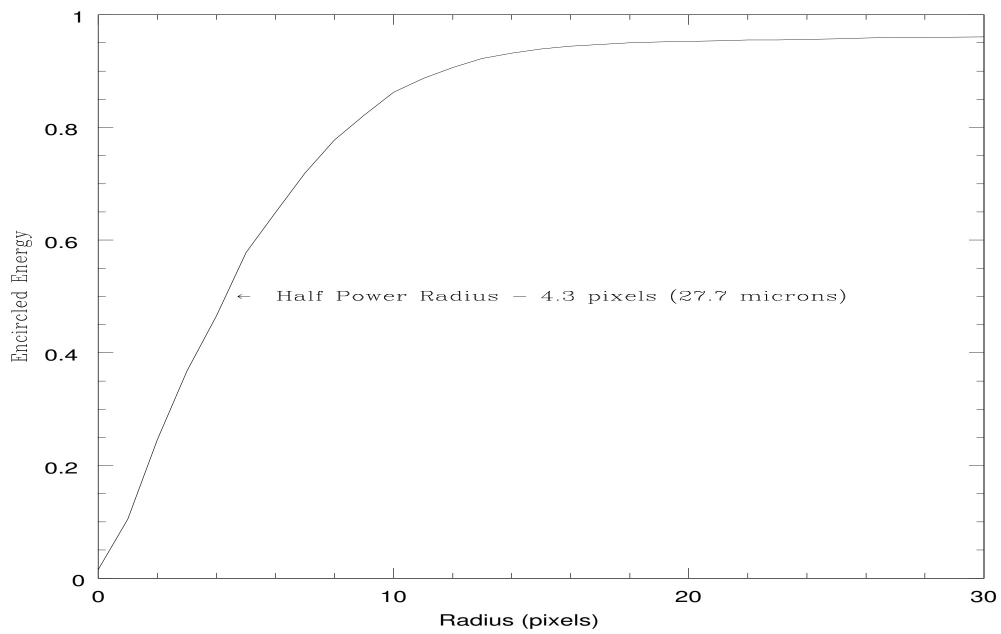

Figure 43: Encircled energy versus radius of the HRC-S/HRMA in focus at 277 eV.

UV/Optical Sensitivity Measurements

We have measured the optical and UV sensitivity of the HRC-S wing segments. These segments have the thinnest Al and polyimide, and will therefore have the largest UV/optical sensitivity. The UV sensitivity was measured using a filtered mercury lamp (2537 Å), and the optical response with a filtered tungsten-halogen lamp (4500 Å). The absolute intensities of these lamps were measured to within 10% using a NIST calibrated photodiode. A model of the predicted HRC-S UV/optical response (UVIS transmission times CsI coated MCP response) is contained in Figure 44. The UVIS transmission was determined from a combination of laboratory measurements and a calculation using published optical constants. The CsI coated MCP response was estimated using previously published results. Also plotted is the maximum acceptable (HRC specification) UV/optical sensitivity of the flight instrument. Note that the y axis of the plot covers 10 decades in response. The uncertainties in these models are fairly large. As can be seen from Figure 44, the measured 2537 Åsensitivity agrees surprisingly well with the prediction. The optical measurement only provided an upper limit that is orders of magnitude below the prediction. The modeled optical sensitivity of the CsI MCP depends heavily on one previous (unpublished) measurement made at SAO. The bandgap of CsI is ~6.2 eV (2000 Å), and it would be reasonable to expect that the sensitivity drops rapidly beyond this wavelength. We will continue to study this issue by measuring the UV/optical sensitivity of backup HRC MCPs and UVISs.

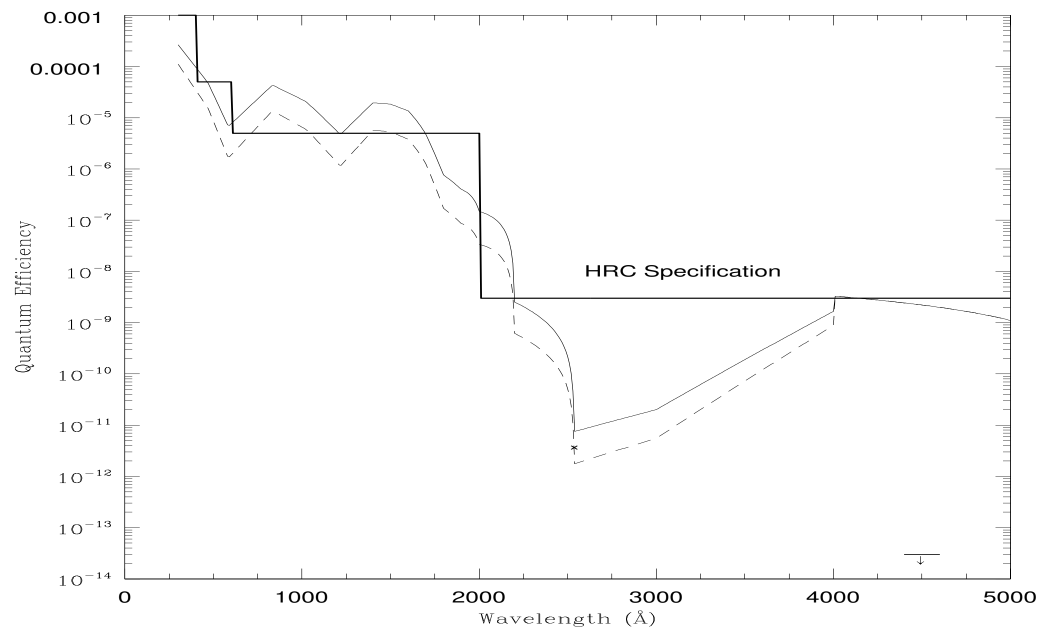

Figure 44: The calculated UV/optical QE of the wing segments of the HRC-S (the thin solid line) versus wavelength. The dashed line is the predicted QE for the nominal UVIS thickness plus the 2 sigma uncertainty. The measured values at 2537 Åand 4500 Å(an upper limit only) are also plotted. The dark solid line is the maximum UV/optical sensitivity specification. Note the logarithmic scale of the Quantum Efficiency axis.

Table 4: Summary of line energies, filters, thicknesses, anode voltages, and predicted line-to-continuum ratio of the X-ray source for HRC-S flat fields.

Line	Energy	Filter	MFPs	V_A	L/C	Seg
B K_α	183 eV	7 μm parylene-C	5.87	600 V	48.4	-1,0,+1
C K_α	277 eV	33 μm polypropylene	5.94	1000 V	171	-1,0,+1
O K_α	525 eV	2 μm Cr	4.67	1000 V	29.3	-1,0,+1
Ni L_α	851 eV	2 μm Cu	3.80	2500 V	2.55	0
Al K_α	1487 eV	50 μm Al	5.40	4000 V	38.9	-1,0,+1
Ag L_α	2984 eV	10 μm Ag	4.86	6000 V	0.60	0
Ti K_α	4511 eV	150 μm Ti	6.80	10000 V	6.73	0
Fe K_α	6404 eV	125 μm Fe	6.97	10000 V	1.78	0

4.3.2 Laboratory Flat Field Measurements

Flat fields of the HRC-S were made after the XRCF calibration and after the electrical fixes were made in order to measure the absolute quantum efficiency and detector uniformity. A schematic diagram of the experimental setup is given in Figure 45. The HRC-S was attached to a vacuum pipe by a mechanical snout which ensured that only one segment was illuminated at any time, and the HESF was blocked by a mechanical paddle. X-rays were generated by a multi-anode electron impact source. Beam filters were inserted at the source to reduce the flux (typically $\sim$ 1200 cts/s in the HRC) and remove continuum contamination. The central segment was calibrated at 8 energies, and each of the wing segments at 4. A summary of the anodes, filters, and predicted line-to-continuum ratios is given in Table 4. Measurements were also made of the reflectivity of the HESF by illuminating the flat and blocking the direct beam onto the detector with a mechanical paddle. The results of these latter measurements are not in this report.

Two proportional counters were used for absolute normalization of the beam. A beam normalization detector (BND) could be inserted (or withdrawn) via a vacuum feedthrough directly between the X-ray source and the HRC. The BND and the HRC were never run simultaneously because of the proximity of the two detectors and a slow gas leak through the thin BND window. A monitor detector (MD) was placed at 90 degrees to the beam to monitor temporal variations. The take-off angle between the electron impact source and either proportional counter was 45 degrees, so the intensity at either detector should be the same, assuming that the beam filters are identical (we do not rely on this, however). Our calibration technique was to simultaneously illuminate the BND and MD to make an absolute measurement of the X-ray intensity and cross-calibrate the two proportional counters. The HRC and MD were then illuminated.

Surface plots and projections of the flat fields (for the flight configuration of the HRC-S) at Al K_α for segments 0, -1, and +1 are shown in Figures 46, 47, and 48, respectively. The flat fields are similar at other energies (excepting for the UVIS structure at low energies). There is a small ($\sim$10%) gradient in the QE across the dispersion direction of all three segments. This gradient is present at all energies. This structure is not mimicked in the HRC-I (which was measured with the identical setup). Additionally, segment +1 has a region of slightly lower gain and QE.

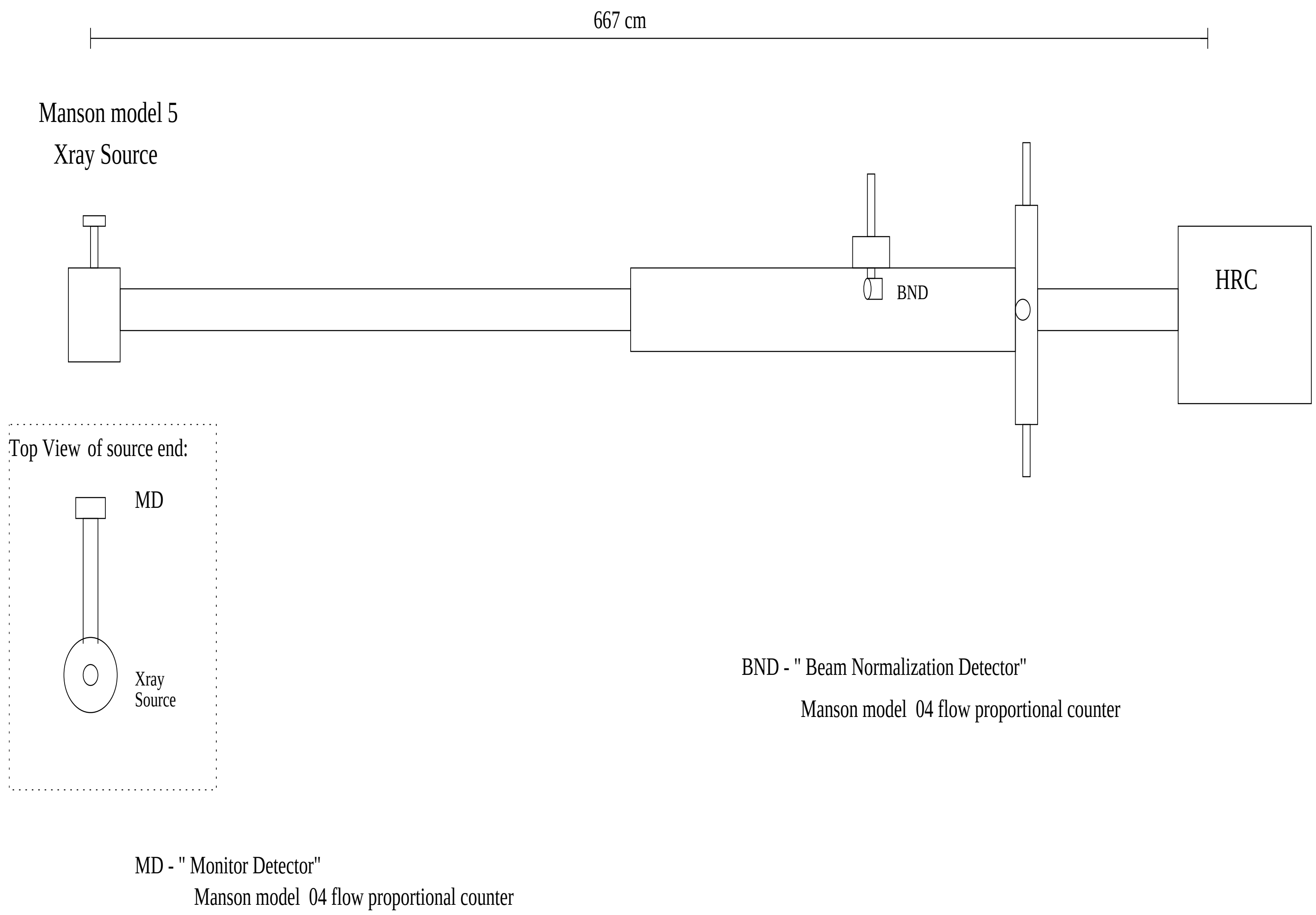

Figure 45: Schematic diagram of experimental setup for HRC flat field measurements.

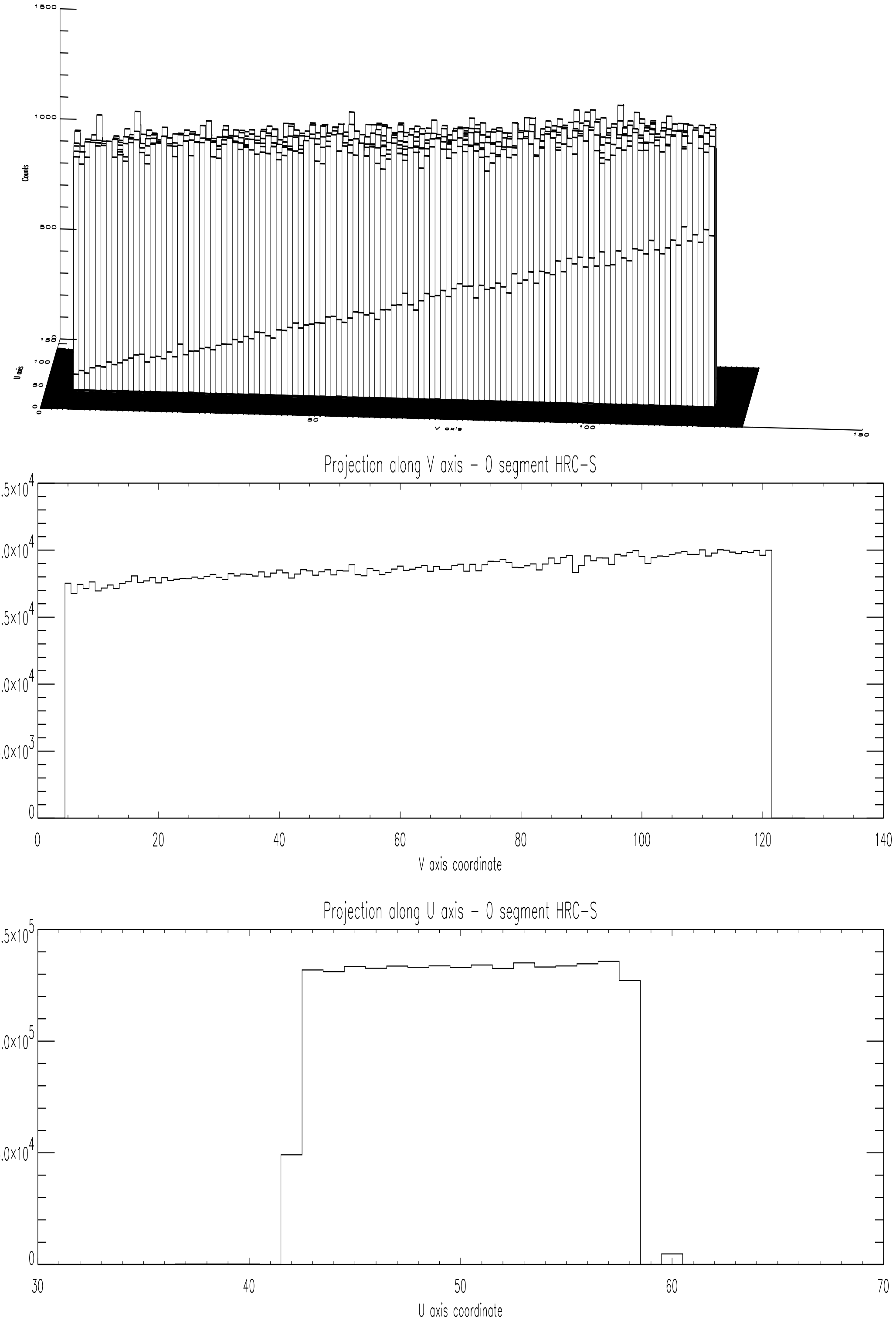

Figure 46: Surface plot and projections along the U and V axes of HRC-S segment 0, Al K_α. Each pixel is 0.82 mm.

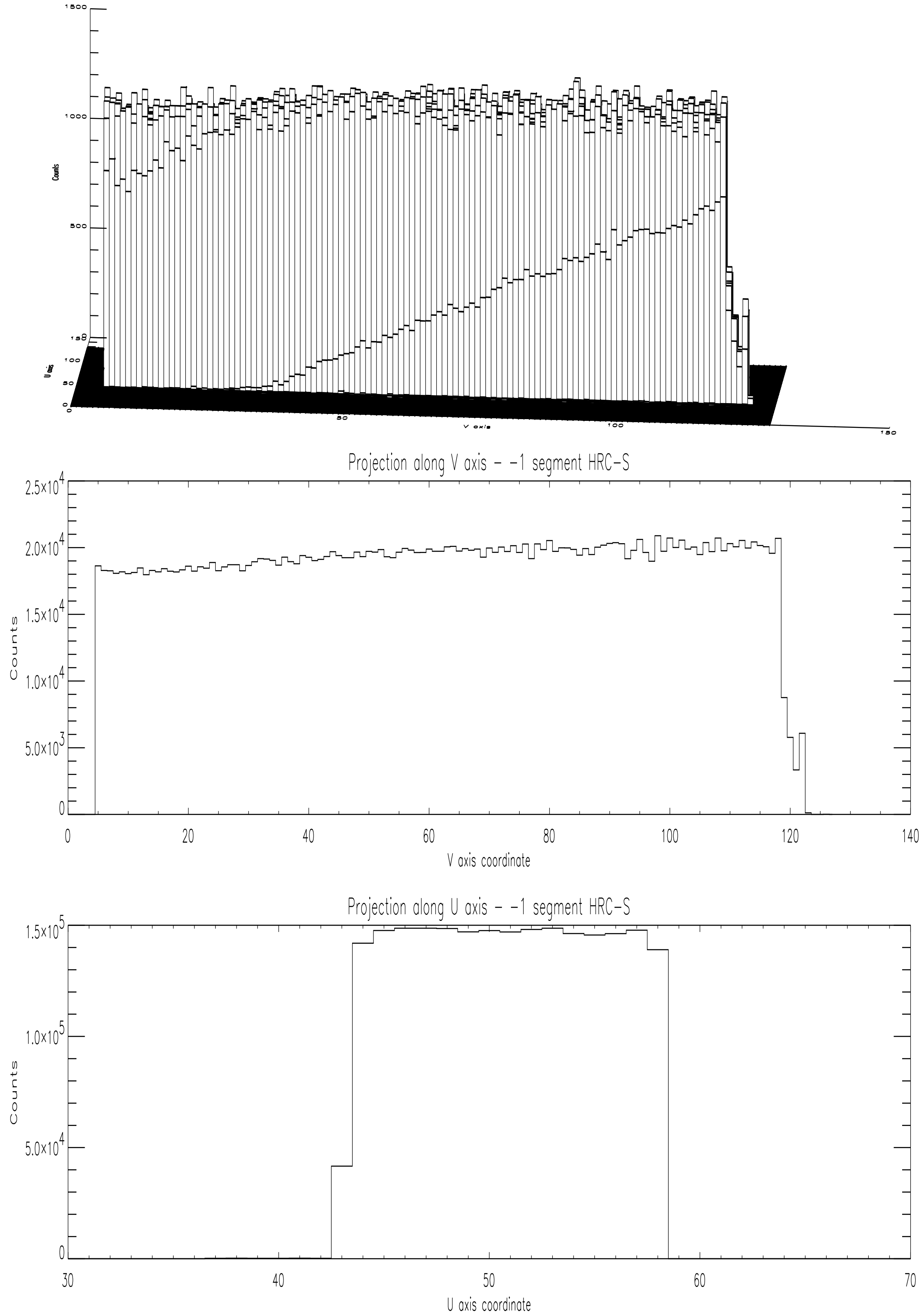

Figure 47: Surface plot and projections along the U and V axes of HRC-S segment -1, Al K_α. Each pixel is 0.82 mm.

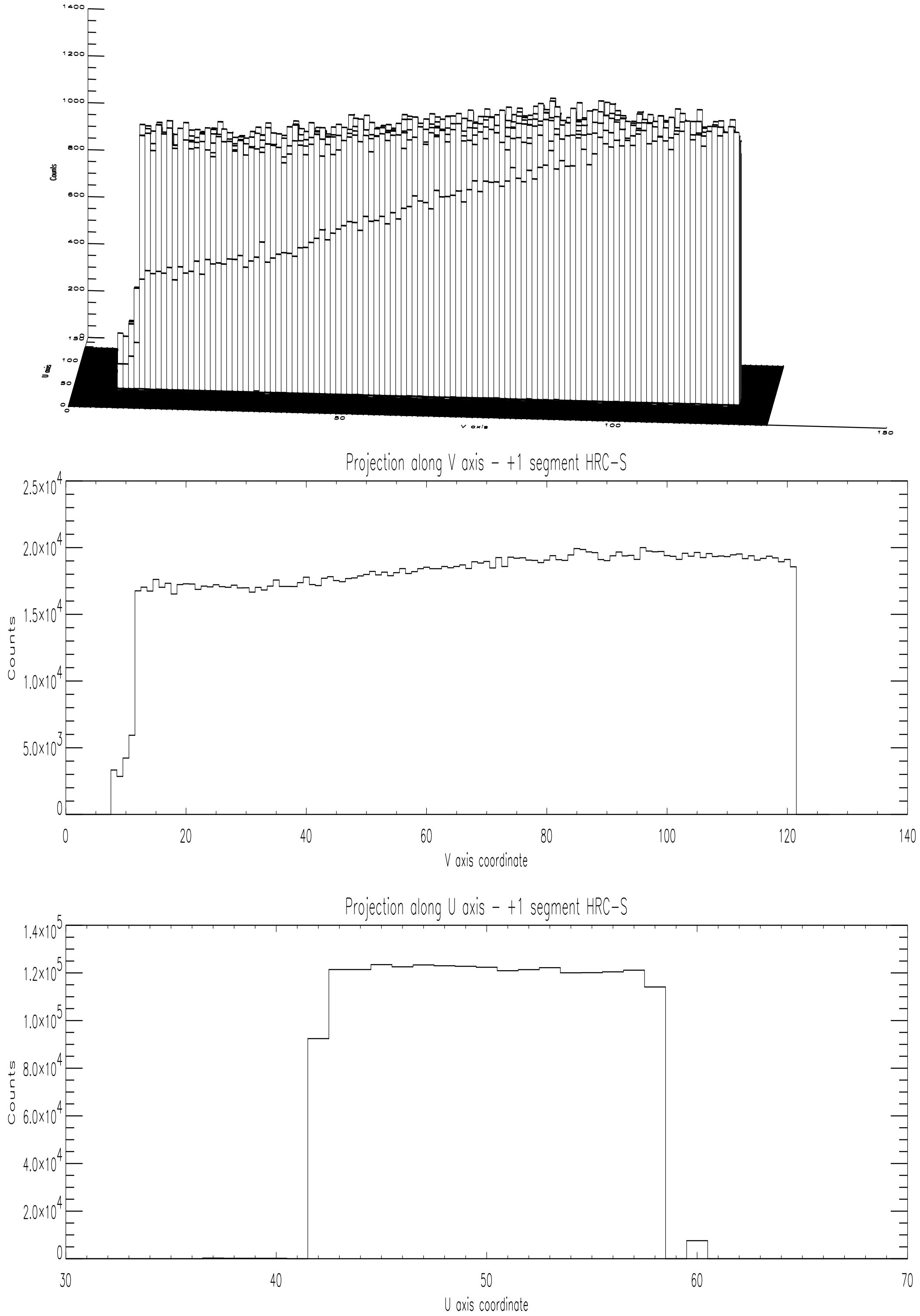

Figure 48: Surface plot and projections along U and V axis of HRC-S segment +1, Al K_α. Each pixel is 0.82 mm.

The absolute QE of a given region of the detector is given by

$$Q_{HRC} = \frac{R_{HRC}}{I_{HRC}\Omega_{HRC}},$$

where R_{HRC} is the rate (cts/s) in the HRC, I_{HRC} is the x-ray intensity (phot/s sr) at the HRC, and Ω_{HRC} is the solid angle subtended by the region. The absolute intensity, I_{HRC}, is determined from the BND and MD rates, and is given by

$$I_{HRC} = \frac{R_{BND}^{CC}}{Q_{BND}\Omega_{BND}} \times \frac{R_{MD}}{R_{MD}^{CC}},$$

where R_{BND}^{CC} and R_{MD}^{CC} are the BND and MD rates measured in the cross-calibration, Q_{BND} is the calculated BND quantum efficiency, Ω_{BND} is the solid angle subtended by the BND, and R_{MD} is the MD rate during the HRC integration.

All QE flat field maps have been dead time corrected. The HRC electronics are non-paralyzable with an event processing time of $68.5\mu s$. The true MCP rate, r_t, is then given by

$$r_t = \frac{r_m}{1 - \tau r_m},$$

where r_m is the measured HRC-S rate (cts/s) over the entire detector, and τ is the event processing time. The dead time correction ranges from 2% for the O K_α measurements to 10% for the Al K_α measurements.

There are seven files for each QE map. The QE map itself is a FITS file. Each pixel has been binned by a factor of 128 in each axis over the full HRC-S spatial resolution. There are also two degapped images (one at 32x and one at 128x binning) of the flat field, and a degapped gain map image (at 32x binning). These three files are square arrays of two byte unsigned integers that can be read directly into saoimage using the -u2 flag. There are also several ASCII files, including a projection file (.prj) which contains the projections of each image along the U and V axes at full resolution, a PHA file (.pha), and a degap map that can be used with the standard HRC analysis software. A more detailed description of the degap maps is given below.

The central segment was flat fielded at eight energies (183 eV, 277 eV, 525 eV, 851 eV, 1487 eV, 2980 eV, 4511 eV, and 6404 eV), and each of the wing segments at four energies (183 eV, 277 eV, 525 eV, and 1487 eV). The flat field at 2980 eV (the Ag anode in the electron impact source) of the central segment was not included in this analysis for two reasons. First, there is evidence in the HRC-I images of considerable spatial non-uniformity of the beam. Second, this data point is difficult to normalize using the proportional counter data because of the complex, polychromatic source spectrum. There are 4 strong L complex lines plus bremsstrahlung continuum which straddle the Ar K edge of the proportional counter gas. The Ag L_α line is below the Ar K edge, but an escape peak was seen in the proportional counter spectrum indicating that a significant fraction of the flux is above the edge.

There is one additional complication with the Ti measurement. The Ti K_α line is at 4.511 keV, and the K_β line is at 4.932 keV. The I L_{III} edge is at 4.557 keV, so the flux in the K_β line is above the edge. A significant fraction of the flux from this anode is above the I L_{III} edge. The fluorescence ratio, K_β/K_α, is 0.1153 for Ti. A thick Ti filter was used to filter out the bremsstrahlung continuum, but this will also have the effect of enhancing the K_β flux relative to K_α. The K_β/K_α ratio of the transmission of this filter is $\sim$4.4. The QE that we state in the QE maps is actually some average value between the lower value below the edge, and the large value above the edge. We have good XRCF DCM measurements of the structure around the edge and will use this information to disentangle this effect sometime in the future, but the user should be warned that we have overestimated the 4.511 keV QE in the maps. The measurement of the uniformity of the QE is, of course, unaffected by this result. The same problem exists with the Fe anode as well, but there is less significant.

All of the QE measurements described here were made at normal incidence. Little error is introduced using the normal incidence QE of the HRC-S MCPs instead of the angle integrated QE over the AXAF cone angles except at the lowest energies (below 500 eV). We are currently making detailed measurements of the MCP response at the AXAF cone angles at several energies below 500 eV. These results will be posted on the HRC calibration web site when completed.

A plot of the ratio of post-fix QE to pre-fix QE versus in energy in a region around the center of the central segment is shown in Figure 49. A cubic spline has been fit to the data points to provide a continuous estimate of the fractional change in QE as a function of energy. The endpoints were arbitrarily chosen to ensure that the spline fit was relatively flat over the AXAF bandpass. Given the large spatial non-uniformities in the pre-fix configuration, the data and curve shown in Figure 49 are not necessarily representative of the change in QE over the entire detector. Most of the spatial non-uniformity present in the detector at XRCF settings has been removed, however. There is a slight (~10%) QE gradient across each segment. The QE gets larger with increasing V coordinate for a given segment. The region of low QE and low gain on the +1 segment is still present, but at a very low level. There is also a large hotspot at the edge of the central segment.

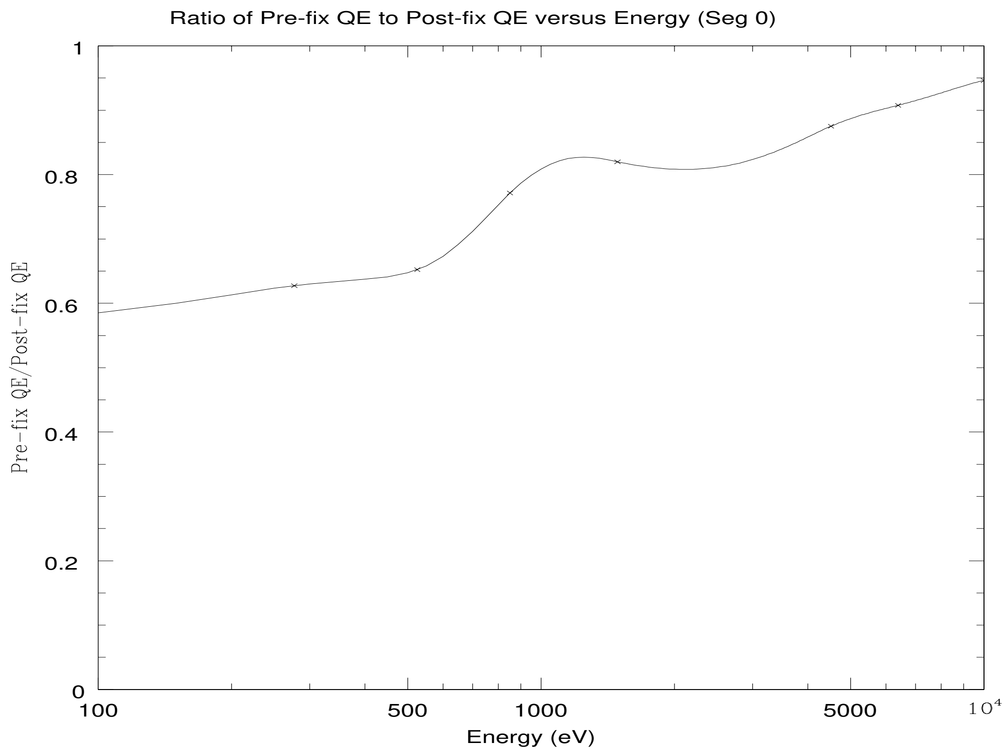

Figure 49: Ratio of pre-fix QE to post-fix QE versus energy in a region around the zeroth order position.

Degap Maps

The program mkdegap was used to create all of the degap maps. It is part of the standard HRC analysis software and is available from the HRC instrument team or the ASC. It creates a second order degap for each tap in both axes and outputs the coefficients to an ASCII file. The second order degap is important for the HRC-S postfix analysis because the undegapped projections in the U axis show considerable scalloping that cannot be corrected with a linear degap. There is a degap maps for each flat field measurements. In general, We find that the degap parameters have little or no dependence on pulse height.

HRC-S Quantum Efficiency versus Energy

In addition to the QE measurements at a few energies, a model of the HRC-S QE versus energy over the AXAF bandpass is required for LETG analysis. The XRCF data is of limited use in developing this model because of the large spatial non-uniformities in the detector at the time, and the large changes in QE and spatial uniformity due to the electronic modifications. We have decided to develop a flight model of the QE based largely on the post-fix flat fields, and selectively use the XRCF data to compare against and to understand the QE structure around detector absorption features (see discussion of Ti K_α flat fields above).

We have chosen to use a model outlined by Mike Juda based on earlier work on photocathodes (Henke, Knauer, and Premaratne 1981). In this simple model, it is assumed that the MCP QE can be described by the mass absorption coefficients of Cs and I and a *range* parameter, Λ. A complete description of this model is given elsewhere:

(http://hea-www.harvard.edu/~juda/memos/mcad_QE_model.ps)

.

The HRC UV/Ion shields are well calibrated, so the underlying MCP QE can be determined from the HRC QE measurements, which can be used to determine Λ at the calibrations energies. An interpolation scheme is then used to estimate Λ as a function of energy over the AXAF bandpass. This empirical determination of the electron range parameter can then be used to estimate the MCP QE as a function of energy.

This model was applied to data from a region of segment 0 under the central 'T' of the UVIS, essentially the region around the zeroth order of the LETG spectrum. The QE measurements and derived MCP QE versus energy are shown in Figure 50 (this and all other plots are also contained on the HRC-S post-fix calibration web site, as well as the data tables used to generate the plots). A plot of the HRC-S QE (MCP QE times UVIS transmission at zeroth order) is contained in Figure 51.

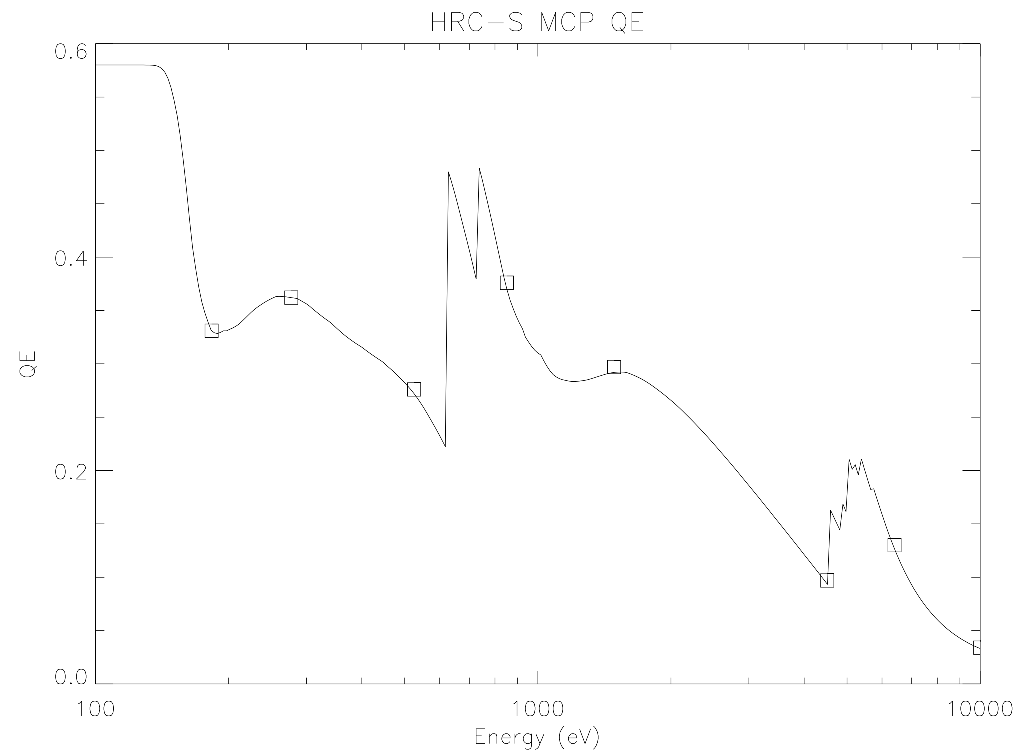

Figure 50: Measured (points) and modeled (smooth curve) HRC-S MCP QE versus energy.

There are several additional considerations that must be taken into account to determine the HRC-S QE as a function of energy for the LETGs in first order because the spectrum is dispersed along the detector.

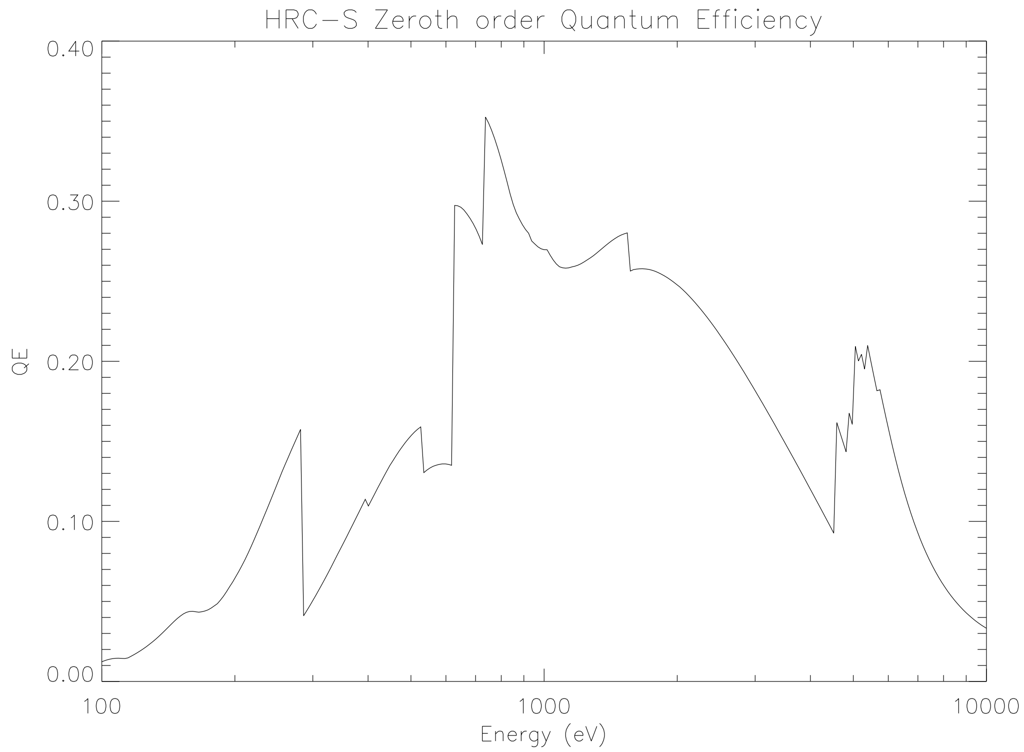

Figure 51: HRC-S QE versus energy in zeroth order.

These include the complex spatial structure of the UVIS, the spatial non-uniformity of the MCPs (the gradient described above), and the slight differences in MCP QE between the three segments. The HRC-S QE versus energy at the position on the detector where first order falls at that energy is plotted in Figure 52.

The uncertainty in this QE model is clearly limited by systematic uncertainty in flat field measurements (statistical uncertainties are negligible). The model also has several known deficiencies that we are currently working to improve, but that the user should be aware of. First, and perhaps most importantly for LETG analysis, we have considerably overestimated the jump in QE across the I and Cs *M V* edges, and the model does not adequately describe the structure across these edges. We have made synchrotron measurements of the detailed edge structure in this region, and will include this data in the model as soon as they are fully analyzed. Likewise, we have overestimated the jump across the I and Cs *L* edges. This is probably not critical for LETG analysis, but we can use XRCF data and the Ti measurements described above to constrain the QE in this region. We also have synchrotron measurements around these edges that must be included. Third, we have overestimated the QE below 200 eV, perhaps by as much as 50%. This is due to a limitation in the empirical model. At these low energies, the X-ray penetration depth is so small that the model predicts that all electrons would escape the photocathode and the QE is given by the open area fraction of the pores (about 58%). Based on previously published synchrotron measurements (Pearce *et al.* 1995), this is not the case. In this energy range, a more detailed surface physics/electron transport model is probably required. Fourth, all measurements described here are made at normal incidence to the MCP surface, whereas the X-rays reflected from the HRMA will come in over a range of incidence angles. This effect is negligible above about 500 eV, but is significant at lower energies. In the worst case, it is a 10% correction at 183 eV.

Figure 52: HRC-S QE versus energy in first order. The solid line is the +1 order, the dashed line is the -1 order. The difference between the two orders is due to the spatial gradients along the segments.

4.4 HRC Fine Structure Response - Synchrotron Measurements

In an effort to determine the quantum efficiency of the HRC detectors throughout the range of energies at which AXAF is expected to operate, two test detectors with near-identical MCPs to the HRC flight plates were taken to the Synchrotron Radiation Source (SRS) facility at Daresbury (UK). The measurement of quantum efficiency features relating to absorption edges of the photocathode (and the underlying lead silicate glass) was of particular interest, especially in terms of the HRC-S detectors where instrument features must not be confused with line features from astrophysical sources. We here describe the efficiency measurements of two plates installed on beamline 1.1 (450 eV to 1200 eV) and beamline 4.2 (4.5 keV to 9.5 keV) in October 1997.

The two stage 'chevron' test detectors comprised Philips Photonics low noise glass MCPs, 36 mm in diameter with a microchannel bias angle of 6°. Channel diameter and pitch were 12.5μm and 15μm respectively, with a length-diameter ratio of 120:1 and nominal 63% open area fraction. The detector was coated on one half of the front plate with $\sim$14000 $\AA$ CsI, the other half was left bare for comparison.

Measurements of the MCP detector efficiencies were made during SRS low ring current ($\sim$20 μA) operation, providing the reduced X-ray flux necessary to prevent electronic overload and also damage to the front MCP. The $\frac{1}{e}$ lifetime of the beam in this mode was $\sim$50 hours. Previous campaigns at Daresbury have led us to realize that the source energy spectrum measured using a charge replacement foil at the time of single ($\sim$20 mA) or multi-bunch ($\sim$150 mA) operation of the SRS is not a good description of the beam energy profile during low ring current. Therefore, the beam flux was monitored on both beamlines using separate single-wire, gas filled proportional counters (PCs).

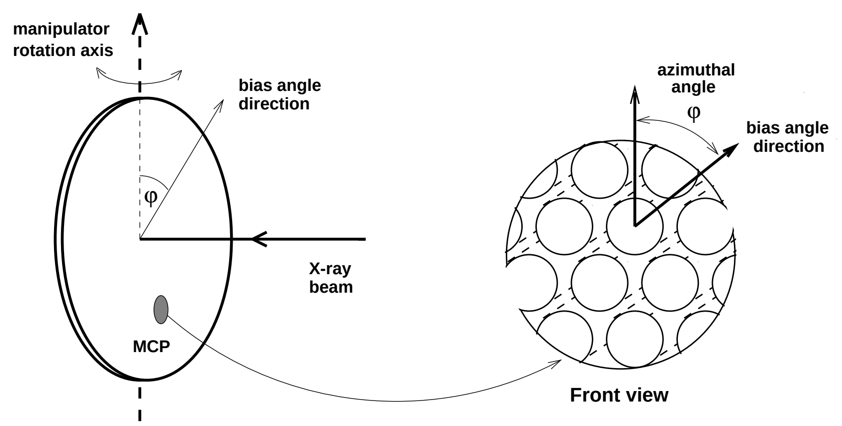

Figure 53: Definition of the azimuth angle ϕ. A *normal incident* beam will have a *channel incidence* of 6° (i.e. equal to the bias angle) regardless of ϕ.

Both MCP detectors were secured on a manipulator capable of linear movement along the two axes orthogonal to the beam, and rotation about a vertical axis. Upon assembly, the front MCP of the 1.1 detector was orientated such that the channel bias direction in the plane of the plate was parallel to the detector rotation axis (i.e. ϕ=0°, see Fig. 53). Thus, a minimum *channel incidence* angle of 6° with respect to the beam occurred with the beam at *normal incidence* to the plate. The front plate of the 4.2 detector however, was rotated by 90° with respect to this (ϕ=90°) such that a minimum channel incidence of 0° could be achieved. Efficiency measurements were made at various beam angles to the front plate normal to simulate the AXAF cone angles of ±1.8° and ±3.4°, due to X-ray reflections off the inner and outer shells of the High Resolution Mirror Assembly (HRMA).

Beamline 1.1 The beamline optics of 1.1 consist of a horizontally deflecting, water-cooled cylindrical mirror (Pt coated CVD SiC), three interchangeable spherical nickel (Ni) and gold (Au) coated gratings with ion etched rulings of (1) 1050, (2) 1500 and (3) 1800 lines mm^{-1}, and a post-focusing Pt coated spectrosil ellipsoid mirror. Switching between the Ni and Au coated grating sections provides practical flux in the ranges 250 to 850 eV and

700 to 1200 eV respectively. Initial tests showed the Ni(3) and Au(1) gratings to be best suited to our needs[2] with energy resolutions of about 0.5 eV and 1.0 eV respectively.

The gas filled proportional counter (P10 at ~1 bar) was situated some 60 cm up-beam from the MCP detector on a pneumatically operated vertical linear drive. Moving the PC in and out of the beam allowed us to interleave energy scans using either the PC or MCP detector. Initial measurements were necessary to determine the drive position at which the beam was aligned with the PC window.

The polypropylene window on the PC was supported by a 46% transmission mesh and was ~1.0μm thick. The window was aerosol coated on its interior with a carbon spray to form a conductive layer and prevent localized charging of the polypropylene which would compromise the PC performance. Prior measurements of window transmission on beamline 1.1 showed evidence of oxygen absorption at 534 eV hypothetically due to aerosol solvent OH groups being absorbed into carbon coat during drying. This effect was modeled and included in the window transmission data used during analysis. The absorption efficiency of the P10 gas was calculated as 100% over the beamline 1.1 energy range.

Ni(3) grating, 450 to 800 eV The proportional counter allowed us to not only measure the low current photon flux but, by recording pulse height distributions (PHDs) at 20 eV energy intervals, determine the spectral purity of the beam. Figure 54 shows four such PHDs recorded from the Ni(3) grating. Substantial second order contamination is obvious at the lower energies. By fitting Gaussian distributions to these PHDs and correcting for PC window transmission we were able to quantify the contamination due to second and third order harmonics (see Fig. 55). Unfortunately, carbon contamination of the Ni(3) grating increased the second and third order dominance of the flux from the C-K edge (284 eV) to about 450 eV. The quality of the PHD fits in this range was poor, therefore data will not be presented within this region. Oxygen contamination of the beamline was also a well known feature and is apparent by the large drop in countrate at 534 eV.

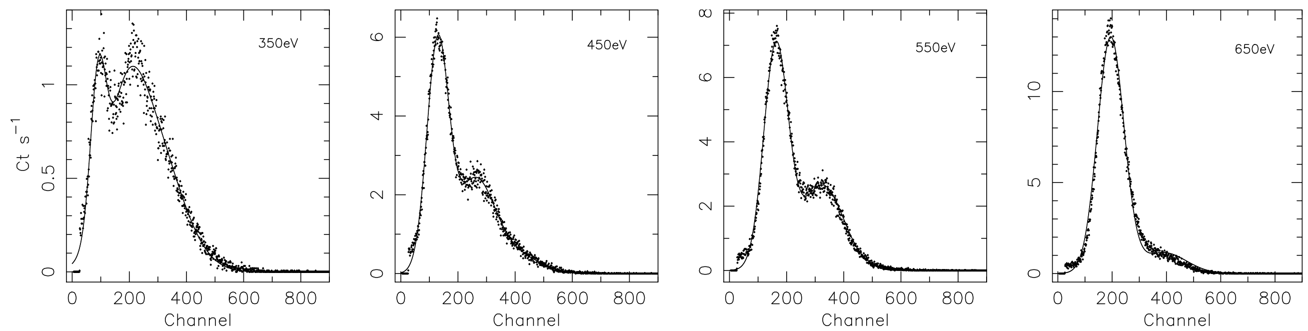

Figure 54: PC pulse height distributions of the Ni(3) grating on beamline 1.1. The solid curve represents three Gaussian fits with second and third order peak positions frozen in association with that of the fitted first peak.

We can represent the incident flux at the MCP detector ($I_{\rm MCP}$) for any given energy as,

$$I_{\rm MCP} = T_{\rm mesh}\,(e_1 I_1 + e_2 I_2 + e_3 I_3) \tag{44}$$

where $e_{1..3}$ are the detector efficiencies and $I_{1..3}$ are the count rates due to the first, second and third orders, respectively. The transmission of a metal mesh in front of the detector MCP ($T_{\rm mesh}$) was assumed as 0.9 throughout. Previous quantum efficiency measurements of CsI coated MCP detectors were used to estimate values for e_2 and e_3, allowing the first order efficiency to be computed.

Figure 56 shows the absolute quantum efficiency of the CsI coated section of the MCP calculated using Eqn. 44 where $I_{1..3}$ are as shown in Fig. 55b. The model shown in Fig. 56 was generated by software initially developed and cited by Fraser and is discussed at length by Pearce. The feature at 541 eV has not previously been observed and is most likely a complication due to the oxygen contamination of the beamline and PC window. Of particular interest is the slow onset of the I and Cs-M$_{\rm iv\text{-}v}$ edges shown in Fig. 56b & c. This effect, previously observed at the SRS using an identical MCP detector, and in the photocurrent and reflectivity measurements of several high-Z metals, is primarily a characteristic of the 3d$\rightarrow$f atomic transition.

[2] Unfortunately, contamination of the Au(2) and (3) gratings was seen to seriously degrade the spectral purity of the beam flux.

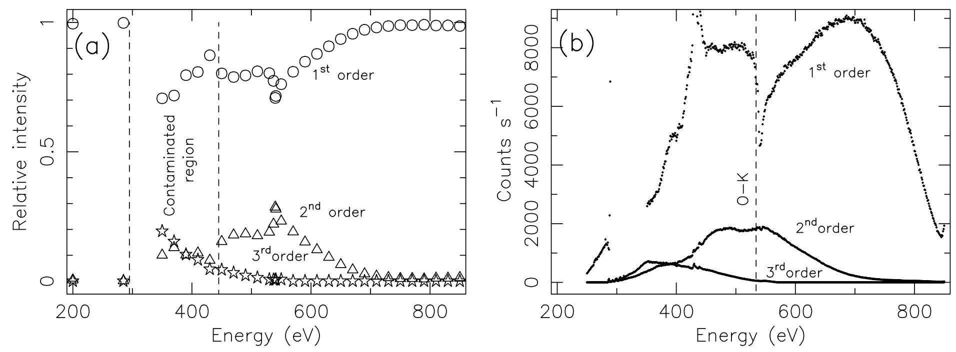

Figure 55: (a) Degree of second and third order contamination of the beamline 1.1 flux from the Ni(3) grating. Data has been corrected for 1.0μm polypropylene and 46% transmission support mesh on the PC window. (b) Calculated first, second and third order beam flux.

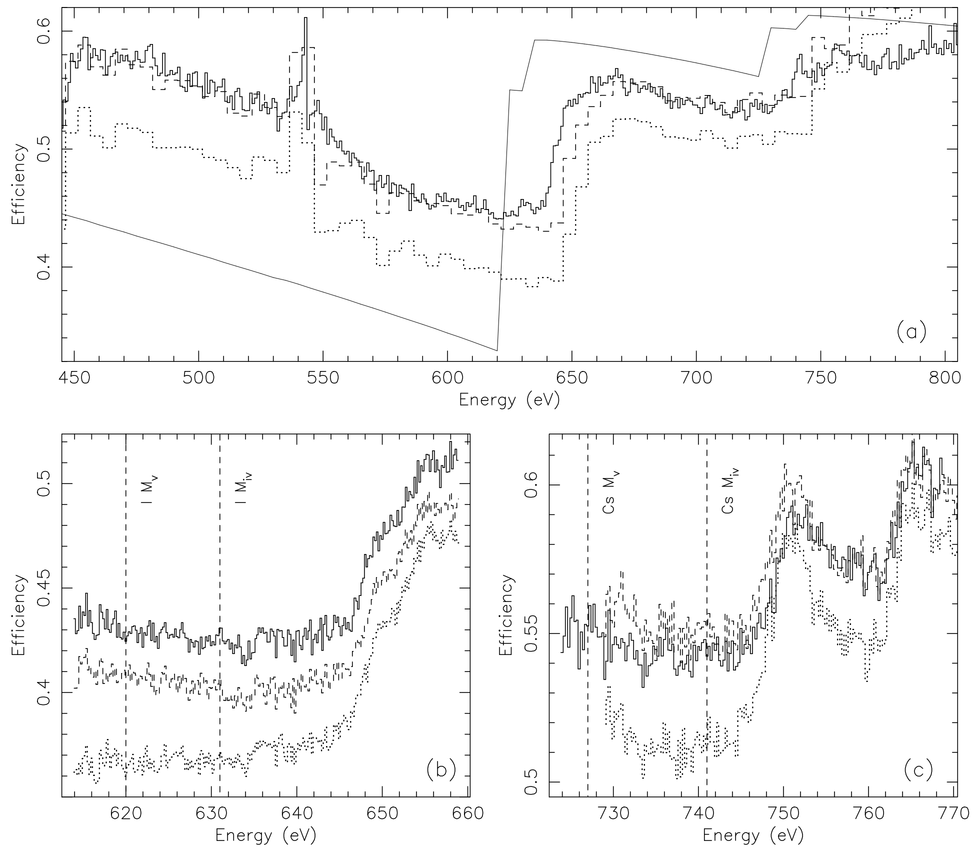

Figure 56: Absolute quantum efficiencies of the CsI coated section of the MCP detector measured on beamline 1.1 using the Ni(3) transmission grating. Beam angles with respect to detector normal incidence are 0° (solid), 1.8° (dashed) and 3.4° (dotted). Solid curve represents modeled data for 0° normal incidence. High resolution scans across the I (b) and Cs (c) M_{iv-v} edges are in energy steps of 0.2 eV and 0.25 eV respectively.

Au(1) grating, 700 to 1200 eV Proportional counter PHDs of the beam from the Au(1) grating were recorded in 20 eV energy steps as before, and confirmed that the flux was free from second and third order harmonics. After switching gratings the beam position was checked using the MCP imaging electronics as

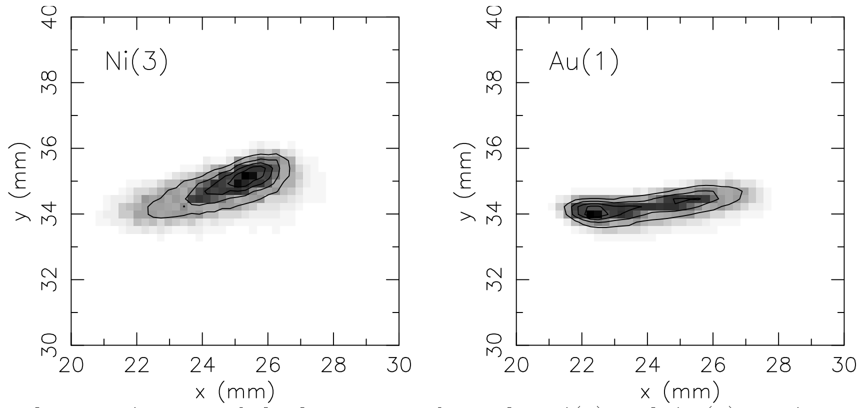

Figure 57: MCP detector images of the beam spot from the Ni(3) and Au(1) gratings at 600 eV and 850 eV, respectively. Contours are at 0.2, 0.4, 0.6 and 0.8 fractions of the peak height.

movement would require re-alignment of the PC. Initial checks suggested that the beam had not significantly moved with respect to the MCP. Unfortunately, post-analysis indicated that the flux had moved within the bounds of the beam spot, to the very edge of the PC window[3] resulting in some loss of counts (see Fig.57) and an artificially high MCP efficiency. A single multiplication factor was therefore applied to all the data such that the normal incidence (0°) efficiency curve at 930 eV corresponded to the laboratory derived value at Cu-L. As before, the data was corrected for a carbon coated 1.0μm polypropylene window and the transmission of the support mesh.

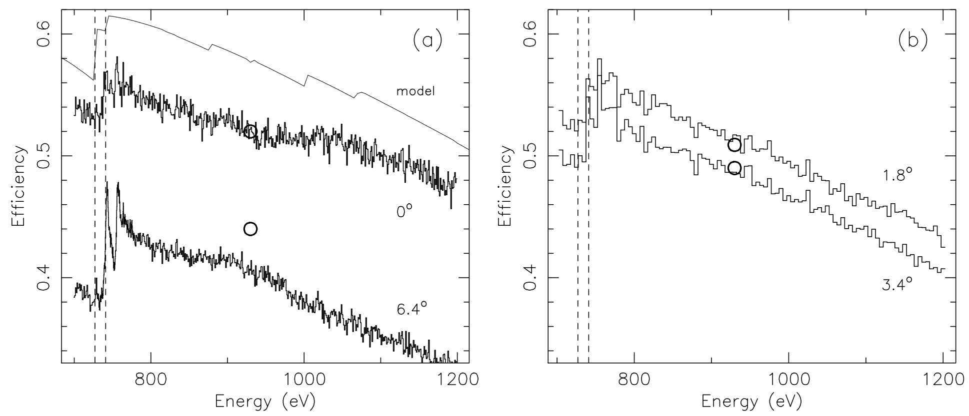

Figure 58: Absolute quantum efficiencies of the CsI coated section of the MCP detector measured on beamline 1.1 using the Au(1) transmission grating. Beam angles are with respect to detector normal incidence. Circles indicate quantum efficiency measurements at Cu-L (930 eV) recorded in the laboratory at Leicester University. Dashed lines are at 727 eV and 741 eV (Cs $M_{v,iv}$ edges, respectively).

Figure 58 shows the measured quantum efficiency at angles of 0°, 1.8°, 3.4° and 6.4° to the normal incidence of the MCP. The curves shows good consistency with the modeled data and the 930 eV efficiency values at 1.8° and 3.4° closely match the data from the laboratory. The high resolution scans across the Cs $M_{iv\text{-}v}$ edges (see Fig. 59) exhibit the ~20 eV shift observed using the Ni(3) grating with very similar quantum efficiencies. Evidence of white lines and EXAFS are more prominent at the higher incident angles, an effect previously observed by Pearce. High resolution scans across the I M_{ii} edge at 931 eV (not shown) revealed no significant structure.

[3]an effect made worse since the beam focus was at the front channel plate and not at the PC window further up-beam.

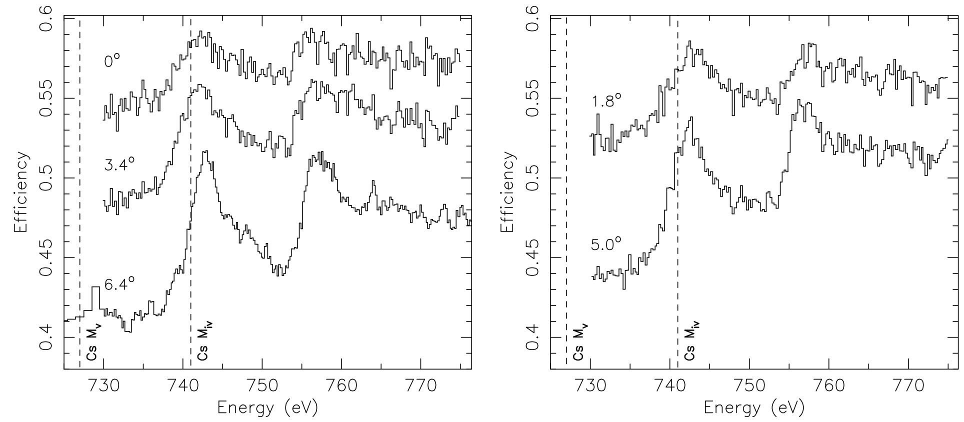

Figure 59: High resolution scans across the Cs $M_{iv\text{-}v}$ absorption edges using the Au(1) grating.

Analysis Figure 60 shows the combined efficiency curves from the Ni(3) and Au(1) gratings. The data shows good consistency in the overlapping energy range (700 to 800 eV) and the 'delays' in the Cs $M_{iv\text{-}v}$ edges repeat well. There is also reasonable agreement with the modeled efficiency. None of the $M_{i\text{-}ii}$ edges are seen with any significance.

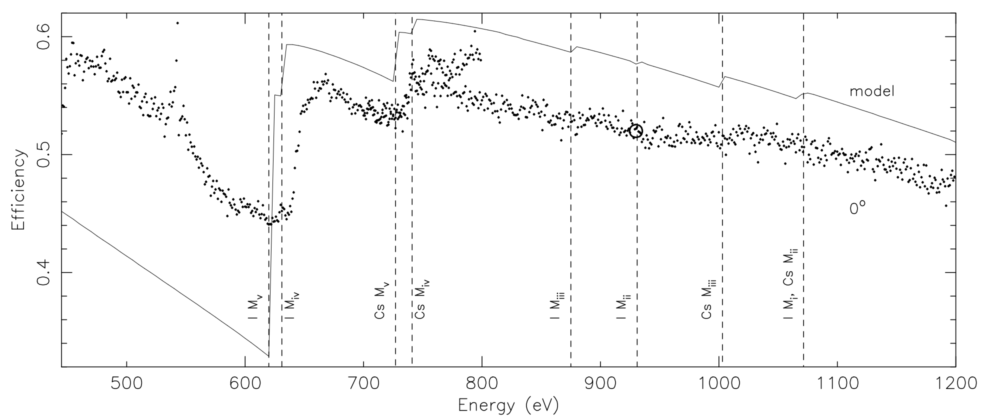

Figure 60: The absolute quantum efficiency of the CsI coated MCP detector at 0° beam incidence measured using the Ni(3) (450 to 800 eV) and Au(1) (700 to 1200 eV) gratings on beamline 1.1. The Leicester laboratory derived efficiency at 930 eV (circle) to which the Au(1) data is normalized is also shown.

Figure 61 illustrates the quantum efficiency of the uncoated (bare glass) region of the MCP measured on beamline 1.1 using the Ni(3) and Au(1) gratings. The Ni(3) data has been corrected for second and third order contamination as described previously. The data shows good consistency with the models (given that the specification of the MCP bias angle is 6°±1°) and reemphasizes the efficiency gains made by using a CsI photocathode. The most significant feature is the O-K (543 eV) absorption edge where a white line and significant EXAFS are seen. Other structures associated with the contaminates of the lead glass can also be seen and have been previously observed at other energies. The feature at ~745 eV is possibly the late onset of the Cs M_{iv} edge due to a slight contamination of CsI on the masked side of the MCP during coating.

Beamline 4.2 The beamline optics of 4.2 consists of a primary and secondary pre-mirror coated with platinum and chromium respectively, and a silicon (311) double crystal monochromator providing a useable flux in the range 4500 to 9500 eV. The narrow rocking curve associated with these crystals made it necessary to modify the station software such that the feedback to the rocking electronics came from the MCP detector.

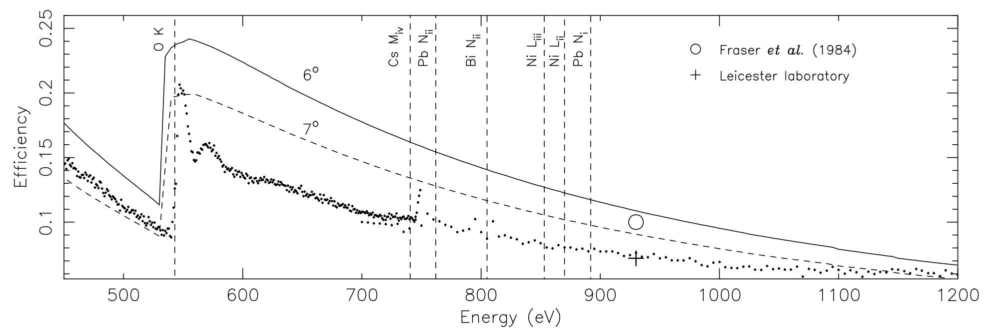

Figure 61: Absolute quantum efficiency of the bare (glass) section of the MCP detector. Solid and dashed lines represent efficiency models for flux at 6° and 7° *channel incidence* respectively. Data is normalized to the Leicester laboratory efficiency value measured at 930 eV (cross).

Beam reference was provided by a beryllium bodied gas filled (97% Xe, 3% CO_2 at 1.2 bar) single wire proportional counter positioned in the beam behind the MCP detector. The body of the PC was 254μm thick with an internal diameter of 2.34 cm. PC reference scans were interleaved with MCP measurements by driving the MCP detector in and out of the beam. The transmission of the PC body and the efficiency of the gas were modeled and extracted from the data during analysis.

As previously discussed, the MCP detector was fixed to a linear drive such that it could be rotated about the vertical axis with a front plate azimuth angle of 90°. Efficiency measurements were made at various beam angles to the front plate microchannel walls to again simulate the AXAF cone angles.

Analysis Unfortunately, during data analysis it was realized that the MCP detector signal wires obscured the beam while recording the PC reference countrate. It was therefore necessary to scale the PC readings to form a continuous curve and normalize the efficiency curves to a previously published value of 12.5% at 5.9 keV for a similar MCP detector. Figure 62a shows the corrected beam intensity as measured using the PC *prior* to removing the gas efficiency and Be window transmission functions (shown in Fig 62b). The feature seen at 5989 eV corresponds to the Cr-K edge due to the coating on the secondary pre-mirror.

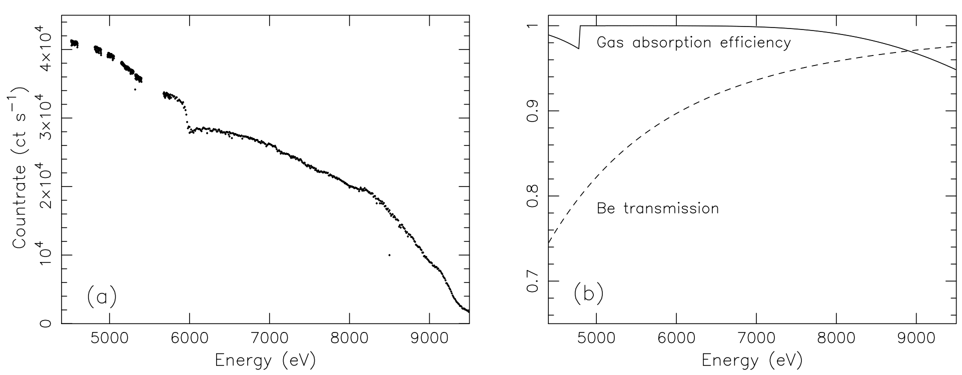

Figure 62: (a) Beamline 4.2 countrate measured using the Be-bodied proportional counter, prior to correcting for (b) the PC gas efficiency and window transmission.

Figure 63 shows the measured efficiency of the MCP detector over the full range from 4.5 to 9.5 keV at normal incidence to the CsI coated front plate (i.e. 6° channel incidence). As discussed previously, the data is normalized to 12.5% at 5.9 keV. The data show consistency of form with the both the model and previously published work. High resolution energy scans across the Cs and I L_{III} edges were made at various channel incidence angles and are shown in Fig. 64. Strong evidence of white lines is observed across the Cs L_{III} edge in particular, although it is thought that the features observed at 5042 eV and 5058 eV are due to poor 'rocking' of the monochromator crystals during the period of beam reference measurement.

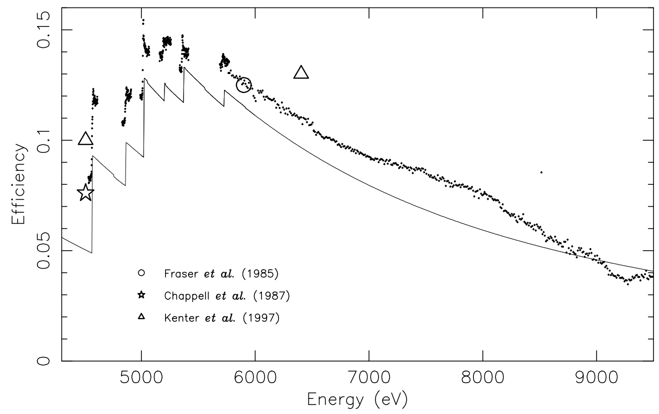

Figure 63: Absolute quantum efficiency of the CsI coated section of the MCP detector at normal incidence to the front plate (6° channel incidence). Solid curve represents the modeled MCP efficiency for 6° channel incidence.

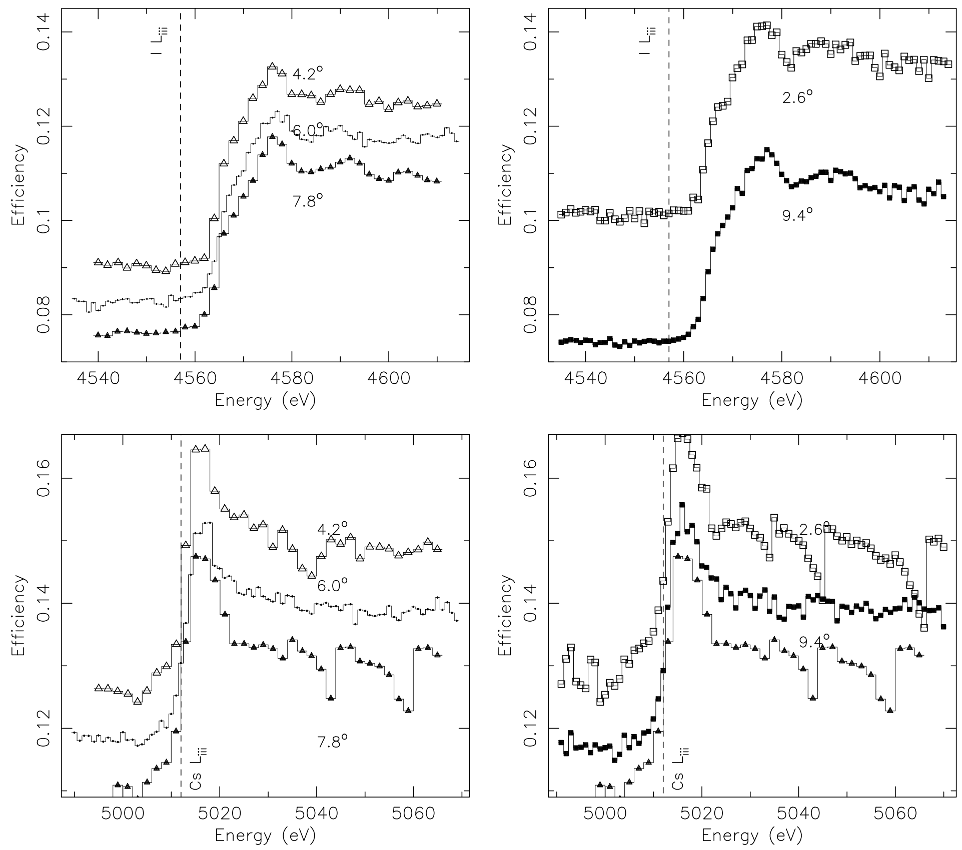

Figure 64: High resolution scans across the I L_{III} and Cs L_{III} absorption edges. Beam angles are with respect to the channel axis.

It is unfortunate that the spectral contamination of the Ni(3) grating on beamline 1.1 has compromised the quality of the data below ~500 eV although this does emphasize the importance of using the reference proportional counters, both of which performed well. It is also unfortunate that absolute efficiencies could not be calculated from the SRS data alone, however, current improvements in PC design and SRS operating procedures will eliminate the need for data normalization from future experiments.

4.5 Summary of the HRC Quantum Efficiency and Uncertainties

We summarize here all HRC QE calibration data taken to date, and present a discussion and estimation of the uncertainties in this calibration.

Each of the major HRC QE calibration data sets are summarized in the table below. A brief description of each is given, and the strengths, limitations, and uncertainties are outlined.

1. XRCF calibration: The effective area of the HRMA+HRC was calibrated at the XRCF at many closely spaced energies. There are several difficulties in using this dataset for determining the HRC QE. First, as stated above, the instrument was returned to SAO after these calibrations and was substantially modified. The flight performance of the instrument will be somewhat different. Second, there are potentially large systematic uncertainties in a large subset of this data taken using the HIREFS source. Third, extraction of the HRC QE requires a model or other measurements of the HRMA effective area, introducing another uncertainty. We have therefore only used this data to compare with the pre-fix flat field measurements.

2. SAO flat fields: After the flight instrument was returned to SAO, flat field measurements were made in the pre-fix and post-fix configurations. A gas-flow proportional counter (PC) was used as an absolute detector. These measurements were made at eight (HRC-I and HRC-S segment 0) or four (HRC-S segments +1 and -1) energies. The most important uncertainty in these measurements is the determination of the PC QE. Each flat field contained $\sim 10^8$ events (10000 per mm^2). The statistical uncertainty is therefore negligible compared to the systematic uncertainties. We have relied heavily on these measurements for generating the calibration data products located on our website.

3. CsI coated MCP synchrotron measurements: The QE of CsI coated Phillips MCPs (similar to HRC-S flight plates) was recently measured at the Daresbury Synchrotron Radiation Center in two energy bandpasses: 450 eV to 1200 eV and 4500 eV to 9500 eV. These measurements were made primarily to determine the absorption fine structure around the Cs and I M and L edges, but are also useful maps of the continuous curves between the edges. These data have not yet been incorporated into the QE models. The statistical uncertainty in these measurements is negligibly small.

4. UVIS transmission and uniformity measurements: Several different measurements have been made on the UV/Ion shields. First, several witness samples were taken to BESSY in Berlin to measure the absorption fine structure around the elemental edges. Second, the transmission of these samples was also measured in the HRC lab using the McPherson monochromator. These two sets of measurements typically agree within 1%. The best fit areal densities typically have a formal 90% confidence interval that is a few percent of the thickness. Third, the transmission and uniformity of flight backup UV/Ion shields was measured in the HRC laboratory using shadowgraphs. The UV/Ion shields are well calibrated, and any uncertainty in $T(E)$ for any of the shields is small compared to uncertainties in $Q_{MCP}(E)$.

5. Angular dependence of QE: The angular dependence of CsI coated MCPs (both Galileo and Phillips plates) over the AXAF cone angles has recently been measured in the HRC laboratory and is reported in this document. Statistical uncertainty in these measurements is also small. These results have not yet been incorporated into the QE models, however. The angular dependence is a $\sim$10% correction below 200 eV. This correction decreases with increasing photon energy, and is negligible above 1 keV.

The difficulty in determining the HRC QE lies in combining these datasets of varied completeness and usefulness. The post-fix flat fields are obviously the most useful since the instrument was then in the flight state, but are sparsely spaced in energy. The XRCF measurements are not representative of the flight QE, particularly for the HRC-S, and are generally useless below 1.5 keV at any rate because of complications with the X-ray source (HIREFS). We have provided some preliminary estimates of $Q_{HRC}(E)$ on the HRC calibration website relying primarily on the post-fix flat fields, the UVIS witness sample measurements, and on a semi-empirical model suggested by Mike Juda[8] to generate a continuous curve for $Q_{MCP}(E)$. The UVIS is well calibrated, so the major uncertainty in the QE models is in the MCP QE. More information about the current

QE model can be found on the HRC calibration website. The main problems with relying on the post-fix flat fields are that we have measurements at only a few energies, and there may be systematics in the absolute normalization. There are then two major uncertainties in the HRC QE curve as it now exists. First, how precise are the flat field measurements, and second, assuming the errors in the flat field measurements are small, how accurately does the model reflect the real $Q_{MCP}(E)$?

The first issue is not easy to address, but we can compare the pre-fix data with the XRCF data at the few energies that overlap. We find that, in general, the two measurements agree to within a few percent, giving us some confidence that our post-fix values are accurate within this same uncertainty of a few percent.

If we had more points (energies), the semi-empirical curve would be very accurate. Given that we only have 8 (only 7 useful) energies from which to base our interpolation, we are required to make continuous estimates over large energy steps for which we have no data. As above, we can use the XRCF data as a guide. Above 1.5 keV, the general shape of the QE curve measured at XRCF agrees well with the modelled curve except around the Cs and I L edges. The model overestimates the jump across the edge by about a factor of 2. The same situation probably occurs around the Cs and I M edges below 1 keV, but the XRCF data does not provide a useful comparison at these energies. The synchrotron data is useful around both sets of edges, and provides supporting evidence that the size of the jumps has been over estimated. In addition, the model predicts that the QE of the MCPs will be the open area ratio ($\sim$60%) at low energy end of the bandpass. Based on earlier synchrotron measurements[9], this is clearly not correct.

From this analysis, what conclusions can be drawn about the uncertainties in the HRC QE? There are two major deficiencies in the QE model that must be addressed in the future. First, the jumps across the edges are too large. The current models my be off as much as a factor of two around the edges. Second, the low energy QE has been considerably overestimated, perhaps also by a factor of 2. The smooth portion of the interpolated curve is probably more accurate, we estimate within 10% or so. Both of these numbers will be improved when the recent synchrotron measurements are incorporated. The synchrotron data provides a direct measurement of the jumps across the edges and the shape of the curve between the edges. Any systematic uncertainties in the synchrotron data are smaller than the uncertainties that exist in the current QE model. In addition to the synchrotron data, we also have an extensive on-orbit calibration program planned that will allow us to test and further refine our QE model.

4.6 HRC Quantum Efficiency versus Angle of Incidence

4.6.1 Introduction

The quantum efficiency of MCPs depends strongly on the angle of the incident flux of radiation with respect to to the MCP pore angles. Since this angular QE dependence is due to absorption and grazing reflection down the pores, it is affected by pore coating, surface finish and X-ray energy.

Previous work and analysis has shown that given the range of AXAF cone angles, CsI coated input MCPs with bias angles of $\sim 6°$ have one major benefit. This benefit is a combination of better overall Effective Area (EA) for the HRMA/HRC and less variation over the range of AXAF cone angles.

The downside to the $\sim 6°$ bias angle MCPs is that the vacuum deposition process we have employed does not uniformly coat the walls of the MCP pores. As a result there is an azimuthal dependence of photocathode coating and a resulting azimuthal dependence of QE. 0° bias input MCPs such as used on the Einstein and ROSAT, are by definition azimuthally symmetric, aesthetically pleasing but not necessarily optimum for AXAF.

We have been investigating the angular dependence of the quantum efficiency of coated HRC type MCPs. These investigations are intended to provide data products to those trying to better understand and refine the HRC final calibration.

This information will be of particular interest and use to those applying flat field HRC QE values to grating data, EA measurements, off-axis response and High Energy Suppression Filter (HESF) data.

Previous measurements have been done to investigate and quantify these effects however in most cases these previous investigations were limited in the number of energies and range of angles.

Using a soft X-ray monochromator (McPherson 1 meter VUV scanning monochromator), and two orthogonal rotary stages, the QE versus angular dependence of HRC type detectors has been investigated over a large set (~ 10) energies and a large set of angles. The energies investigated were all $\leq$ 1487eV. These lower energies were most important as this is where the QE vs angle effect is largest and where the HRMA "effective cone angle" (relative contribution from outer-most shell) is largest. The scanned angles were chosen to cover the important AXAF range and mimic the values of the actual average HRMA shell cone angles.

We discuss analysis and results using both HRC-S (ie Philips mfg.) and HRC-I detector (GEOC mfg.) representative MCPs.

4.6.2 Applicability and Caveats

In flight, X-rays from the HRMA converge at the "cone"angles down to the size of the HRMA PSF ($\sim 50\mu$m). On such a small spatial scale, one would expect large variations in the detector uniformity, however in flight dithering will average out these variations in response over a much larger area.

In the laboratory, the effects of the cone angles and the averaging were performed by using two orthogonal rotary stages to recreate the effect of the AXAF angles and a large fraction of the detector was illuminated.

There are several caveats that one must consider in applying these results. These caveats stem primarily from the fact that we are using test items; we used flight-spare coated MCPs that we believe are representative of the actual flight HRC-I and HRC-S.

The MCPs were nominally specified to have a 6° bias angle, though for the actual flight items, this was never verified.

Even though coating of the flight HRC MCPs and of these test MCPs was performed in the same coating deposition facility, using the same written procedure, by the same personnel -differences do exist. The most obvious difference is that the final CsI coating thicknesses were different.

4.6.3 Laboratory Setup

Experimental Setup

The laboratory aparatus consisted of the HRC $\sim$ 6m X-ray pipe. A McPherson 1 meter VUV scanning monochromator was mounted on the source end. During operation, no monitoring of the X-ray beam was performed for either temporal or spectral variation or content. Extensive previous experience with this source has shown that it is temporally stable and spectrally pure.

The chevron pair of test MCPs were assembled into a laboratory HRC-I type MCP holder with an aluminized polypropylene shield. The MCP asembly was incorporated with a laboratory version 10 kΩ Crossed Grid Charge Detector (CGCD). The resulting detector was placed on a two axis rotary stage in the HRC test chamber. During assembly, transport and configuration, the test detector was continuously kept in a dry nitrogen atmosphere to protect the photo-cathode.

The stages were configured to ensure that the axes of motion passed through the center of the front surface of the input MCP. The two rotary stages were New England Affiliated Technology (NEAT) models RT-10-SM and RT-6-SM . The motion of the stages was under computer/software control. The two stage system was mounted to cast aluminum alignment plate inside the test chamber. The two axes are the "tilt" angle θ and the azimuthal angle ϕ. The motion control set-up is depicted in Figure 65.

The flight HRC focal plane layout is depicted in Figure 66; it indicates the orientation of the pore bias angles with respect to the space craft and detector coordinates.

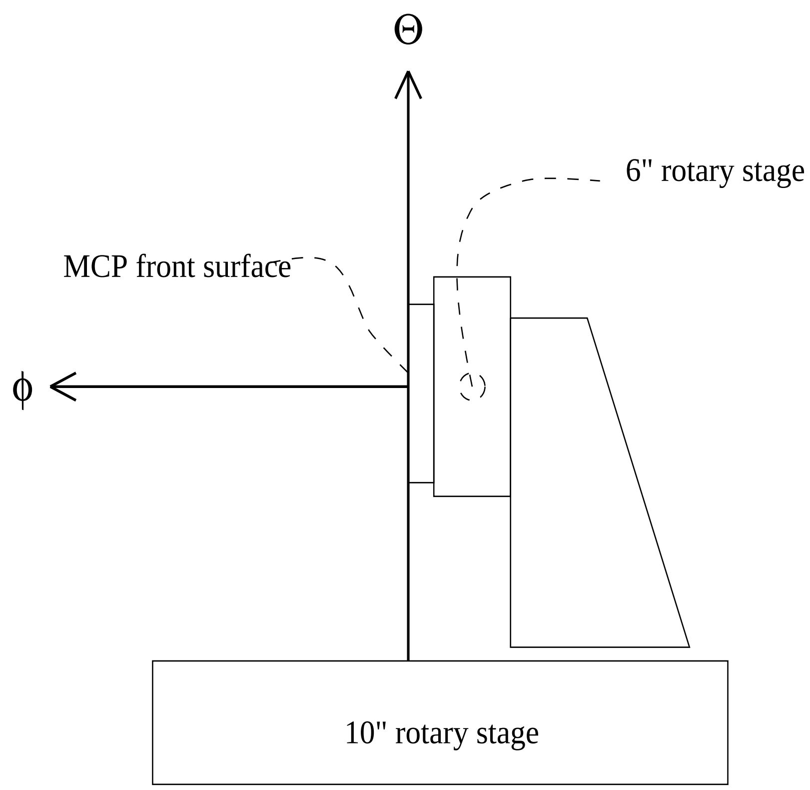

Figure 65: Stages used for measuring QE versus angle of X-ray incidence. Rotation axes were engineered to go through the center and face of the input MCP. The two axes, θ and ϕ are as indicated

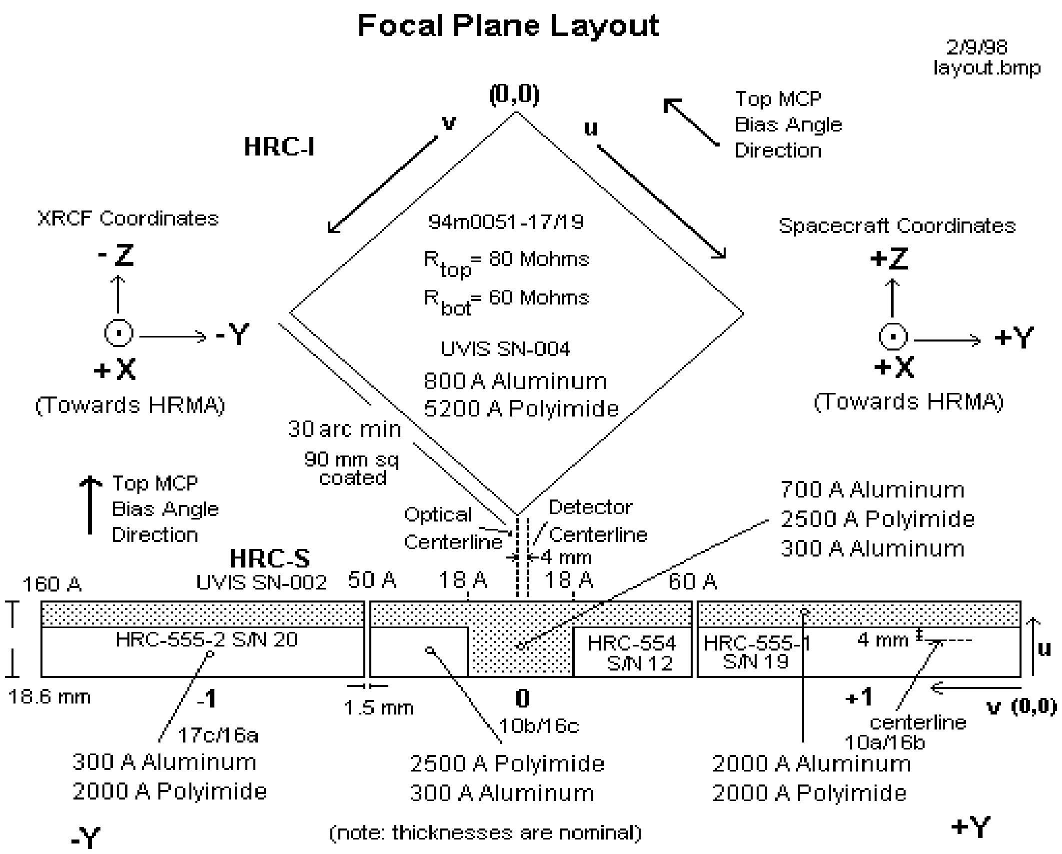

Figure 66: Layout of the HRC focal plane. The MCP pore angle orientations are as indicated; note that for the HRC-S the pore angles are perpendicular to the dispersion direction and tilting away from the High Energy Suppression Filter (HESF)

Data acquisition was done with a laboratory version of the HRC electronics (Unit I) that was specifically modified to keep track of the motion control.

Data was analyzed off-line.

Components

Both HRC detectors (HRC-S and HRC-I) consist of pairs of MCPs in a chevron configuration. Each chevron pair consists of two MCPs with a 6° (nominal) bias angle. The front surface of the input MCPs of both detectors were coated with a CsI photocathode to enhance the QE over the AXAF band.

The HRC-I type MCPs were manufactured by the Galileo Electro Optics Corp. (GEOC). They are 100mm x100mm in size, they have 10 μm pores on 12.5 μm centers. and hey have a nominal 120: L/D ratio - they are 1.2mm thick. The MCPs were nominally specified to have a 6° bias angle, though this was never verified. The actual flight HRC-I MCPs are serial #s GEOC 94m0051-17 (input) and GEOC 94m0051-19 (output). The input MCP was coated at the SAO coating deposition facility according to procedure SAO-HRC-PROC-95-165. The final coating thickness as determined by witness sample was $1,440\AA$

The HRC-S type MCPs were manufactured by Philips Components. They have 12 μm pores on 15 μm centers. They have a nominal 120: L/D ratio - they are 1.5mm thick. Philips MCPs were nominaly specified to have a 6° bias angle, though this was never verified for the actual flight items. The flight HRC-I MCPs are serial numbers: NH002- 10-a, 10-b, 17-c (input) and 16-b, 16-c, 16-a (output). The input MCPs was coated at the SAO coating deposition facility according to procedure SAO-HRC-PROC-95-165. The final coating thickness as determined by witness sample was $1,400\AA$

Test article MCPs were selected from our limited selection of flight spares. Both HRC-S and HRC-I test MCPs were 100mm $\times$ 100mm format. The test item input MCPs had CsI coatings of $1,875\AA$ for the Philips (HRC-S) and unknown thickness ($1,500\AA$?) for the GEOC (HRC-I).

4.6.4 The Measurements

The first measurement determined the MCP bias angle by exposing the detector to 1487eV X-rays from the monochromator and scanning through the θ angle. The QE versus theta angle curve was then used to determine the MCP bias angle as the position of the $\theta = 0°$ (normal incidence) was known from the mechanical setup.

This measurement confirmed the 6° bias angle for the Philips (HRC-S type) MCPs. In contrast, similar analysis shows that the GEOC MCPs (HRC-I type) have a bias angle of only 4.7°

4.6.5 Tests and Data Products

Following the MCP bias angle determination, the detector was scanned in θ from $-12°$ to $15°$ with respect to normal incidence in 0.1° steps. Data integration times and rates were adjusted to ensure $\sim 2,000$ -10,000 events per data point.

This data set, presented in Figures 69 through Figure 82, shows the QE dropping to a minimum as the X-rays reflect/pass down the MCP pores. The relationship of critical angle versus energy is apparent from the width of the "dip" in QE; sharper at higher energies and broader at lower energies. In addition, it is apparent that the data is not symmetric about the QE "dip"; this is due to the azimuthal dependence of the CsI photocathode coating. On the low QE side of the QE dip, the X-rays are impinging on the sides of the MCP pores with minimum photocathode coating. On the high QE side of the QE dip, the X-rays are impinging on the sides of the MCP pores with maximum photocathode coating (See Figure 67). The GEOC MCPs, with the smaller pore angle, show greater symmetry about the QE-dip as would be expected. Furthermore, bare plates should and do show symmetry about the pore-bias angle; Figure 68 shows that the QE response is symmetrical about the pore axis; this proves that the QE asymmetry about the pore axis in coated plates is due to the asymmetry of the CsI coating.

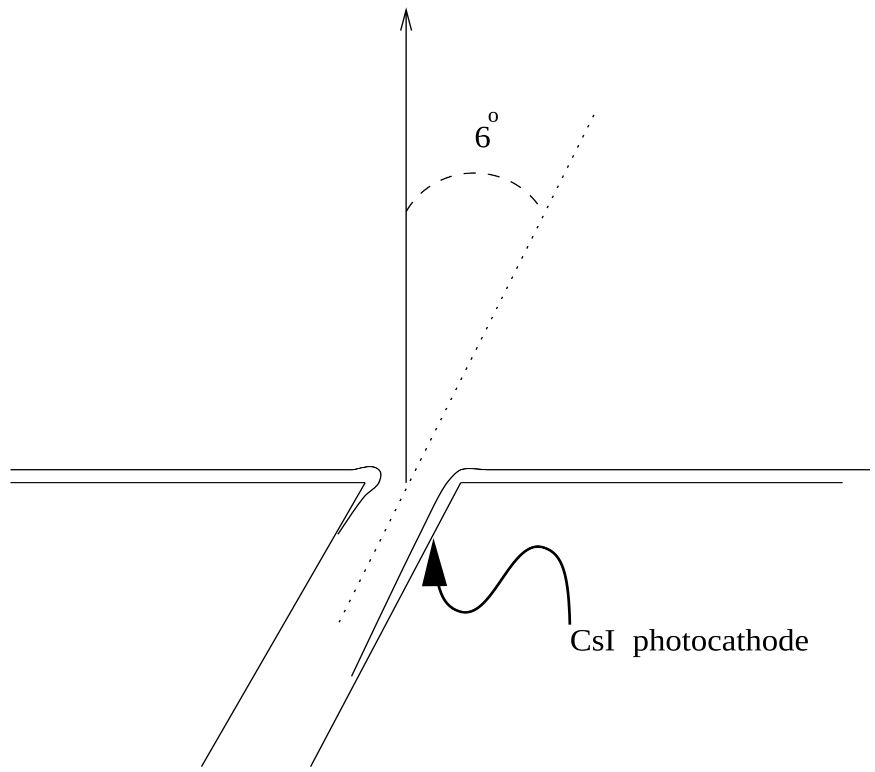

Figure 67: Coating asymmetry due to pore bias. Dimensions are for illustration purposes only. QE will not by symmetric about the pore angle due to the differing amounts of coated pore exposed.

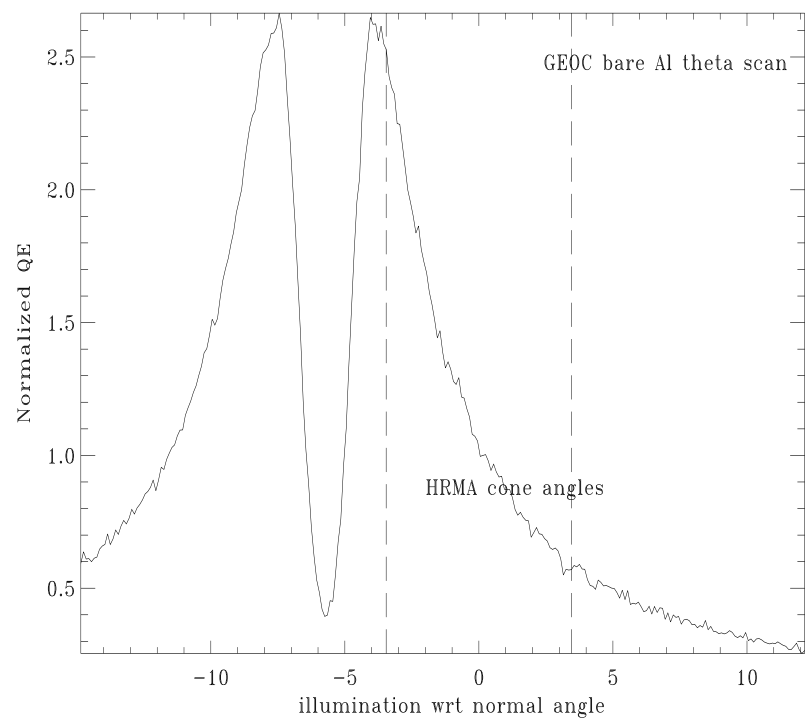

Figure 68: QE versus angle for bare GEOC MCPs. This data set shows that the QE asymmetry about the pore axis for coated MCPs is due to the asymmetry of the CsI coating. Note: these GEOC MCPs have bias angles of $\sim 6°$.

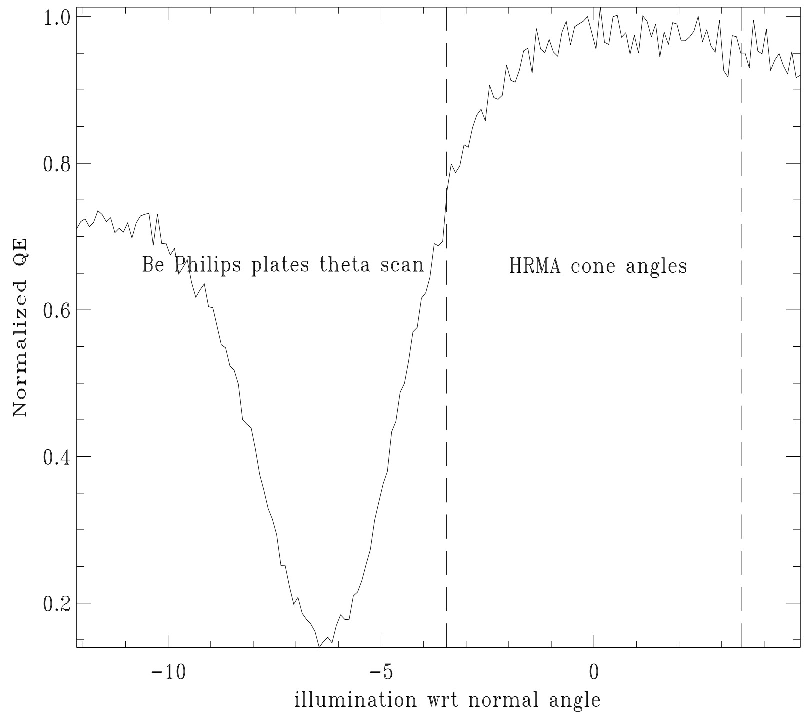

Figure 69: Relative QE versus θ at $E = 108.5$eV for HRC-S type MCPs. The range of the AXAF HRMA cone angles is indicated. QE values have been normalized so that $QE = 1$ at $\theta = 0°$

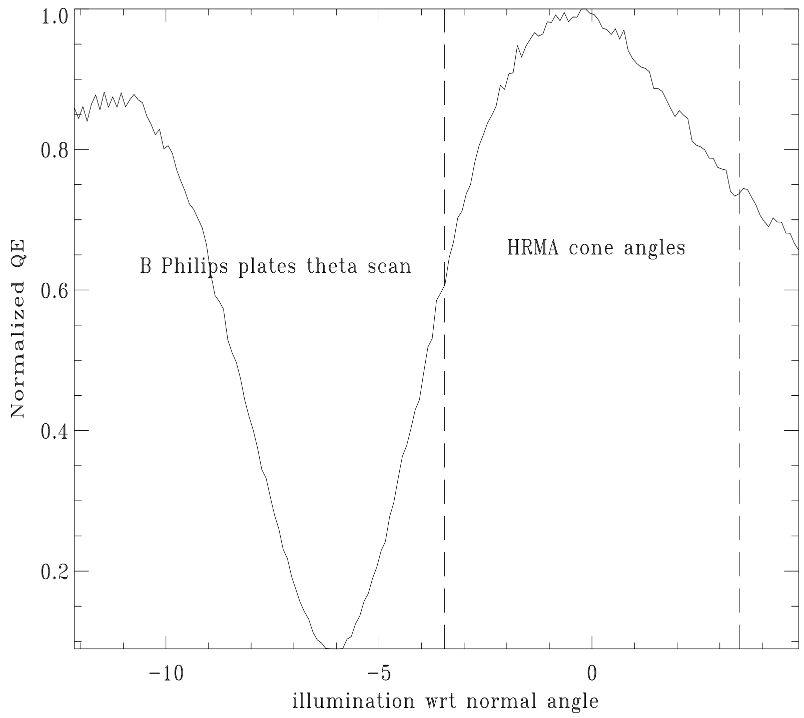

Figure 70: Relative QE versus θ at $E = 183.3$eV for HRC-S type MCPs.. The range of the AXAF HRMA cone angles is indicated. QE values have been normalized so that $QE = 1$ at $\theta = 0°$.

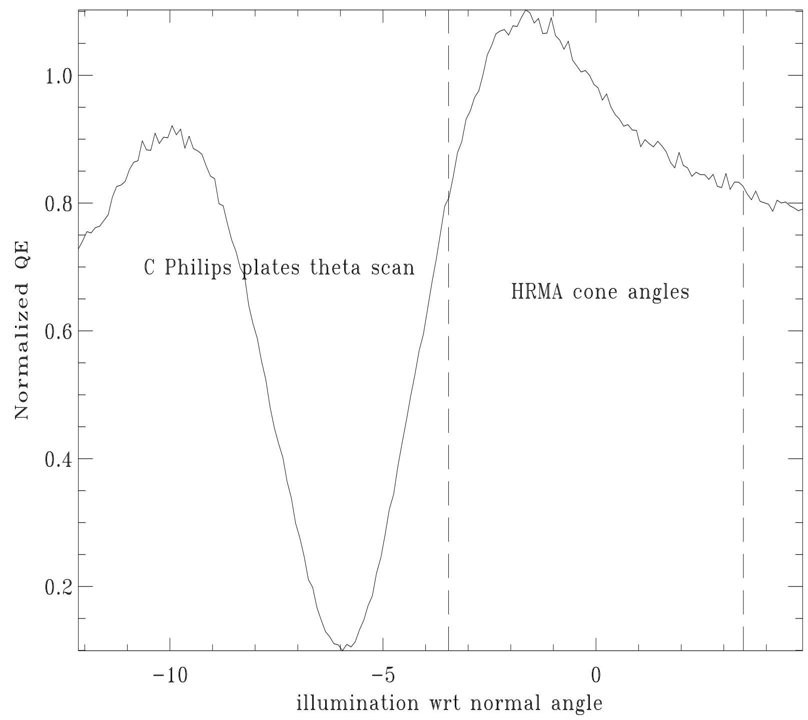

Figure 71: Relative QE versus θ at $E = 277.0$eV for HRC-S type MCPs.. The range of the AXAF HRMA cone angles is indicated. QE values have been normalized so that $QE = 1$ at $\theta = 0°$.

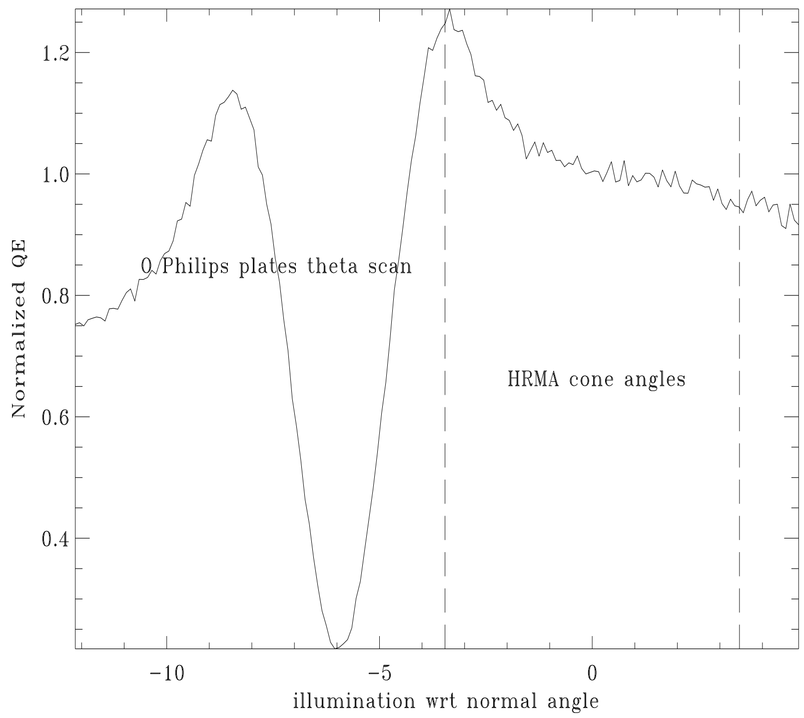

Figure 72: Relative QE versus θ at $E = 524.9$eV for HRC-S type MCPs.. The range of the AXAF HRMA cone angles is indicated. QE values have been normalized so that $QE = 1$ at $\theta = 0°$.

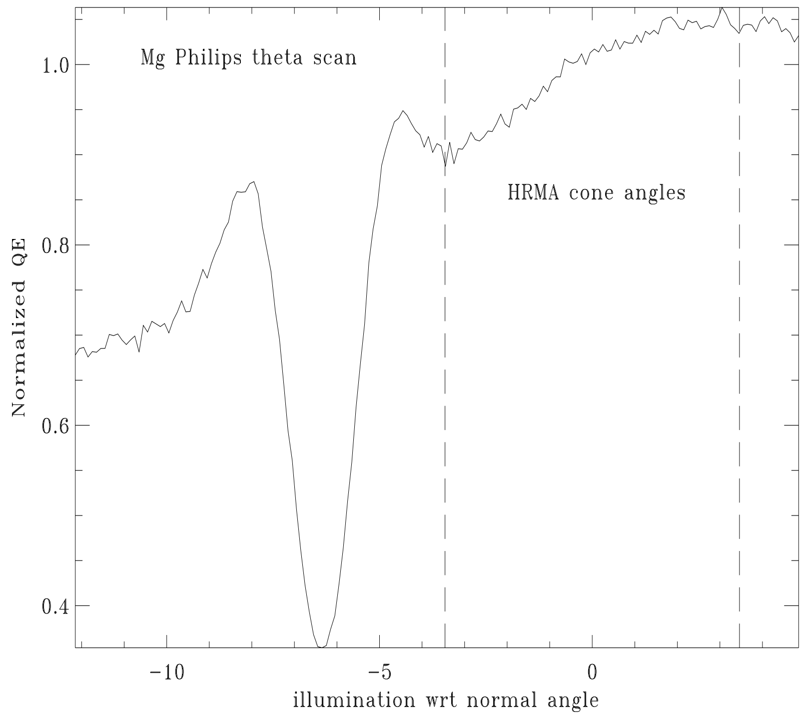

Figure 73: Relative QE versus θ at $E = 1253.6$eV for HRC-S type MCPs.. The range of the AXAF HRMA cone angles is indicated. QE values have been normalized so that $QE = 1$ at $\theta = 0°$.

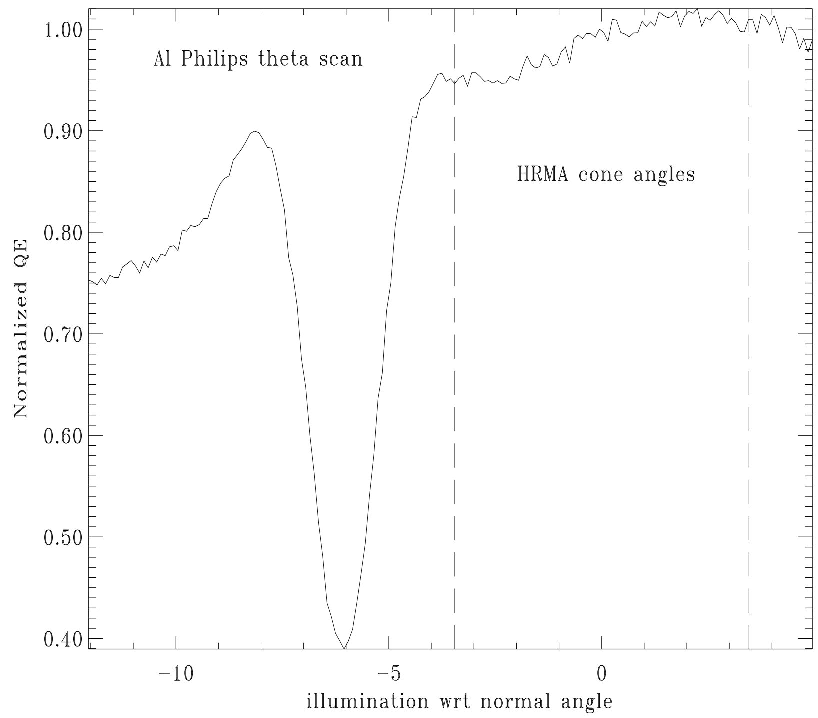

Figure 74: Relative QE versus θ at $E = 1486.7$eV for HRC-S type MCPs.. The range of the AXAF HRMA cone angles is indicated. QE values have been normalized so that $QE = 1$ at $\theta = 0°$.

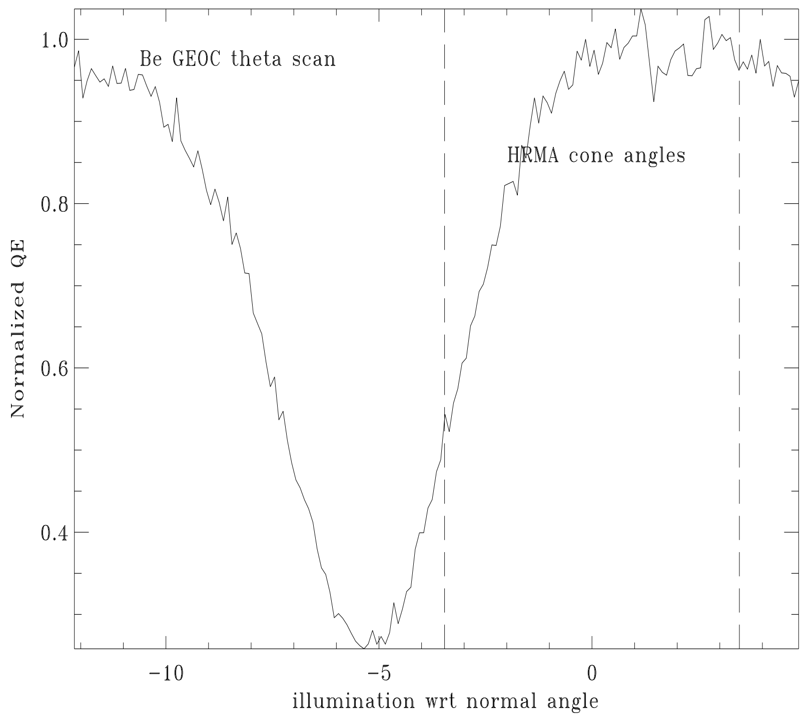

Figure 75: QE versus θ at $E = 108.5$eV for HRC-I type MCPs. The range of the AXAF HRMA cone angles is indicated. QE values have been normalized so that $QE = 1$ at $\theta = 0°$

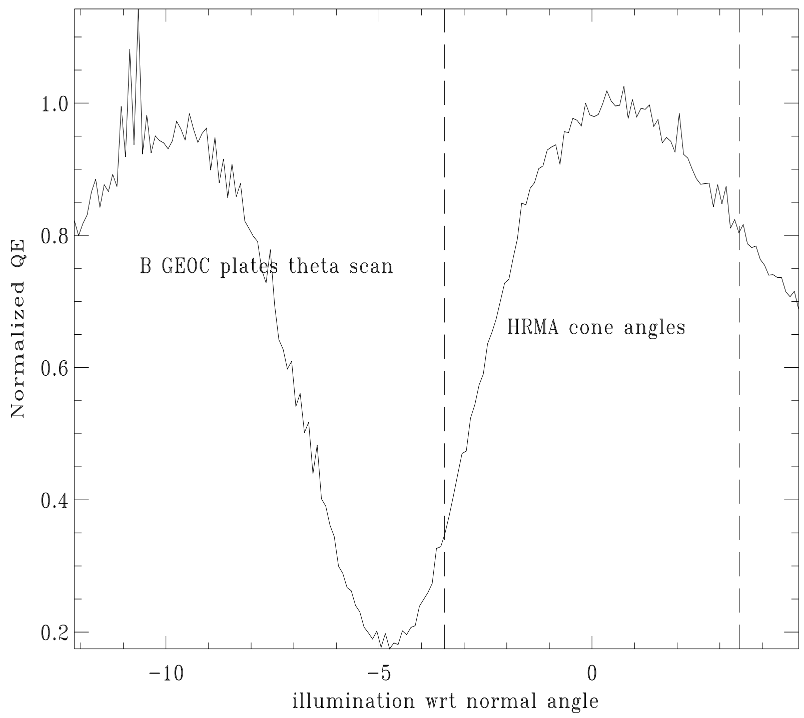

Figure 76: Relative QE versus θ at $E = 183.3$eV for HRC-I type MCPs. The range of the AXAF HRMA cone angles is indicated. QE values have been normalized so that $QE = 1$ at $\theta = 0°$.

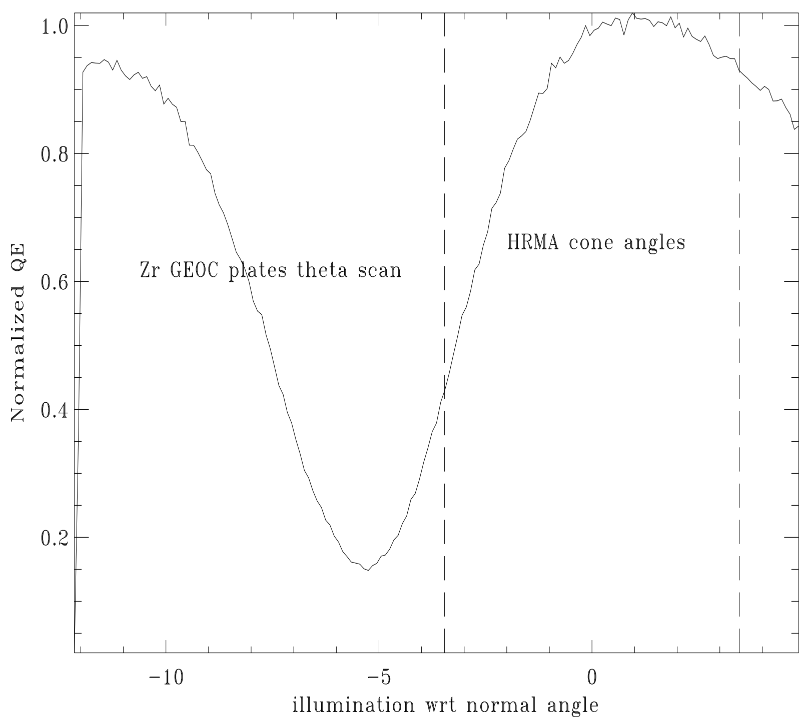

Figure 77: Relative QE versus θ at $E = 151.1$eV for HRC-I type MCPs. The range of the AXAF HRMA cone angles is indicated. QE values have been normalized so that $QE = 1$ at $\theta = 0°$. Glitch at $\sim -12°$ is not real and is due to operator error.

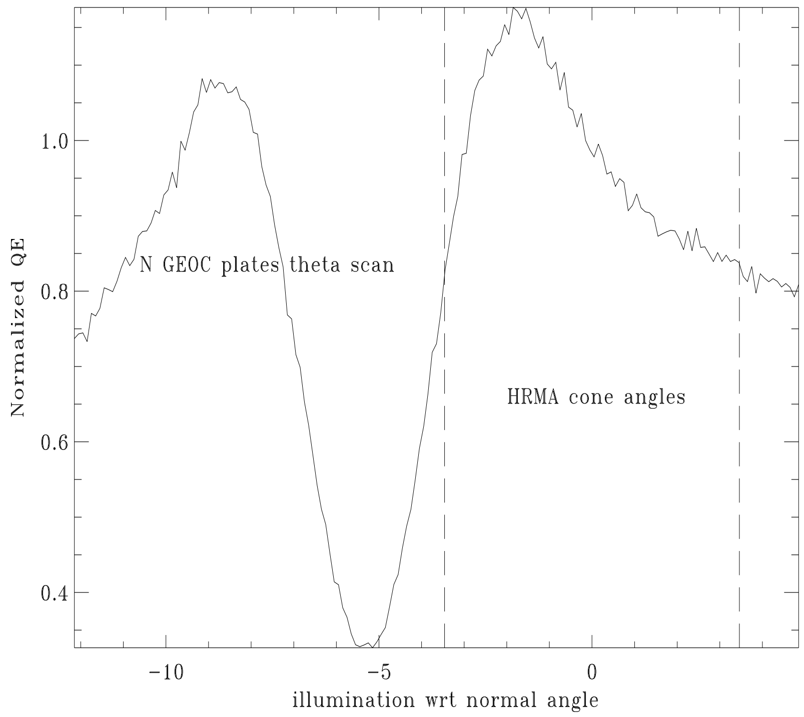

Figure 78: Relative QE versus θ at $E = 392.4$eV for HRC-I type MCPs. The range of the AXAF HRMA cone angles is indicated. QE values have been normalized so that $QE = 1$ at $\theta = 0°$.

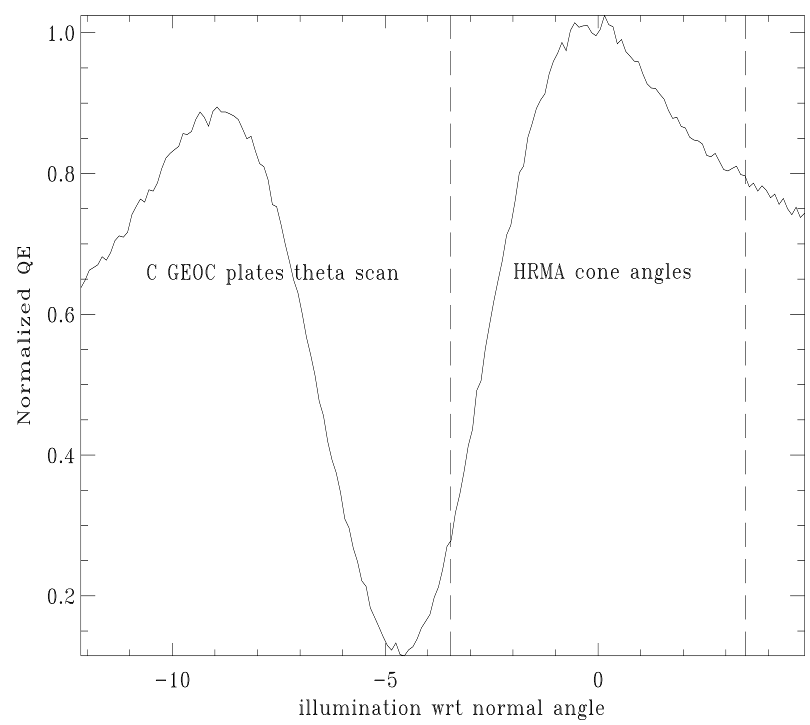

Figure 79: Relative QE versus θ at $E = 277.0$eV for HRC-I type MCPs. The range of the AXAF HRMA cone angles is indicated. QE values have been normalized so that $QE = 1$ at $\theta = 0°$.

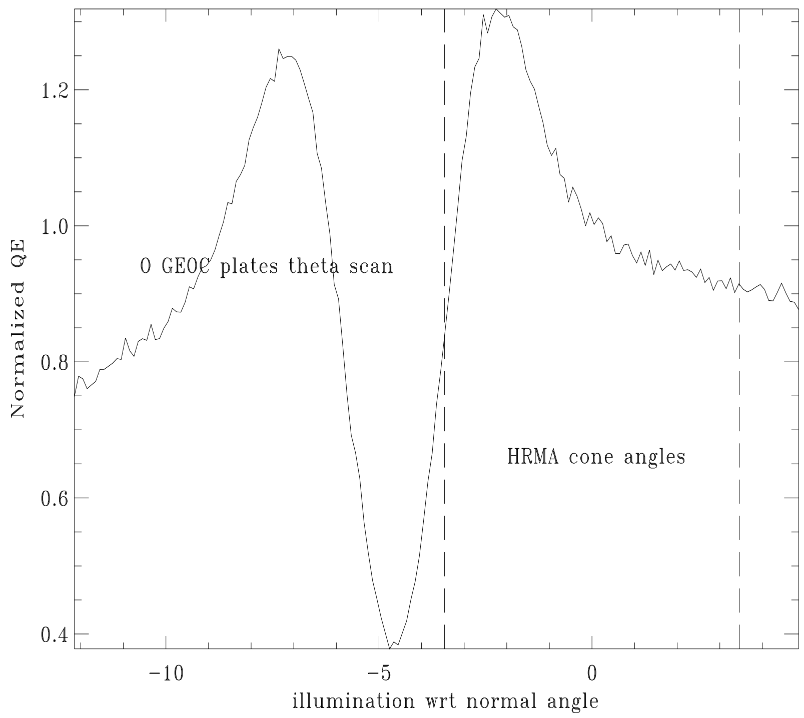

Figure 80: Relative QE versus θ at $E = 524.9$eV for HRC-I type MCPs. The range of the AXAF HRMA cone angles is indicated. QE values have been normalized so that $QE = 1$ at $\theta = 0°$.

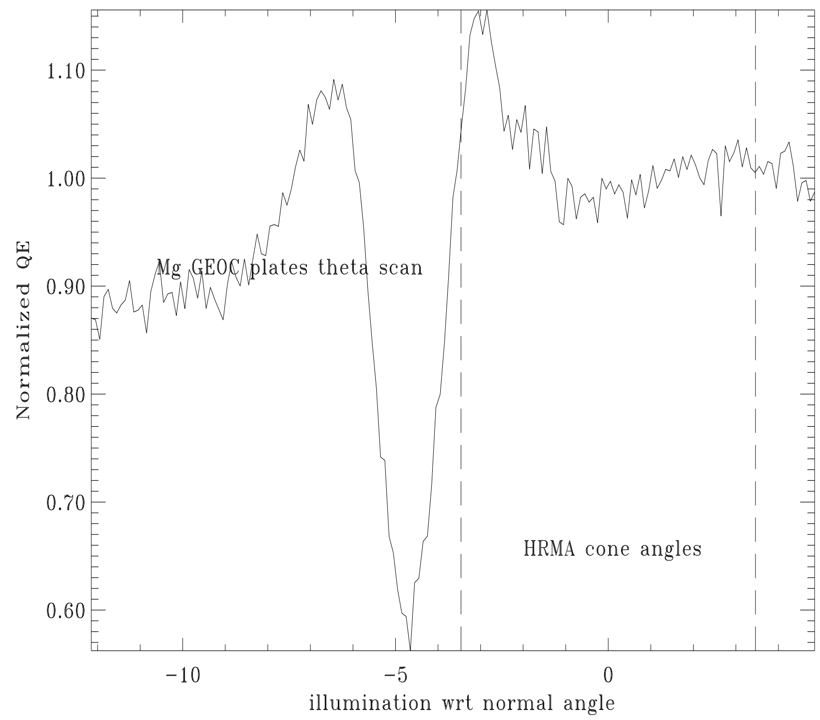

Figure 81: Relative QE versus θ at $E = 1253.6$eV for HRC-I type MCPs. The range of the AXAF HRMA cone angles is indicated. QE values have been normalized so that $QE = 1$ at $\theta = 0°$.

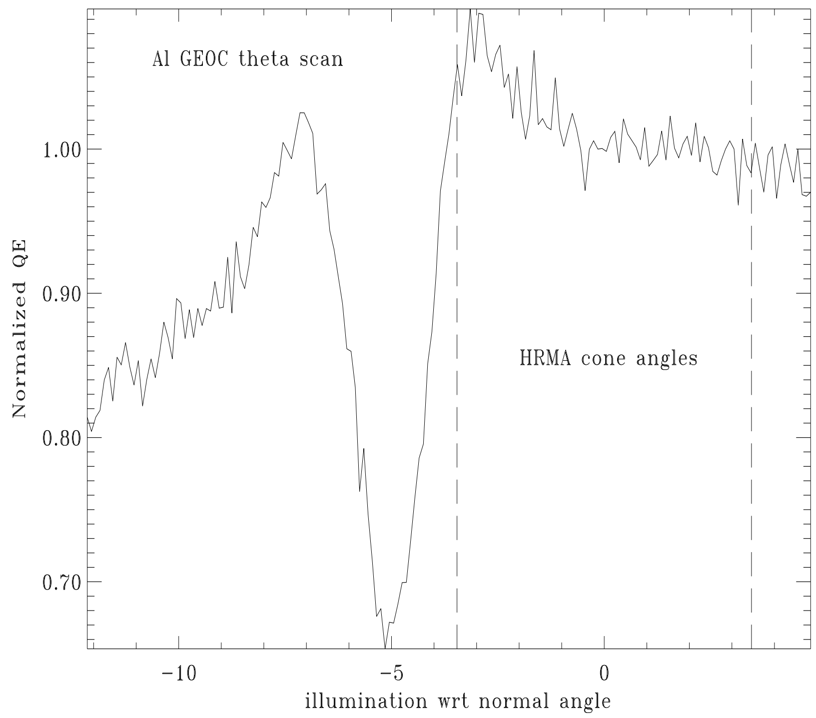

Figure 82: Relative QE versus θ at $E = 1486.7$eV for HRC-I type MCPs. The range of the AXAF HRMA cone angles is indicated. QE values have been normalized so that $QE = 1$ at $\theta = 0°$.

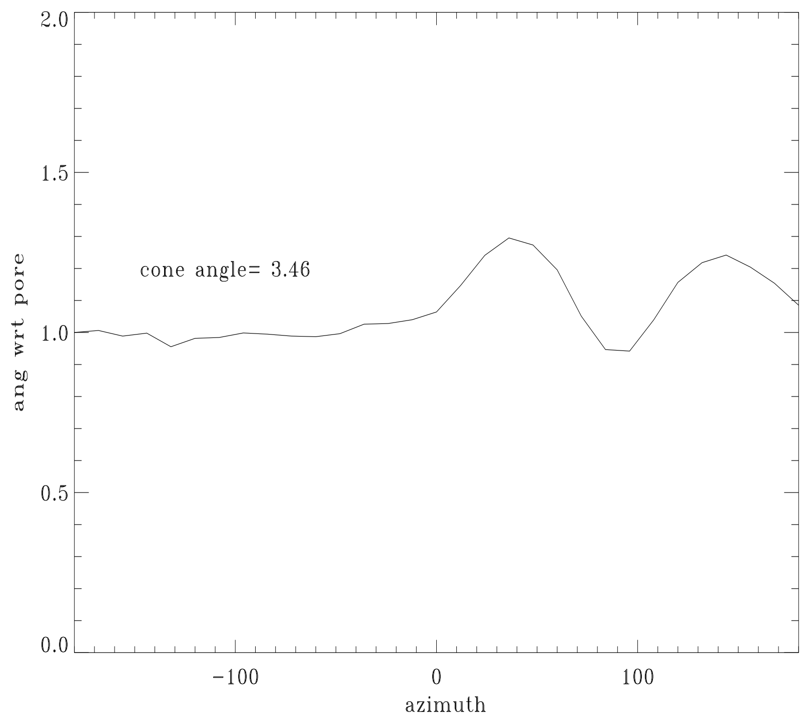

Figure 83: Laboratory measurement to determine relative QE for C X-rays (277eV) versus azimuth for outermost HRMA shell. Structure is due to sampling within the broad dip in QE versus angle for C X-rays. (HRC-S type Philips MCPs).

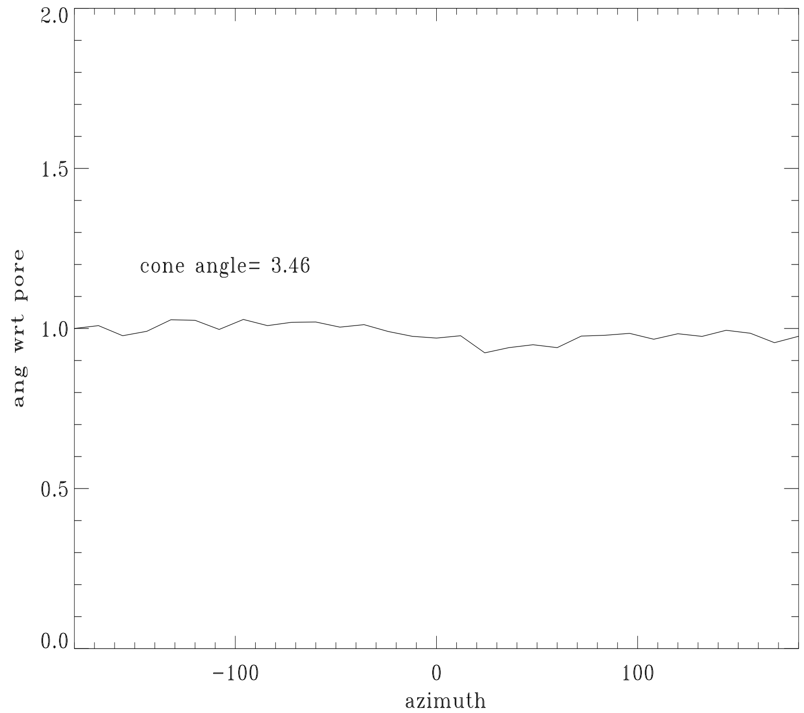

Figure 84: Laboratory measurement to determine relative QE for *Al* X-rays (1487eV)versus azimuth for outer-most HRMA shell. No structure is evident. (HRC-S type Philips MCPs)

The AXAF cone angles never see the "dark" side of the pores; they are limited to a small range of the QE versus theta curve as indicated in Figures 69 through Figure 74 Indicating the range of the HRMA cone angles on such a figure does not necessarily imply that these QE versus θ curves can represent the generalized QE variation with angle of x-ray incidence. The QE versus theta scans are limited in sampling the azimuthal dependence at only $\phi = 0$ and $180°$. However as will be shown, this equivalence turns out to be a reasonable approximation over the limited range of the AXAF cone angles.

The second set of measurements were intended to simulate the AXAF-HRMA cone geometry; the detector was first tilted in θ to $+$ average cone angle. The detector was then scanned in ϕ from -180 to $0°$. The measurement was then repeated at $\theta = -$ average cone angle. These two measurements effectively scan the entire HRMA cone in azimuth. These measurements were repeated for all four of the HRMA average cone angles. Some representative QE versus ϕ measurements are shown in Figures 83 and 84.

Using the QE versus θ result, as a generalized QE versus angle "model" the expected response of the coated MCPs was determined by calculating the angle of incidence of X-rays with respect to the MCP pores as a function of cone angle and azimuth:

$$QE(\alpha) = QE(\Theta, \Phi).$$

Thie angle, α can be written as

$$\alpha = cos^{-1}(\mathbf{p} \bullet \mathbf{C}),$$

where p is a unit vector in the direction of the MCP pores. C is a unit angle in the negative direction of the impinging X-rays. The angle between the pore channels and an X-ray from would then be

$$\alpha = cos^{-1}(\mathbf{p} \bullet \mathbf{C}),$$

where

$$\mathbf{p} = sin(\omega)cos(\phi)\hat{x} + sin(\omega)sin(\phi)\hat{y} + cos(\omega)\hat{z}$$

and

$$\mathbf{C} = sin(\theta)cos(\Phi)\hat{x} + sin(\theta)sin(\Phi)\hat{y} + cos(\theta)\hat{z}.$$

The geometry of the angles involved is depicted in Figure 85.

The value of α (angle of X-ray incidence with respect to MCP pore axis) is depicted in Figure 86 for 6° bias MCPs.

Expected QE versus azimuth was calculated using $QE(\alpha)$ and the range of α as depicted in Figure 86. This result was compared with the laboratory HRMA cone angle scan for the outer-most shell. The comparison is presented in Figure 87. It is apparent that the QE versus angle data presented in Figure 69 through Figure 82 can be used to predict the entire angular QE dependence for the HRC over the range of the HRMA cone angles.

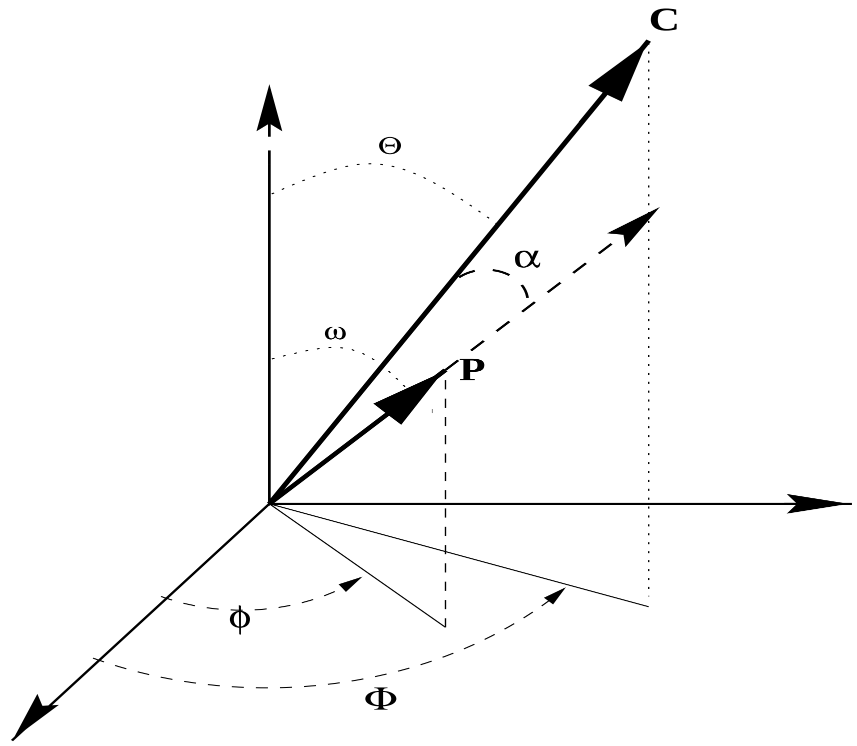

C cone angle from HRMA

P pore angle

α angle between Xray and pore axis

Figure 85: Geometry of pore angles and angle of X-ray incidence.

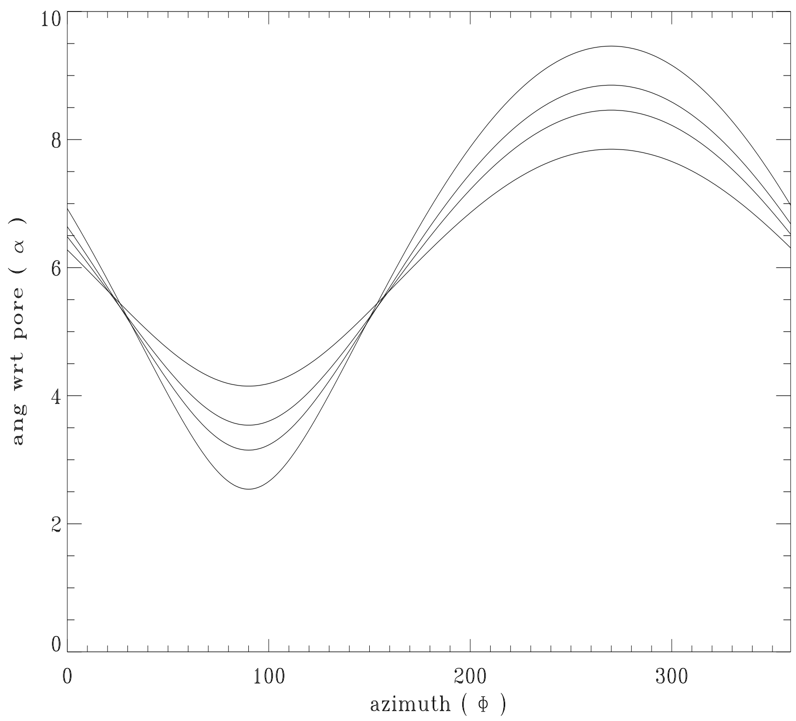

Figure 86: Angle of incidence of X-rays with respect to MCP pore from the four HRMA shells versus azimuth for a 6° bias MCP.

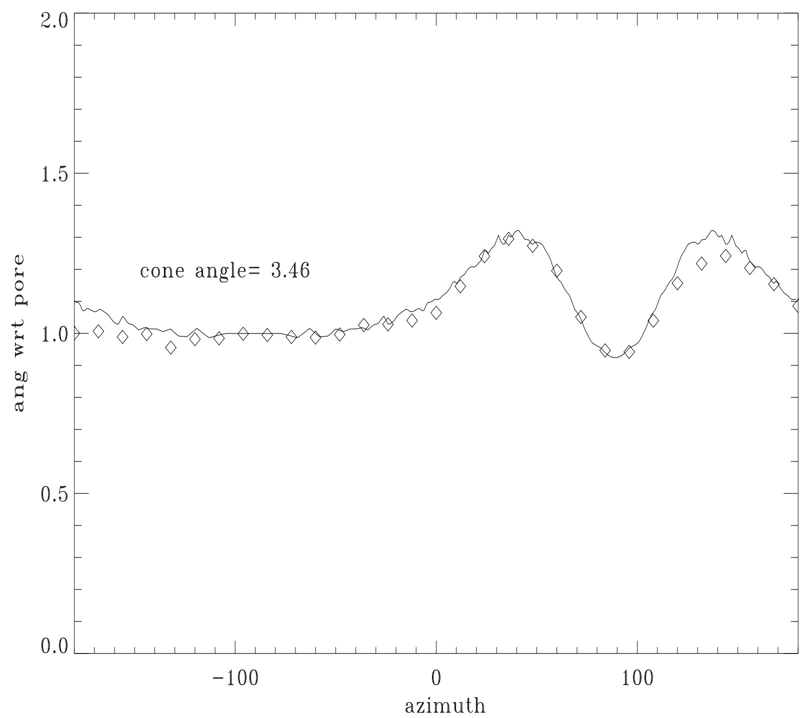

Figure 87: Comparison of scan in Φ with expected response using QE versus θ data as a “model”. Statistical errors are $\sim 3\%$. Data from Philips MCPs, C (277eV) X-rays. Range of incident angles is as depicted in Figure 86.

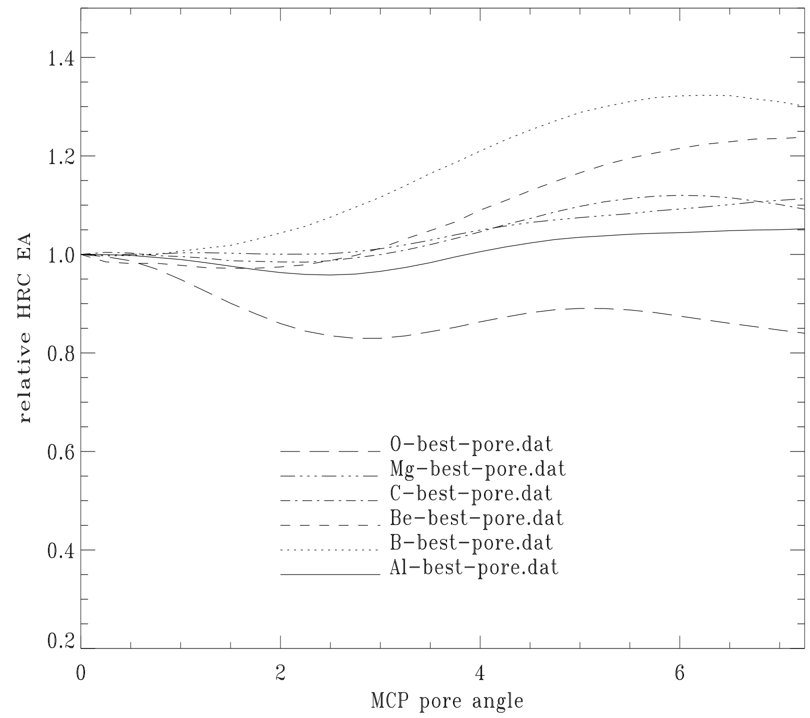

Figure 88: Relative HRC EA with HRMA versus choice of MCP bias angle angle . The measured Philips (HRC-S) type MCP had 6° bias. The measured GEOC (HRC-I) type MCP had a 4.7° bias angle.

Application of Results

Two applications of the above data set are herein presented. Both sets of results are based on using QE versus θ as representative of the angular response of CsI coated MCPs.

Re-verifying the 6° bias Choice

Using the QE versus θ data sets, one can determine the pore angle bias which maximizes the HRMA/HRC Effective Area. $EA(E,\omega)$ i.e. the effective area versus MCP pore bias angle (ω) and Energy, E can now be calculated. The result

$$\sum_i^4 EA_i < QE_i(\omega) >$$

(in arbitrary units) is depicted in Figure 88, where $< QE_i(\omega) >$ is the expected QE of the HRC appropriately averaged over incident angles from the i^{th} HRMA shell:

$$< QE_i(\omega) >= \int_0^{2\pi} QE(\theta_i, \phi) d\phi.$$

EA_i is the effective area of the appropriate shell at the energy of interest, and θ_i is the cone angle of that particular shell.

As can be seen from Figure 88, the choice of 6° pore bias is about optimum.

Applying "flat field" results to HRMA EA values

Post XRCF, the HRC detectors were modified and a series of x-ray flat field illumination QE measurements were performed. In these measurements the HRC detectors were illuminated with X-rays from a Manson Model 5 electron impact source. Filters were used to improve the line to continuum ratio and the x-ray flux was measured with flow proportional counters. The resultant absolute QE values were used as the basis for the "final" HRC QE and EA models.

The HRC team has repeatedly claimed that for higher energies ($\sim$ 1keV) that normal incidence flat field QE data are a good approximation of the QE of the detector when it is operated behind the HRMA. This claim has been verified using the above data sets. Such simple averaging, however, does not apply for lower energies. The net result is that the detector QE and EA, as derived from flat field measurements, must be de-rated. The de-rating factors have been determined by

$$QE_{HRMA} : QE_{flat-field} = \frac{\sum_i^4 EA_i < QE_i >}{\sum_i^4 EA_i}.$$

$< QE_i >$ is the expected QE of the HRC appropriately averaged over incident angles from the i^{th} HRMA shell:

$$< QE_i(\omega) > = \int_0^{2\pi} QE(\theta_i, \phi) d\phi.$$

EA_i is the effective area of the appropriate shell at the energy of interest.

The de-rating factors are presented in Figures 89, 90 and Tables 5, 6. The de-rating factors vary from $\sim$ 12% to less than 0.1% over the set of energies tested.

Verifying or checking the de-rating factors by comparing XRCF determined QE values with flat field determined QE values is problematic as the HRC detectors were modified in the interim period.

HRMA to flat-field de-rating factors

Energy	Derate factor
108.5	0.959
183.3	0.883
277.0	0.934
524.9	0.996
1253.6	0.999
1486.7	0.995

Table 5: HRMA De-rating factors to convert flat field QE or EA values to corresponding values when HRC-S type 6° bias MCPs are used.

HRMA to flat-field de-rating factors

Energy	Derate factor
108.5	0.932
151.1	0.938
183.3	0.888
277.0	0.834
392.4	0.947
524.9	0.988
1253.6	1.03
1486.7	1.01

Table 6: HRMA De-rating factors to convert flat field QE or EA values to corresponding values when HRC-I type 4.7° bias MCPs are used.

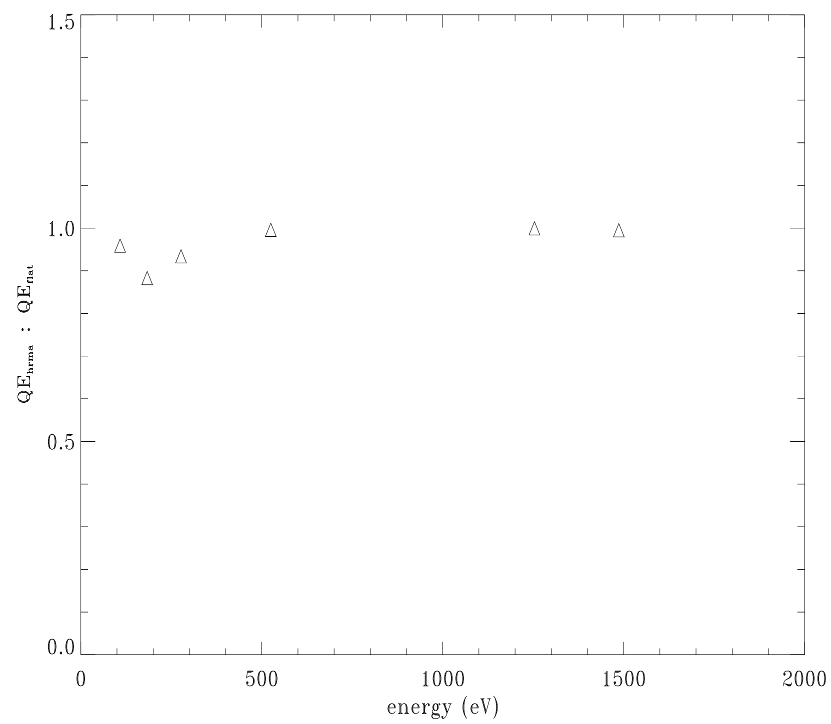

Figure 89: De-rating factors for applying HRC-S flat field data to operation in the converging beam of the HRMA (assuming 6° pore bias).

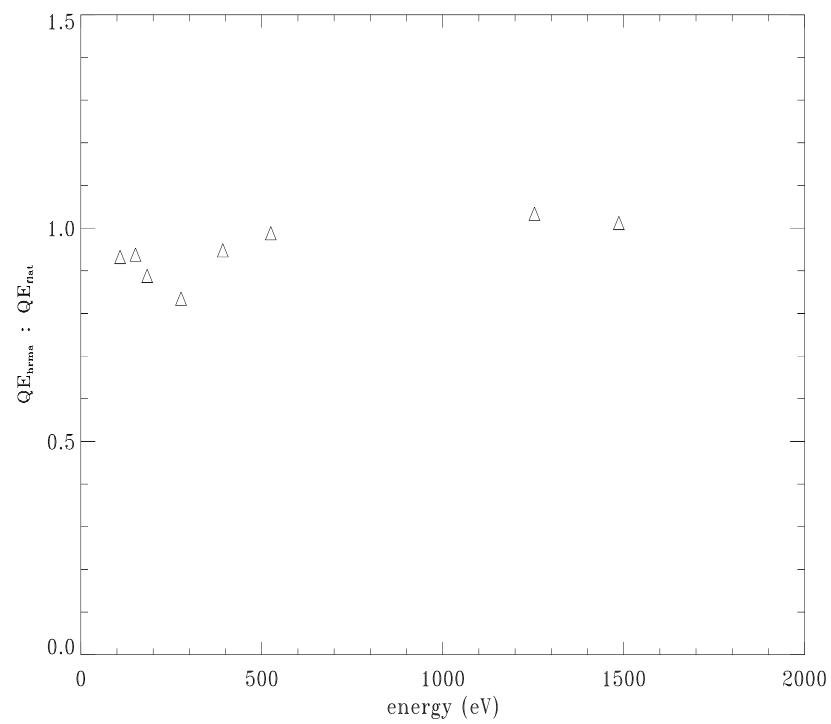

Figure 90: De-rating factors for applying HRC-I flat field data to operation in the converging beam of the HRMA (assuming 4.7° pore bias).

4.6.6 Conclusions and Discussion

Using representative coated MCPs we have measured the relative QE versus x-ray angle of incidence for ~ 10 energies. We have scanned over angles that cover the pertinent AXAF HRMA cone angles. Using this data as representative of the flight detectors, correction factors for flat-field determined QE values to QE values obtained in the converging HRMA beam have been determined.

We have reaffirmed the advantages of using CsI coated MCPs with $6°$ pore angles to optimize the HRMA/HRC Effective Area, however it is quite probable that the flight GEOC MCPs have only $4.7°$ bias angles.

The errors in applying these data are primarily systematic; these data were taken with representative MCPs; not the actual flight items CsI coating thicknesses may be different as well as pore angle. Statistical errors have all been kept $\sim 3\%$ by appropriate integration times.

Table 7: HRC Count Rates

Energy (keV)	HRC-I Rate Range (cts/s)	HRC-S Rate Range (cts/s)
0.277	3.1 – 19.8	0.5 – 19.0
2.560	2.1 – 6.4	0.5 – 5.4
3.500	—	3.7 – 19.3

4.7 HRC (Count Rate Linearity, Spatial Linearity, Detector Geometry)

4.7.1 Point Source Count Rate Linearity

The point source count rate linearity (CRL) of the HRC characterizes the response of the detector microchannel plates (MCPs) as a function of incident flux for a focused pont source. When a photon is absorbed by a pore in an MCP, producing a cascade of electrons, the charge available for re-establishing the electric field in the pore is temporarily reduced. If the interval between photon absorptions in a given pore is shorter than the charge replenishment time, the electric field will not be completely re-established leading to a temporary, localized reduction in the gain. This in turn may lead to a reduction in the quantum efficiency, if the the amount of charge detected from an event falls below the Lower Level Discriminator (LLD) cut off.

For most normal operating conditions (flux $<$ 2 cts/s/pore, or 5 cts/s in the focussed beam of AXAF), we expect the response of the detector to be linear requiring no correction. However, there remains the possibility via either serendipitous detections or transient phenomena that the normal operation limitation (5 cts/s) may be violated. This section presents three analyses of the data collected at the XRCF for both the imaging and spectroscopic detectors (HRC-I and HRC-S).

Setup and Procedure

At the X-Ray Calibration Facility (XRCF), CRL tests were performed by placing the HRC-I and HRC-S stationary at the focus of the HRMA (ie. no dithering). The CRL of both detectors was measured at energies of 0.277 keV using the Electron Impact Point Source(EIPS) with a carbon anode, and 2.56 keV using the Double Crystal Monochromator(DCM). Supplemental data for the HRC-S were also taken with the DCM at 3.5 keV. The incident source fluxes were monitored by four Flow Proportional Counters located around the perimeter of AXAF's High Resolution Mirror Assembly (HRMA) as Beam Normalization Detectors (BND-H's). Since the response of the BND-H's are linear throughout the count rate regime of these tests, the measure of CRL is performed by directly comparing the HRC count rate versus the BND-H count rates. The range of rates obtained for the HRC-I and -S are outlined in Table 7.

The Data

The raw BND-H data were reduced to spectral line (ie. energy) count rates using the JMKMOD in XSPEC. The data were corrected for non-uniformities in the X-ray beam, using data supplied by John Everett (for the EIPS) and by Project Science (for the DCM). The effects of the beam uniformity corrections are quite noticeable. Figures 91 and 92 show the data for the HRC-S at 0.277 keV before and after the correction was made. At this time, the BND-H's have not been calibrated absolutely. Thus, there still exist intrinsic variations among the four BND-H's. By first correcting for beam non-uniformities and then taking an 'Average BND-H', we are able to compensate for the small remaining variations and improve the overall signal-to-noise ratio of the BND-H count rates. We note that even with the application of the beam uniformity corrections and the calculation of an average BND-H, the errors in the BND-H data remain rather large, $\sim 5 - 10\%$.

The HRC count rates were calculated from the total counts within a 40 pixel radius and corrected for the live

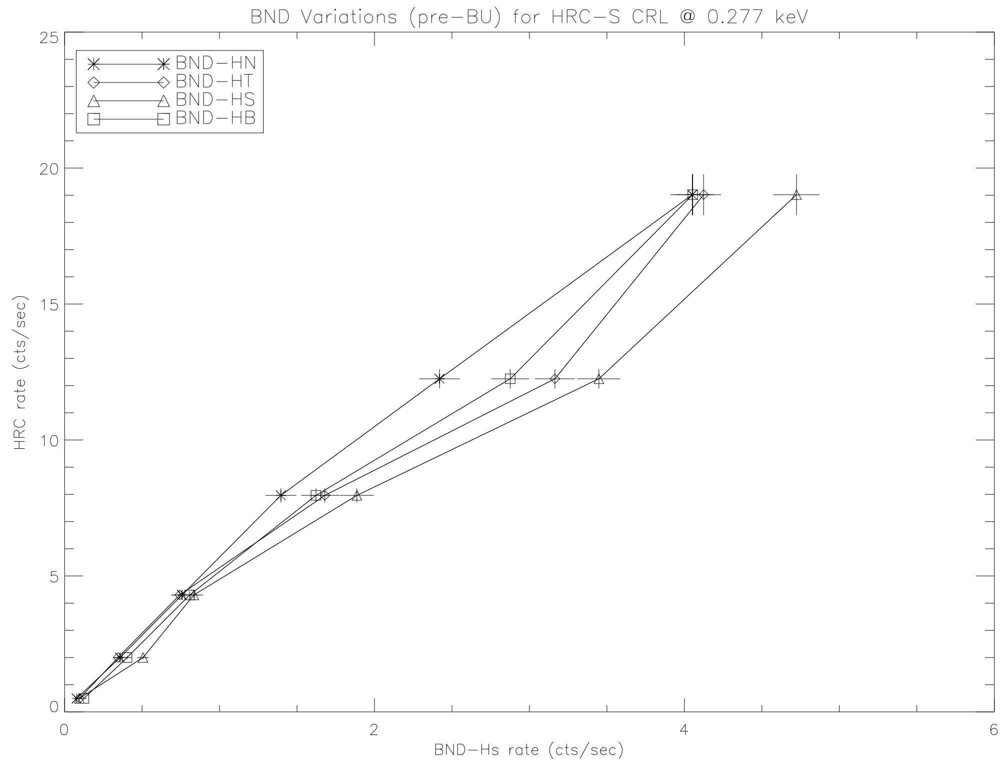

Figure 91: An example of the variations among the 4 BND-Hs. These plots show the HRC-S CRL at 0.277 keV as seen by all 4 BND-Hs before and after the application of the beam uniformity data. Note that the North and Top detectors show extremely good agreement. (pre-BU)

time of the test. We did *not* remove a background for the HRC, however we expect that the total contribution from this source to be negligible ($0.04\ cts/s/cm^2 \times 0.0021\ cm^2 = 8.31 \times 10^{-5}\ cts/s$).

While the BND-H data (after fitting) represent only the data in the line, the HRC count rate includes response from any continuum photons present as well as those in the line of interest. Although the data taken using the DCM had no continuum component, we estimate that the continuum contribution for the EIPS source at 0.277 keV was $\sim 40\%$.

Although this is a significant component of the source count rate, we note two important characteristics about the EIPS continuum. First, for the case of the Carbon anode at 0.277 keV, the continuum extends only from the energy of the line up to $\sim 4\times$ the line energy (i.e. 1.108 keV) which is the source voltage. Second because both line and continuum flux are determined by the current applied to the anode, the continuum flux should also increase proportionately to the line flux. Thus we are actually characterizing the CRL response in a band from slightly below 0.277 to 1.108 keV with an emphasis on the flux at 0.277 keV.

We also note that there is some uncertainty in the amount of background in the FPC's. Nominally, the total background over all of the channels should be ~ 0.5 cts/s, and thus any error in the global background determination should be relatively small.

We present the total count rate in HRC compared with the average, beam uniformity corrected, count rate in the line only from the BND-H's. A complete compilation of the data is found in Figure 93. The data are available in an RDB table located at:

/data/aschrc5/pease/hrc_tex/CRL/data/hrc_crl_rates.rdb

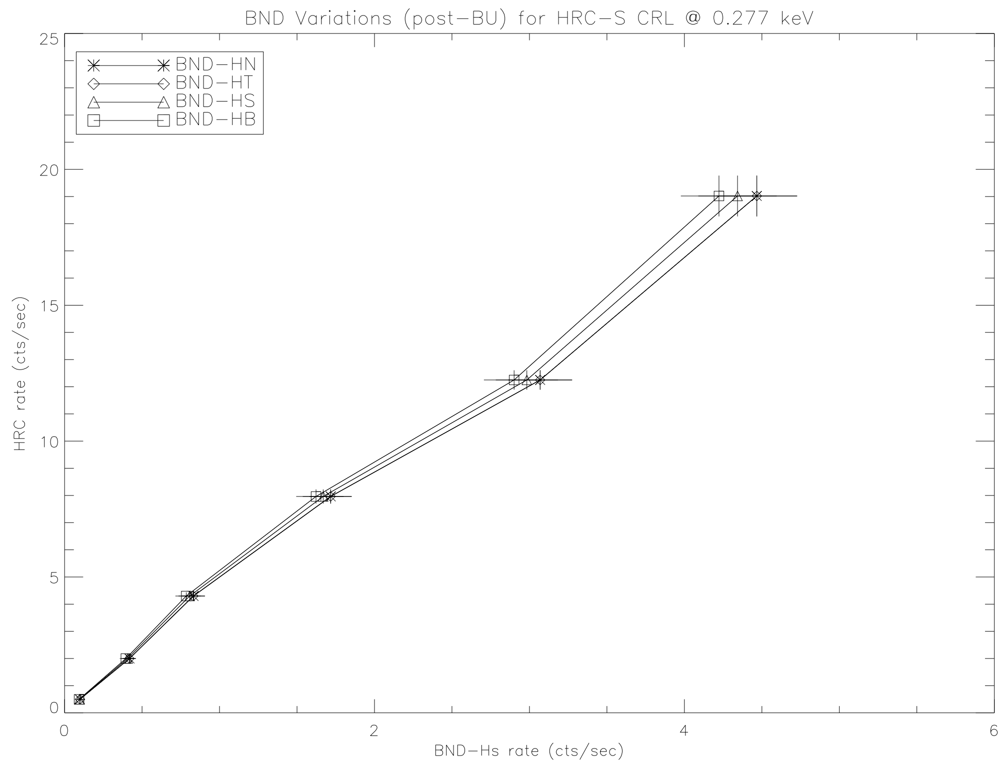

Figure 92: An example of the variations among the 4 BND-Hs. These plots show the HRC-S CRL at 0.277 keV as seen by all 4 BND-Hs before and after the application of the beam uniformity data. Note that the North and Top detectors show extremely good agreement. (post-BU)

Table 2: The HRC Count Rate Linearity Data

Test ID	Energy	HRC						BND-H	
		Total Rate	Error	Core Rate	Error	Annulus Rate	Error	Rate	Error
	(keV)	cts s^{-1}	cts s^{-1}	cts s^{-1}	cts s^{-1}	cts s^{-1}	cts s^{-1}	cts s^{-1}	cts s^{-1}
G-IHI-CR-4.003	0.277	3.113	0.1152	1.093	0.0697	1.442	0.0795	0.389	0.0458
G-IHI-CR-4.005	0.277	4.892	0.1620	1.547	0.0926	2.355	0.1133	0.931	0.0825
G-IHI-CR-4.007	0.277	9.191	0.2106	3.027	0.1212	4.138	0.1413	1.973	0.1329
G-IHI-CR-4.009	0.277	13.716	0.4566	4.321	0.2493	6.222	0.2997	3.214	0.2168
G-IHI-CR-4.011	0.277	19.754	0.6692	5.738	0.3368	9.475	0.4392	5.433	0.3419
G-IHI-CR-2.003a	2.560	2.153	0.0621	0.511	0.0311	1.185	0.0465	0.735	0.0559
G-IHI-CR-2.005a	2.560	4.034	0.0903	1.005	0.0459	2.187	0.0669	1.587	0.1016
G-IHI-CR-2.007a	2.560	6.424	0.1972	1.653	0.1017	3.256	0.1409	2.656	0.1875
G-IHS-CR-4.002	0.277	0.496	0.0294	0.134	0.0161	0.259	0.0217	0.097	0.0150
G-IHS-CR-4.004	0.277	1.998	0.0646	0.441	0.0314	1.168	0.0498	0.410	0.0406
G-IHS-CR-4.006	0.277	4.300	0.1336	1.119	0.0697	2.292	0.0982	0.813	0.0727
G-IHS-CR-4.008	0.277	7.962	0.2605	2.136	0.1359	4.121	0.1870	1.681	0.1328
G-IHS-CR-4.010	0.277	12.250	0.3571	2.964	0.1738	6.679	0.2602	3.005	0.2019
G-IHS-CR-4.012	0.277	19.020	0.7520	4.571	0.3394	9.898	0.5117	4.375	0.2549
G-IHS-CR-1.004	2.560	0.455	0.0152	0.111	0.0078	0.236	0.0111	0.192	0.0175
G-IHS-CR-2.004	2.560	1.905	0.0600	0.548	0.0330	0.981	0.0435	0.918	0.0648
G-IHS-CR-2.006	2.560	5.397	0.1413	1.267	0.0698	3.032	0.1063	2.736	0.1618
G-IHS-CR-99.062	3.500	3.698	0.1106	0.673	0.0488	1.948	0.0809	3.184	0.2108
G-IHS-CR-99.063	3.500	7.318	0.2346	1.777	0.1171	4.811	0.1899	6.408	0.3969
G-IHS-CR-99.064	3.500	19.292	0.4202	3.292	0.1689	11.462	0.3172	17.819	0.9733

Figure 93: HRC count rate linearity data

Analysis

Comparison of Total Rates

The most direct method for investigating the CRL is a simple comparison of the total HRC count rates with the BND count rates (see Figures 95 through 97). We have attempted linear fits for all of the data sets and find excellent agreement with the data except for the highest count rate ($\sim$ 20 cts/s in the HRC-I) test performed at 0.277 keV. Excluding this data point significantly improved the quality of this particular fit. The fit results are shown as dotted lines on the plots, with solid lines connecting the data from point-to-point for comparison. The HRC-I shows a departure from non-linearity at the highest counting rate, while the HRC-S shows no evidence of non-linearity even at the highest rates ($\sim$ 20 cts/s).

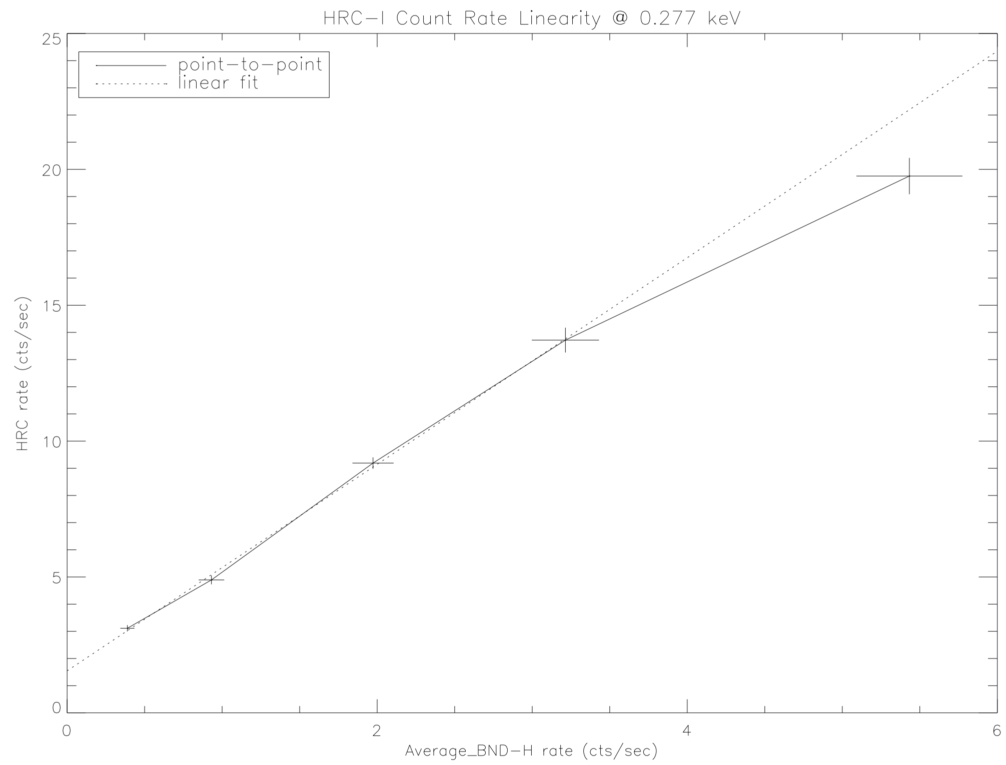

Figure 94: HRC-I count rate versus BND-H count rate (0.277 keV). Solid lines are point-to-point; dotted lines represent linear model fits. Departure from linearity is apparent only at the highest rate.

We note that while the relative placement of the data is correct, because of the effects mentioned above (HRC and FPC backgrounds, Continuum Contributions) the *absolute* placement is not. In other words, including one of the above effects would move the ensemble of points along one axis or the other, but would not affect the linear (or non-linear) nature of their relation. For this reason we have not forced the fits through the origin. In most cases (e.g. the DCM fits) the offset is small indicating that any potential effect is small.

Gain Depression

Electron emission from the walls of the of the microchannel plate pores results in a temporary depletion of charge. The charge depletion manifests itself as temporary local depression in the gain of the detector. In turn, the lowered gain causes the Pulse Height Amplitude (PHA) distribution of events to shift to lower PHA channels.

In the absence of any other effects, a higher incident photon rate will cause a larger gain depression and thus a

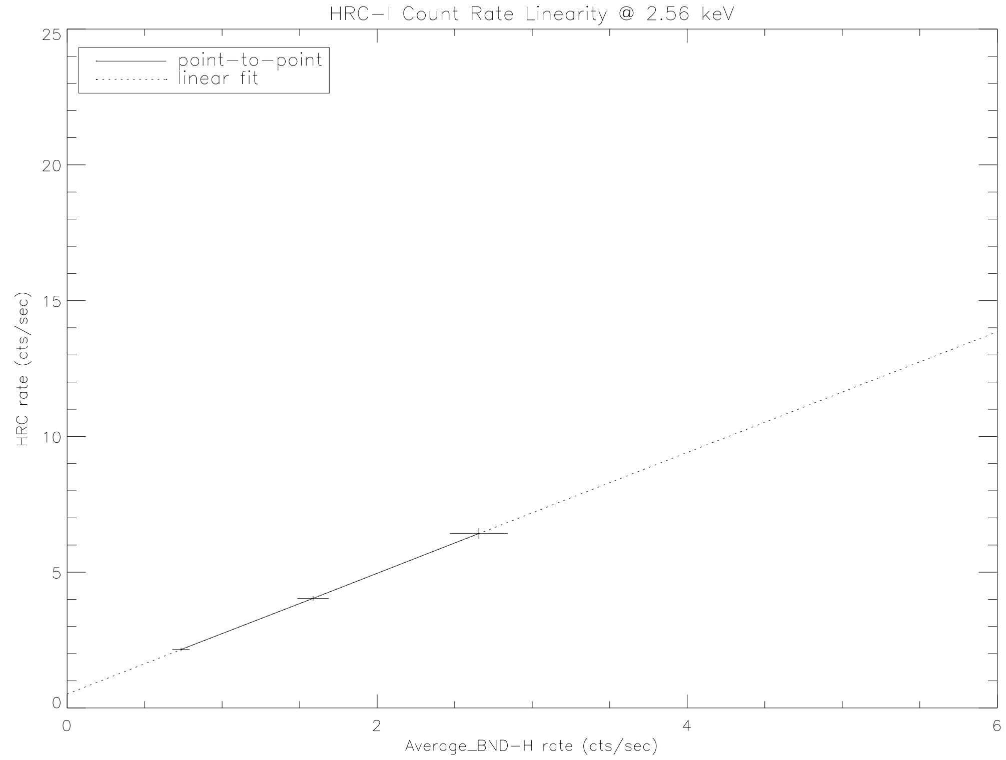

Figure 95: HRC-I count rate versus BND-H count rate (2.56 keV). Solid lines are point-to-point; dotted lines represent linear model fits.

larger shifting of the PHA distribution. However, the HRC is equipped with a Lower Level Discriminator (LLD) which rejects events below a set PHA channel. This is used to reduce/eliminate the noise that would otherwise be detected from the amplifiers. Count rate non-linearity occurs when, due to the temporarily depressed gain, real events fall below the LLD and are rejected.

For the PHA distribution from each CRL test, we fit a completely empirical function consisting of a 'large x' approximation Poisson function plus a Gaussian function of the form:

$$f_\mu(x) = A\left(e^{-(x-\mu)^2/2\mu} + Be^{-(x-\mu+C)^2/2\sigma^2}\right) \tag{45}$$

to the data. The 'shape' of the distribution – defined by σ, the Gaussian width, and C, the constant difference between the Poisson mean and the Gaussian mean – were fixed. This left a single parameter, μ, describing the "aggregate" location of the fit. Figures 98 and 99 show typical examples of our fits to the PHA.

We expect in the linear regime, as μ declines, that the shape of the PHA distribution will remain constant. When non-linearity occurs, i.e. the PHA distribution encounters the LLD, the quality of fit should degrade while the behavior of μ is uncertain, perhaps remaining relatively constant. Figure 100 shows the comparison of the fit, μ, versus the HRC rate for the 0.277 keV data with the HRC-I and HRC-S.

The value of μ for HRC-I declines as the rate increases, remaining constant at rates greater than 10 cts/s. At the same time χ^2 remains constant increasing at the same rate that μ stalls. For the HRC-S the data is less clear, and may indicate that the detector never enters the non-linear regime.

Core-Annulus Analysis

Due to the sharply peaked character of the AXAF Point-Spread-Function (PSF), the inner core region of

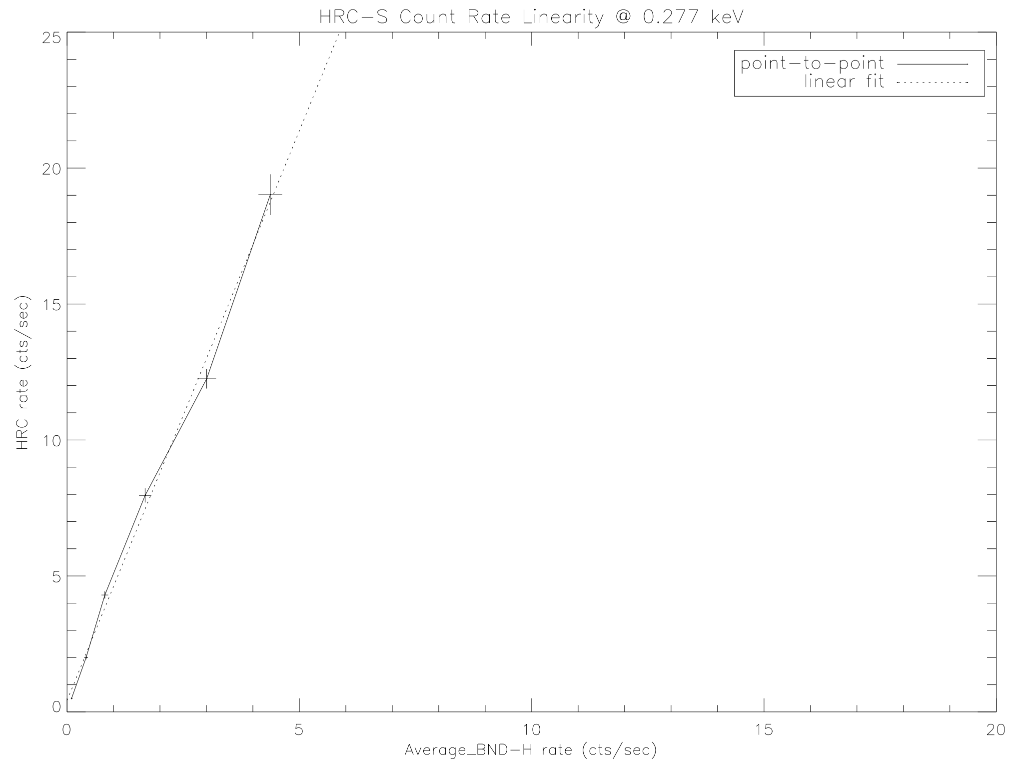

Figure 96: HRC-S count rate versus BND-H count rate at 0.277 keV. Solid lines are point-to-point; dotted lines represent linear model fits.

the X-ray spot in an HRC image has a higher rate of photon incidence per pore than the outer areas. Thus the charge depletion in the core region is greater than that in the wings. From this, we expect that the core may be a more sensitive indicator of non-linearity than the complete image.

The expected FWHM of the AXAF PSF is $\sim$ 0.5 arcsec, or $\sim$ 3.9 HRC pixels. The HRC has an intrinsic resolution element of $\sim 20\mu \simeq 3$ pixels. We defined the core region radius to be 3 pixels, thus including approximately 4 resolution elements. Smaller radii were rejected due to the poor statistics resulting from the low count rate. The annulus region was defined with an inner radius of 3 pixels and an outer radius of 8 pixels. This gives a reasonable representation for most of the counts in the PSF. Figure 102 shows an example of the focused count rate linearity image with core and annulus regions indicated.

To facilitate comparison of the core and the annulus CRLs, the core data were normalized to the annulus data at the lowest count rate, as we expect the lowest rate to always fall within the linear regime of the detectors.

We find that, unlike the comparisons of the total count rates, at rates above 10 cts/s the core regions do appear to show noticeable divergences compared to the annuli (see Figures 104 through 107).

Results

We expect the counting behavior of the HRC (both I and S) to be linear for all normal operating conditions ($<$ 5 cts/s). In fact even for serendipitous or accidental exposures to rates as high as 10 cts/s we expect that the detector response is linear.

Above these rates the significance of the departures from linearity is mixed. The total rate analysis for the HRC-I clearly demonstrates count rate non-linearity at the XRCF at rates above $\sim$ 14 cts/s. The PHA fitting and Core-Annulus analyses suggest that the transition to non-linearity may begin at rates as low as 10 cts/s.

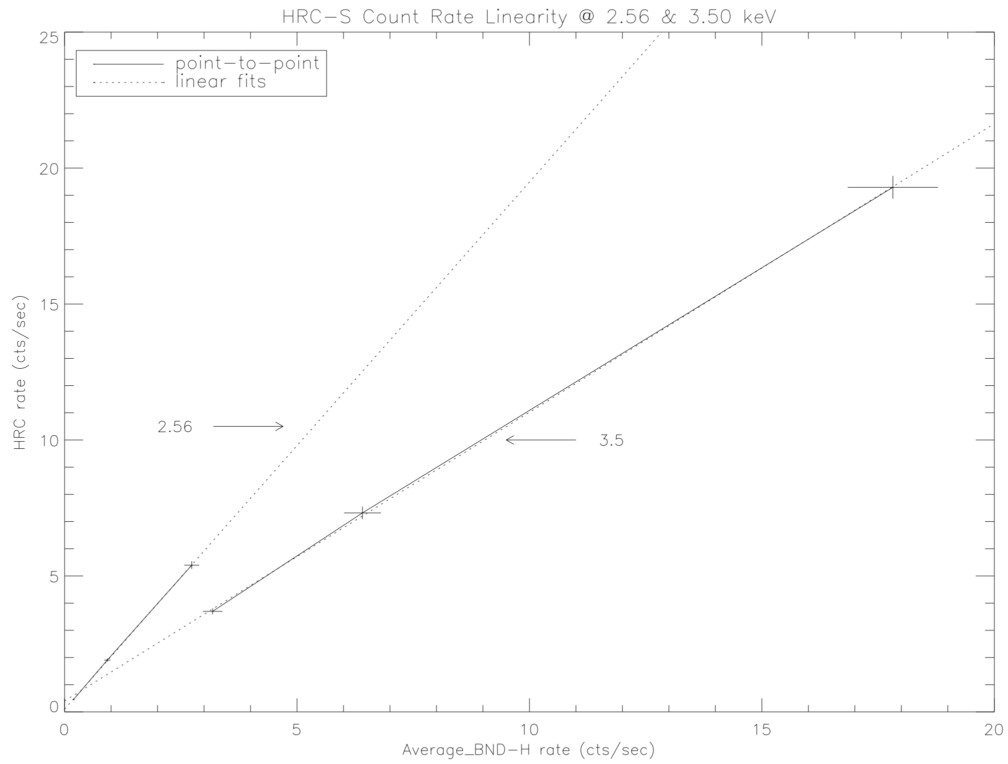

Figure 97: HRC-S count rate versus BND-H count rate at 2.56 keV and 3.5 keV. Solid lines are point-to-point; dotted lines represent linear model fits.

For the HRC-S, we find suggestive indications from the core-annulus studies that the HRC-S may also have demonstrated count rate non-linearities at rates above $\sim$ 10 counts/s. This is *not* supported by the total rate analysis, while the PHA fitting analysis is inconclusive. As such the assertion of non-linearity for the HRC-S above 10 cts/s should be considered as tentative.

As a primitive empirical quantization of the HRC-I's behavior we have fit a quadratic function of the form:

$$Rate_{HRC-I} = 1.19 + 4.46 Rate_{BND} - 0.191 Rate^2_{BND} \tag{46}$$

to the three highest rates observed with the EIPS data at 0.277 keV. Figure 108 shows the composite plot of the linear portion (dotted line) with the quadratic model fit (solid line). In a more useful form this becomes

$$True\ Rate_{HRC-I} = 45.91 - (2058.4 - 75.60 \times Obs.\ Rate_{HRC-I})^{\frac{1}{2}}. \tag{47}$$

A correction factor versus observed count rate in the HRC-I is shown in Figure 109. We expect that above $\sim$ 24 cts/s the correction factor becomes *highly* unreliable and is indefinite above 27.2 cts/s, while below 12.2 cts/s we expect linear performance. We emphasize that any use of this correction factor should be done with extreme caution by the user.

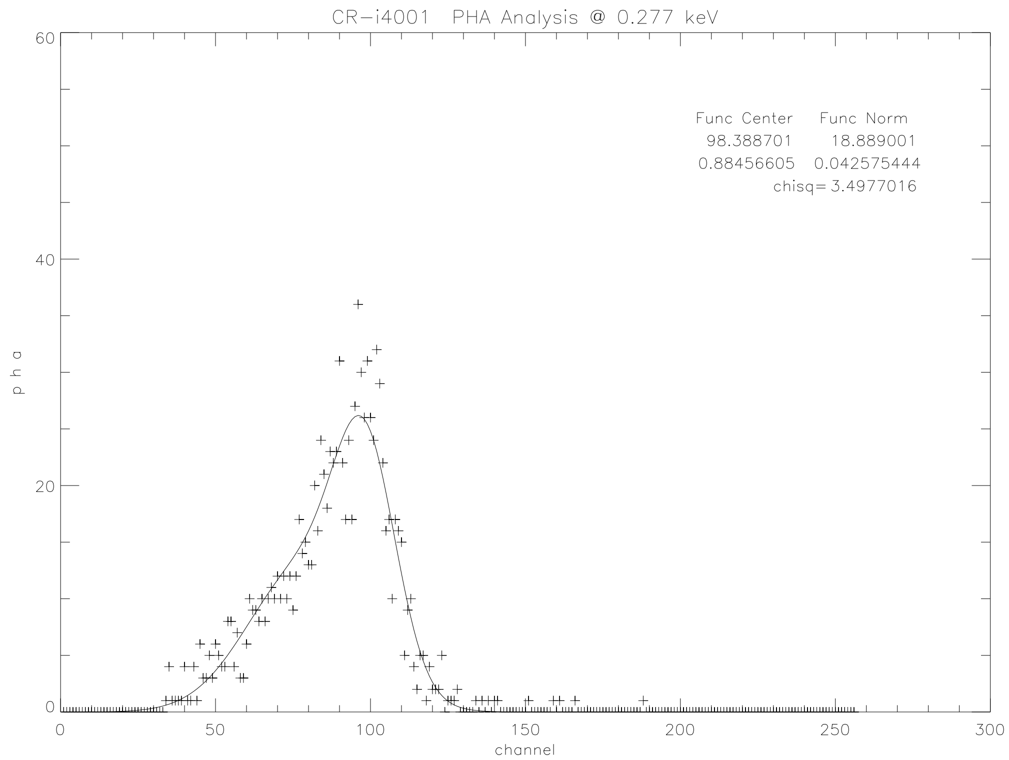

Figure 98: Example of PHA distributions with Poisson+Gaussian function fits; HRC-I 0.277 keV data set. CR-i4001. The Poisson mean μ is used to show the potential shift in the distribution to lower channels as a result of charge depletion on the MCPs.

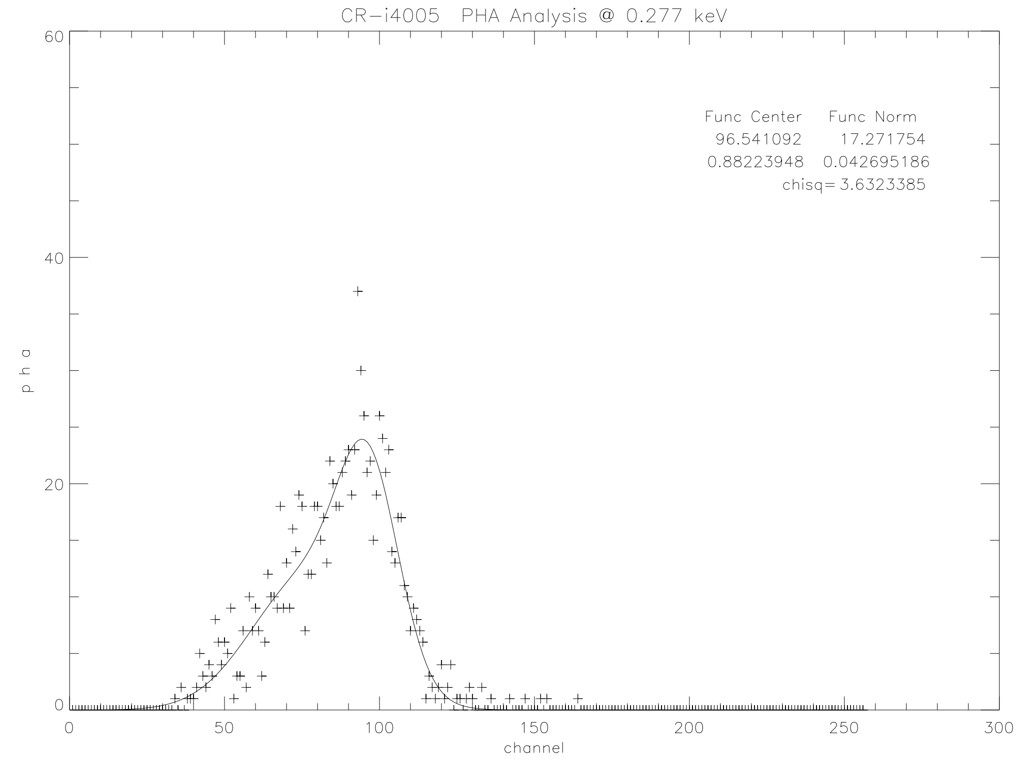

Figure 99: Example of PHA distributions with Poisson+Gaussian function fits; HRC-I 0.277 keV data set. CR-i4005. The Poisson mean μ is used to show the potential shift in the distribution to lower channels as a result of charge depletion on the MCPs.

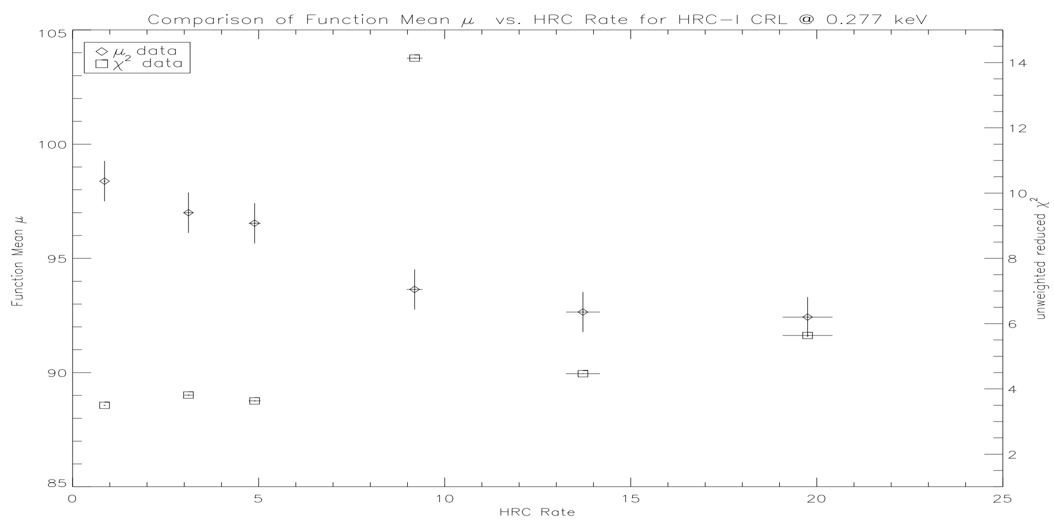

Figure 100: Comparison of the fit function value of μ to the count rate in the HRC-I at 0.277 keV. We expect to see μ decrease as incident rate increases. Also plotted are the χ^2 values for each fit.

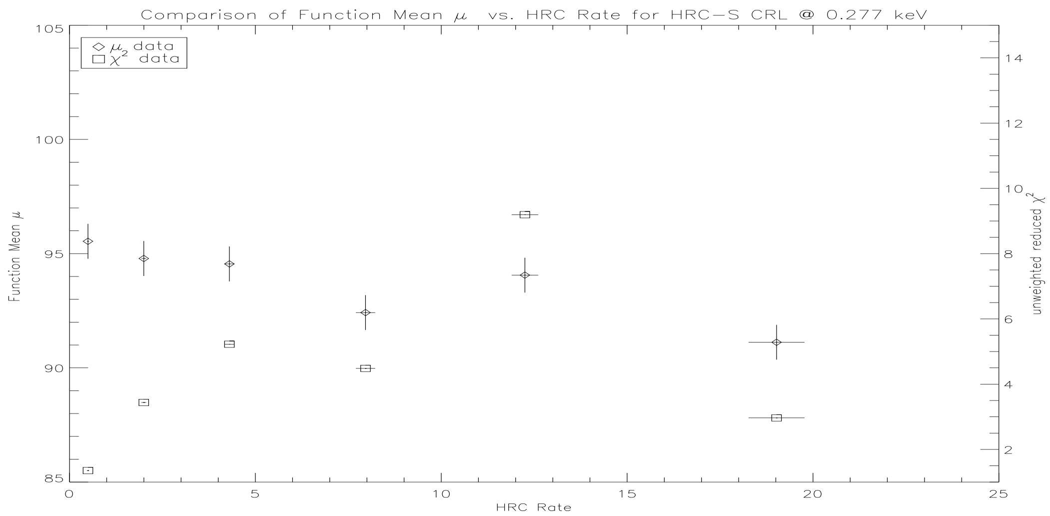

Figure 101: Comparison of the fit function value of μ to the count rate in the HRC-S at 0.277 keV. We expect to see μ decrease as incident rate increases. Also plotted are the χ^2 values for each fit.

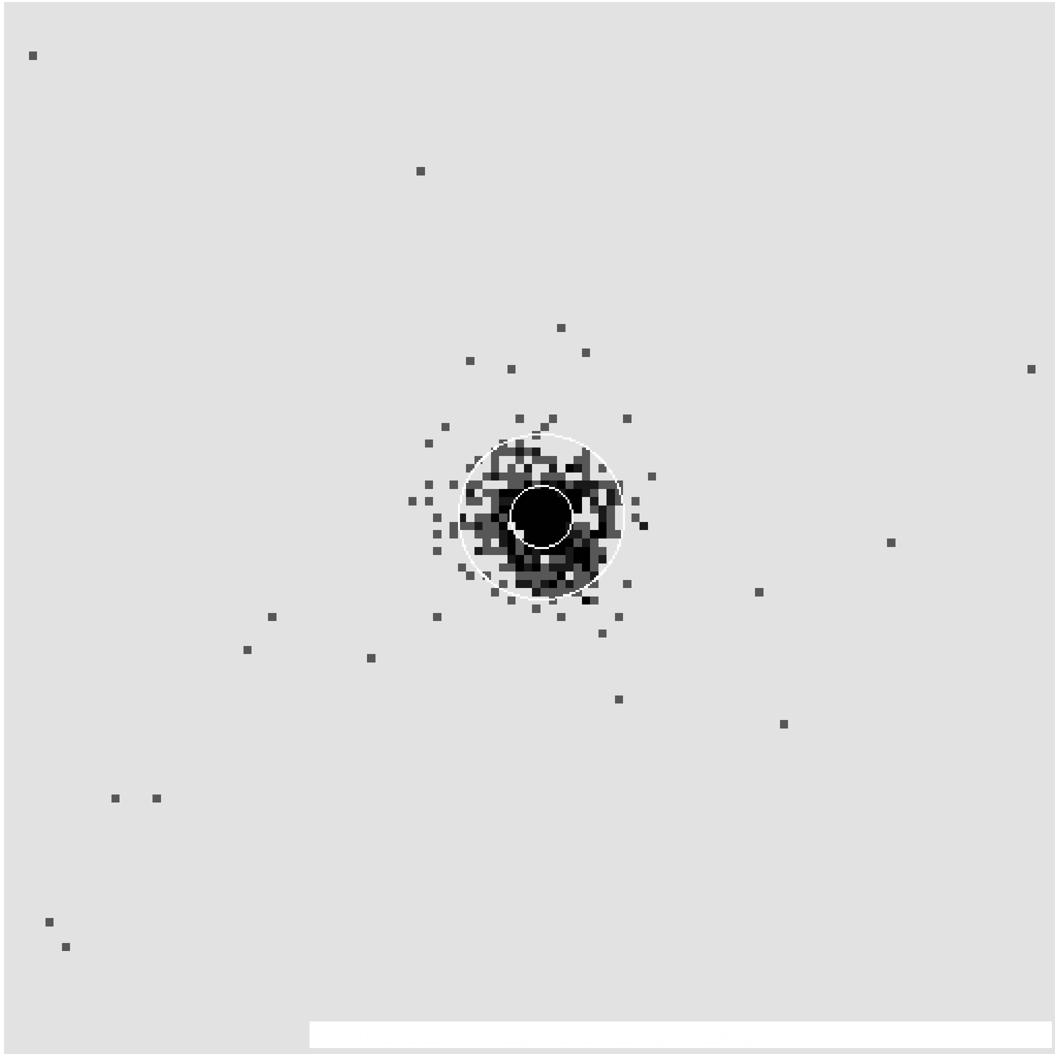

Figure 102: Example of the focussed count rate linearity image with core (r = 3 pixels) and annulus (r_{inner} = 3 pixels, r_{outer} = 8 pixels) regions shown; HRC-I 0.277 keV data set.

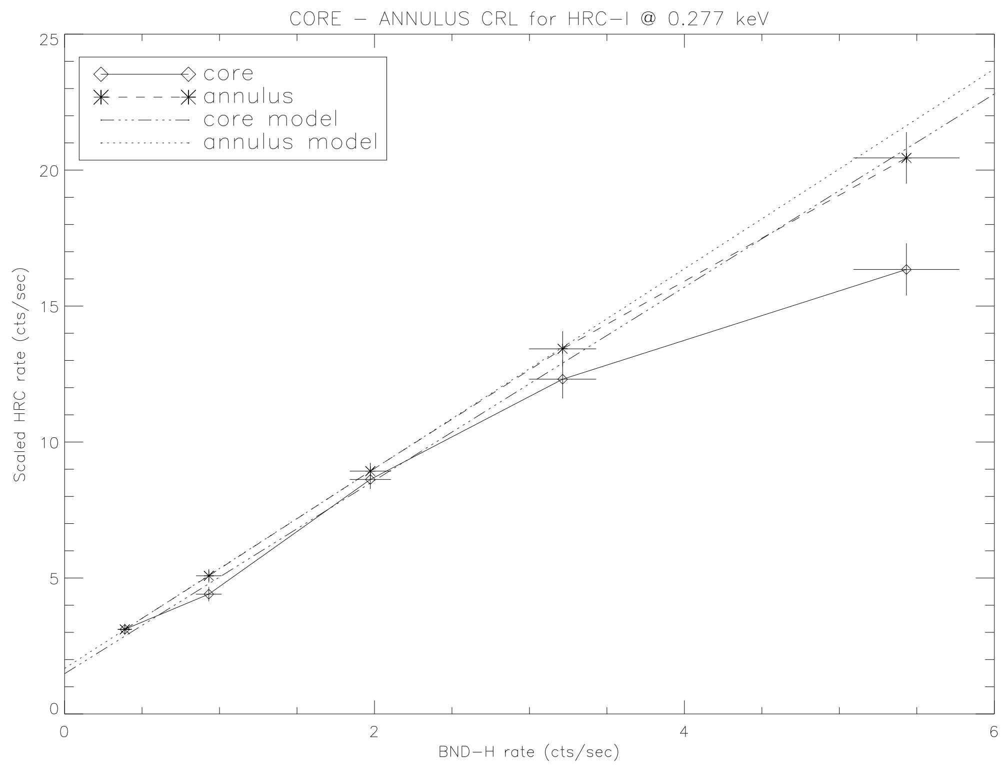

Figure 103: A comparison of the HRC-I count rate linearity in the core region with that in the annulus region at 0.277 keV. Solid lines are point-to-point for the core; dashed lines are point-to-point for the annulus; dash-dot-dot-dot lines are linear model fits to the core data; and dotted lines are linear model fits to the annulus data. Significant non-linearity in the core is apparent.

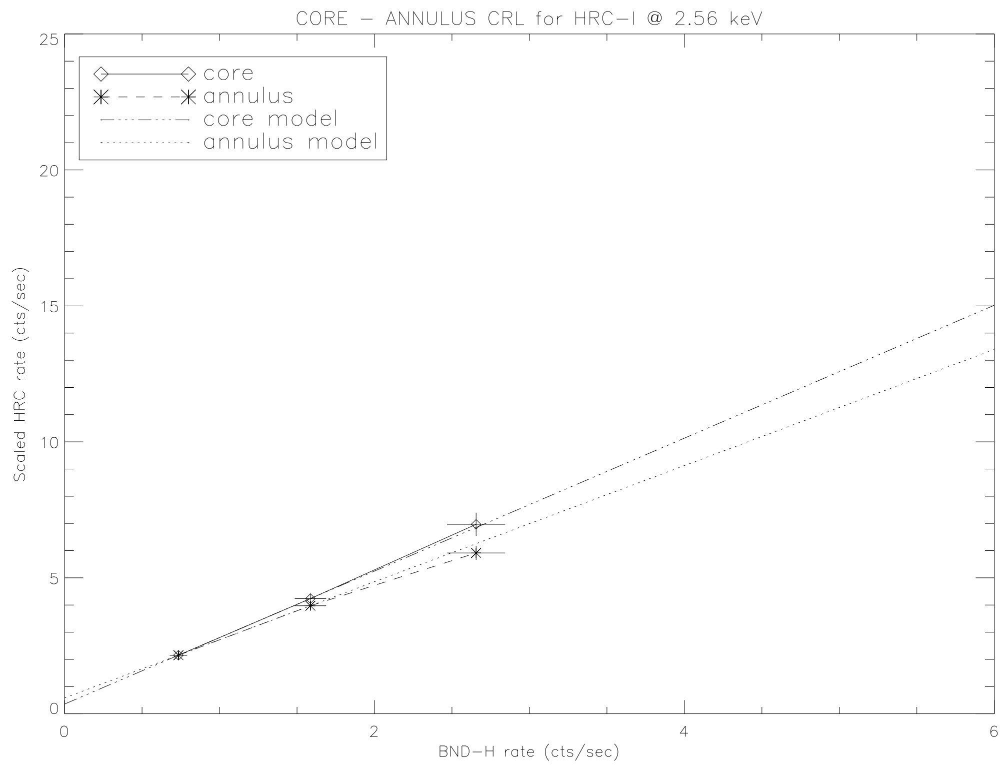

Figure 104: A comparison of the HRC-I count rate linearity in the core region with that in the annulus region at 0.277 keV. Solid lines are point-to-point for the core; dashed lines are point-to-point for the annulus; dash-dot-dot-dot lines are linear model fits to the core data; and dotted lines are linear model fits to the annulus data. Significant non-linearity in the core is apparent.

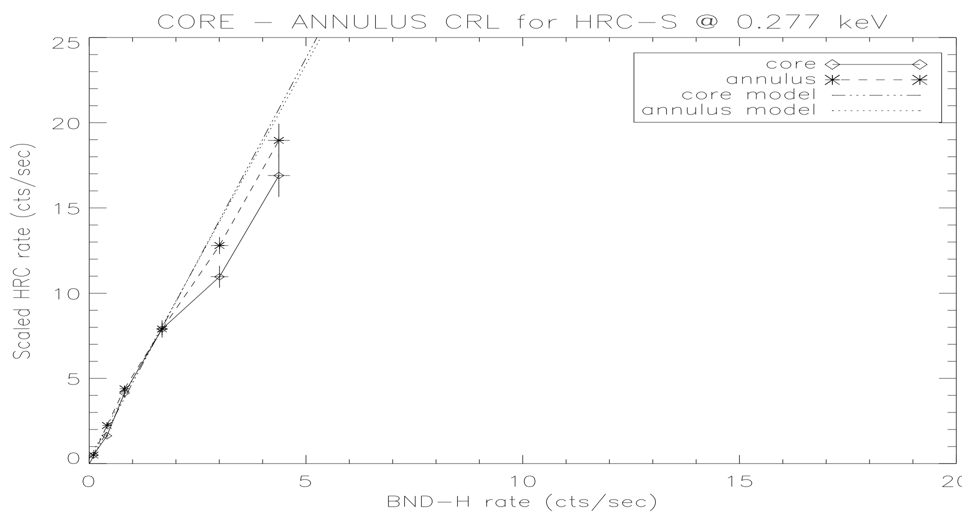

Figure 105: A comparison of the HRC-S count rate linearity in the core region with that in the annulus region at 0.277 keV. Solid lines are point-to-point for the core; dashed lines are point-to-point for the annulus; dash-dot-dot-dot lines are linear model fits to the core data; and dotted lines are linear model fits to the annulus data. The data is suggestive of non-linearity in the core.

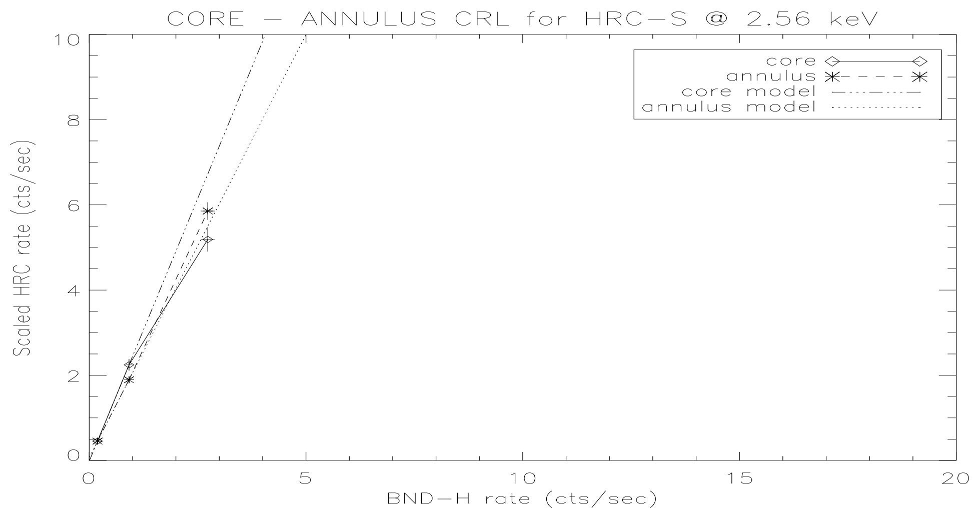

Figure 106: A comparison of the HRC-S count rate linearity in the core region with that in the annulus region at 2.56 keV. Solid lines are point-to-point for the core; dashed lines are point-to-point for the annulus; dash-dot-dot-dot lines are linear model fits to the core data; and dotted lines are linear model fits to the annulus data. Note augmented scale.

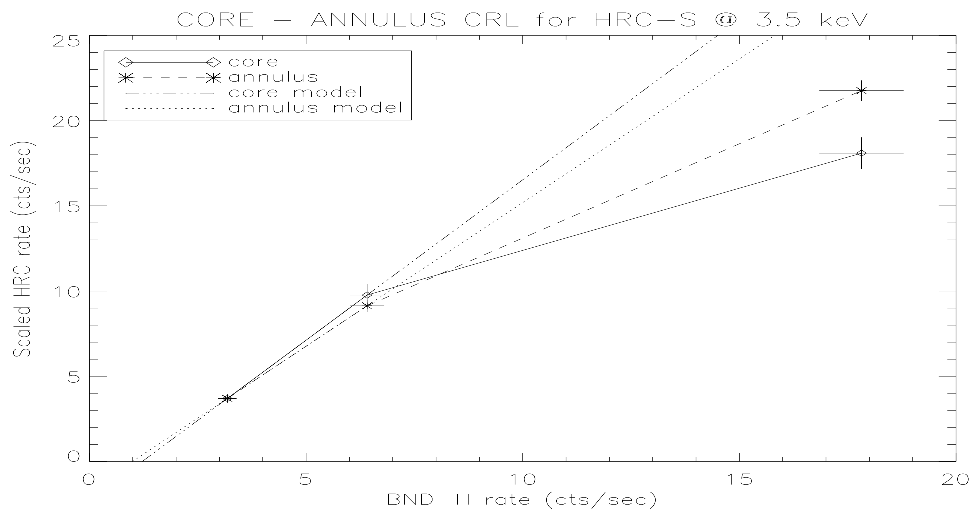

Figure 107: A comparison of the HRC-S count rate linearity in the core region with that in the annulus region at 3.56 keV. Solid lines are point-to-point for the core; dashed lines are point-to-point for the annulus; dash-dot-dot-dot lines are linear model fits to the core data; and dotted lines are linear model fits to the annulus data. The data is suggestive of non-linearity in the core.

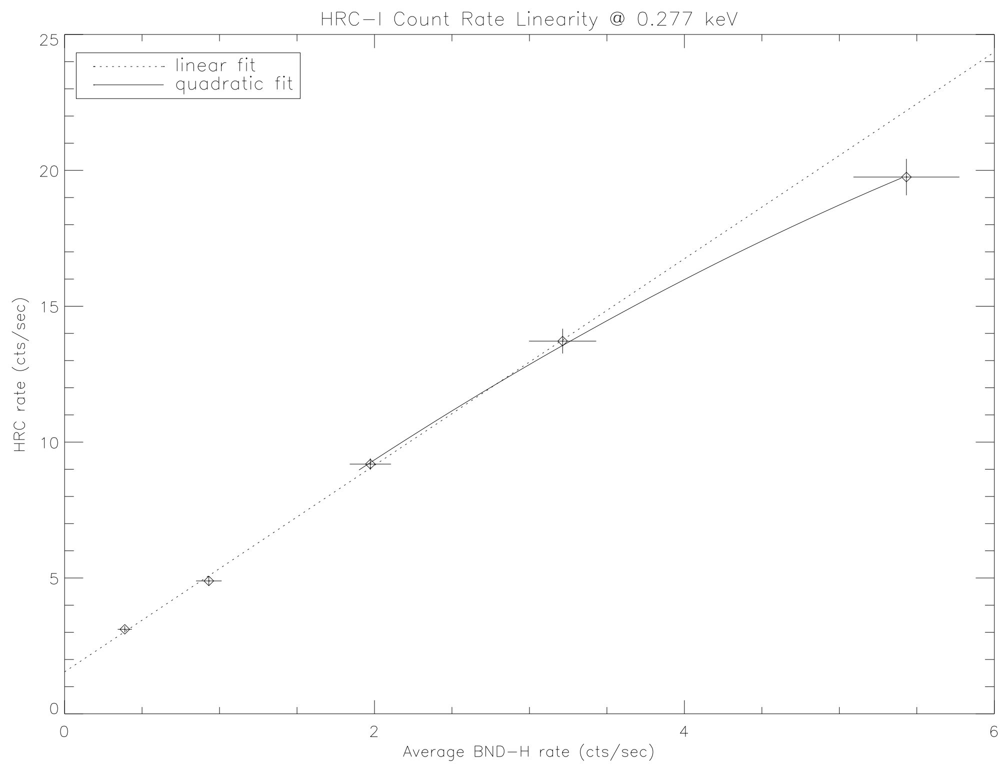

Figure 108: The linear (dotted line) + quadratic (solid line) fit to the HRC-I response to high rates achieved in the 0.277 keV data set. The equation of the quadratic part is $f(x) = 1.19 + 4.46x - 0.191x^2$.

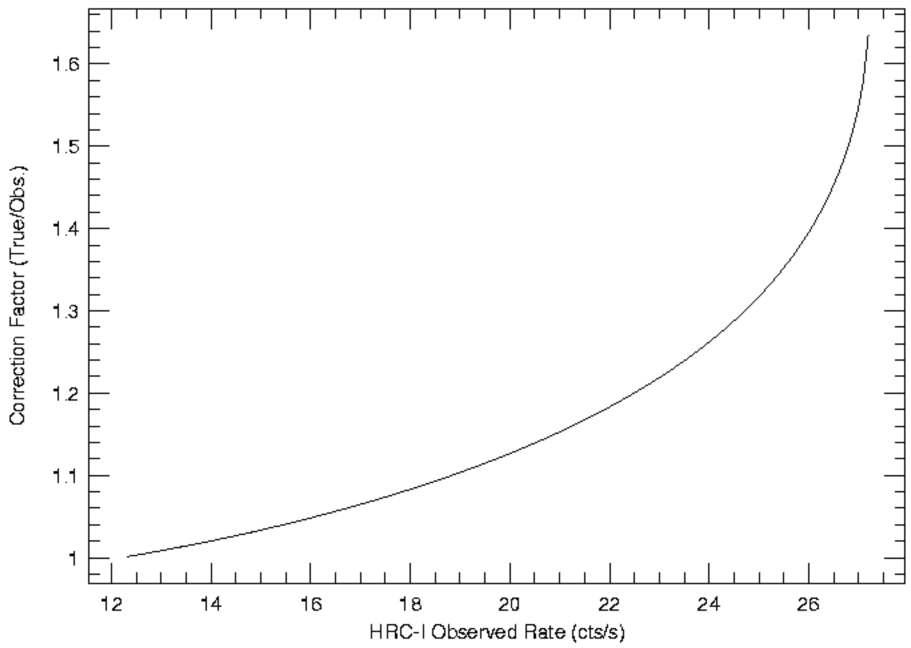

Figure 109: The correction factor to convert from observed count rate in the HRC-I to true incident count rate. Only rates below 27.3 cts/s are shown, as the correction factor becomes meaningless above these rates.

4.7.2 Diffuse Source Count Rate Linearity (Electronic deadtime)

There are two sources of electronic deadtime within the HRC. The first is due to the time the HRC takes to process the information from an event registered by the MCP. The second is telemetry saturation; the AXAF has a limited telemetry bandwidth that results in a maximum allowed number of telemetered events per major frame (32.8 s) for the focal plane science instruments. When the HRC has the observing mode telemetry allocation (24 kbps of serial digital data), the telemetry has 378 "slots" available for event information every 2.05 s, for a mean event rate maximum of ~ 184.39 events s^{-1}. Observations of bright, diffuse sources could exceed this mean rate resulting in a deadtime as events cannot be put into the telemetry stream.

HRC Event Processing

When the HRC MCPs are triggered by an event it is counted and a series of hardware checks are performed to decide whether it should be processed and telemetered to the ground; this takes $\sim 19.5\mu$s. If the event passes these checks it is counted as a valid event and the hardware processing that generates the telemetered event information is usually started. The processing will not occur if the hardware is already processing an event. From the time of the trigger to the time that the event information for telemetry has been generated is 68.5 μs. The HRC hardware is effectively "dead" to event processing during the 19.5 μs interval for the rejected events or the 68.5 μs interval for the accepted events. In simple terms these two times are the deadtime per rejected and accepted events respectively.

The HRC contains a hardware buffer that queues events for output into the telemetry slots. This "primary" science FIFO is large enough to hold the event information for 128 events. If events arrive faster than they can be telemetered, the FIFO will fill. Once it is full the hardware will hold the last event it receives, stop processing, and wait until one event has been removed from the FIFO; at this point it moves the event information it is holding into the FIFO and resumes processing. It is the fact that the hardware stops processing when the FIFO fills that creates the possibility for telemetry saturating deadtime. Even though the "valid" events are not being processed, they are still being counted.

Simulation Description

In an effort to understand the HRC performance at sustained rates near telemetry saturation, we have written a set of software tools that simulates the process. The simulation operates in a series of steps.

The simulation starts with the generation of event times; a Poissonian process is simulated by generating a sequence of times with an exponential distribution of times between events. The mean event rate is controlled by the mean of the exponential distribution. These event times are piped to a tool that determines where the times occur relative to the telemetry major frames and minor frames. Additional information that can be used for other simulation purposes are also generated.

The event time information is then passed on to a tool that simulates how the HRC hardware processing works. All events are assumed to have passed the hardware tests, i.e. they are considered to be "valid" events. An event time is compared to the previous time to see if it arrived while the hardware was processing that event; if so it is counted as a piled-up event and not put into the FIFO storage space. If the event wasn't piled-up, the event time is compared to the current telemetry time to see if events should be taken from the FIFO.

If the time of the next telemetry slot occurs before the event time the event information is taken from the FIFO storage space and the major frame, minor frame, and event slot within the minor frame in which the event is telemetered is added to it. This process is repeated as many times as necessary, either the time of the slot is after the event time or there are no more events in the FIFO storage space.

If the time of the next telemetry slot is after the event time, the FIFO is checked to see if there is room for an event; if there is the event timing information is put into the FIFO storage space. If the FIFO is full, the event is not put into the FIFO storage space. The time from when the FIFO fills to when the next set of event information is transfered from the FIFO storage space to a telemetry slot is accumulated. At the end of the

Table 8: Telemetry Saturation Simulations — 1000 s exposures

	Number of Events				Time
Mean Rate	Total Valid	Telemetered	Piled-up	FIFO-full	FIFO-Full
10	10016	10007	9	0	0.000
100	100090	99422	668	0	0.000
150	150250	148721	1529	0	0.000
180	180233	177996	2237	0	0.000
185	185284	182857	2365	62	0.403
190	190312	184493	2501	3318	18.065
195	195317	184489	2636	8192	43.714
200	200346	184514	2788	13044	67.718
210	210412	184511	3090	22811	112.388
220	220362	184515	3385	32462	152.731
230	230257	184514	3694	42049	188.999
240	240361	184511	4030	51820	223.909
250	250327	184515	4354	61458	254.340
260	260596	184515	4679	71402	283.804
270	270627	184516	5062	81049	311.018
280	280634	184516	5413	90705	336.072
290	290517	184515	5795	100207	358.590
300	300579	184516	6195	109868	381.057

simulation the total time spent with the FIFO full is reported along with the total number of events input, the number of telemetered events, the number of piled-up events, and the number of events that occurred while the FIFO was full.

The tools and a README file describing their use are in `/data/juda1/juda/asc/hrc/code/timing/new`.

Simulation Results

Simulator runs where performed for a range of mean event rates up to 300 events s^{-1}. Each simulation was run for an exposure of 1000 s. Table 8 contains the summary results from several simulation runs. As expected, the time spent with the FIFO full is zero until the mean rate is higher than the telemetry saturation rate. For rates above the telemetry saturation rate the deadtime increases rapidly with event rate. The deadtime fraction is plotted as a function of mean input rate in Figure 110.

In addition to the information from the events, the HRC telemeters the total event rate (total triggers of the MCP in 1 s intervals) and the valid event rate (those triggers that pass the hardware tests). We can use these to derive the instrument deadtime.

At rates below telemetry saturation, the deadtime t_d for a selected interval is given by:

$$t_d = t_1 N_{total}(1 - \frac{N_{valid} - N_{telem}}{N_{valid}}) + t_2 N_{telem}, \tag{48}$$

where t_1 is the time for the hardware checks (19.5 μs), t_2 is the time to complete the event information processing (49 μs), N_{total} is the number of events that triggered the MCPs, N_{valid} is the number of events that passed the hardware tests, and N_{telem} is the number of events that was telemetered.

At rates above telemetry saturation a simple approximation to the deadtime is given by

$$t_d = T \frac{N_{valid} - N_{telem}}{N_{valid}} \tag{49}$$

where T is the duration of the interval. Note that this is just the fraction of the events that were acceptable for processing and inclusion in telemetry but which didn't make it. This approximation is plotted as a dashed line in figure 1; it provides a reasonably close match ($< 2\%$ different) to the simulation result near the point of telemetry saturation.

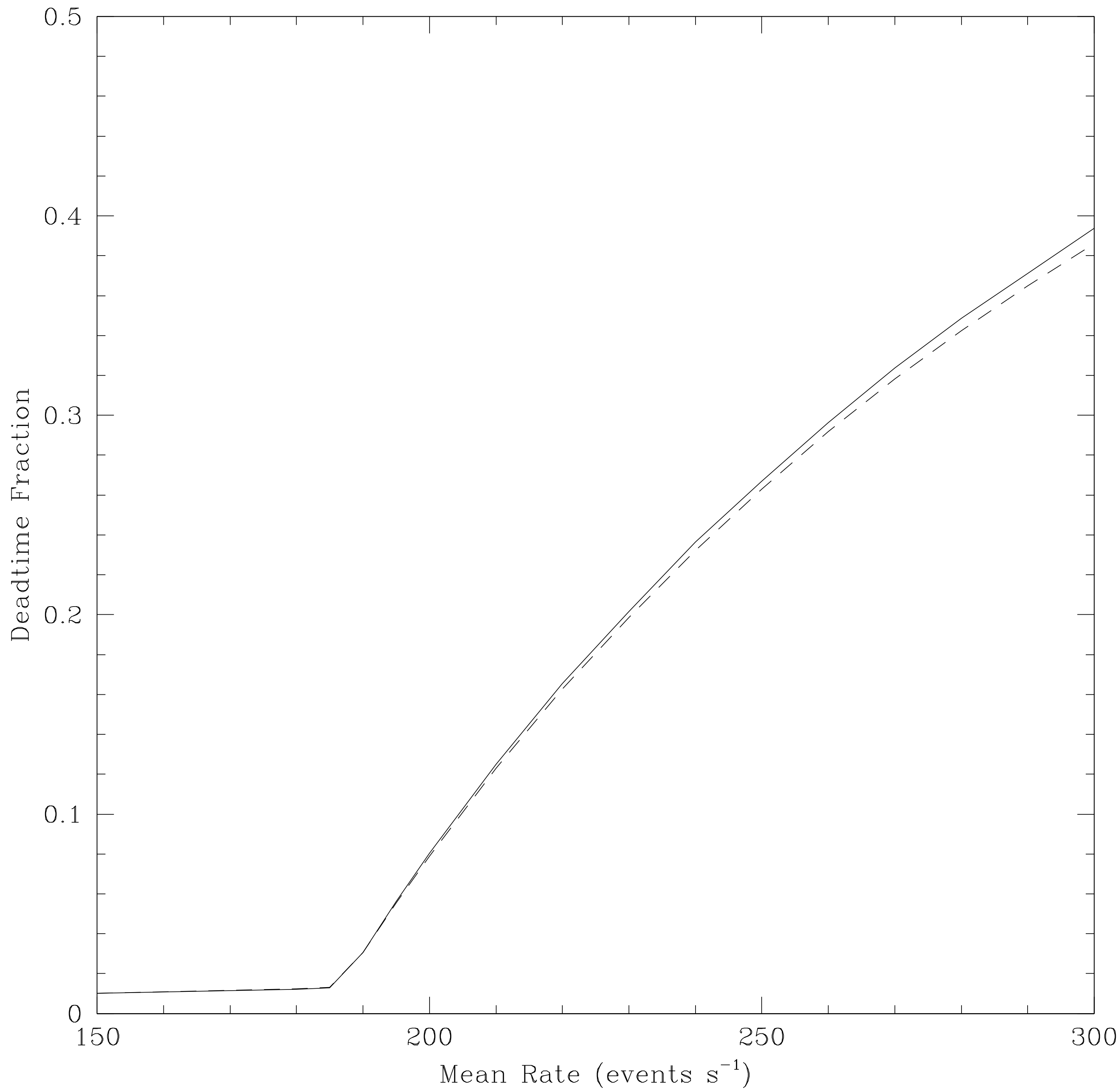

Figure 110: Deadtime fraction as a function of mean input event rate. The solid line is the result of the simulations. The dashed line is an approximation given by the fraction of the total number input that were not telemetered.

4.7.3 Spatial Linearity

HRC-I Linearity

TBS

HRC-S Linearity

TBS

LETG/HRC-S Linearity

We have carried out an analysis of the XRCF data set LHS-FC-1.002 to determine whether there are any unexpected non-linearities or geometrical distortions of the HRC-S. The processing was carried out using the standard HRC data system *HUTDAS* HRC UNIX Tools Data Analysis System , modified to support the larger size of the full HRC-S. When properly analyzed, these data indicate no anomalies or non-linearities in the HRC-S when used as a readout for the LETG. Discontinuities in the HRC-S V-axis coordinate readout (which occur at the segment boundaries) must be taken into account in the analysis.

The HRC EGSE data file corresponding to the TRW Test ID LHS-FC-1.002 is s0910430.rd, indicating an HRC-S data file taken on day 091 (at XRCF) beginning at about 04hr 30min GMT. This file was obtained from the standard HRC XRCF data archive. Since this was a test with the FAM operating in dither mode, the corresponding FAM data files were also required. These files were obtained from the ASC XRCF data archive.

Since the data were taken in the "pre-fix" state of the HRC-S, We used the PHA averaged de-gap maps for each HRC-S segment, derived from Flat Field testing at SAO by Ralph Kraft, as posted on the HRC WWW page (http://hea-www.harvard.edu/HRC/prefix/prefix.html). These de-gap maps are two dimensional tap-by-tap second order polynomial corrections to the raw fine position determination algorithm. The HRC-S (as well as the HRC-I) is designed so that any de-gapping errors are not cumulative, i.e., the spacing of the taps is set by physical construction of the detectors and the de-gapping only can effect pixels within a tap. Errors in de-gap are usually at the few pixel level regardless of where an event is detected and the difference in processing is most likely not significant.

The FAM dither correction process used for this analysis consists of determining "good time intervals" (gti) during which the FAM was not moving, and selecting only those HRC events that correspond to these times. For each interval, the photon positions are corrected for the FAM location relative to the zero point of the observation. Such details as the FAM scale factor (0.99937) and FAM axes orientation relative to the HRC-S (10.171 arcminutes) are included in the FAM correction. The only "free" parameter is the relative time offset of the FAM and HRC IRIG clock data. For day 091 this has been determined to be about 10 seconds.

Figure 111 shows the FAM dither pattern during the observation time. The serpentine pattern steps most rapidly in the Y-axis and less rapidly in the Z-axis. The dither extent is about 1mm in Y and 0.3mm in Z. The FAM Y-axis is in the direction of the HRC-S V-axis, and the FAM Z-axis is in the opposite direction of the HRC-S U-axis.(Some independent tests suggest that when in dither mode the FAM requires additional settling time between steps, but this was not considered necessary since the added blur is of order a single HRC pixel, and the loss of data would have been about 50%.) The FAM good time interval file is derived from the FAM readout data that spans the same time as the HRC data.

Included for completeness are the series of processing steps used to obtain the data products used for analysis.

We are interested in determining the locations of the Mg-K_α peak (at about 1.2536 keV) for the various orders that are detected in this test. Thus the strip of data along the dispersion direction was selected for further analysis. The original data file included about 250,000 events. About half of these are rejected as being detected while the FAM indicated it was in motion. Of these good time interval events, about 108,000 were included in the selected strip of data.

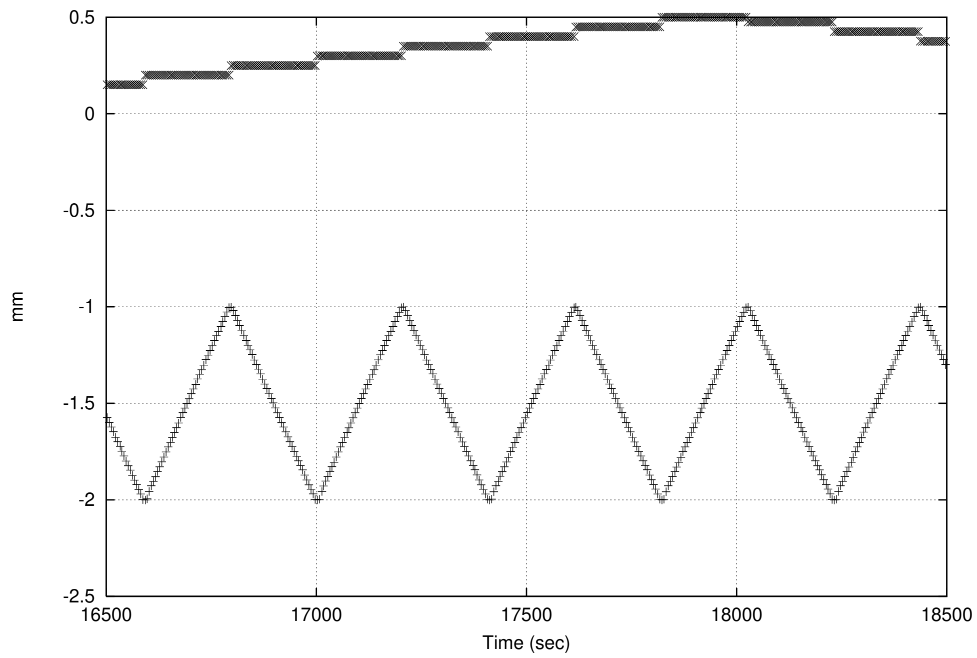

Figure 111: FAM Serpentine dither pattern during the observation

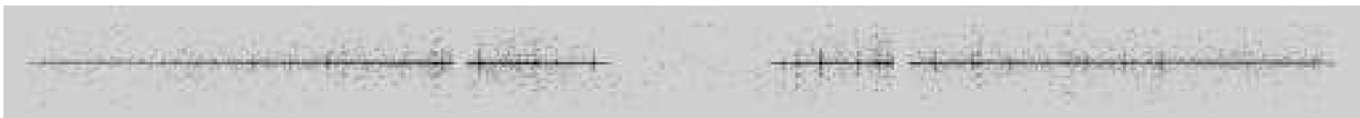

Figure 112: Full image of the HRC-S/LETG measurement for Mg-K.

Figure 112 shows the resulting image of the entire HRC-S. The knife blades were used to block the zeroth and first order images from the detector to avoid over exposure. The gaps between segments are also visible (but since the data are de-dithered, these are slightly washed out). Peaks from the Mg line are seen out to about 15-th order. Using a simple threshold detect algorithm, determining the position centroid, and fitting to a Gaussian profile, the resulting positions for these orders are listed in Table 9. Only the peaks corresponding to the Mg-K$_{\alpha 1}$ line are listed. Beyond the 3-rd order line, the satellite K$_{\alpha 2}$ line is completely resolved and is not confused or blended. For the 3-rd order lines, the peak position is not effected by this satellite line due to the large (x10) intensity difference between the lines. Both the centroid calculation and Gaussian fit positions are listed in the table. It appears that in the cross dispersion direction (U) the peak locations vary systematically with the location along the HRC-S, but more of less symmetrically about the 0-th order. The variation is only 5-10 pixels at the maximum and is not significant with regard to the dispersion direction locations of the peaks.

In Figure 113 an example of the line profile is shown This is the 8-th order line along with a Gaussian fit. The fit gives a line width σ of 8.2 pixels. The separation of the two components is 81.2 pixels, corresponding to about 9.3eV higher energy for the weaker satellite line than the primary line. According to the MIT HETG web site (http://space.mit.edu/HETG/xrcf_sources/sources.html), the Mg Anode yields the Mg-K$_{\alpha}$ at 1.2356 keV, and two satellite lines at 1.2618 and 1.2632 keV with relative intensity (with respect to the main line) of 0.086 and 0.062 respectively. With the LETG/HRC-S combination we are seeing a blend of these satellite lines. Note that at the 8-th order the LETGS resolution (assuming that the primary line width is entirely due to the grating/detector resolution) is 0.0074Å (R=1330)

If one assumes a "perfect" spectrometer, then the various orders should be located at spacings given by the

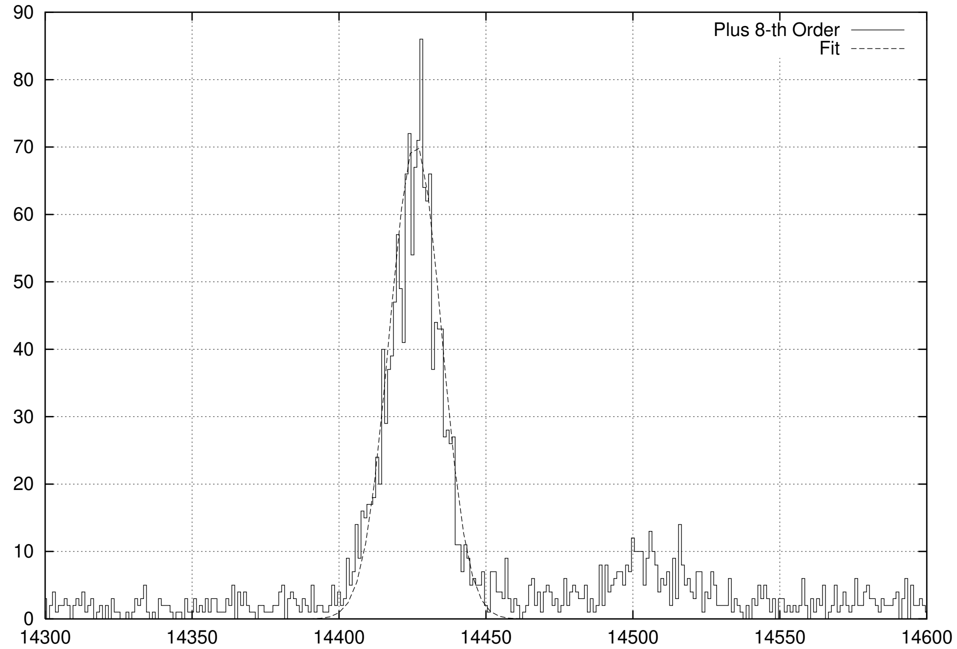

Figure 113: The Minus 8-th order Mg-K_α line complex. The brighter line is at 1.2536 keV, and the dimmer satellite line is at 1.2629 keV. A Gaussian fit to the primary line is plotted, with σ = 8.2 pixels. The same Gaussian shape is fit to the satellite line, which is clearly resolved in this order (81.2 pixels separate the peaks).

relationship:

$$\sin(\theta) = m\lambda/d \tag{50}$$

where m is the order number, λ is the X-ray wavelength (9.890Å), and d is the grating period (9912.16Å).

Given the Rowland Circle spacing (RC) for the LETG, the expected locations of the orders on the HRC-S can be calculated. We take the value $RC = 8788.10mm$ as given in the HETG WWW page (URL: http://space.mit.edu/HETG/xrcf.html revised 05/08/98). Since the location of the zeroth order is not measured (due to the knife blades blocking the beam) the relevant calculation is the spacing of the orders, which can be compared directly with the measurements.

Using Equation 1 and the value of RC, the spacing of the orders is 1363.9 pixels. (This estimate ignores the small deviations of the HRC-S surface from the Rowland Circle which are no more than about $0.1mm$ at any point along the detector and therefore less than 1 pixel in the location of any feature. The de-gapped coorected pixel scale for HRC-S in the V-axis is 6.4294 $\mu m/pixel$.) Table 9 lists the expected spacing of the orders compared with the measurements and shows that there is an anomalous spacing for the pair of orders that span the transition from the Center segment to the Plus wing. All other spacings are very close to nominal. The mean measured spacing (22 samples) is 1364.3 pixels, to be compared with the expected vale of 1363.9, excellent agreement. The RMS deviation in data sample is 2.6 pixels which is in good agreement with the expected HRC-S performance, the readout alone is characterized by a Gaussian $\sigma = 1.6$ pixels.

The anomalous value for the spacing of orders 6 to 7 is explained by a detailed consideration of the HRC-S construction. This is illustrated in Figure 114 which shows the effect of the 1.4321 degree angle between the center segment and the Plus segment. The HRC-S readout is essentially continuous across the segments; however, the MCPs meet at a height of about 4mm above the readout, at the same angle therefore producing a sudden jump in readout coordinates of about 102.3μm (actually 15.90 pixels). This correction to the spacing gives a value 1369.0 which is consistent with the other measurements.

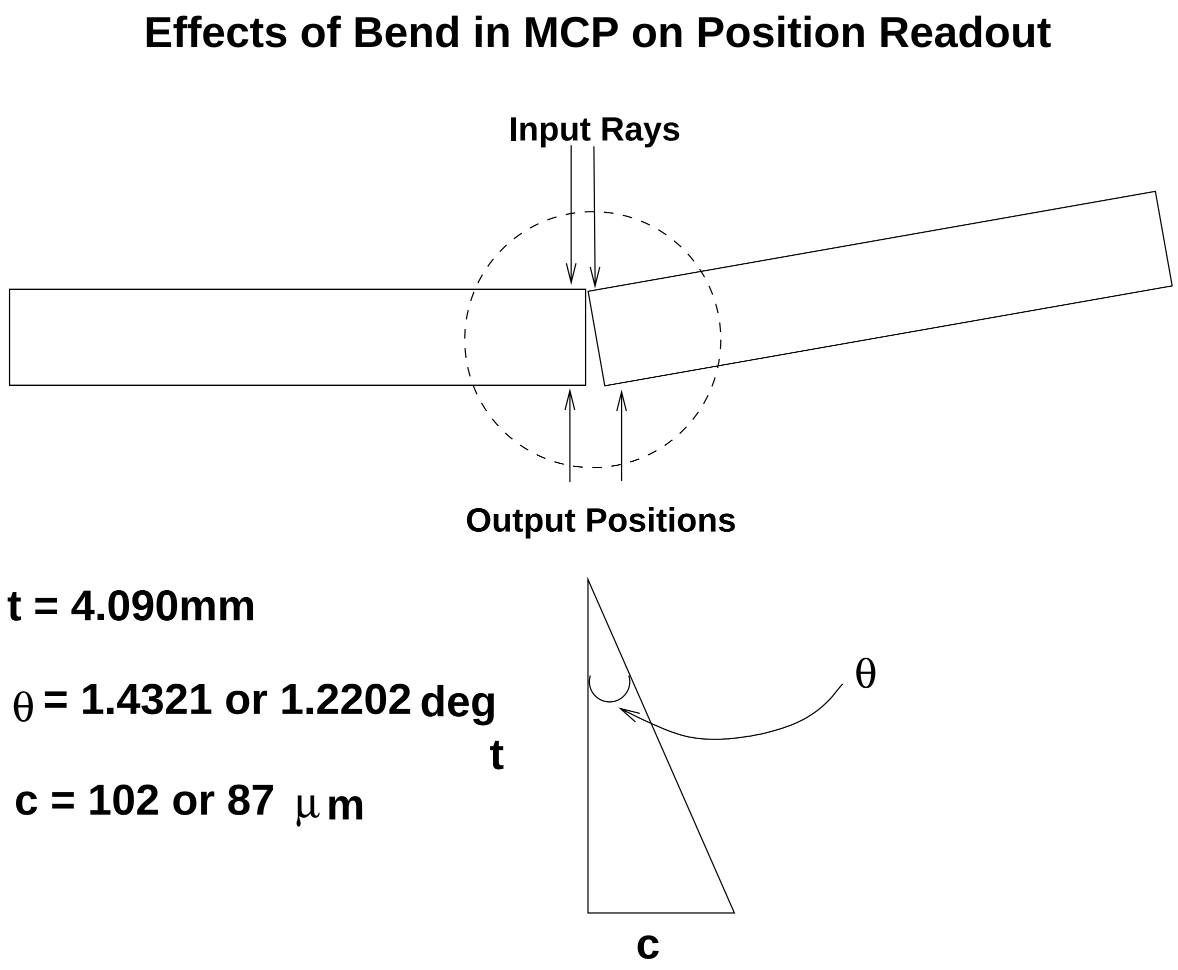

Figure 114: MCPs meet at an angle at their tops and thus are separated at the bottom by the distance 'c' shown in the figure. This distance is a jump in the readout which results in positions which are too large by the corresponding number of pixels.

On the Minus side, the 5-th order line happens to fall on the inter-segment gap and is not detected. The spacing of orders -4 to -6 should be twice the expected value plus the extra spacing due to the tilt of the Minus segment. This jump value is slightly less than for the Plus segment due to the smaller tilt angle (1.2202 degrees), it is about 87.1μm (13.55 pixels). The measured spacing is 2741.8 and the corrected expected value is 2741.4, again in excellent agreement with the observation.

Note that the corrected +6 order value is slightly higher than the expected 1363.9 and may be indictive of a systematic error in the "predicted" value of the discontinuity at the segment boundary. More data sets with multiple orders that cross the segment boundaries are needed to examine this effect in a statistically meaningful way. Also other construction effects that might effect the detector performance at the segment boundaries need to be considered. Regardless, there is no evidence within any single segment of any errors regarding the linearity or tilt angle of the segment. Within a segment the order spacings appear to be correct and have no significant systematic trends. The difference betweeen the observed and expected order spacings are shown in Figure 115. For the orders on Segment -1, the mean spacing is 1364.4 ± 2.4, for Segment -0, the means spacing is 1365.5 ± 2.3, and for Segment +1, the mean spacing is 1363.9 ± 3.3.

Another analysis of the data can be made by taking the average position of corresponding Plus and Minus orders. The average position should correspond to the location of the zeroth order, and be the same for each

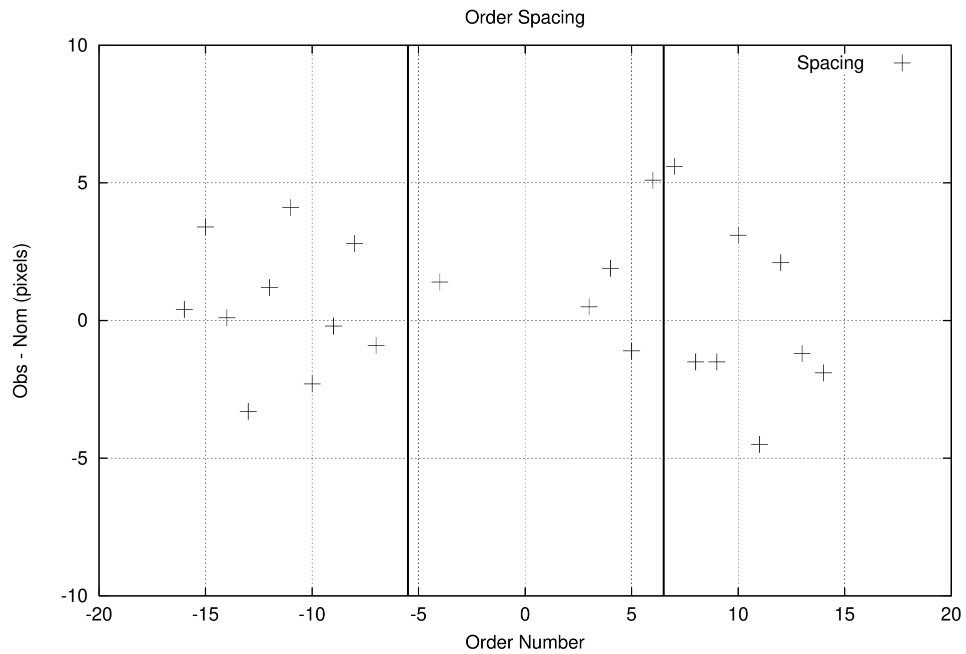

Figure 115: The difference between observed and nominal order spacings versus order. The vertical lines denote the segment boundaries.

pair of higher orders. In Table 9, this analysis is also included. The measured line positions are first corrected for the jumps at each segment, and then the average position for Plus and Minus pairs is calculated. The mean zeroth order position obtained (in corrected coordinates) is 25344.6 pixels, with an RMS deviation of 1.9 pixels. With these corrections, there appears to be no significant residual systematic errors.

The HRC-S performance is excellent with regard to large scale linearity over its entire length. The construction of the detector requires a correction to the calculated v-coordinate which is completely understandable from the geometry of the detector, and can be calculated based on the dimensions of the unit. The precision of these correction terms is slightly uncertain due to some potential assembly variations in the detector from the design values (e.g. the precise thickness of the MCP stack and distance from the CGCD). A similar analysis of additional data could be useful in attempting to model the detector to obtain best fit values for the corrections. However, even at this level of analysis, all of the RMS uncertainties are at the few pixel level.

Table 9: Measured HRC-S v-axis coordinates of the various orders of the Mg-K$-\alpha$ line, and separation of orders. All values in HRC-S pixels (6.4294 μm).

Order	Measured	Separation	Corrected	Center
15	4884.207		4884.2	
14	6246.198	1362.0	6246.2	
13	7608.945	1362.7	7608.9	
12	8974.886	1366.0	8974.9	
11	10334.289	1359.4	10334.3	
10	11701.250	1367.0	11701.3	
9	13063.595	1362.4	13063.6	
8	14425.994	1362.4	14426.0	
7	15795.458	1369.5	15795.5	
6	17180.364	1384.9	17164.5	
5	18543.175	1362.8	18527.3	
4	19908.971	1365.8	19893.1	
3	21273.355	1364.4	21257.5	
-3	29452.237		29436.3	25346.9
-4	30817.452	1365.3	30801.6	25347.4
-5				
-6	33559.298		33529.8	25341.2
-7	34922.269	1363.0	34892.8	25345.2
-8	36289.039	1366.7	36259.5	25342.8
-9	37652.650	1363.7	37623.2	25343.4
-10	39014.256	1361.6	38984.8	25343.1
-11	40382.307	1368.0	40352.8	25343.6
-12	41747.439	1365.1	41717.9	25346.4
-13	43108.003	1360.6	43078.5	25343.7
-14	44471.978	1364.0	44442.5	25344.4
-15	45838.288	1367.3	45808.8	25346.5
-16	47202.588	1364.3	47171.1	

4.7.4 Detector Geometry

Relative Focus Position of HRC-I and HRC-S

During Phase G of the XRCF calibration, HRC-I and HRC-S shutter focus tests were made in order to determine the position of best focus for each detector. Based on these tests, the relative position (along the x-axis) of the plane of the HRC-I detector with respect to the HRC-S (center segment) detector is shown in Figure 116, i.e., the HRC-I lies 0.663 mm closer to the HRMA than the HRC-S.

HRC-I As-built Dimensions

The dimensions of the major components of HRC-I are shown in Figure 117. The HRC-I CGCD (Crossed-Grid Charge Detector) is produced by winding wire around a ceramic block and removing wire from the back side to produce a linear array of parallel wires for each axis. There are 473 wires along each axis at a pitch (distance between wires) of 0.008100 in (0.20574 mm) and amplifier taps every eighth wire, resulting in a distance between taps of 1.6459 mm (8 x 0.20574 mm) and an overall span of 97.109 mm (472 x 0.20574 mm). This range is larger than the open area of the HRC-I MCP of 92.57 $\pm$0.05 mm (u-axis) x 92.77 $\pm$0.05 mm (v-axis), as measured at SAO using flat field data. The HRC-I CGCD uses 59 taps per axis with a tap at each end provided with charge amplifiers connected to wires 1 and 473. A de-gapped HRC-I pixel is 0.006429 mm (1.6459 mm / 256) square.

As measured at the XRCF, the HRC-I active area center is at $u = 7672$, $v = 7719$ and the electronic readout center is at $u = 8192$, $v = 8192$.

HRC-S As-built Dimensions

The dimensions of the HRC-S are shown in Figure 118. The HRC-S CGCD is similar in concept to the HRC-I CGCD. However, the "long wires", those that give the position in the cross-dispersion direction (u-axis) are produced by patterning a layer of gold deposited directly on a ceramic block. The wires for the dispersion direction are produced by winding wire around the ceramic block and removing it from the back side. There are 1513 wires along the dispersion (v axis) , 121 "wires" along the cross-dispersion (u-axis) and taps every eighth wire. The distance between the v-axis wires is 0.20574 mm; between the u-axis "wires" is 0.2000 mm. The HRC-S CGCD provides a continuous position readout along the dispersion direction 311.1 mm (1512 x 0.20574 mm) long. Three 100 mm long MCP segments nearly span this distance. Taps spaced apart by 64 are connected to a single charge amplifier. The u-axis uses 16 taps to span its 121 "wires". A de-gapped HRC-S pixel is 0.006429 mm (1.6459 mm / 256; v-axis) x 0.006250 mm (1.6000 mm / 256; u-axis).

Figure 119 is a sketch of the HRC-S showing the HRC V coordinates (after a reasonable degap) of the active region of the three segments, and also indicating the preliminary values of the coordinate discontinuities at the segment boundaries.

For Segment +1 (i.e., the segment in the +Y spacecraft direction) the physical edge of the detector is at V = 1196 pixels, the beginning of the active area is at V=1665 pixels. The end of the active area is at V = 16404 pixels, and the physical edge is at V = 16444 (not shown).

For the middle segment (Segment -0), the physical edge is at V = 16900 (not shown), and the active area starts at V = 17060, at the other edge the active area ends at V = 32165, and the physical edge is at V = 32250.

For Segment -1 (i.e., the segment in the -Y spacecraft direction) the physical edge is at V = 32930, and the active area starts at V = 32975. At the other end, the active area ends at V = 47605, while the physical edge extends to V = 48117.

The tilt angles are 1.4321 degrees for Segment +1 and 1.2202 degrees for Segment -1. The discontinuities are given in pixels assuming these tilts and a thickness of 4.090mm. These discontinuities have NOT been applied to the V-coordinate values given above, which are the readout values (degapped, but otherwise uncorrected for geometry) as generated by the electronics. The degapping used is good to about 1 pixel so there should not be too much uncertainty in these values.

The nominal zero points for the HRC-S should be set so that the origin of the physical system is at the middle of the electrical system (before corrections). That would be at V - 24576 (coarse position 96). In the U axis the origin should be at U = 2048 (coarse position 8).

The conversion of pixels to mm is different for U and V. For U, the correct value is 0.006250 mm/pixel. For V, the correct value is 0.0064294 mm/pixel.

The geometry of the detector in the U-axis is not as well known as in the V-axis. For the time being, it is safe to use a physical size of U = 0 to U = 4096 pixels (for all segments) and an active area of U = 560 to U = 3536 (a total active width of 18.6mm).

Getting the relationship of the various UVIS regions in HRC-S coordinates is not a simple matter. It involves some effort to find contrast differences in flat field images that were taken after the final assembly of the detector. Unfortunately the HESF (aka the Drake/Murray Flats) and the orientation of the detector and the calibration facility make these data ambiguous in determining the exact geometry in the U direction.

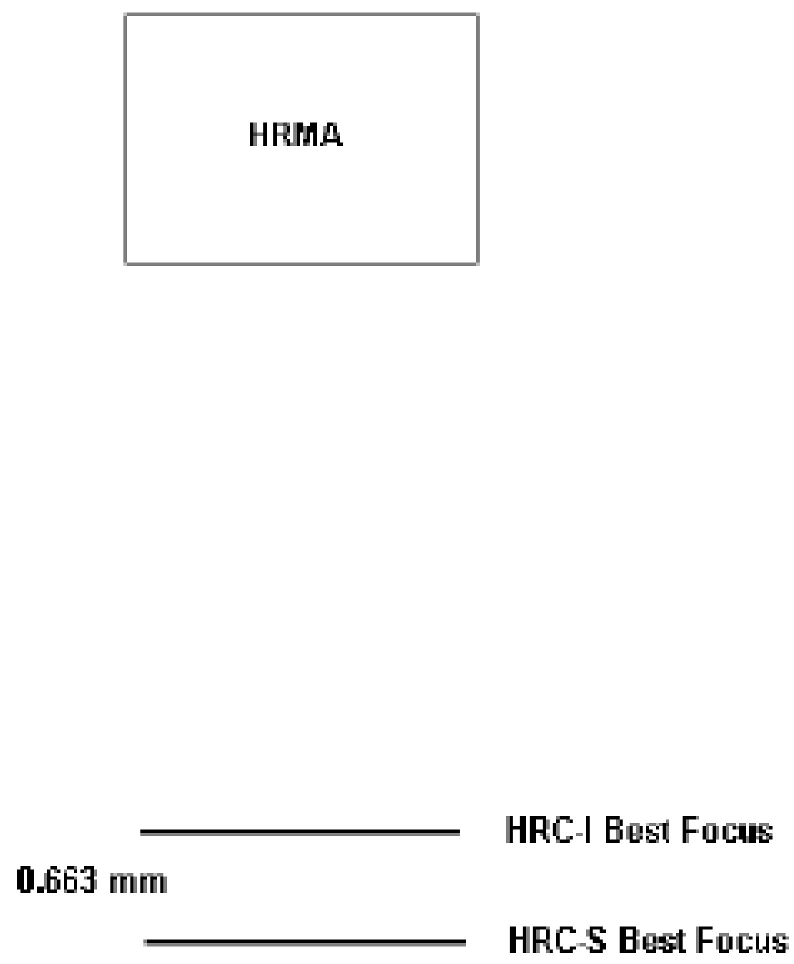

Figure 116: Relative location of the best focus positions of the plane of HRC-I with respect to the center segment of HRC-S.

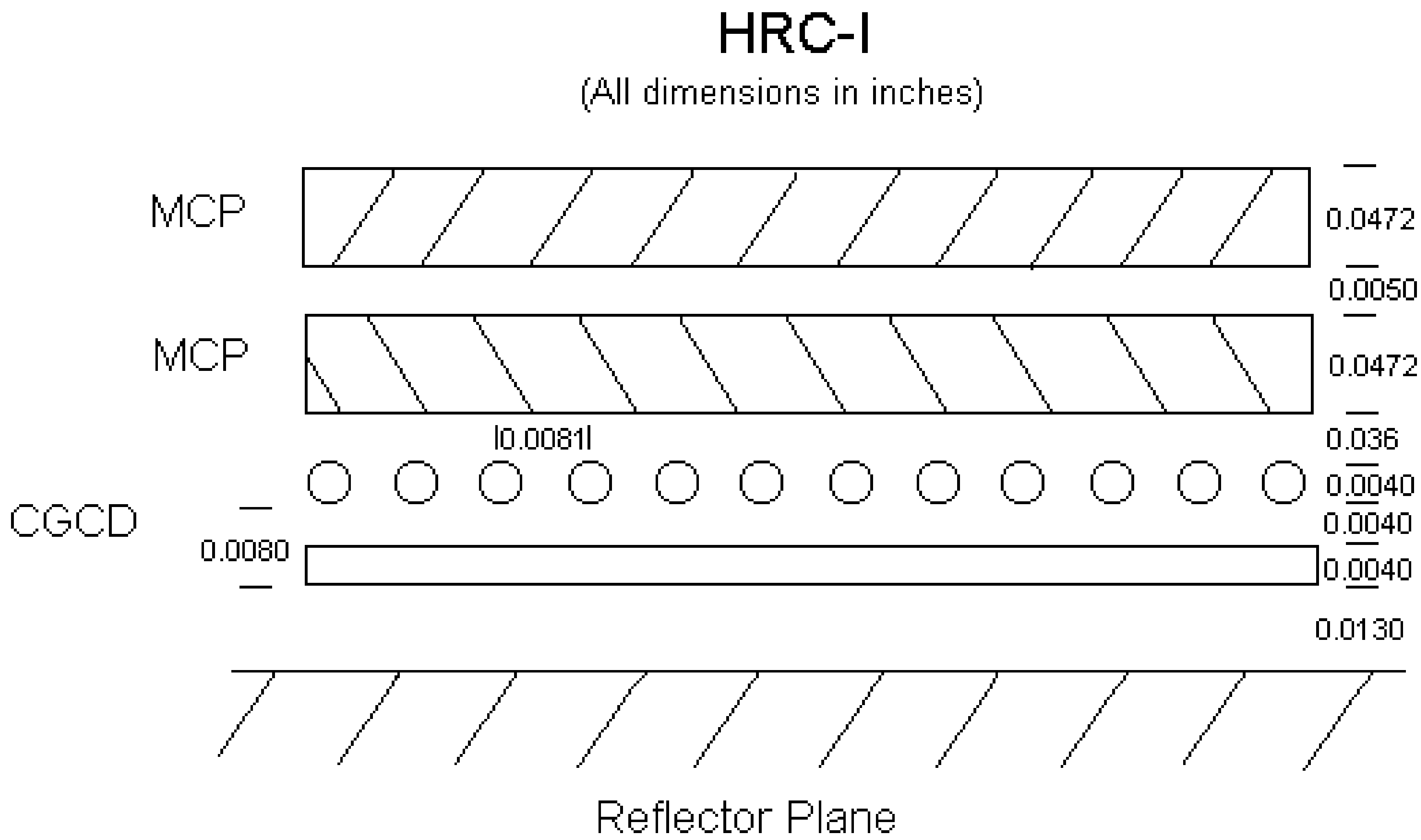

Figure 117: The dimensions and separations (in inches) of the major components of HRC-I.

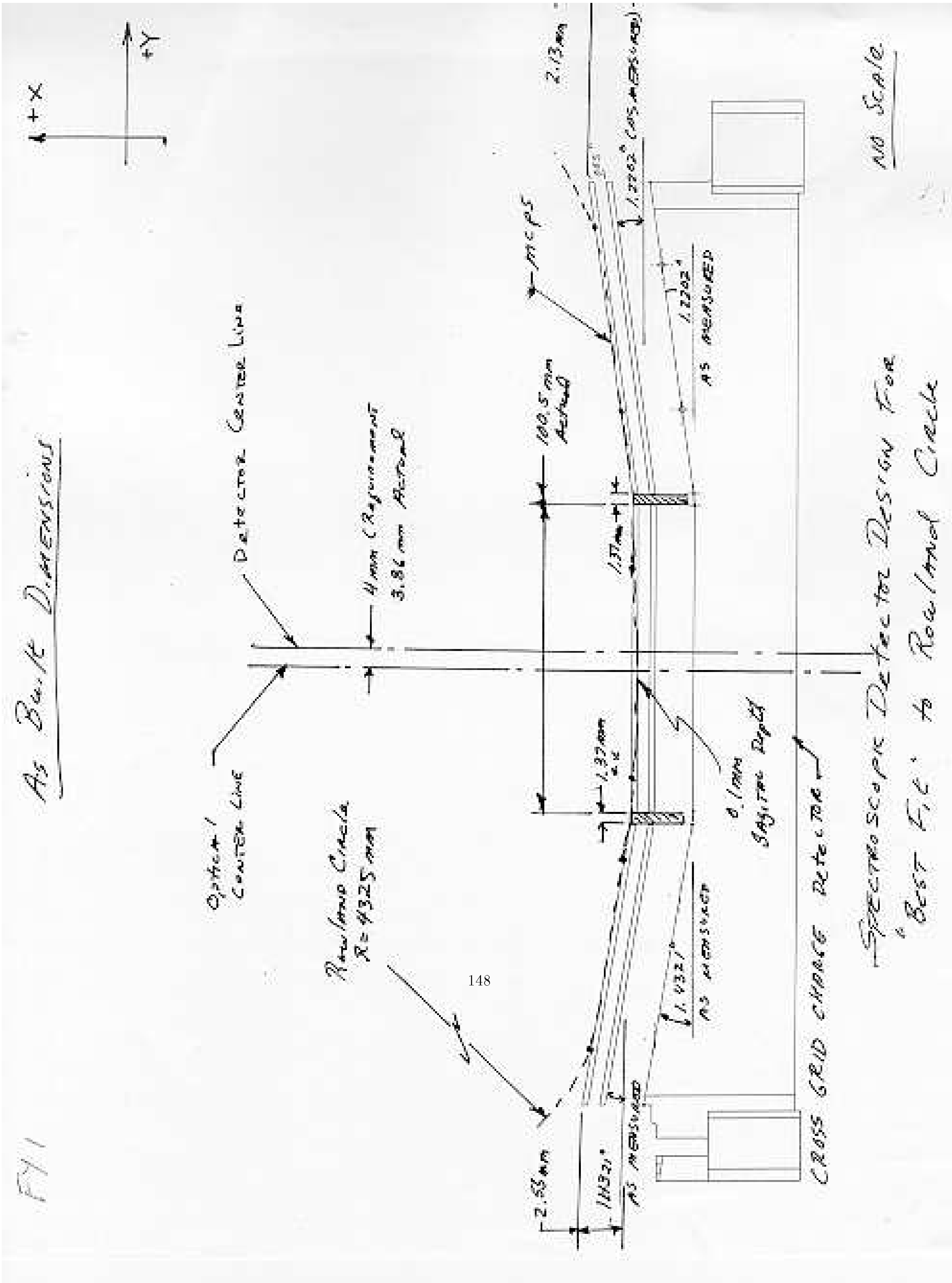

Figure 118: The dimensions of (in inches) the HRC-S.

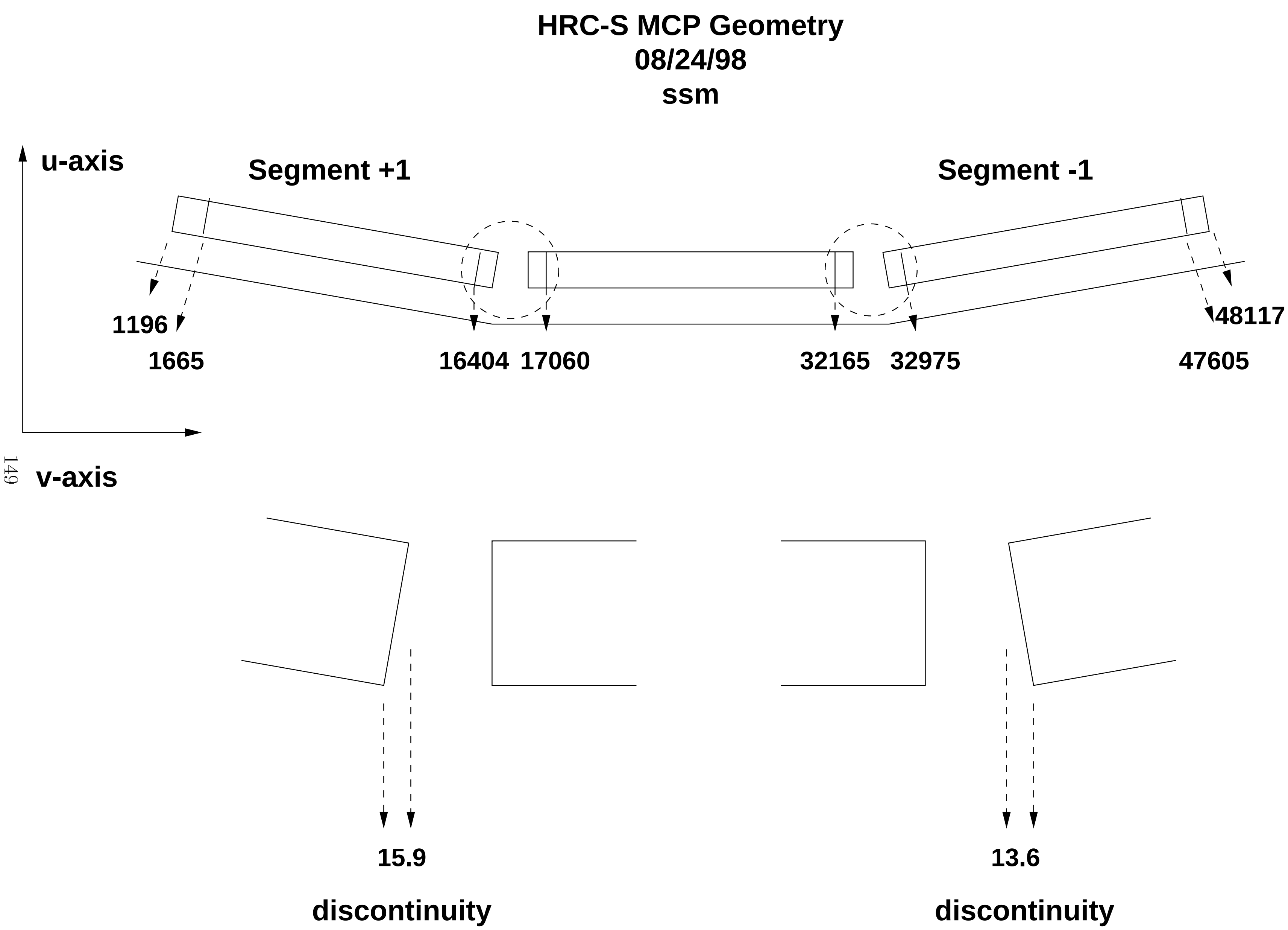

Figure 119: The HRC-S Coordinates

Table 10: Description of the witness samples that were tested with the SAO x-ray monochromator, and at the BESSY1 Synchrotron Light Source Facility. The material composition and flight status of each filter is included.

Witness Sample	Run Number	Composition and Luxel Thickness Measurements	Status	Test Method
TF100-354	6569-8	Aluminum $305 \pm 30Å$ Polyimide $1940 \pm 100Å$	Flight	Synchrotron
TF100-565	6567-8	Aluminum $315 \pm 30Å$ Polyimide $2040 \pm 100Å$	Flight	SAO Monochromator
TF101-883	6747-8	Aluminum $790 \pm 50Å$ Polyimide $5215 \pm 100Å$	Non-Flight	SAO Monochromator
TF101-891	6567-8	Aluminum $315 \pm 30Å$ Aluminum $1710 \pm 50Å$ Polyimide $2040 \pm 100Å$	Flight	Synchrotron
TF101-914	6492-8	Polyimide $5039 \pm 100Å$ Aluminum $735 \pm 50Å$ Carbon $240 \pm 25Å$	Non-Flight	SAO Monochromator
TF101-1052	6550-8	Aluminum $665 \pm 50Å$ Polyimide $2500 \pm 100Å$ Aluminum $307 \pm 30Å$	Flight	SAO Monochromator
TF101-1053	6550-8	Aluminum $665 \pm 50Å$ Polyimide $2500 \pm 100Å$ Aluminum $307 \pm 30Å$	Flight	Synchrotron
TF101-1054	6547-8	Aluminum $643 \pm 50Å$ Aluminum $302 \pm 30Å$ Polyimide $2500 \pm 100Å$	Non-Flight	SAO Monochromator
TF100-1063	6080-5	Polyimide $2265 \pm 100Å$	Non-Flight	SAO Monochromator
TF101-1092	6569-8	Aluminum $1663 \pm 50Å$ Aluminum $305 \pm 30Å$ Polyimide $1940 \pm 100Å$	Flight	SAO Monochromator
TF101-1174	6788-8	Aluminum $795 \pm 50Å$ Polyimide $5300 \pm 100Å$	Flight	SAO Monochromator Synchrotron
TF101-1175	6788-8	Aluminum $795 \pm 50Å$ Polyimide $5300 \pm 100Å$	Flight	SAO Monochromator

4.8 UV/Ion Shields (UVIS)

4.8.1 SAO X-ray Monochromator Transmission Measurements

Every UV/ion shield supplied to us by the Luxel Corporation (Friday Harbor, WA) was accompanied by two witness samples, each of which is 16mm in diameter. Each pair of witness samples comes from the same filter production run as its associated flight filter, and are taken from different regions of the larger filter sheet. The experimental setup precluded any effort to perform spatial uniformity measurements on a given witness sample. Rather, each measurement represents an average transmission over a filter. However, we know from previous uniformity measurements of a candidate HRC-I UV/ion shield, that it was spatially uniform in transmission within 5% relative error at a spatial scale of 1 mm. All of the flight witness samples, and several non-flight witness samples, tested within this work are listed in Table 10. Included in this table are the thickness values of the constituent layers as reported by Luxel. Figure 120 shows the nominal thickness values of the HRC-I and HRC-S UV/ion shields.

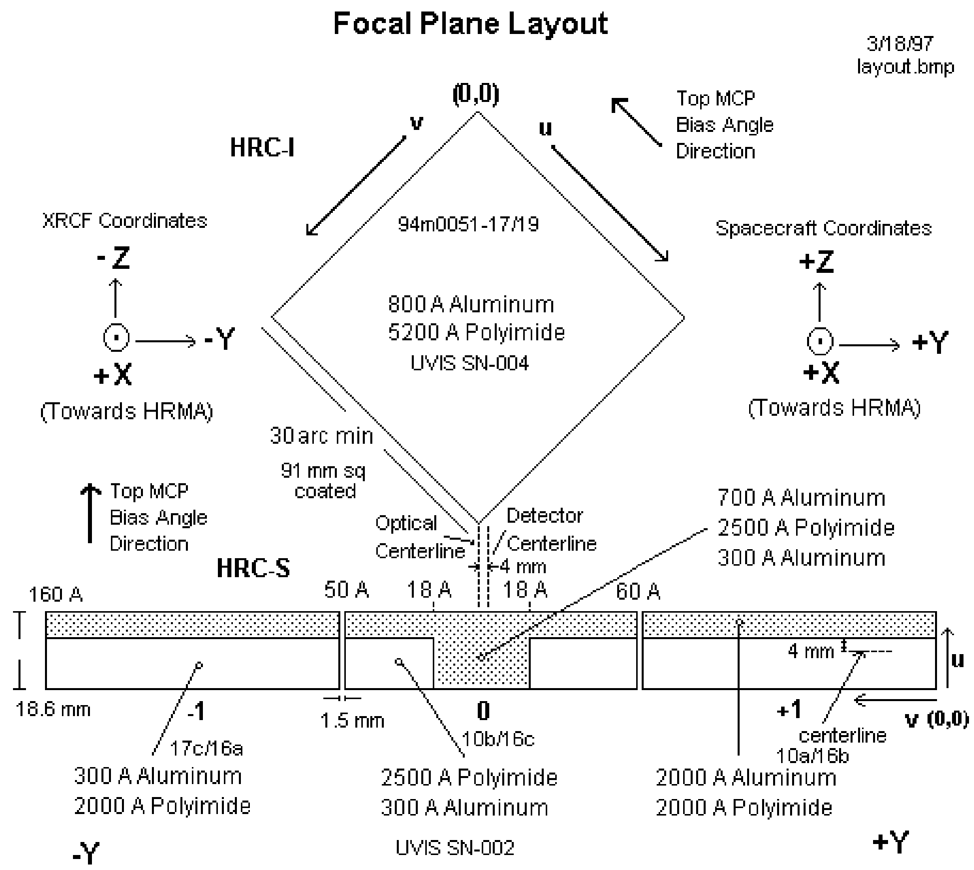

Figure 120: The material composition of the UVIS-I and UVIS-S are shown above. The thicknesses are nominal. Where there is only a single side coated with aluminum, that side faces the High Resolution Mirror Assembly (HRMA) of AXAF. For the HRC-S Inner "T", it is the side with the 700Å coating that faces the HRMA. The figure also shows the relative orientation of the HRC-I and HRC-S in the instrument focal plane.

Instrumental Setup

The transmission measurements were carried out at the SAO using a McPherson model 248/310 G 1-meter diameter grazing incidence monochromator. It is equipped with a 600 G/mm grating that has a 1^o blaze angle and a 580Å blaze wavelength, which yields an operating range of 6 Å to 681 Å and a resolution of 0.5 Å. The monochromator entrance and exit slits were set to a nominal 15 μm width to minimize contamination by the x-ray continuum. Figure 121 represents a typical monochromator beam scan to identify the fluorescent lines associated with the anode selected for use in the Manson model 2 single-anode soft x-ray source. In this case, titanium. The scan shows that the Ti L_α and L_η lines dominate over the continuum by about a factor of 10. The O K_α line is even more dominant. When a line is selected, the monochromator is adjusted to operate at the line peak. The instrument is also equipped with a pair of filter wheels, each of which has enough holders to accommodate up to five witness samples. However, one holder of each wheel was intentionally left unoccupied so that x-ray spectra could be obtained without a filter in the x-ray detector beam path as part of the transmission measurement procedure. Spectra were acquired with a Manson model 851 gas-flow proportional counter equipped with a VYNS window, and which utilized methane as the fill gas.

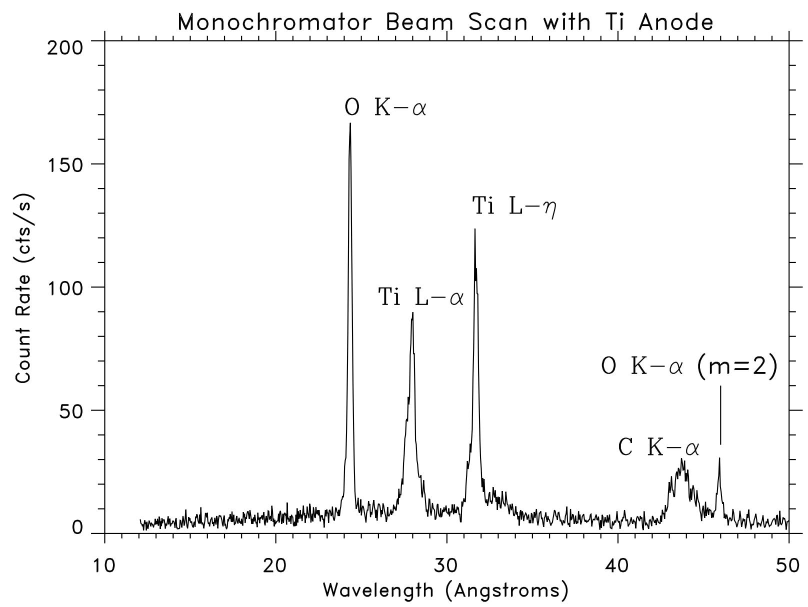

Figure 121: Example of a typical monochromator beam scan to identify the first order x-ray fluorescent lines associated with an anode. In this case, titanium. Note how the primary lines of interest, Ti L_α and L_η, dominate over the continuum.

Results

The procedure for making a transmission measurement involved obtaining a pair of filter-in/filter-out spectra, as well as a background spectrum. Once the background contribution was subtracted from both x-ray spectra, the value of the transmission simply involved dividing the number of remaining counts in the filter-in measurement by the number of remaining counts in the filter-out measurement. The measurement results are shown as the data points in figures 122 through 126.

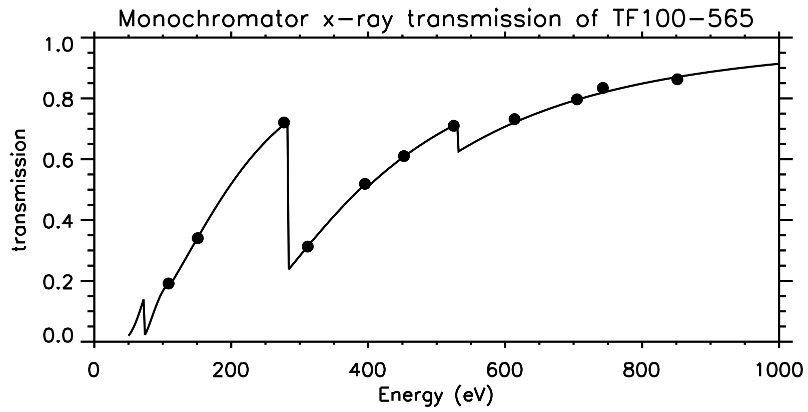

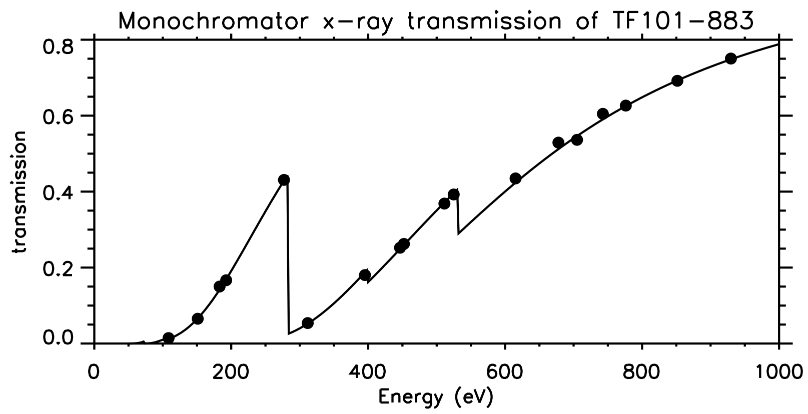

Figure 122: Modeled transmission curves for Luxel witness samples TF100-565 (top) and TF101-883 (bottom) based on the monochromator data. The transmission measurements taken with the SAO x-ray monochromator are plotted, also. The statistical error bars are smaller than the data points.

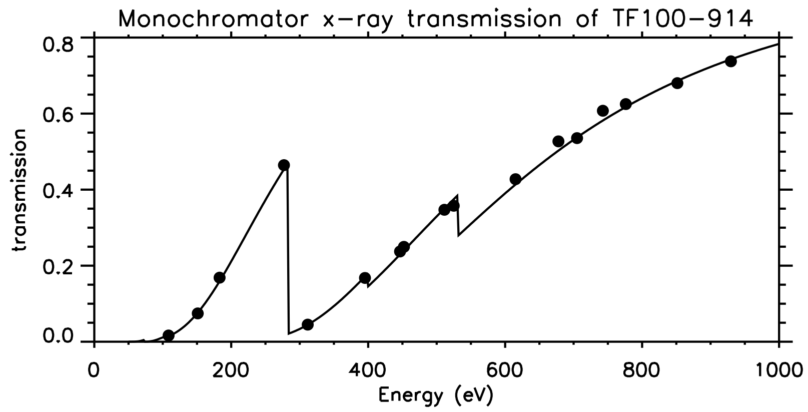

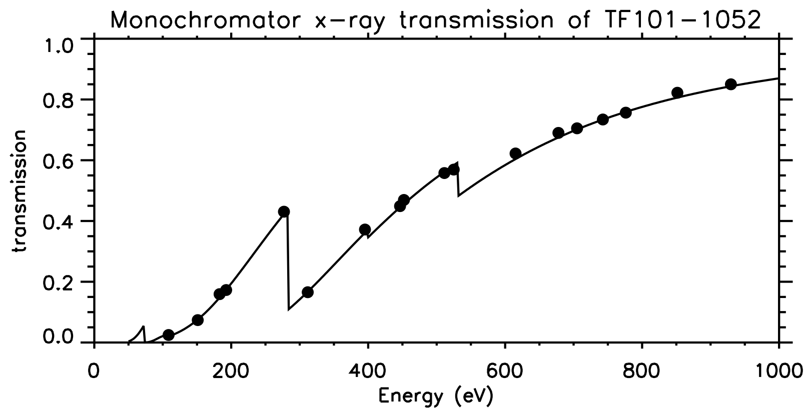

Figure 123: Modeled transmission curves for Luxel witness samples TF101-914 (top) and TF101-1052 (bottom) based on the monochromator data. The transmission measurements taken with the SAO x-ray monochromator are plotted, also. The statistical error bars are smaller than the data points.

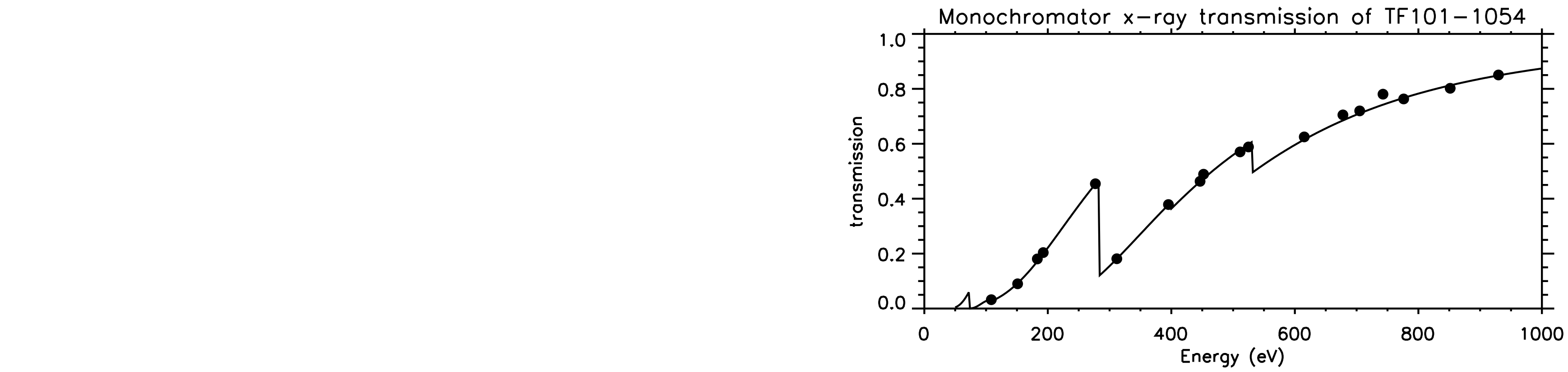

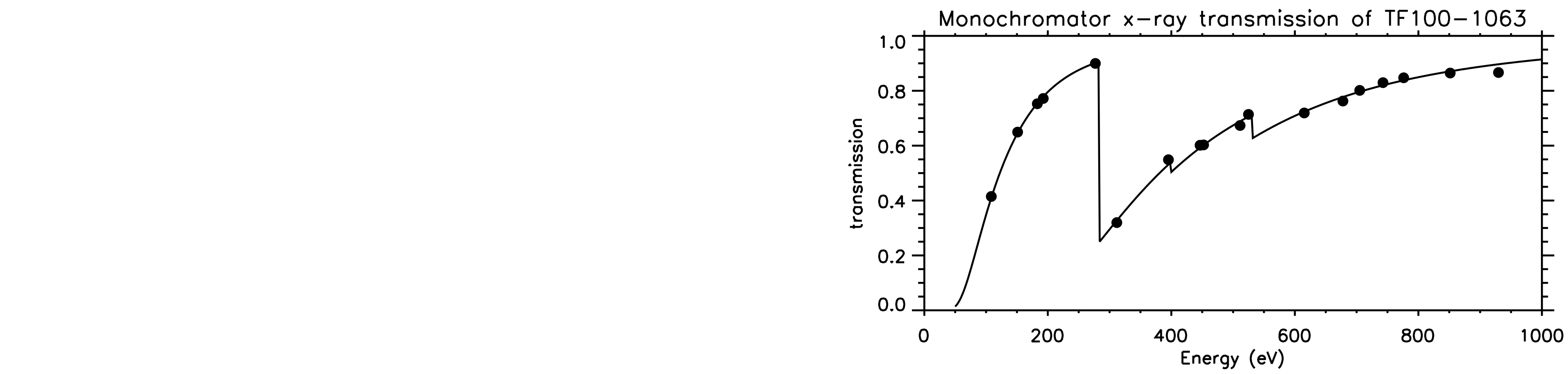

Figure 124: Modeled transmission curves for Luxel witness samples TF101-1054 (top) and TF100-1063 (bottom) based on the monochromator data. The transmission measurements taken with the SAO x-ray monochromator are plotted, also. The statistical error bars are smaller than the data points.

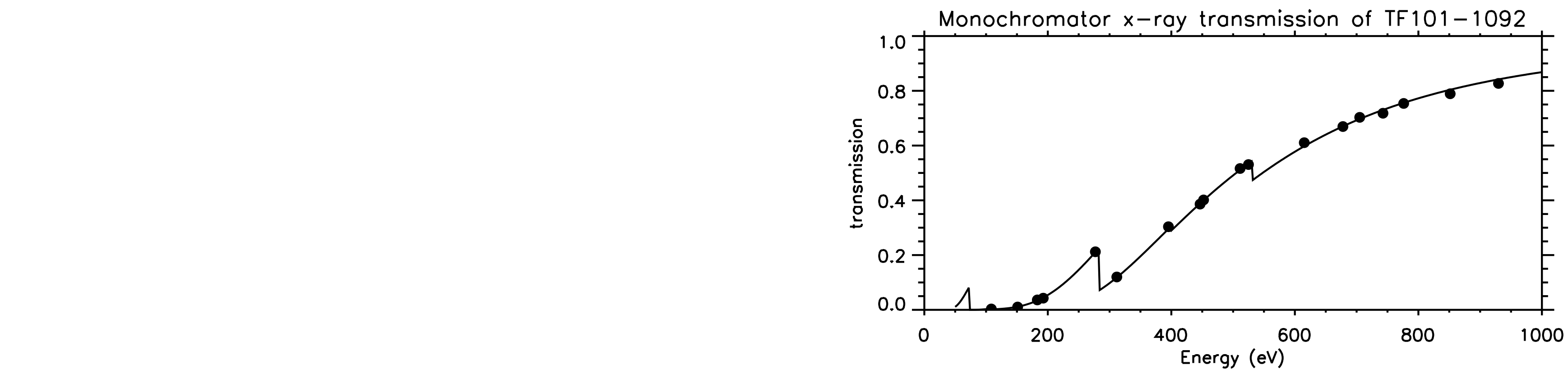

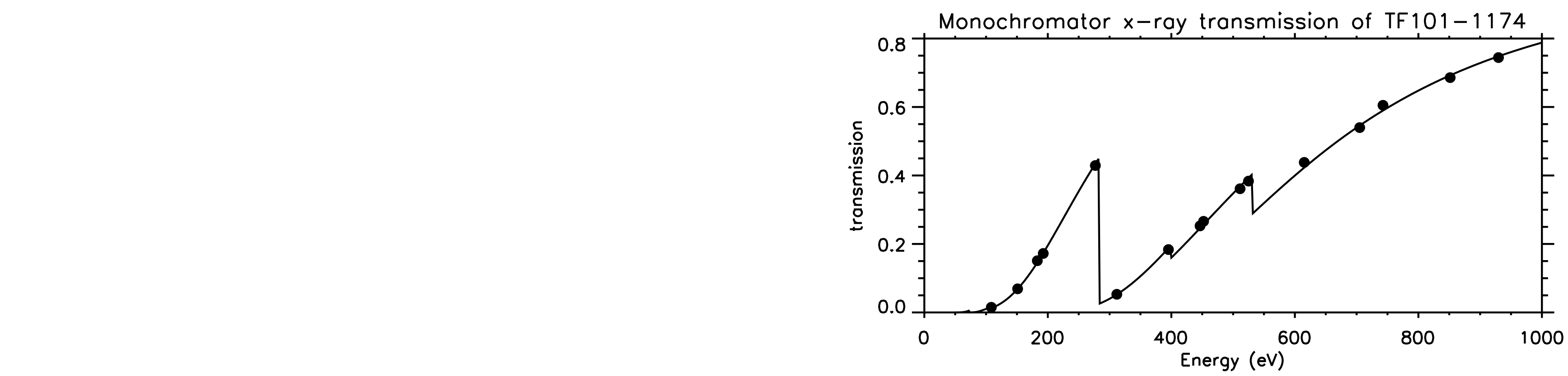

Figure 125: Modeled transmission curve for Luxel witness samples TF101-1092 (top) and TF101-1174 (bottom) based on the monochromator data. The transmission measurements taken with the SAO x-ray monochromator are plotted, also. The statistical error bars are smaller than the data points.

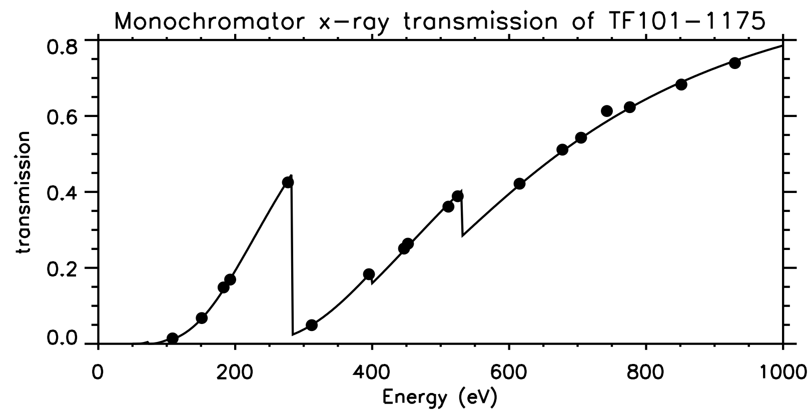

Figure 126: Modeled transmission curve for Luxel witness sample TF101-1175 based on the monochromator data. The transmission measurements taken with the SAO x-ray monochromator are plotted, also. The statistical error bars are smaller than the data points.

Modeling the X-ray Transmission

A model of x-ray transmission for each witness sample was obtained by applying a nonlinear fitting routine (the Levenberg-Marquardt algorithm) to each data set. The transmission of x-rays through N layers of material is represented by

$$T(E) = \prod_{i=1}^{N} e^{-(\frac{\mu(E)}{\rho})_i (\rho t)_i} \tag{51}$$

where the product of the material density and thickness, ρ and t, respectively, is called the mass areal density. In fitting a model to the data, the mass areal densities of Al, C, N and O were adjusted in such a way as to minimize the reduced χ^2 value of the fit. The mass absorption coefficient of a particular element, $(\frac{\mu}{\rho})$, is related to the imaginary part of the atomic scattering factor, f_2, by the expression

$$\frac{\mu(E)}{\rho} = 2 r_e h c N_o \frac{f_2}{AE} \tag{52}$$

where r_e is the classical electron radius, h is Plank's constant, c is the speed of light, N_o is Avogadro's number, and A is the atomic mass of the element.

The mass absorption coefficients are taken from Henke, *et al*, (1982), as opposed to the 1993 values. We believe that the 1993 Henke values for carbon and aluminum are suspect. We have come to this conclusion for the following three reasons. First, from the results of an unrelated experiment to measure the counter depth of our gas-flow proportional counters, we were able to conclude that the 1982 values for carbon yielded counter depths consistent with the manufacturer's specifications. However, computations using the 1993 values resulted in counter depths that were 20% larger, exceeding the physical size of the detectors themselves. Indeed, Gullikson concurs with these particular findings pertaining to the carbon data. As a second example, the 1993 values consistently yield reduced χ^2 values for our transmission models that are greater than what are obtained when the 1982 values are used. And third, the resultant aluminum thickness of all witness samples agreed well with Luxel's values for only the 1982 coefficients. This is brought out clearly in Table 11, where Luxel's measurement of aluminum thickness for each witness sample is compared with the thickness values that we derived from using the 1982 and 1993 Henke coefficients. Note that the canonical density of aluminum, when deposited in a thin layer, is 2.50 g-cm^{-3}. In each case, only the 1982 coefficients yield values of aluminum thickness that agree with Luxel's, within the limits of error.

The areal densities of Al, C, N and O for each witness sample are listed in Table 12. The reduced χ^2 for both the 1982 and 1993 Henke coefficients are included. The modeled transmission curve for each witness sample, along with the associated data set, is shown in figures 122 through 126. A plot of the relative residuals, $(\frac{data-fit}{data})$ for one transmission curve is shown in figure 127. The dashed horizontal line in the plot represents the median of the relative residuals. The fact that the median is close to zero for the filter shows that systematic errors are negligible. The other transmission curves are similar.

By adding up the areal densities of C, N and O for any given witness sample, one obtains the areal density of polyimide. Dividing by the canonical density of polyimide, 1.40 gm-cm^{-3}, yields the thickness of the material. The areal density (and hence thickness) of polyimide is slightly underestimated, as the hydrogen areal density is not included in the thickness derivation. However, its contribution is negligible compared to the other three elements. The derived polyimide thicknesses of the samples are shown in Table 13 .

Table 11: Comparison of aluminum thickness values as measured by Luxel, with the thickness values derived from the SAO x-ray monochromator data fitted using the 1982 and 1993 Henke coefficients. Note that only the 1982 Henke values yield thickness values that agree with Luxel's measurements, within the statistical uncertainties.

Witness Sample	Run Number	Luxel (Å)	Henke 1982 (Å)	Henke 1993 (Å)
TF100-565	6567-8	315 ± 30	316.8 ± 18.8	277.2 ± 17.2
TF101-883	6747-8	790 ± 50	777.6 ± 19.6	652.4 ± 18.4
TF101-914	6492-8	735 ± 50	693.2 ± 20.0	592.8 ± 18.4
TF101-1052	6550-8	972 ± 58	952.8 ± 18.0	792.8 ± 18.4
TF101-1054	6547-8	945 ± 58	866.0 ± 18.0	714.8 ± 17.2
TF100-1063	6080-5	0	0.0 ± 5.6	4.8 ± 7.2
TF101-1092	6569-8	1968 ± 58	1906.0 ± 26.8	1678.4 ± 26.0
TF101-1174	6788-8	795 ± 50	759.6 ± 20.4	640.6 ± 18.1
TF101-1175	6788-8	795 ± 50	766.0 ± 19.2	642.8 ± 18.8

Table 12: Computed mass areal densities based on 1982 Henke coefficients for witness samples measured with the SAO x-ray monochromator. The reduced χ^2 values of the data fits for both the 1982 and 1993 Henke coefficients are included to show that the 1982 Henke values yield significantly improved fits.

Witness Sample	Al (μg/cm^2)	C (μg/cm^2)	N (μg/cm^2)	O (μg/cm^2)	Reduced χ^2 (1982)	Reduced χ^2 (1993)
TF100-565	7.92 ± 0.47	21.10 ± 0.66	1.05 ± 1.00	6.62 ± 1.25	1.139	3.650
TF101-883	19.44 ± 0.49	53.79 ± 1.16	6.33 ± 1.22	16.26 ± 1.35	2.785	17.23
TF101-914	17.33 ± 0.50	58.50 ± 1.20	6.98 ± 1.28	15.43 ± 1.34	6.289	19.453
TF101-1052	23.82 ± 0.45	26.33 ± 0.71	2.34 ± 0.91	9.83 ± 1.19	3.997	26.238
TF101-1054	21.65 ± 0.45	25.73 ± 0.71	2.18 ± 0.90	9.70 ± 1.15	3.404	23.511
TF100-1063	0.00 ± 0.14	24.32 ± 0.54	2.31 ± 0.81	6.11 ± 0.53	2.888	5.313
TF101-1092	47.65 ± 0.67	21.74 ± 0.83	1.79 ± 0.96	6.62 ± 1.38	3.499	16.529
TF101-1174	18.99 ± 0.51	54.01 ± 1.13	6.80 ± 1.21	16.02 ± 1.47	2.448	18.119
TF101-1175	19.15 ± 0.48	55.09 ± 1.13	5.91 ± 1.21	16.76 ± 1.35	1.688	19.856

Table 13: The derived polymide thicknesses for the witness samples are compared against Luxel's measured values. Thicknesses are derived from both the SAO monochromator and the synchrotron data. The hydrogen areal density was not incorporated into the derived values, though it makes a negligible contribution to the polyimide areal density.

Witness Sample	Run Number	Luxel Thickness ($\AA$)	Derived Thickness ($\AA$)	Test Method
TF100-354	6569-8	1940 ± 100	2120 ± 64	Synchrotron
TF100-565	6567-8	2040 ± 100	2060 ± 124	SAO Monochromator
TF101-883	6747-8	5215 ± 100	5460 ± 154	SAO Monochromator
TF101-891	6567-8	2040 ± 100	2100 ± 91	Synchrotron
TF101-914	6492-8	5039 ± 100	5780 ± 158	SAO Monochromator
TF101-1052	6550-8	2500 ± 100	2750 ± 118	SAO Monochromator
TF101-1053	6550-8	2500 ± 100	2620 ± 79	Synchrotron
TF101-1054	6547-8	2500 ± 100	2670 ± 116	SAO Monochromator
TF100-1063	6080-5	2265 ± 100	2340 ± 79	SAO Monochromator
TF101-1092	6569-8	1940 ± 100	2150 ± 134	SAO Monochromator
TF101-1174	6788-8	5300 ± 100	5490 ± 158	SAO Monochromator
TF101-1174	6788-8	5300 ± 100	5490 ± 119	Synchrotron
TF101-1175	6788-8	5300 ± 100	5550 ± 152	SAO Monochromator

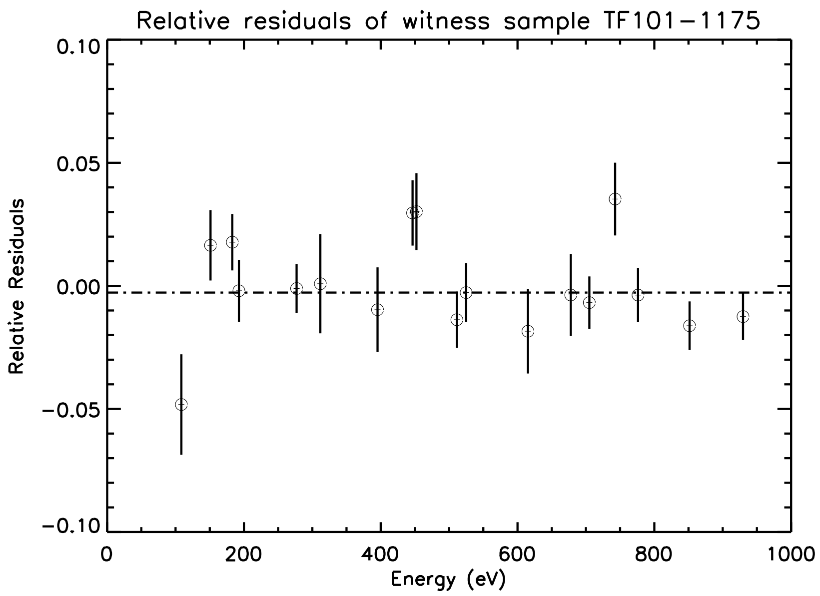

Figure 127: A plot of the relative residuals for witness sample TF101-1175, whose transmission was measured with the SAO x-ray monochromator. As discussed in the text, the fact that the median is close to zero indicates that there are no systematic errors.

Table 14: Summary of setup parameters for UVIS shadowgraph measurements.

Line	C K_α	O K_α
Anode	Graphite	$Mg(OH)_2$
Filter	33 μm poly	2 μm Cr
Energy	277 eV	525 eV
IN filename	P1971007a.rd	P1971007d.rd
Integration time	7200 s	12400 s
MD rate	222.434 cts/s	378.369 cts/s
OUT filename	P1971007b.rd	P1971007c.rd
Integration time	7200 s	7200 s
MD rate	97.573 cts/s	375.685 cts/s

4.8.2 Spatial Uniformity Measurements

We were not able to make spatial uniformity measurements on the flight UV/Ion shields. The flight delivery schedule precluded this. We have, however, made these measurements on flight backup shields and the results are reported here. We argue that the flight shields should have similar spatial uniformity since they were similarly manufactured. This hypothesis is supported by the fact that previous measurements on flight candidate shields gave quantitatively similar results as the backup shield measurements.

UVIS-I Shadowgraph

We made X-ray shadowgraph measurements on the backup HRC-I UV/Ion shield (filter is marked HRC-1007 Rev C S/N 009). The results of these measurements are summarized in this memo. The experimental setup was quite simple. All measurements were made in pipe #1 of the HRC laboratory. The model 5 Manson source (and source filters for the shadowgraphs) at one end of the pipe was used to create characteristic X-rays from several different anodes. An MCP detector was attached to the other end of the pipe (uncoated plates were used). The UVIS was mounted to translation stages which could be used to align the shield in both axes perpendicular to the beam, and to insert/remove the UVIS from the beam. The side arm proportional counter (monitor detector - MD) was used to monitor the temporal stability of the beam.

Shadowgraphs of the UVIS were made at two energies (C K_α and O K_α) to measure the large scale uniformity of the shield. At each energy, two flat fields were taken, one with the shield in the beam and one with it withdrawn. The ratio of the two images then reflects any large scale non-uniformity in the shield. Any spatial variation in the beam or detector divides out. The integration time was chosen to accumulate approximately 1000 cts/mm^2. A summary of relevant test parameters is given in Table 14. The raw data were converted to images with the standard processing software, and was binned by a factor of 128 in both axes (pixels are 823 μm on a side).

These data were analyzed using two different techniques. In the first method, the distribution of the pixel values in the IN, OUT, and RATIO (IN/OUT) images at each energy was considered. The mean (counts) and variance of the distribution of pixel values for each of images was computed. These results are summarized in Tables 15 and 16 (for the C K_α and O K_α measurements respectively). In all cases, the standard deviation of the distributions is considerably larger than the square root of the mean value, indicating the presence of some beam/detector non-uniformity. The ratio and standard deviation of the means (from counting statistics alone) is also given. A Gaussian was then fit to the distribution of pixel values in each RATIO image. Plots of the distribution of pixel values in the ratio images and the best fit Gaussians are contained in Figures 128 and 129. As can be seen from Tables 15 and 16, the centroid and width of these Gaussians agree quite well with the ratio of the means and the statistical standard deviation of this ratio. We therefore conclude that any variation in the ratio image (i.e. non-uniformity in the UVIS) is consistent with statistical fluctuations (5%). The shield is

Table 15: Transmission of UVIS S/N 009 at C K_α.

	Mean	Variance	Std Dev	$\sqrt{Mean}$
IN image	763.13 cts	2537.25	50.37 cts	27.62 cts
OUT image	768.60 cts	2516.28	50.16 cts	27.72 cts

Ratio of means	0.993
Statistical std dev of ratio	0.051
Gaussian mean of ratio image	0.988
Gaussian sigma of ratio image	0.050
Transmission at C K_α	0.433

Table 16: Transmission of UVIS S/N 009 at O K_α.

	Mean	Variance	Std Dev	$\sqrt{Mean}$
IN image	513.88 cts	4237.02	65.09 cts	22.67 cts
OUT image	713.046 cts	7923.84	89.02 cts	26.70 cts

Ratio of means	0.721
Statistical std dev of ratio	0.042
Gaussian mean of ratio image	0.715
Gaussian sigma of ratio image	0.043
Transmission at O K_α	0.411

uniform to at least the 5% level.

The ratios can be used to compute the transmission of the shields when combined with the MD data and the appropriate integration times. We measure the transmission of this shield to be 0.433 at C K_α and 0.411 at O K_α.

In the second (more sensitive) analysis method, wavelet decomposition was used to search for sources of emission (i.e. non-uniformity) at various scale. Two (similar) programs were provided by Alexey Vikhlinin for this analysis. We assume that all the small scale structure is related to the detector (e.g. hot spots). We use the wavelet decomposition software to find all small scale structures, subtract them from the raw data, and determine what remains. Contour plots of this residual structure divided by the Gaussian mean (determined above) are contained in Figures 130 and 131 for the C K_α and O K_α shadowgraphs, respectively. Note that the structure of the two contour plots are quite different, and the level of variation across either is $\sim$1%. The level of signifigance of these variations is difficult to assess without further analysis (i.e. Monte Carlo simulations), but it is reasonable to conclude that there are no statistically significant large scale non-uniformities at the 2-3% level.

UVIS-S Shadowgraph

We made x-ray shadowgraph measurements of the backup HRC-S UVIS. The set of shields is marked as S/N 03. These measurements were similar to measurements made on the backup HRC-I UVIS as described above. Shadowgraph measurements were made on all three segments of the shield. The shield was mounted on two translation stages that provided motion in the two axes orthogonal to the x-ray beam. A model 5 Manson source was used to generate characteristic X-rays, and beam filters were used for the shadowgraphs to reduce continuum contamination. A microchannel plate detector (MCP) with uncoated plates was mounted at the other end of the pipe. These HRC-S UVIS measurements were made with different plates and a different CGCD than were used for the HRC-I UVIS measurements. The different plates were used because the original set

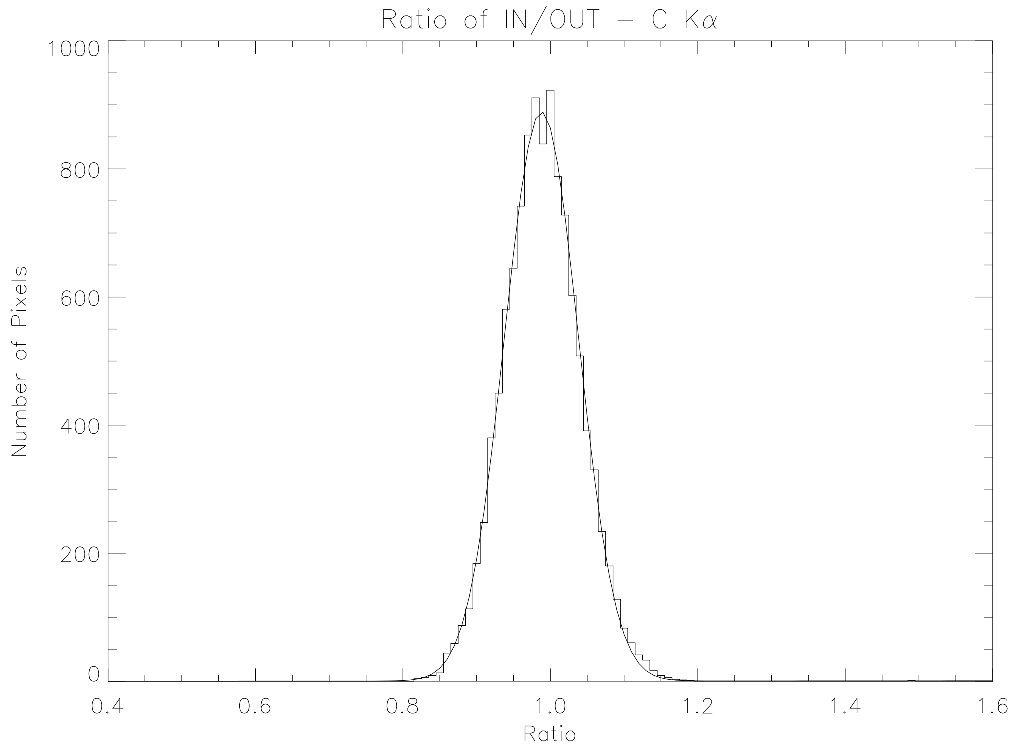

Figure 128: Distribution of pixels in C K_{α} ratio image (histogram) and best fit Gaussian (smooth curve).

developed a region of low gain in the center. The MCP images showed considerably more hot spots than the HRC-I UVIS measurements. A different CGCD were used for these measurements because the size of the gaps in the HRC-I measurements was quite large in one axis. A linear degap parameter of 1.13 was required to make the flat fields appear flat. Neither of these effects will influence the measurements, however.

Shadowgraphs of each segment of the HRC-S UVIS were made at C K_{α} and O $K_{\alpha}$to measure the large scale uniformity of the shield. In addition, a shadowgraph of segment -1 was made at B K_{α}. The experimental technique was identical to the HRC-I UVIS measurements made last year. Two flat fields were taken for each measurement, one with the shield in the beam (referred to as the IN measurement) and one with the shield out of the beam (referred to as OUT). The ratio image (RATIO=IN/OUT) is a map of the transmission of the UVIS. All detector and beam non-uniformities present in the IN or OUT images will be divided out in the RATIO image. The monitor detector (MD) was run for the C K_{α} and O K_{α} flat fields, so that absolute transmissions can be derived. The MD was not run for the B K_{α} measurement because we were concerned about carbon buildup on the anode. There is no beam stability monitor for this measurement, and the derived transmission may have a large systematic error associated with it. Summaries of the relevant test parameters is given in Tables ?? through 19 for the C K_{α}, O K_{α}, and B K_{α} shadowgraphs, respectively. Note that we took two separate shadowgraphs of the central segment shield at C K_{α} to determine the repeatability of the measurements. The integration time was chosen to accumulate approximately 1000 cts/mm^2 in each image. The raw data were converted to images with the standard processing software, and was binned by a factor of 128 in both axes (pixels are 823 μm on a side) for the C and O shadowgraphs, and by a factor of 256 in each axes for the B shadowgraph.

We used the same two techniques for analyzing this data as was used for the HRC-I UVIS shadowgraph, a statistical analysis of the distribution of transmission values and a wavelet analysis of the RATIO images. In the first method, the distribution of the pixel values in the IN, OUT, and RATIO images at each energy was considered. The mean and variance of the distribution of pixel values for each of images was computed.

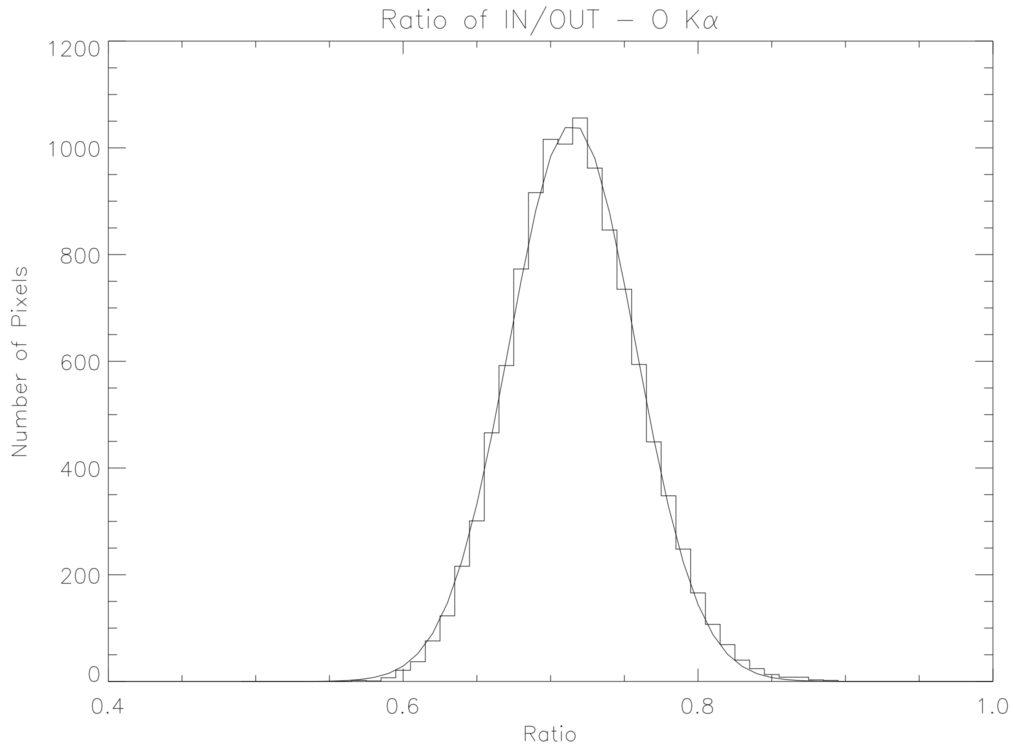

Figure 129: Distribution of pixels in O K_α ratio image (histogram) and best fit Gaussian (smooth curve).

Table 17: Summary of parameters for C K_α shadowgraphs of backup HRC-S UVIS

Line	C K_α	C K_α	C K_α	C K_α
Anode	Graphite	Graphite	Graphite	Graphite
Filter	33 μm poly	33 μm poly	33 μm poly	33 μm poly
V_A	1 kV	1 kV	1 kV	1 kV
Segment	0	+1	-1	0
IN filename	P1980206a.rd	P1980206c.rd	P1980206d.rd	P1980206f.rd
Counts	3.82E6	4.37E6	4.52E6	3.83E6
Integration time	3600 s	3600 s	3600 s	3600 s
MD counts	122835	147331	150943	123795
OUT filename	P1980206b.rd	P1980206b.rd	P1980206b.rd	P1980206e.rd
Counts	3.99E6	3.99E6	3.99E6	3.99E6
Integration time	3600 s	3600 s	3600 s	3600 s
MD counts	60661	60661	60661	78607

Unlike the HRC-I UVIS, the HRC-S UVIS has large scale structure associated with the regions of differing Al thickness, and each spatial region must be considered separately. For the C and B shadowgraphs, the different spatial regions were sorted by transmission value in the RATIO image. The difference in transmission between thin and thick Al on any segment is not large enough at O K_α, so these data were sorted spatially. The results for the three segments are summarized in Tables ?? through 35.

In all cases, the standard deviation of the IN and OUT distributions is considerably larger than the square

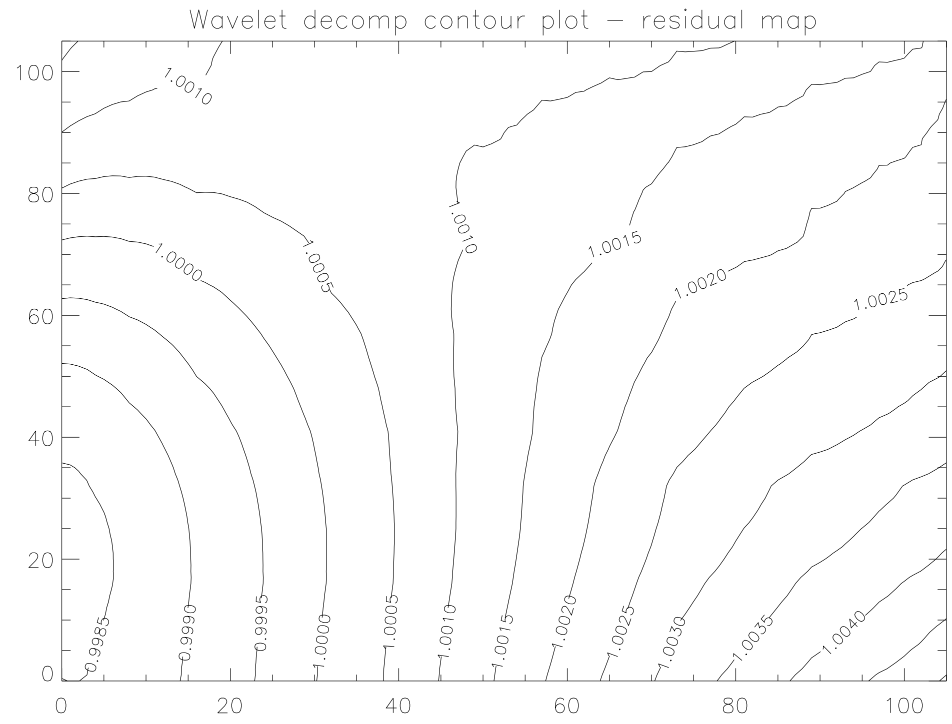

Figure 130: Contour plot of large scale residual non-uniformity of UVIS at C K_α

Table 18: Summary of parameters for O K_α shadowgraphs of backup HRC-S UVIS

Line	O K_α	O K_α	O K_α
Anode	MgOH	MgOH	MgOH
Filter	2 μm Cr	2 μm Cr	2 μm Cr
V_A	1 kV	1 kV	1 kV
Segment	0	+1	-1
IN filename	p1980209a.rd	p1980210c.rd	p1980209b.rd
Counts	2.92E6	2.86E6	2.97E6
Integration time	14400 s	14400 s	14400 s
MD counts	288620	285114	279019
OUT filename	p1980210b.rd	P1980210b.rd	P1980210b.rd
Counts	2.67E6	2.67E6	2.67E6
Integration time	7200 s	7200 s	7200 s
MD counts	139555	139555	139555

root of the mean value of these distributions, indicating the presence of some type of spatial non-uniformity in the beam, detector, or shield, or a combination of all three. The ratio and standard deviation (assuming counting statistics alone) of these means is also given. For comparison, a Gaussian was fit to the distribution of pixel values in each RATIO image. As can be seen from Tables 20 and 33 (the C K_α and O K_α shadowgraphs), the centroid and width of these fit Gaussians agree quite well with the ratio of the means and the statistical standard deviation of the ratios. We therefore conclude that any spatial variation in the RATIO image (i.e. non-uniformity in the UVIS) must be well below the level of statistical fluctuations (5%). The quantitative

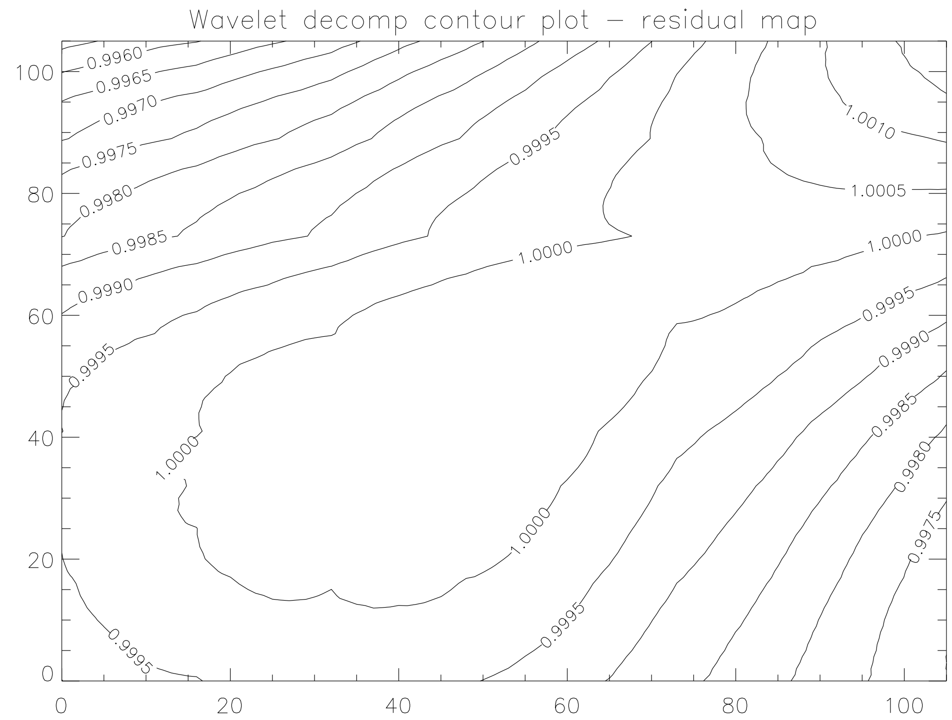

Figure 131: Contour plot of large scale residual non-uniformity of UVIS at O K_α

Table 19: Summary of parameters for B K_α shadowgraphs of backup HRC-S UVIS

Line	B K_α
Anode	B on Mg
Filter	5 Par-C
V_A	0.7 kV
Segment	-1
IN filename	p1980213a.rd
Counts	583943
Integration time	25200 s
MD counts	N/A
OUT filename	p1980214(a and b).rd
Counts	649743 (both images)
Integration time	7200 s each
MD counts	N/A

upper limit on that this places spatial variations in the shield depends on the uncertainty in the width of the Gaussian fit to the distribution of pixel values in the RATIO image, but is probably on the order of 2% or less. This is in general agreement with the results obtained previously on the HRC-I shield. Also, we conclude that the spatial non-uniformity found in the IN and OUT measurements is due to detector non-uniformity; previous measurements have found the beam to be uniform.

The average transmission of the shield was determined by two techniques. First, the mean counts in the IN

Table 20: Transmission of UVIS S/N 003 segment 0 (region of thick Al) at C K_α.

	Mean (counts)	Variance	Std Dev	$\sqrt{Mean}$
IN image	859.05 cts	3889.48	62.37 cts	29.31 cts
OUT image	964.07 cts	3377.65	58.12 cts	31.05 cts

Ratio of means ($\mathrm{Mean}_{IN}/\mathrm{Mean}_{OUT}$)	0.891
Transmission at C K_α(IN/OUT)	**0.440**
Statistical std dev of ratio	**0.042**
Gaussian mean of RATIO image	0.888
Transmission at C K_α(Gaussian)	**0.438**
Gaussian sigma of RATIO image	**0.044**

Table 21: Transmission of UVIS S/N 003 segment 0 (region of thin Al) at C K_α.

	Mean (counts)	Variance	Std Dev	$\sqrt{Mean}$
IN image	1416.47 cts	6815.80	82.56 cts	37.64 cts
OUT image	964.07 cts	3377.65	58.12 cts	31.05 cts

Ratio of means ($\mathrm{Mean}_{IN}/\mathrm{Mean}_{OUT}$)	1.469
Transmission at C K_α(IN/OUT)	**0.726**
Statistical std dev of ratio	**0.061**
Gaussian mean of RATIO image	1.439
Transmission at C K_α(Gaussian)	**0.711**
Gaussian sigma of RATIO image	**0.073**

and OUT images were used, corrected by the MD rate. Second, the best fit Gaussian centroid of the region in the RATIO image (again corrected by the MD rate) was used.

The B shadowgraph is a bit more complex. The detector background is insignificant in the C and O shadowgraphs, but is not negligible in the B shadowgraph. The S/N ratio is only ~2 in the region under the thick Al. A uniform background was subtracted from both the IN and OUT images, and hot spots were rejected by the region selection described above. We did not operate the monitor detector, so we have no measure of the temporal or spectral stability of the beam. As can be seen from Tables 34 and 35, the best fit Gaussians are considerably broader than the width one would expect based on counting statistics alone. This would indicate that there may be some level on non-uniformity in the shield. The statistical confidence of the data (particularly under the thick Al) is considerably below the C and O shadowgraphs, and the B shadowgraph images are binned a factor of 4 larger. Considering the lower quality of these data, I regard this result as inconclusive without further evidence. It may be an artifact of the low count rate and non-negligible background. Given the low rate from the anode, the long required integration time, and the generally low quality of this data (two full working days were required to take the limited data set presented here), I believe that this is not a useful measurement.

We also performed the wavelet decomposition on all RATIO images to search for large scale non-uniformities in the shield. Unlike the HRC-I shield, all three segments of the HRC-S shield have large scale structure associated with the regions of different Al thickness. One can visualize the shield as having two distinct regions of differing *emission*. The wavelet decomposition should subtract off the higher *emission* from the region associated with the thinner Al at the smaller spatial scales. The residual *emission* image is then the transmission of the shield with the thicker Al, and any variations are the large scale variations in the thickness of the shield. In practice, this works quite well if the bright *emission* features have spatial scale much less than

Table 22: Transmission of UVIS S/N 003 segment +1 (region of thin Al) at C K_α.

	Mean (counts)	Variance	Std Dev	$\sqrt{Mean}$
IN image	1651.68 cts	6441.81	80.26 cts	40.64 cts
OUT image	963.19 cts	3359.91	57.96 cts	31.03 cts
Ratio of means ($Mean_{IN}/Mean_{OUT}$)				1.715
Transmission at C K_α(IN/OUT)				**0.706**
Statistical std dev of ratio				**0.070**
Gaussian mean of RATIO image				1.702
Transmission at C K_α(Gaussian)				**0.701**
Gaussian sigma of RATIO image				**0.057**

Table 23: Transmission of UVIS S/N 003 segment +1 (region of thick Al) at C K_α.

	Mean (counts)	Variance	Std Dev	$\sqrt{Mean}$
IN image	495.32 cts	1366.67	36.97 cts	22.26 cts
OUT image	963.19 cts	3359.91	57.96 cts	31.03 cts
Ratio of means ($Mean_{IN}/Mean_{OUT}$)				0.514
Transmission at C K_α(IN/OUT)				**0.212**
Statistical std dev of ratio				**0.028**
Gaussian mean of RATIO image				0.500
Transmission at C K_α(Gaussian)				**0.206**
Gaussian sigma of RATIO image				**0.030**

the size of the image. If these features are on the spatial size of the image, however, the wavelet decomposition will not subtract them out properly. The mean value of the final image of the wavelet decomposition was always between the transmission of the regions. The decomposition did not correctly subtract the excess *emission*. Any structure found by the decomposition is probably not real. I have discussed this issue with Alexey Vikhlinin, and we are in complete agreement that the wavelet decomposition is not appropriate because of the large spatial scale of the shield features.

Table 24: Transmission of UVIS S/N 003 segment -1 (region of thin Al) at C K_α.

	Mean (counts)	Variance	Std Dev	$\sqrt{Mean}$
IN image	1693.54 cts	7367.30	85.83 cts	41.15 cts
OUT image	963.95 cts	3407.49	58.37 cts	31.05 cts
Ratio of means ($Mean_{IN}/Mean_{OUT}$)				1.757
Transmission at C K_α(IN/OUT)				**0.706**
Statistical std dev of ratio				**0.071**
Gaussian mean of RATIO image				1.739
Transmission at C K_α(Gaussian)				**0.699**
Gaussian sigma of RATIO image				**0.078**

Table 25: Transmission of UVIS S/N 003 segment -1 (region of thick Al) at C K_α.

	Mean (counts)	Variance	Std Dev	$\sqrt{Mean}$
IN image	519.91 cts	1281.56	35.80 cts	22.80 cts
OUT image	963.95 cts	3407.49	58.37 cts	31.05 cts
Ratio of means ($\mathrm{Mean}_{IN}/\mathrm{Mean}_{OUT}$)				0.539
Transmission at C K_α(IN/OUT)				**0.217**
Statistical std dev of ratio				**0.029**
Gaussian mean of RATIO image				0.515
Transmission at C K_α				**0.207**
Gaussian sigma of RATIO image				**0.031**

Table 26: Transmission of UVIS S/N 003 segment 0 (region of thick Al) at C K_α (second measurement).

	Mean (counts)	Variance	Std Dev	$\sqrt{Mean}$
IN image	857.42 cts	3025.20	55.00 cts	29.28 cts
OUT image	1212.91 cts	4659.23	68.25 cts	34.83 cts
Ratio of means ($\mathrm{Mean}_{IN}/\mathrm{Mean}_{OUT}$)				0.707
Transmission at C K_α(IN/OUT)				**0.449**
Statistical std dev of ratio				**0.032**
Gaussian mean of RATIO image				0.706
Transmission at C K_α(Gaussian)				**0.448**
Gaussian sigma of RATIO image				**0.024**

Table 27: Transmission of UVIS S/N 003 segment 0 (region of thin Al) at C K_α (second measurement).

	Mean (counts)	Variance	Std Dev	$\sqrt{Mean}$
IN image	1433.26 cts	4629.19	68.04 cts	37.86 cts
OUT image	1212.91 cts	4659.23	68.25 cts	34.83 cts
Ratio of means ($\mathrm{Mean}_{IN}/\mathrm{Mean}_{OUT}$)				1.182
Transmission at C K_α(IN/OUT)				**0.750**
Statistical std dev of ratio				**0.046**
Gaussian mean of RATIO image				1.150
Transmission at C K_α(Gaussian)				**0.730**
Gaussian sigma of RATIO image				**0.047**

Table 28: Transmission of UVIS S/N 003 segment 0 (region of thick Al) at O K_α.

	Mean (counts)	Variance	Std Dev	$\sqrt{Mean}$
IN image	746.843 cts	5715.57	75.60 cts	27.33 cts
OUT image	622.50 cts	7377.48	85.89 cts	24.95 cts
Ratio of means ($\mathrm{Mean}_{IN}/\mathrm{Mean}_{OUT}$)				1.120
Transmission at O K_α(IN/OUT)				**0.580**
Statistical std dev of ratio				**0.065**
Gaussian mean of RATIO image				1.193
Transmission at O K_α(Gaussian)				**0.577**
Gaussian sigma of RATIO image				**0.063**

Table 29: Transmission of UVIS S/N 003 segment 0 (region of thin Al) at O K_α.

	Mean (counts)	Variance	Std Dev	$\sqrt{Mean}$
IN image	831.20 cts	3744.44	61.19 cts	28.97 cts
OUT image	621.09 cts	1783.17	42.23 cts	24.92 cts
Ratio of means ($\mathrm{Mean}_{IN}/\mathrm{Mean}_{OUT}$)				1.350
Transmission at O K_α(IN/OUT)				**0.653**
Statistical std dev of ratio				**0.072**
Gaussian mean of RATIO image				1.336
Transmission at O K_α(Gaussian)				**0.646**
Gaussian sigma of RATIO image				**0.072**

Table 30: Transmission of UVIS S/N 003 segment -1 (region of thin Al) at O K_α.

	Mean (counts)	Variance	Std Dev	$\sqrt{Mean}$
IN image	849.95 cts	7812.38	88.39 cts	29.15 cts
OUT image	597.51 cts	4665.47	68.30 cts	24.44 cts
Ratio of means ($\mathrm{Mean}_{IN}/\mathrm{Mean}_{OUT}$)				1.423
Transmission at O K_α(IN/OUT)				**0.696**
Statistical std dev of ratio				**0.076**
Gaussian mean of RATIO image				1.413
Transmission at O K_α(Gaussian)				**0.692**
Gaussian sigma of RATIO image				**0.076**

Table 31: Transmission of UVIS S/N 003 segment -1 (region of thick Al) at O K_α.

	Mean (counts)	Variance	Std Dev	$\sqrt{Mean}$
IN image	663.997 cts	1.13E6	1061.57 cts	25.77 cts
OUT image	642.554 cts	5468.34	73.95 cts	25.35 cts

Ratio of means ($Mean_{IN}/Mean_{OUT}$)	1.033
Transmission at O K_α(IN/OUT)	**0.506**
Statistical std dev of ratio	**0.057**
Gaussian mean of RATIO image	1.085
Transmission at O K_α	**0.531**
Gaussian sigma of RATIO image	**0.056**

Table 32: Transmission of UVIS S/N 003 segment +1 (region of thin Al) at O K_α.

	Mean (counts)	Variance	Std Dev	$\sqrt{Mean}$
IN image	859.42 cts	5846.75	76.46 cts	29.32 cts
OUT image	615.81 cts	4034.30	63.52 cts	24.82 cts

Ratio of means ($Mean_{IN}/Mean_{OUT}$)	1.396
Transmission at O K_α(IN/OUT)	**0.698**
Statistical std dev of ratio	**0.074**
Gaussian mean of RATIO image	1.387
Transmission at O K_α(Gaussian)	**0.693**
Gaussian sigma of RATIO image	**0.072**

Table 33: Transmission of UVIS S/N 003 segment +1 (region of thick Al) at O K_α.

	Mean (counts)	Variance	Std Dev	$\sqrt{Mean}$
IN image	714.04 cts	6611.65	81.31 cts	26.72 cts
OUT image	661.497 cts	6197.85	78.73 cts	25.72 cts

Ratio of means ($Mean_{IN}/Mean_{OUT}$)	1.079
Transmission at O K_α(IN/OUT)	**0.540**
Statistical std dev of ratio	**0.058**
Gaussian mean of RATIO image	1.072
Transmission at O K_α(Gaussian)	**0.536**
Gaussian sigma of RATIO image	**0.062**

Table 34: Transmission of UVIS S/N 003 segment -1 (region of thick Al) at B K_α.

	Mean (counts)	Variance	Std Dev	$\sqrt{Mean}$
IN image	31.48 cts	110.383	10.51 cts	5.61 cts
OUT image	428.935 cts	763.127	27.62 cts	20.71 cts
Ratio of means ($Mean_{IN}/Mean_{OUT}$)				0.0734
Transmission at B K_α(IN/OUT)				**0.042**
Statistical std dev of ratio				**0.0136**
Gaussian mean of RATIO image				0.0632
Transmission at B K_α(Gaussian)				**0.036**
Gaussian sigma of RATIO image				**0.0300**

Table 35: Transmission of UVIS S/N 003 segment -1 (region of thin Al) at B K_α.

	Mean (counts)	Variance	Std Dev	$\sqrt{Mean}$
IN image	384.582 cts	685.492	26.18 cts	19.62 cts
OUT image	428.935 cts	763.127	27.62 cts	20.71 cts
Ratio of means ($Mean_{IN}/Mean_{OUT}$)				0.897
Transmission at B K_α(IN/OUT)				**0.513**
Statistical std dev of ratio				**0.063**
Gaussian mean of RATIO image				0.889
Transmission at B K_α(Gaussian)				**0.508**
Gaussian sigma of RATIO image				**0.103**

4.8.3 Synchrotron X-ray Transmission Measurements

In order to define an accurate model of X-ray Absorption Near Edge Structures (XANES), high spectral resolution x-ray transmission measurements in the energy range of 70-1950 eV were conducted on four witness samples at the BESSY 1 synchrotron in Berlin, Germany.

Instrumental Setup

The measurements were conducted at station 11.31 of the Physikalisch-Technische Bundesanstalt (PTB) radiometry laboratory at the BESSY 1 synchrotron. The beam-line includes an SX-700 type plane grating monochromator with a useful photon energy range of 60 - 2000 eV and spectral resolution ranging from $E/\Delta E = 2500$ at 100 eV to $E/\Delta E = 700$ at the Al-K edge. A test chamber (700 mm long, 600 mm in diameter) was provided with a vacuum-compatible micro-positioning system for the manipulation of witness samples and detectors. Two detectors were used: a GaP/Au Schottky-type photodiode (Hamamatsu G1963) with a sensitive area of 4.6 mm$\times$4.6 mm; and a VALVO X913 BL channel electron multiplier (CEM). The photodiode performs well and is actually used at all surveyed energies with the exception of the 283-300 eV range, where the CEM is more appropriate because of the low flux available in that region.

The four samples that were studied are listed in Table **??**. They were mounted on a five-position fixture (one position left open) attached to a micro-positioning system allowing complete two dimensional scans of the samples. A 400 μm spot size was chosen as the best compromise between flux stability and spatial resolution. Table 36 describes the energy scans in detail.

Each individual measurement at a given energy is the average of 3 independent consecutive detector readings. If the readings are not consistent with each other to within 1%, the measurement is automatically repeated. Each measurement is normalized by the current of the beam in the storage ring. This procedure accounts for the time dependence of the beam, ensuring measurement stability at the 1% level over a time scale of 30 minutes. In order to ensure no significant drift between measurements at the open and sample positions, all of our measurement sets were taken over time scales shorter than 10 minutes.

The measurement technique described above ensures a statistical uncertainty within 1% at all energies. Stray light contribution in the monochromatic radiation between 1.0 and 1.7 keV is up to 2%, resulting in a transmission uncertainty within 1% for measured samples like ours. Above 1.7 keV, the stray light contamination is higher, and results in a measurement uncertainty up to 3%. Second order contamination is particularly significant at low energies ($E < 130$ eV), and in a small region above the carbon edge (290-300 eV), resulting in a measurement uncertainty of up to 30%. Outside of these regions, the measurement uncertainties are always lower than 3%.

Table 36: Energies surveyed in the synchrotron transmission measurements.

Beam Filter	Energy range (eV)	energy step (eV)	Absorption Edge
Beryllium 0.25 μm	$60 - 71$	1	
Beryllium 0.25 μm	$71.2 - 75$	0.2	Aluminum LII,LIII
Beryllium 0.25 μm	$76 - 110$	1	
No Filter	$100 - 250$	2	
Titanium 1 μm	$250 - 280$	2	
Titanium 1 μm	$280.5 - 293$	0.5	Carbon K
Titanium 1 μm	$295 - 400$	5	
Titanium 1 μm	$400.2 - 415$	0.2	Nitrogen K
Titanium 1 μm	$416 - 450$	1	
Iron 0.5 μm	$450 - 520$	3	
Iron 0.5 μm	$521 - 529$	1	
Iron 0.5 μm	$529.2 - 540$	0.2	Oxygen K
Iron 0.5 μm	$541 - 565$	1	
Iron 0.5 μm	$541 - 600$	1	
Iron 0.5 μm	$605 - 700$	5	
Copper 0.5 μm	$700 - 900$	5	
Berylium 7 μm	$900 - 1540$	10	
Berylium 7 μm	$1542 - 1600$	2	Aluminum K
Berylium 7 μm	$1605 - 1700$	5	
Berylium 7 μm	$1710 - 1950$	10	

Results

Previous synchrotron measurements conducted on witness samples of candidate HRC UV/Ion shields revealed no significant spatial variation of the near edge absorption structures. We therefore tested only one witness sample for spatial variations of the fine structures. Figure 132 shows in detail the transmission measurements near the absorption K-edges of C, N, O, and Al for the two locations surveyed on the witness sample TF101-1174. These measurements again confirm that no significant spatial variations (at 0.4 mm resolution) are observed for the absorption fine structures. We expect a similar variation in transmission at this spatial scale for the flight HRC-I UV/ion shield, as it is derived from the same multi-layer sheet of film as this witness sample.

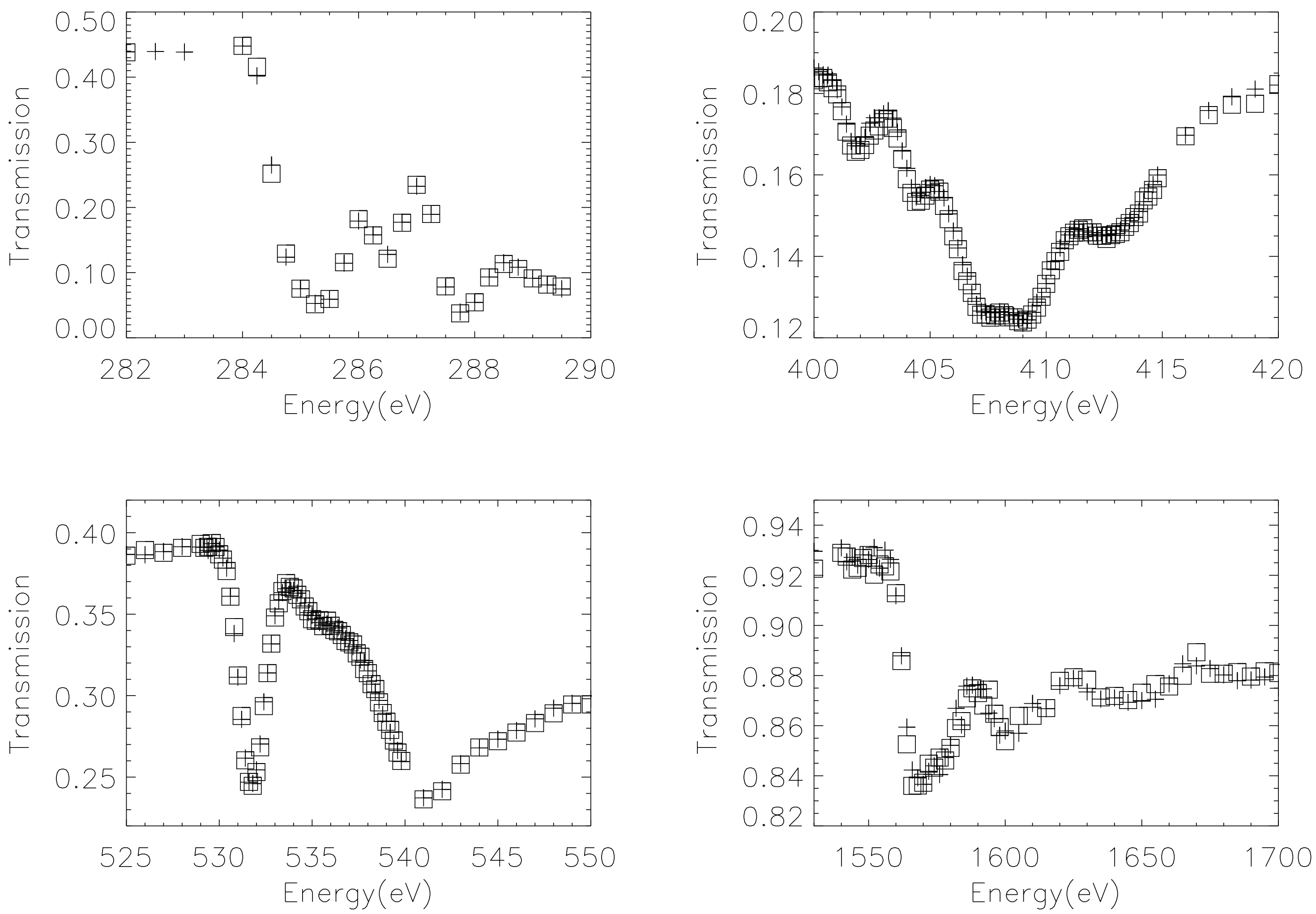

Figure 132: Absorption fine structures of the C, N, O, and Al K-edges measured in two different locations (plus symbol and square symbol) of witness sample TF101-1174.

The measured transmission for the four tested samples are reported in figures 133 through 136. In these plots, the transmission data (along with the associated error bars) are superimposed over the best-fit curve. The data, with the exception of small energy regions around the absorption edges, have been fitted with the x-ray transmission model described in section 2.3. Table 37 reports the best fit parameters for the mass areal density of C, N, O, and Al. For comparison, those witness samples with matching run numbers that were measured with the SAO x-ray monochromator are included. Notice that the best fit parameters derived from the two test methods for the two witness samples associated with run number 6550-8 (which have the same material thicknesses) agree within the error limits. A similar statement can be made for the witness samples associated with run number 6788-8. The pair of witness samples associated with run number 6569-8 (TF100-354 and TF101-1092), and the pair of witness samples associated with run number 6567-8 (TF101-891 and TF100-565), each represents different regions of an HRC-S outer segment flight UV/ion shield. For a given pair of witness samples, the best fit parameters for C, N and O are comparable, within the uncertainties. This is consistent with the fact that the polyimide thickness of the filter pair is the same. Since a given pair of witness samples represents different regions of a flight HRC-S filter, the aluminum thicknesses are not equal. This is reflected by the difference in their respective mass areal densities. Table ?? shows that, for each such pair of witness samples, the ratio of the mass areal densities of aluminum agrees with the ratio of the thickness values measured by Luxel, within the uncertainties. Table 13 lists the derived polyimide thicknesses for the samples tested with the synchrotron source, while Table 39 lists their derived aluminum thicknesses. For comparison, Luxel's thickness measurements are included in both tables.

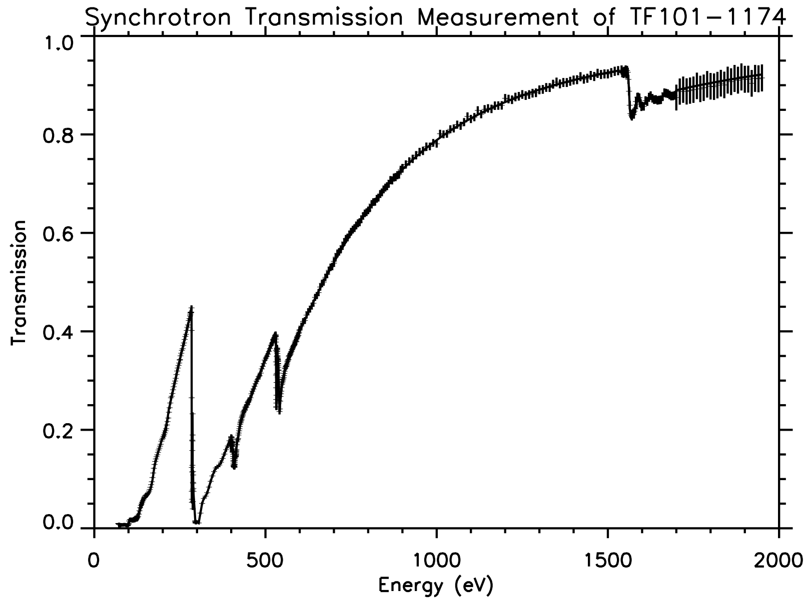

Figure 133: The measured transmission (the data points with error bars) for witness sample TF101-1174 at location 1. The best fit model, which incorporates the derived mass attenuation coefficients near the absorption edges, appears as the solid line.

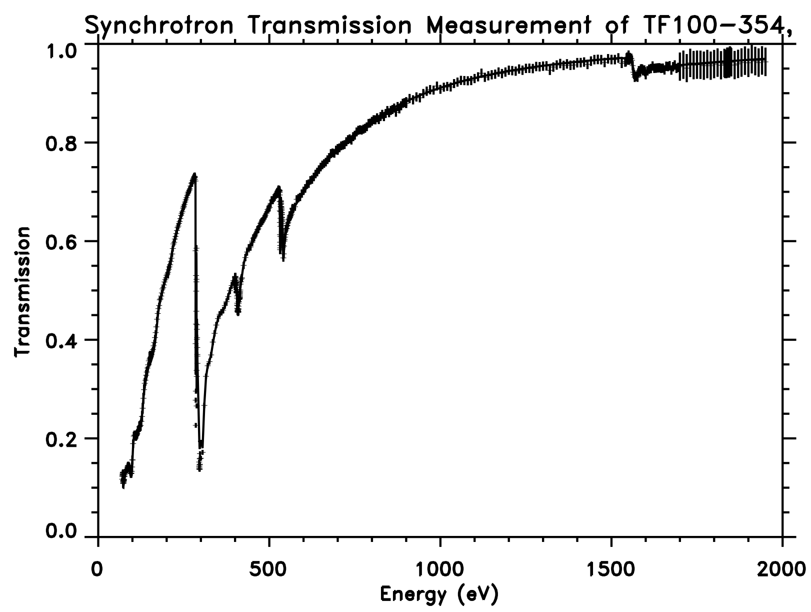

Figure 134: The measured transmission (the data points with error bars) for witness sample TF100-354. The best fit model, which incorporates the derived mass attenuation coefficients near the absorption edges, appears as the solid line.

Table 37: The mass areal densities from the best fit results of the x-ray synchrotron transmission measurements, compared to matching witness samples (run numbers) from the SAO monochromator results.

Witness Sample	Run Number	Al (μg/cm^2)	C (μg/cm^2)	N (μg/cm^2)	O (μg/cm^2)	Test Method
TF100-354	6569-8	7.26 ± 0.16	20.94 ± 0.62	1.68 ± 0.52	7.11 ± 0.40	Synchrotron
TF101-1092	6569-8	47.65 ± 0.67	21.74 ± 0.83	1.79 ± 0.96	6.62 ± 1.38	SAO Monochromator
TF101-891	6567-8	50.34 ± 0.45	20.00 ± 0.93	1.84 ± 0.75	7.54 ± 0.45	Synchrotron
TF100-565	6567-8	7.92 ± 0.47	21.10 ± 0.66	1.05 ± 1.00	6.62 ± 1.25	SAO Monochromator
TF101-1053	6550-8	24.54 ± 0.25	25.68 ± 0.78	2.06 ± 0.65	8.88 ± 0.44	Synchrotron
TF101-1052	6550-8	23.82 ± 0.45	26.33 ± 0.71	2.34 ± 0.91	9.83 ± 1.19	SAO Monochromator
TF101-1174	6788-8	19.93 ± 0.18	55.37 ± 1.25	5.75 ± 0.99	15.75 ± 0.49	Synchrotron
TF101-1174	6788-8	18.99 ± 0.51	54.01 ± 1.13	6.80 ± 1.21	16.02 ± 1.47	SAO Monochromator
TF101-1175	6788-8	19.15 ± 0.48	55.09 ± 1.13	5.91 ± 1.21	16.76 ± 1.35	SAO Monochromator

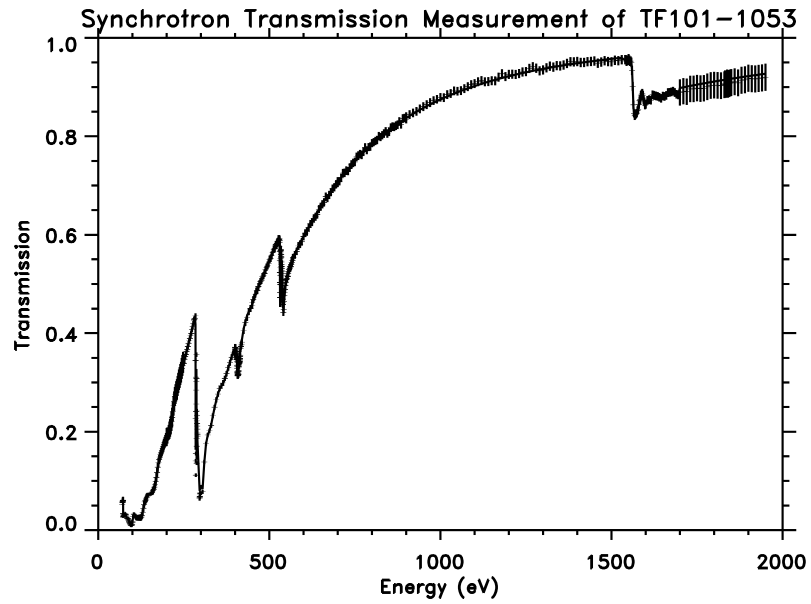

Figure 135: The measured transmission (the data points with error bars) for witness sample TF101-1053. The best fit model, which incorporates the derived mass attenuation coefficients near the absorption edges, appears as the solid line.

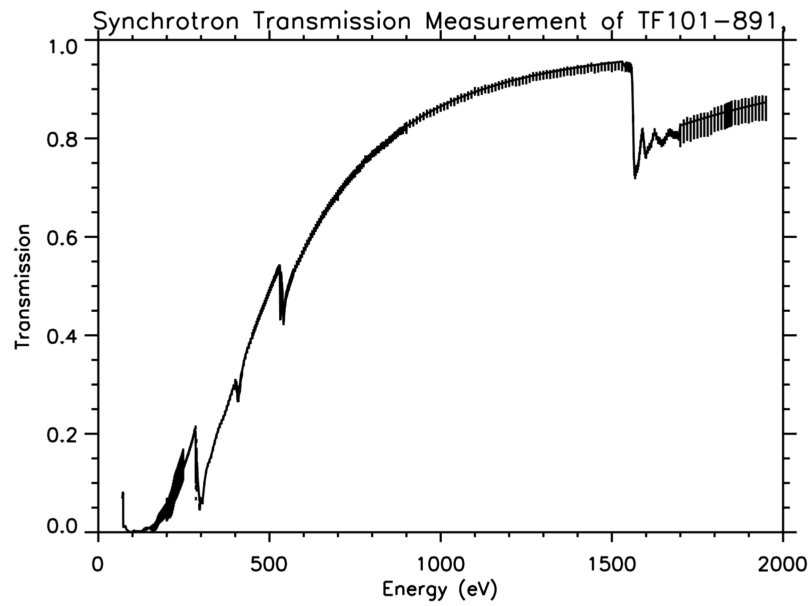

Figure 136: The measured transmission (the data points with error bars) for witness sample TF101-891. The best fit model, which incorporates the derived mass attenuation coefficients near the absorption edges, appears as the solid line.

Table 38: A comparison of the ratio of Al mass areal densities of two pairs of witness samples with the ratio of the aluminum thickness values measured by Luxel.

Witness Sample Pairing	Ratio of Al Mass Areal Densities	Ratio of Luxel Al Thickness values
TF101-1092 TF100-354	6.56 ± 0.17	6.45 ± 0.69
TF101-891 TF100-565	6.36 ± 0.38	6.43 ± 0.66

Table 39: The derived aluminum thicknesses for the witness samples measured with the synchrotron x-ray source are compared to Luxel's measurements. Note that the two sets of values agree, within the statistical uncertainties.

Witness Sample	Run Number	Luxel Al Measured Thickness ($\mathring{A}$)	Derived Al Thickness ($\mathring{A}$)
TF100-354	6569-8	305 ± 30	290 ± 6.4
TF101-891	6567-8	2025 ± 58	2014 ± 18.0
TF101-1053	6550-8	972 ± 58	981.6 ± 10.0
TF101-1174	6788-8	795 ± 50	797.2 ± 7.2

The mass attenuation coefficient derived for a compound by taking into account only the individual atomic coefficients does not take into consideration fine structure features that occur near the absorption edges due to interactions of the photoelectrons with the closer atoms in the molecules of the compound (XANES and EXAFS). In order to define the mass attenuation coefficients of a compound that include these features, direct transmission measurements need to be conducted on the compound material of interest. Following the same technique described by us in an earlier work, we have used the synchrotron measurements and the above mentioned best fit model parameters of witness sample TF101-1174 (the sample with the thickest layer of polyimide) to derive the mass attenuation coefficients of C, N, and O near their K absorption edges. Analogously, we have used the measurements and the best fit model parameters of witness sample TF101-891 (the sample with the thickest layer of aluminum) to derive the mass attenuation coefficients of Al near its K and L absorption edges. Adopting the mass attenuation coefficients now extended to the absorption edge regions, we have built new transmission models for the four samples (refer to figures 133 through 136). The x-ray transmission model, which incorporates the newly derived mass attenuation coefficients near the absorption edges with the literature-based mass attenuation coefficients outside of the absorption edges, is in very good agreement with our measurements. Figure 137 gives a detailed view of how well the transmission model agrees with the measurements near the K-edge absorption regions for C, N, O and Al for filter TF100-354, while figure 138 shows the relative residuals between the transmission measurements of this filter and the associated model. Note that these plots show that there is good agreement between the measurements and the fit, except at several energies near the carbon K-edge absorption region. There are two possible explanations for this discrepancy. The first is that we have under-estimated the error in the measured transmission due to higher order contamination (that is, 3^{rd} order and higher) from carbon. The second is that there is a dependence of the transmission on features in the filter itself, though we consider this to be unlikely. We are continuing to investigate this issue. Despite this discrepancy at carbon, we obtain very good agreement between the measurements and the fits near the K-edge absorption regions for N, O and Al for all four filters that were tested. Also, the peaks of the modeled transmission curves occur at the same energy locations for all four filters in each of the four near-edge absorption regions. This model can be extended to filter samples of the same material composition, but of different thicknesses, provided that the mass areal densities of C, N, O, and Al are derived from the best fit analysis on a small number of measurements like those reported on in section 2. The mass absorption coefficients derived near the K-edge absorption regions of C, N, O and Al are depicted in figure 139. Included in each graph is a line plot that represents the 1982 Henke coefficients.

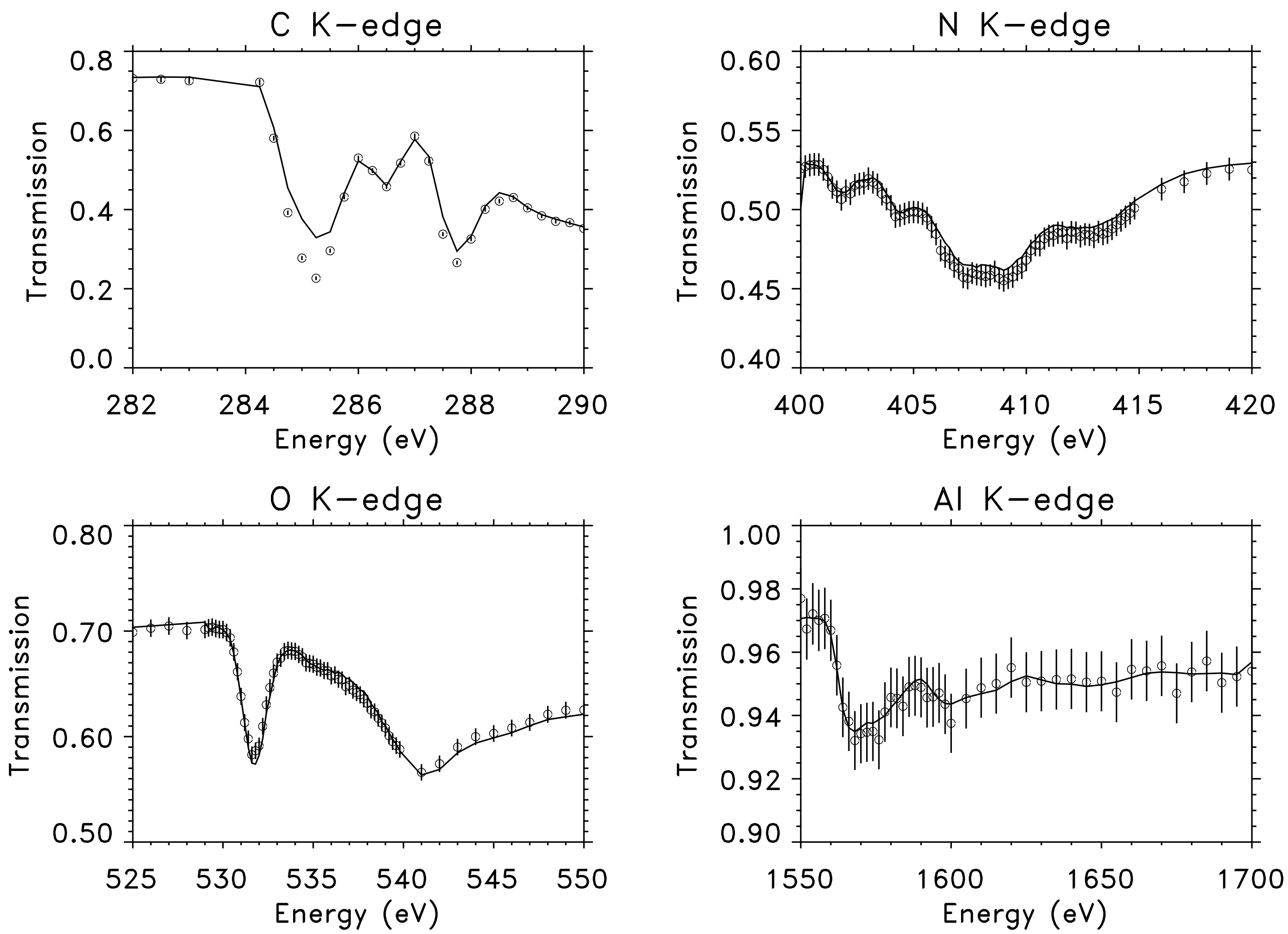

Figure 137: Each of the above plots gives a detailed look at how well the synchrotron transmission model (line plot) agrees with the synchrotron transmission measurements of filter TF100-354 at the absorption fine structure regions for the C, N, O and Al K-edges. Note that there are several energies in the C K-edge absorption region where the model and the data do not agree very well.

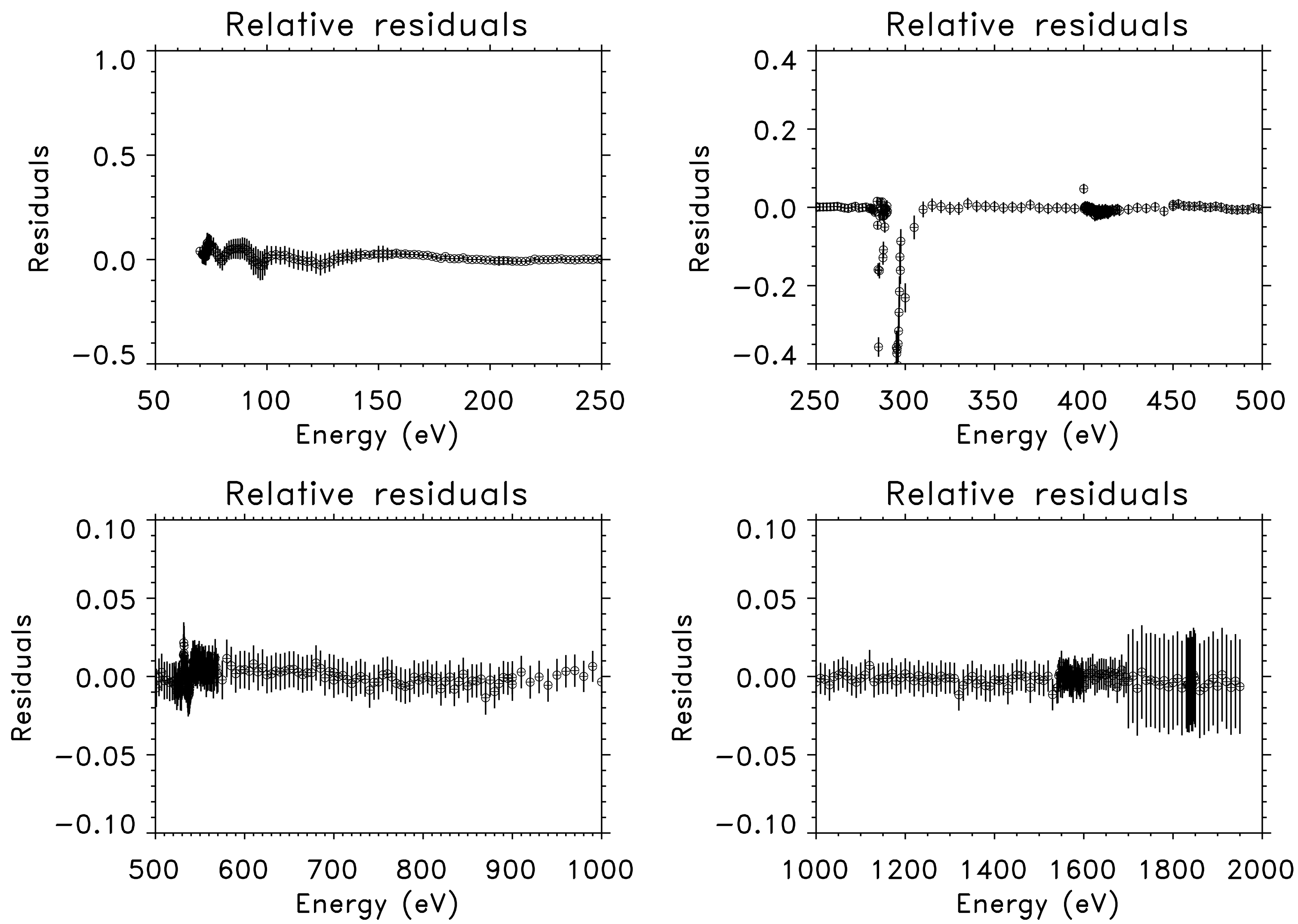

Figure 138: The relative residuals for synchrotron the transmission measurements and the model of filter TF100-354. Note that we obtain good agreement between the fit and the measurements, except at several energies near the carbon K-edge absorption region.

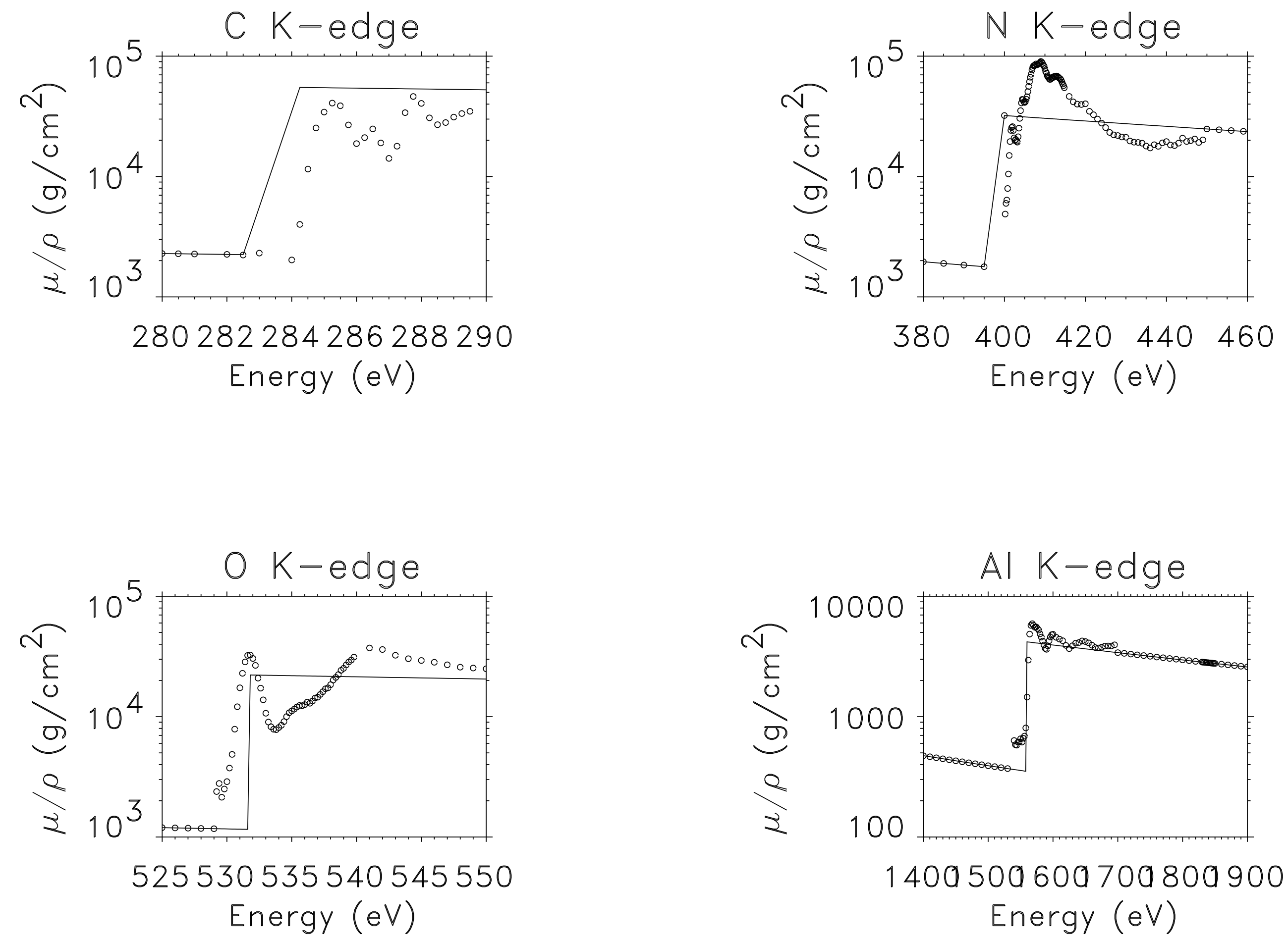

Figure 139: The above plots show the mass absorption coefficients of each element at its respective K-edge absorption region as developed from the transmission model based on the synchrotron measurements. The line plots in the graphs represent the 1982 Henke coefficients.

4.8.4 UV and Visible Light Transmission

A final aspect to the calibration of the UV/ion shield witness samples is the development of UV light transmission models. This is an on-going task, for which it will be necessary to perform transmission measurements in the visible and near UV (at many discrete wavelengths). We have started this process by measuring the UV transmission of the imaging detector witness samples at 1470 Å and at 2537 Å and completed measurements in the visible of imaging and spectroscopy witness samples. We have developed provisional transmission models for the shields based upon these measurements and measurements made on shield components by our group and by others. .

Due to the extremely low UV transmission of the image detector witness samples, the method of performing a sequence of filter-in/filter-out measurements is impractical. Instead, we measured the flux of photons from a UV light source that passed through the witness sample under test. We also determined the photon flux of the UV light source itself. The ratio of the photon flux transmitted through the witness sample to the photon flux of the UV source yields the transmission at that particular wavelength.

To measure the photon flux transmitted through the witness sample, the test configuration shown in figure 140 is used. The witness sample under test is mounted onto a Schlumberger EMR photomultiplier tube (model 541F-09-17). To measure the UV flux through the witness sample at 1470 Å, we employed an ultraviolet calibration xenon lamp (EMR Photoelectric, model 582X-05). A UV interference filter with a peak transmission of 10% at 1470 Å was mounted in front of it. At 2537 Å, we used a mercury light source (Pen-Ray, model 11 SC-1) in combination with an interference filter that has a peak transmission of about 15% at 2537 Å.

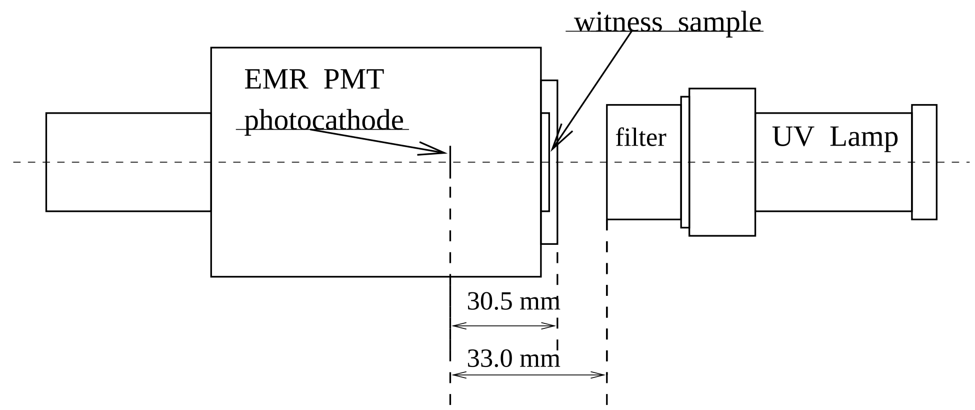

Figure 140: The setup used for witness sample UV flux measurements at 1470 Å and 2537 Å. To measure the flux from the UV light source, the PMT was replaced with a NIST UV photodiode.

The UV beam flux from each lamp was measured with a NIST UV photodiode (Ball Aerospace, serial no. 94-3). Its 25mm-diameter sensitive area was stopped down to 12.5mm so that the detector would subtend the same solid angle at the source as the PMT photocathode did. The photodiode has a quantum efficiency of 9.1% at 1470 Å, and of 14.3% at 2537 Å.

Table 40 lists the UV transmission measurements that have been obtained. In addition, Luxel's broadband visible light transmission measurements are included in the table. Only witness samples TF101-1174 and TF101-1175 are samples for a flight shield, the imaging detector shield. The others are witness samples for former flight shield candidates.

Table 40: The UV transmission measurement results at 1470 $\AA$ and at 2537 $\AA$ that have been completed to-date are listed above. Luxel's visible light measurements are included.

Witness Sample	UV Transmission at 1470 $\AA$	UV Transmission at 2537 $\AA$	Luxel Visible Light Measurement
TF101-883	4.7×10^{-11}	4.4×10^{-12}	4.25×10^{-5}
TF101-1052	7.9×10^{-8}	1.4×10^{-8}	9.57×10^{-6}
TF101-1053	9.3×10^{-8}	7.8×10^{-9}	9.59×10^{-6}
TF101-1054	2.1×10^{-7}	1.1×10^{-8}	3.75×10^{-5}
TF101-1174	4.4×10^{-11}	5.8×10^{-12}	3.73×10^{-5}
TF101-1175	5.0×10^{-11}	4.4×10^{-12}	3.21×10^{-5}

The visible light transmissions of witness samples corresponding to the imaging detector shield and the thinnest outer segment of the spectroscopy detector shield were measured with a Hitachi spectrophotometer over the wavelength range 3000 $\AA$ - 8000 $\AA$. The results of these measurements are shown in Figure 141 and Figure 142. Since the statistics are poor, we have smoothed the data for the low transmission sample corresponding to the imaging detector and fit it with a loess function.

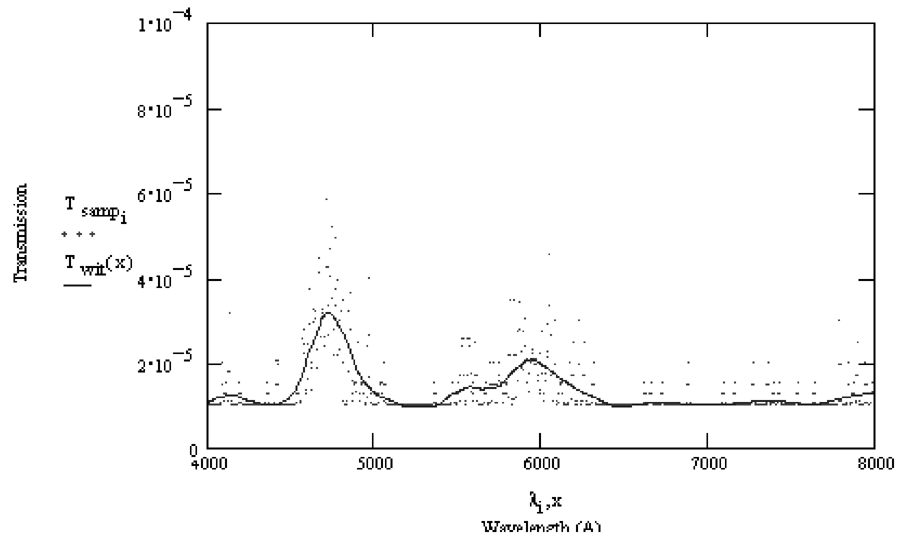

Figure 141: Measured visible light transmission of the witness sample corresponding to the UVIS of HRC-I. The data has been smoothed and fit with a loess function.

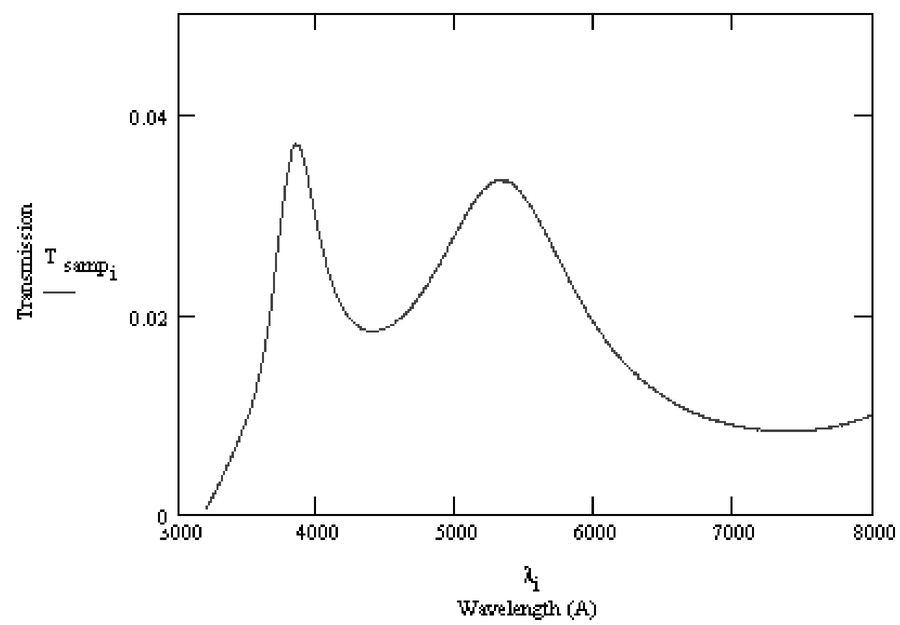

Figure 142: Measured visible light transmission of the witness sample corresponding to the UVIS of HRC-S.

We have generated a transmission model for the imaging detector shield for the wavelength range 100 $\AA$ - 8000 $\AA$ by assuming a slab model (the transmission is equal to the product of the transmission of the polyimide substrate and the aluminum coating) for the wavelength range 100 $\AA$ - 4400 $\AA$ and using the loess function transmission for the wavelength range 4400 $\AA$ - 8000 $\AA$.

We have generated a transmission model for the thinnest outer segment of the spectroscopy detector shield for the wavelength range 100 $\AA$ - 8000 $\AA$ by assuming a slab model for the wavelength range 100 $\AA$ - 3200 $\AA$ and using the measured transmission for the wavelength range 3200 $\AA$ - 8000 $\AA$. The linear attenuation coefficients for the polyimide substrate were determined by our group by making transmission measurements on thin polyimide membranes at the UV laboratory of Berkeley's Space Science Laboratory. The mass attenuation coefficients for the aluminum coating were obtained from the synchrotron measurements of Hagemann, et al. (DESY). We have plotted the coefficients (see Figure 143 and Figure 144). Figure 145 and Figure 146 show the modeled transmissions for the shields. For the imager shield the material thicknesses, based upon the x-ray measurements above, are: polyimide - 5520 $\pm$193 $\AA$, aluminum - 763 $\pm$28 $\AA$. For the spectroscopy shield the material thicknesses, based upon the x-ray measurements above, are: polyimide - 2090 $\pm$140 $\AA$, aluminum - 304 $\pm$20 $\AA$.

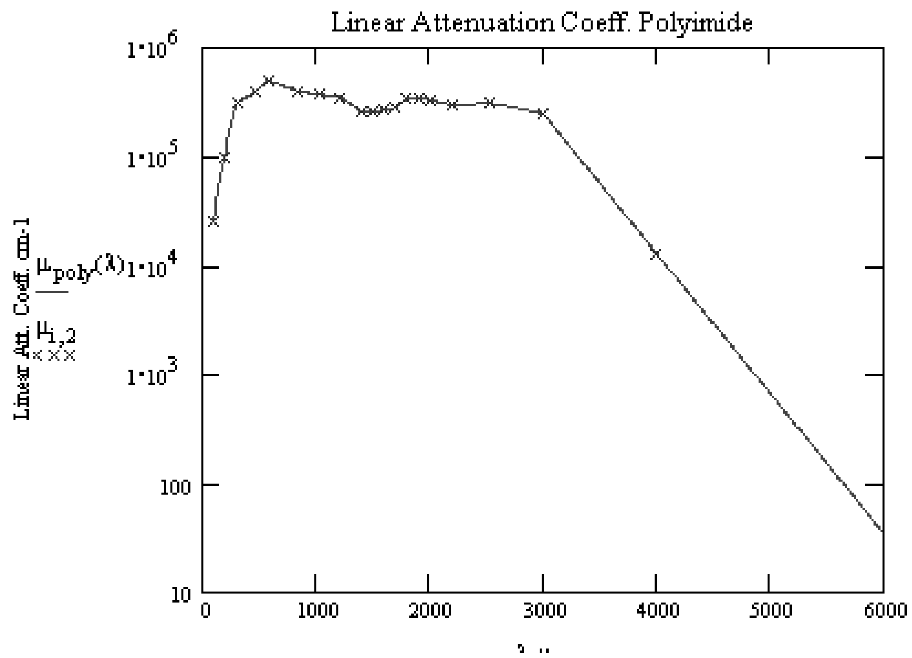

Figure 143: The linear attenuation coefficient of polyimide vs wavelength. An exponential extrapolation has been made beyond 4000 $\mathring{A}$.

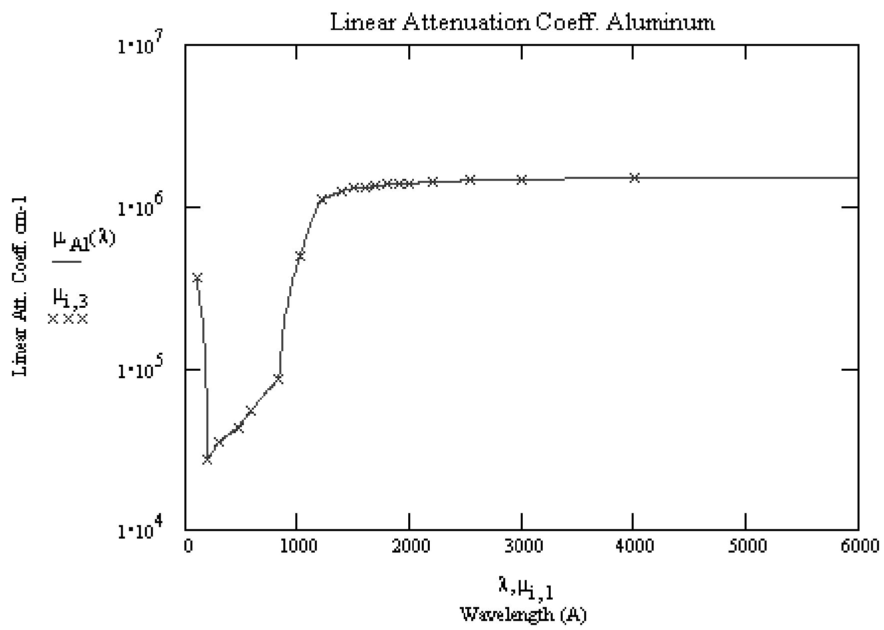

Figure 144: The linear attenuation coefficient of aluminum vs wavelength.

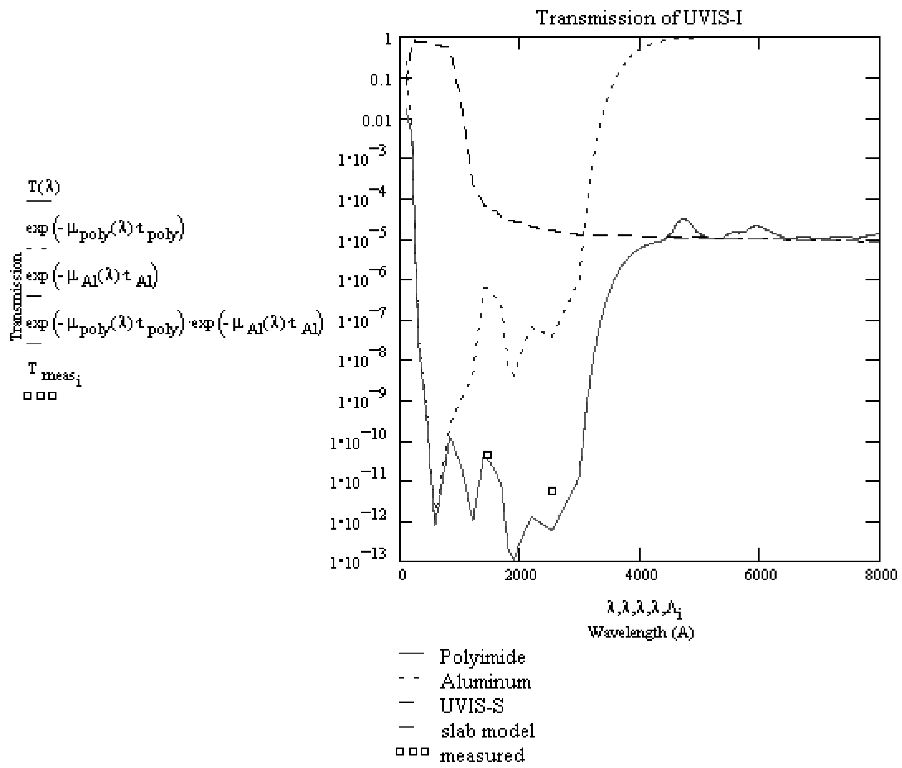

Figure 145: Transmission model of the HRC-I UVIS in the UV and visible.

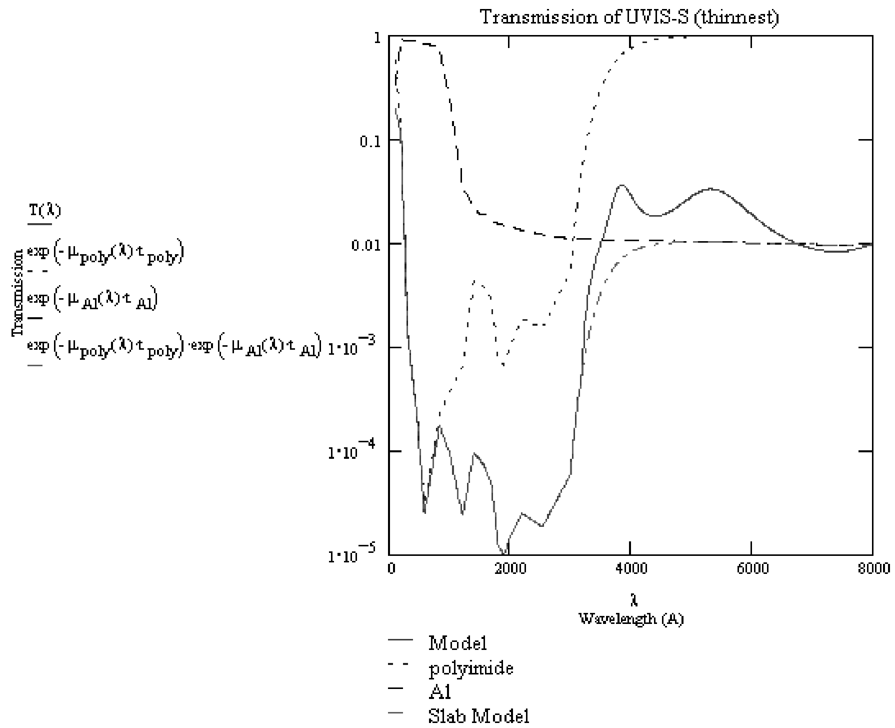

Figure 146: Transmission model of the thinnest section of the HRC-I UVIS in the UV and visible.